EARTH DEEP INTERIOR: HIGH-PRESSURE EXPERIMENTS AND THEORETICAL CALCULATIONS FROM THE ATOMIC TO THE GLOBAL SCALE

EDITED BY: Lidong Dai, Haiying Hu, Jianjun Jiang, Xi Liu, Geeth Manthilake and Vassilios Saltas

PUBLISHED IN: Frontiers in Earth Science

frontiers Research Topics

frontiers

ISSN 1664-8714
ISBN 978-2-88976-543-0
DOI 10.3389/978-2-88976-543-0

About Frontiers

Frontiers is more than just an open-access publisher of scholarly articles: it is a pioneering approach to the world of academia, radically improving the way scholarly research is managed. The grand vision of Frontiers is a world where all people have an equal opportunity to seek, share and generate knowledge. Frontiers provides immediate and permanent online open access to all its publications, but this alone is not enough to realize our grand goals.

Frontiers Journal Series

The Frontiers Journal Series is a multi-tier and interdisciplinary set of open-access, online journals, promising a paradigm shift from the current review, selection and dissemination processes in academic publishing. All Frontiers journals are driven by researchers for researchers; therefore, they constitute a service to the scholarly community. At the same time, the Frontiers Journal Series operates on a revolutionary invention, the tiered publishing system, initially addressing specific communities of scholars, and gradually climbing up to broader public understanding, thus serving the interests of the lay society, too.

Dedication to Quality

Each Frontiers article is a landmark of the highest quality, thanks to genuinely collaborative interactions between authors and review editors, who include some of the world's best academicians. Research must be certified by peers before entering a stream of knowledge that may eventually reach the public - and shape society; therefore, Frontiers only applies the most rigorous and unbiased reviews.
Frontiers revolutionizes research publishing by freely delivering the most outstanding research, evaluated with no bias from both the academic and social point of view. By applying the most advanced information technologies, Frontiers is catapulting scholarly publishing into a new generation.

What are Frontiers Research Topics?

Frontiers Research Topics are very popular trademarks of the Frontiers Journals Series: they are collections of at least ten articles, all centered on a particular subject. With their unique mix of varied contributions from Original Research to Review Articles, Frontiers Research Topics unify the most influential researchers, the latest key findings and historical advances in a hot research area! Find out more on how to host your own Frontiers Research Topic or contribute to one as an author by contacting the Frontiers Editorial Office: frontiersin.org/about/contact

EARTH DEEP INTERIOR: HIGH-PRESSURE EXPERIMENTS AND THEORETICAL CALCULATIONS FROM THE ATOMIC TO THE GLOBAL SCALE

Topic Editors:
Lidong Dai, Institute of geochemistry, Chinese Academy of Sciences, China
Haiying Hu, Institute of Geochemistry, Chinese Academy of Sciences, China/Institute of Geochemistry, China
Jianjun Jiang, Institute of Geochemistry, Chinese Academy of Sciences (CAS), China
Xi Liu, Peking University, China
Geeth Manthilake, UMR6524 Laboratoire Magmas et Volcans (LMV), France
Vassilios Saltas, Hellenic Mediterranean University, Greece

Citation: Dai, L., Hu, H., Jiang, J., Liu, X., Manthilake, G., Saltas, V., eds. (2022). Earth Deep Interior: High-pressure Experiments and Theoretical Calculations From the Atomic to the Global Scale. Lausanne: Frontiers Media SA.
doi: 10.3389/978-2-88976-543-0

Table of Contents

frontiers | Frontiers in Earth Science

EDITORIAL
published: 17 June 2022
doi: 10.3389/feart.2022.915318

Editorial: Earth Deep Interior: High-Pressure Experiments and Theoretical Calculations From the Atomic to the Global Scale

Lidong Dai[1], *Geeth Manthilake*[2], *Vassilios Saltas*[3], *Haiying Hu*[1]*, *Jianjun Jiang*[1] and *Xi Liu*[4]*

[1]Key Laboratory for High-Temperature and High-Pressure Study of the Earth's Interior, Institute of Geochemistry, Chinese Academy of Sciences, Guiyang, China, [2]Laboratoire Magmas et Volcans, CNRS, IRD, OPGC, Université Clermont Auvergne, Clermont-Ferrand, France, [3]Institute of Physics of Earth's Interior and Geohazards, UNESCO Chair in Solid Earth Physics and Geohazards Risk Reduction, Hellenic Mediterranean University Research Center, Crete, Greece, [4]MOE Key Laboratory of Orogenic Belts and Crustal Evolution, School of Earth and Space Sciences, Peking University, Beijing, China

Keywords: synchrotron single-crystal X-ray diffraction, electrical conductivity, elastic wave, partial melting, crystalline structure, rock physics, theoretical calculation, high pressure

Editorial on the Research Topic

Earth Deep Interior: High-pressure Experiments and Theoretical Calculations from the Atomic to the Global Scale

OPEN ACCESS

Edited and reviewed by:
Sergey S. Lobanov,
GFZ German Research Centre for Geosciences, Germany

***Correspondence:**
Haiying Hu
huhaiying@vip.gyig.ac.cn
Xi Liu
xi.liu@pku.edu.cn

Specialty section:
This article was submitted to Solid Earth Geophysics, a section of the journal Frontiers in Earth Science

Received: *07 April 2022*
Accepted: *09 May 2022*
Published: *17 June 2022*

Citation:
Dai L, Manthilake G, Saltas V, Hu H, Jiang J and Liu X (2022) Editorial: Earth Deep Interior: High-Pressure Experiments and Theoretical Calculations From the Atomic to the Global Scale. Front. Earth Sci. 10:915318. doi: 10.3389/feart.2022.915318

This Research Topic, hosted by Frontiers in Earth Science, responds to the eighth "From Atom to Earth" Symposium on High-Pressure Science and Earth Science, held at the Institute of Geochemistry, Chinese Academy of Sciences (IGCAS), Guiyang, China between July 2 and 5, 2021. Professor Lidong Dai from the IGCAS Key Laboratory of High-temperature and High-pressure Study of the Earth's Interior (HTHPSEI) was the conference president. Since 2007, this symposium has been organized as a major platform for Chinese scientists in the high-P research field to share their latest progress and discoveries in the field of physicochemical properties of minerals and rocks at high-temperature and high-pressure conditions. This time, 156 Chinese scholars and researchers from Peking University, Nanjing University, the Chinese Academy of Sciences, etc., participated in the conference. Of these delegates, 65 gave oral presentations, and professors Xi Liu, Duanwei He, Lidong Dai, Chun-An Tang, and Zizheng Gong delivered conference speeches (**Figure 1**). As distinguished and invited delegates, professors Hongsen Xie and Heping Li attend this conference. CAS Key Laboratory of HTHPSEI, together with IGCAS and the Chinese Society of Mineralogy, Petrology, and Geochemistry, provided the conference service.

The Research Topic contains ten papers including nine original studies and one review article reporting on the physicochemical properties of minerals and rocks obtained by using high-temperature and high-pressure experiments and theoretical calculations. The experimental studies mainly focus on high-P crystallographic features, electrical conductivity properties, and the partial melting of minerals and rocks. The theoretical calculations mostly investigate crystalline structures and rock physical parameters including crack density, fluid saturation, scalar field, charge density, and layer charge distribution, etc.

In their review, Berrada and Secco focus on research progress for electrical resistivity of Fe and Fe-alloys from the laboratory-based high-P experiments using diamond anvil cell, multi-anvil press, and shock compression equipment, as well as from first-principles calculations. Special attention is paid to the effects of some light elements (Si, S, O) on the electrical resistivity

FIGURE 1 | Group photo for the eighth “From Atom to Earth” Symposium on High-Pressure Science and Earth Science held in IGCAS, Guiyang, China between July 2nd and fifth, 2021.

of pure Fe and Fe-alloys in the deep interior of the Earth and other planets (Moon, Mercury, Mars, Ganymede).

Some high-P experimental and theoretical calculating investigations have been reported for some minerals and rocks. Using synchrotron-based single-crystal X-ray diffraction (SCXRD) measurements in a diamond anvil cell, Qin et al. investigated the phase structure of the copper-bearing oxide of cuprite (Cu_2O) up to ~30 GPa and ambient temperature conditions and provide insights into the phase stability and elastic properties of copper oxides and chalcogenides in extreme conditions. Li et al. determined the equations of state of pyrope-almandine garnet solid solutions based on SCXRD experiments at 0–20 GPa and 293–700 K using a diamond anvil cell, outlining that the chemical composition has a crucial influence on the thermoelastic properties of garnet. Sun et al. measured the electrical conductivities of hydrous olivine (Ol) aggregates and Ol–H_2O, Ol–NaCl–H_2O (salinity: 1–21 wt%; fluid fraction: 5.1–20.7 vol%), Ol–KCl–H_2O (salinity: 5 wt%; fluid fraction: 10.9–14.0 vol %) and Ol–$CaCl_2$–H_2O systems (salinity: 5 wt%; fluid fraction: 10.7–13.7 vol%) at 2.0–3.0 GPa and 773–1073 K using a YJ–3000t multi-anvil apparatus. They conclude that the Ol–NaCl–H_2O system with its salinity of ~5 wt% NaCl and fluid fraction larger than 1.8 vol% can account for the high-conductivity anomalies observed in the mantle wedges. Zang and Wang conducted partial melting experiments on the system of garnet plagioamphibolite and 90 wt% garnet plagioamphibolite +10 wt% plagioclase slate mixtures at a temperature range of 1123–1273 K and 1. 5 GPa using a piston-cylinder apparatus. They think that the terrigenous sediment made a large contribution to silicic magma generation on both chemical component and melt ratio during the process of partial melting of subducted oceanic crust. Wang et al. performed first-principles theoretical simulations using the density functional theory and obtained the crystalline structure, electrical properties, elasticity, and anisotropy of the observed mantle mineral, CaO_3, within a pressure range of 10–50 GPa. Their results provide further constraints to the compositional and anisotropic issues of the mantle transition zone.

Some acquired theoretical modeling resulting in rock physics parameters are also included in this special topic. An efficient rock physics scheme for the characterization of elastic properties is presented by Jiang et al. The authors applied it to estimate the crack density and fluid saturation of a shale gas reservoir. In the contribution by Wang et al., they conducted molecular dynamic simulations to explore the anisotropic elastic properties of montmorillonite (MMT) with different layer charge densities and layer charge distributions. They think that the density and distribution of layer charges influence the anisotropic elastic properties of MMTs, which may have potential applications to the exploration of unconventional MMT–bearing shale reservoir resources.

In addition, some developments in the high-P instrument and technique are presented in this volume. Ren and Li report on the experimental platform establishment of the six to eight type large-volume high-pressure multi-anvil apparatus in the Key Laboratory of High-temperature and High-pressure Study of the Earth’s Interior, IGCAS. The room-T pressure calibration was completed by using room-T phase transitions of water, ZnTe, ZnS, and GaAs, and its high-pressure calibration was realized with the phase transitions of KCl (850–1,100°C), LiCl (750°C–900°C), KCl + LiCl (450°C–750°C), and SiO_2 (quartz/coesite, 1,000–1,500°C) at high temperature. Yang et al. provided a method for

determining geophone orientations based on the zero-offset vertical seismic profile data constrained by a scalar field. In order to check its accuracy, two examples of synthetic and field data were tested, and their results proved that the scalar field method can solve the issue of signal weakness in the first-arrival P-wave well, meaning it is more advantageous than the conventional eigenvalue method.

ETHICS STATEMENT

Written informed consent was obtained from the individual(s) for the publication of any identifiable images or data included in this article.

AUTHOR CONTRIBUTIONS

All authors listed have made a substantial, direct, and intellectual contribution to the work and approved it for publication.

ACKNOWLEDGMENTS

The topic editors would like to thank all contributing authors to this Research Topic and the editorial staff of Frontiers in Earth Science for making this special collection possible.

Conflict of Interest: The authors declare that the research was conducted in the absence of any commercial or financial relationships that could be construed as a potential conflict of interest.

frontiers in Earth Science

ORIGINAL RESEARCH
published: 20 August 2021
doi: 10.3389/feart.2021.740685

High Pressure Behaviors and a Novel High-Pressure Phase of Cuprous Oxide Cu_2O

Fei Qin[1]*, *Dongzhou Zhang*[2] and *Shan Qin*[3]

[1]School of Earth Sciences and Resources, China University of Geosciences (Beijing), Beijing, China, [2]School of Ocean and Earth Science and Technology, Hawai'i Institute of Geophysics and Planetology, University of Hawaii at Manoa, Honolulu, HI, United States, [3]School of Earth and Space Sciences, Peking University, Beijing, China

In the present study, we extensively explored the phase stabilities and elastic behaviors of Cu_2O with elevated pressures up to 29.3 GPa based on single-crystal X-ray diffraction measurements. The structural sequence of Cu_2O is different than previously determined. Specifically, we have established that Cu_2O under pressure, displays a cubic-tetragonal-monoclinic phase transition sequence, and a novel monoclinic high-pressure phase assigned to the *P*1*a*1 or *P*12/*a*1 space group was firstly observed. The monoclinic phase Cu_2O exhibits anisotropic compression with axial compressibility $\beta_b > \beta_c > \beta_a$ in a ratio of 1.00:1.64:1.45. The obtained isothermal bulk modulus of cubic and monoclinic phase Cu_2O are 125(2) and 41(6) GPa, respectively, and the K_{T0}' is fixed at 4. Our results provide new insights into the phase stability and elastic properties of copper oxides and chalcogenides at extreme conditions.

Keywords: Cu_2O, phase transitions, synchrotron single-crystal X-ray diffraction, copper compounds, high pressure

OPEN ACCESS

Edited by:
Lidong Dai,
Institute of Geochemistry (CAS), China

Reviewed by:
Fang Xu,
University College London, United Kingdom
Xiang Wu,
China University of Geosciences, China

***Correspondence:**
Fei Qin
fei.qin@cugb.edu.cn

Specialty section:
This article was submitted to Earth and Planetary Materials, a section of the journal Frontiers in Earth Science

Received: *13 July 2021*
Accepted: *11 August 2021*
Published: *20 August 2021*

Citation:
Qin F, Zhang D and Qin S (2021) High Pressure Behaviors and a Novel High-Pressure Phase of Cuprous Oxide Cu_2O. Front. Earth Sci. 9:740685. doi: 10.3389/feart.2021.740685

INTRODUCTION

The behaviors of transition metals and their oxides under high-temperature and high-pressure conditions have been studied extensively over a few decades, and knowledge about such material has important applications in physics, materials science, and engineering (Austin and Mott, 1970; Errandonea, 2006). Copper and its oxides are among the most investigated transition-metal materials. Cuprous oxide is a high-temperature semiconductor and one promising candidate materials for photo-electrochemical applications (Maksimov, 2000; Laskowski et al., 2003; Khanna et al., 2007). However, variations in physical properties and structural change of cuprous oxide Cu_2O at extreme conditions have not been fully investigated.

Cu_2O crystalizes in a simple cubic Bravais lattice with space group *Pn*-3*m* under normal thermodynamic conditions, while it has numerous structure forms at extreme conditions (Machon et al., 2003; Cortona and Mebarki, 2011; Feng et al., 2017). Most of previous studies have focused on the structural variations under high *P-T* conditions based on first-principles calculations. Cortona and Mebarki (2011) described the transition from cubic Cu_2O to the CdI_2-type structure (hexagonal, *R*-3*m*) at 10 GPa, while Feng et al. (2017) suggested two phase transitions, one at 5 GPa (*Pn*-3*m*→*R*-3*m*) and the other at 12 GPa (*R*-3*m*→*R*-3*m*1). However, this is hard to reconcile with some experimental results on the pressure-induced structural transformations of Cu_2O. A tetragonal phase was demonstrated by Machon et al. (2003) at pressures between 0.7 and 2.2 GPa using angle-dispersive powder X-ray diffraction (XRD), and another pseudocubic phase was detected at ~8.5 GPa. What is more, Sinitsyn et al. (2004) found a new hexagonal phase with lattice parameters of a = 5.86 Å and c = 18.78 Å at 21 GPa which was significantly different from those

reported earlier by Werner and Hochheimer (1982), who studied a hexagonal phase with $CdCl_2$-type structure with a = 2.82 Å and c = 12.7 Å measured at 18 GPa. Therefore, phase relations of Cu_2O at higher pressures are more sparse and show less mutual agreement. Further investigation is needed to study the exact high temperature and high pressures phases of Cu_2O.

There are limited studies on the behavior of cuprous oxides and copper chalcogenides under high pressure and high temperature conditions. In this present work, we report the phase transformations and elastic properties of Cu_2O up to ~30 GPa at room temperature, by using synchrotron-based single-crystal XRD with diamond anvil cell (DAC). We confirmed the tetragonal phase Cu_2O observed between 10.4 and 13.8 GPa, and a novel monoclinic phase at higher pressures is also reported. As is well-known, physical properties of materials can be modified by tailoring either chemical composition or microstructure. These results can improve our knowledge of how pressure affect their elastic and physical properties. In this report we also present the measured compressibilities and equations of states of these high pressure phases of Cu_2O.

MATERIALS AND METHODS

The cuprite measured in this study was originated from the Tonglushan Copper Miners in Daye, Hubei province. Single-crystal samples of natural, brick-red cuprite were selected as the starting material of our study. We screened several chips and polished them to ~10 μm in thickness. At ambient conditions, the Cu_2O was characterized in an empty diamond anvil cell (DAC) by single crystal X-ray diffraction, at the GSECARS beamline 13-BM-C of the Advanced Photon Source (APS), Argonne National Laboratory (Zhang et al., 2017). Diffraction collected at ambient conditions showed that the cuprite crystal had a *Pn*-3*m* space group with a = 4.2733(7) Å, and the Cu_2O samples with a purity of 99.99% were used for the current study.

High-pressure compression measurements were performed, using short symmetric DACs fitted with Boehler-Almax diamond anvils with 300 μm flat culets and mounted into seats with 60° opening. Rhenium gaskets were preindented to ~40 μm thickness, and holes were drilled to ~170 μm diameter for the samples. On compression, the gasket thickness and sample chamber diameter both decrease to ~20 μm at the highest pressures reached. The polished Cu_2O sample was loaded together into the sample chamber along with Pt foil for pressure calibration (Fei et al., 2007). To achieve quasi-hydrostatic conditions and maintain similar pressure environments everywhere in the sample chamber, we loaded the cell with neon as the pressure-transmitting medium using the COMPRES/GSECARS gas-loading system (Rivers et al., 2008).

In situ high-pressure single-crystal X-ray diffraction experiments on Beamline 13-BM-C used a monochromatic X-ray beam with a wavelength of 0.4340 Å and focused to a 15 × 15 μm^2 spot. The experimental details were also described previously (Qin et al., 2017; Zhang et al., 2017). To obtain adequate number of diffraction peaks of samples and increase the coverage of the reciprocal space, we collected data at four different detector positions. The diffraction images were analyzed using the ATREX/RSV software package (Dera et al., 2013). Integrated diffraction data were analyzing using the DIOPTAS software (Prescher and Prakapenka, 2015), the high-pressure synchrotron XRD patterns were indexed by Dicvol06 (Louër and Boultif, 2007). Lattice parameters were calculated by the program UnitCell and the Le Bail refinement by GSAS (Holland and Redfern, 1997; Toby, 2001).

RESULTS

Tetragonal Phase

In situ X-ray diffraction patterns of Cu_2O were measured up to 29.3 GPa under hydrostatic pressure which presented in **Figure 1A**. At ambient conditions, all peaks can be indexed as the *Pn*-3*m* cubic structure (Hahn et al., 1983). When pressure increased to 16.1 GPa, an abrupt change in the integrated diffraction pattern was observed. As can be seen in the diffraction patterns in **Figure 1B**, reflections from the crystal show diffuse scattering and appear as short streaks at pressures above 16.1 GPa. Some diffraction peaks become fainter at higher angle, making it more difficult to determine the peak positions exactly (**Figure 1B**). We compared our integrated data of the high-pressure phase with previous studies but did not find any compatible structures (Werner and Hochheimer, 1982; Cortona and Mebarki, 2011; Feng et al., 2017).

A suspected phase transition from cubic to tetragonal between 0.7 and 2.2 GPa was reported previously (Machon et al., 2003), and our diffraction measurements confirmed this transition but at a different pressure (between 8.4 and 10.4 GPa, **Figure 2A**). We noticed that all the diffraction peaks deviated from a cubic lattice at pressures above 10.4 GPa, and can be well indexed as tetragonal lattice Cu_2O with space group $P4_2/nnm$. The high-pressure tetragonal phase Cu_2O at 10.4 GPa, was refined by Rietveld method in GSAS program shown in **Figure 2B**. The quality of the refinement is illustrated by the small R-factors and reduced X^2; R_p = 0.18%, R_{wp} = 0.25%, and X^2 = 0.93. As the tetragonal phase is the subgroup of the cubic phase (*Pn*-3*m*) and the two phases have very similar lattice parameters, i.e., for cubic phase, a = 4.267 Å and for tetragonal phase, a = 4.193, a/c = 0.988 (Hahn et al., 1983; Restori and Schwarzenbach, 1986; Machon et al., 2003). This tetragonal structure is also indicated by the asymmetry of the peaks centered at ~8.5°, 14.6°, 17° and 20°, resulting from the overlap of the (110)(011), (211)(112), (220)(202) and (131)(113) pairs of the tetragonal structure, respectively (**Figure 2A**). The tetragonal structure can be regarded as the distorted cubic structure under the uniaxial stress in the DAC.

Novel Monoclinic Phase

During the compression of Cu_2O, all the diffraction peaks move to larger 2θ values, as expected for pressure-induced bond shortening, and their intensities weaken gradually. When the pressure exceeds 16.1 GPa, some new peaks appeared (d spacings at ~2.83. 2.74, 2.42, 2.30, 2.03, 1.97, 1.76 Å and so on) and the d

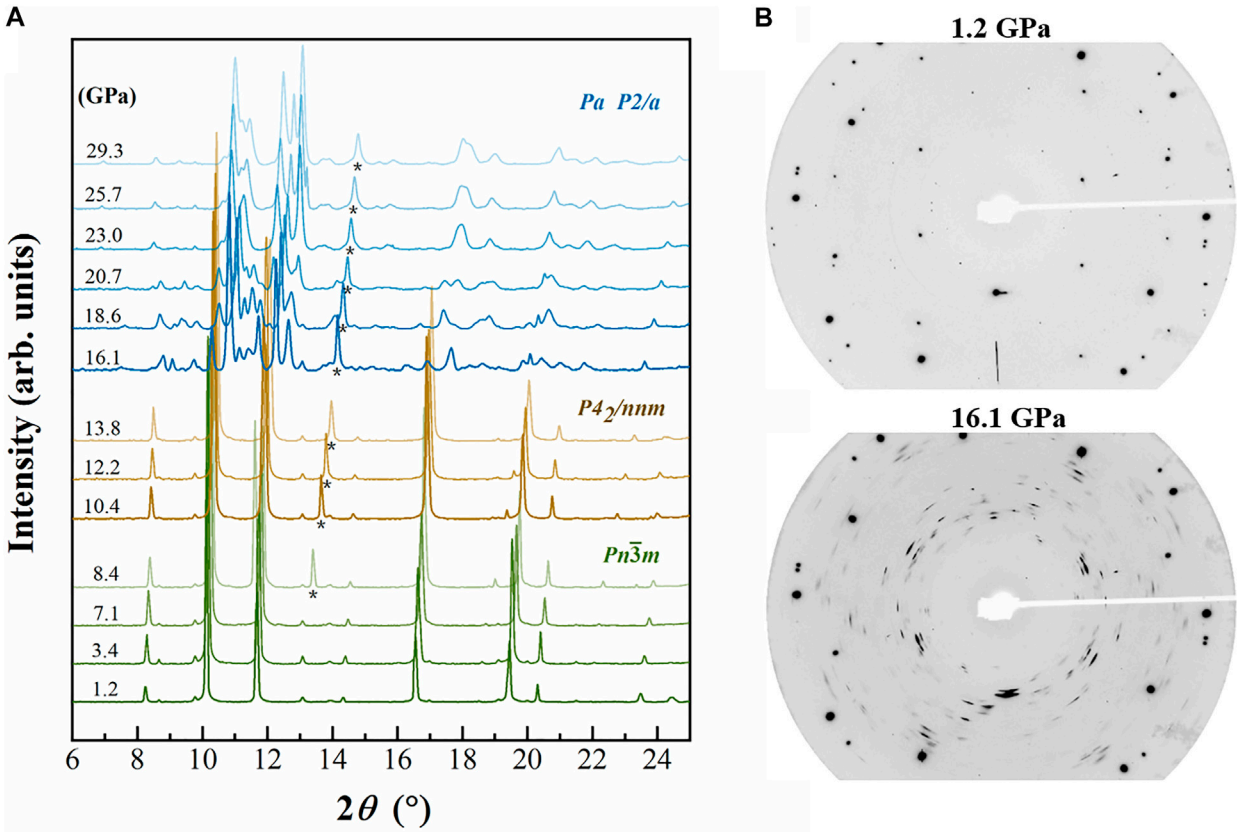

FIGURE 1 | (A) Integrated XRD patterns of Cu_2O at elevated pressures. Backgrounds were subtracted from the origin data. Asterisk (*) represents the scattering peaks of neon. **(B)** Diffraction patterns of Cu_2O at 1.2 and 13.8 GPa, respectively. The very intense diffraction spots are from the diamond anvils. Diamond peaks and diffraction lines attributed to the neon are not marked.

values of these peaks are totally different from those previous patterns, suggesting that the Cu_2O undergoes a reconstructive phase transition, and with further compression to the highest pressure, the structure can persist and no other transition was observed (**Figure 1A**). We have compared our patterns with some predicted hexagonal high-pressure phases of Cu_2O based on previous *ab initio* calculation and measurement results, but none of the predicted structures matches our measured diffraction pattern (Werner and Hochheimer, 1982; Cortona and Mebarki, 2011; Liu et al., 2014; Feng et al., 2017). In this case, the high quality data allow us to determine the crystal structure of the new high-pressure phase of Cu_2O. We chose several recognizable Debye rings, except for the neon rings, to index the crystal lattice using Dicvol06 software (Louër and Boultif, 2007). According to our results, the 16 chosen peaks of high-pressure phase Cu_2O, obtained at 16.1 GPa, can be successfully indexed as a monoclinic structure with the lattice parameters: a = 5.665(3) Å, b = 2.741(2) Å, c = 4.255(2) Å, β = 93.54(8)° and V = 65.94(2) Å^3 (**Table 1**).

Crystal lattice parameters, characteristic X-ray extinctions and diffracted intensities unambiguously documented that the crystal structure of the monoclinic phase Cu_2O belongs to the primitive lattice with no exception. $0k0$ manage the requirement of k = 2n + 1, and $h00$, $00l$ are also fulfilled the rules h = 2n and l = 2n. Consequently, space groups fulfilling these conditions are $P1a1$ (No. 7) and $P12/a1$ (No. 13) (Hahn et al., 1983). However, the quality of our diffraction pattern is not enough to differentiate the two space groups, as the space group Pa is a subgroup of $P2/a$, and both have very similar diffraction peak distributions.

Compressibility of Cu_2O

The P-V data of both Cu_2O phases were fitted using the third-order Birch-Murnaghan equation of state (BM3-EoS) with the data all equally weighted, since the errors in volume and pressure were similar for all measurements (Angle et al., 2014) (**Figure 3**). The refined lattice parameters of Cu_2O at various pressures are listed in **Table 2**. As the tetragonal structure could be regarded as the distorted cubic phase and the volumes of two phases only have marginal difference, thus we used cubic structure model to calculate the equation of state between 10.4 and 13.8 GPa to get higher accuracy. The resulting fitted parameters of volume, bulk modulus and its pressure derivative of cubic Cu_2O are as follows: V_0 = 78.05(3) Å^3, K_{T0} = 137(5) GPa and K_{T0}' = 1.8(7), respectively, which are 4.6% higher compared with the corresponding values from the experimental data from Werner and Hochheimer (1982), who reported 131 GPa when K' is 5.7. In

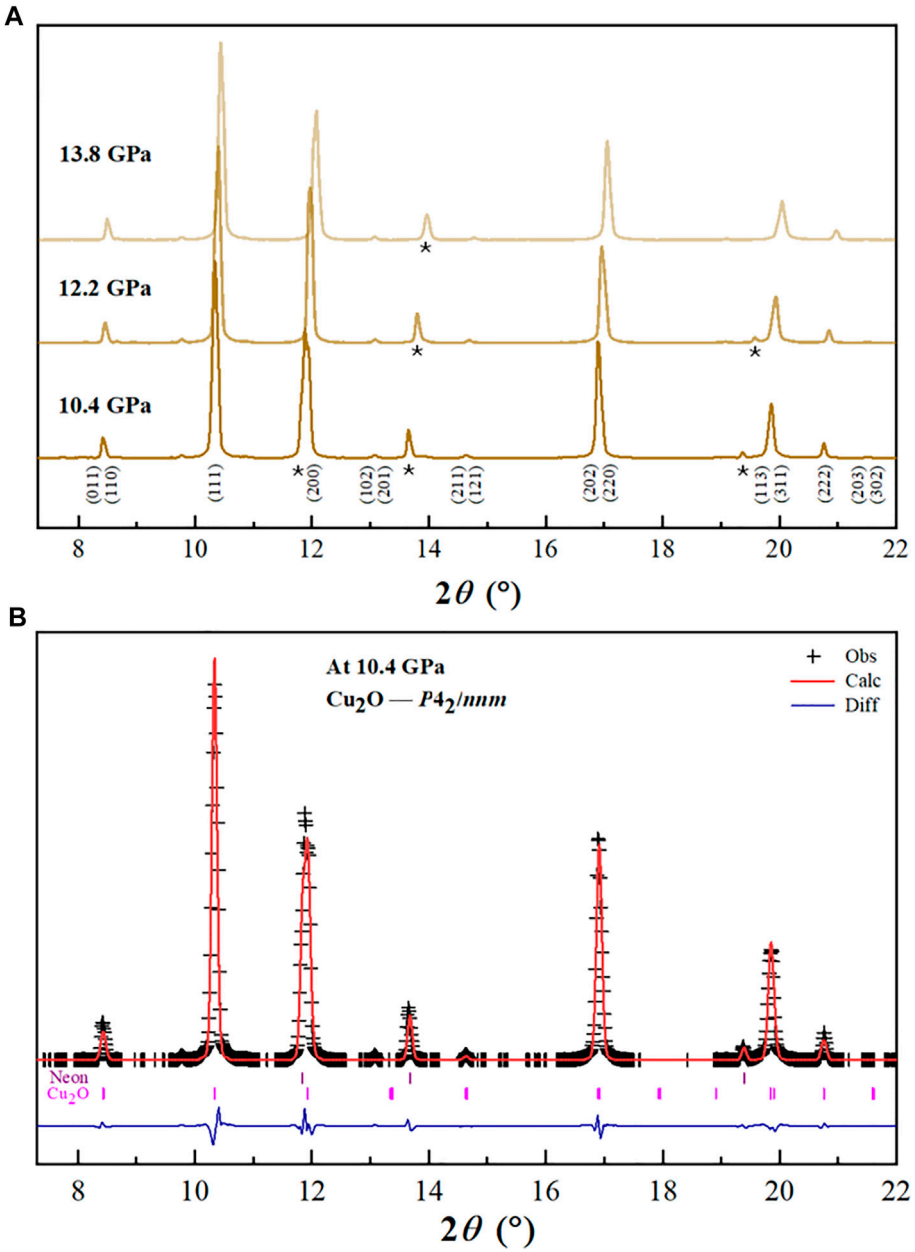

FIGURE 2 | (A) Selected XRD patterns of Cu_2O in the tetragonal phase. Asterisk (*) represents the scattering peaks of neon. **(B)** The Rietveld refinement of Cu_2O ($P4_2/nnm$). Observed and the calculated profiles are shown using black crosses and red solid line, respectively. The residual between them is shown by the blue line at the bottom. Bragg peak positions are indicated by the small ticks.

this present study, we also calculated the equation of state by fixing K_{T0}' at 4, resulting in K_{T0} = 125(2) GPa.

Here, we also firstly determined the elastic properties of the monoclinic phase Cu_2O using the EoSFit7c software (Angle et al., 2014). The measured lattice parameters are also provided in **Table 2**. The derived BM2-EoS (K_{T0}' = 4 implied) parameters yield the following bulk modulus K_{T0} = 41(6) GPa, and it is three times softer than the low-pressure phase. Axial compression behaviors are also presented in **Figure 4**. It is noteworthy that the *b*-axis possesses a larger axial compressibility compared with *a*- and *c*-axes, and therefore being the most compressible direction within the structure. The interaxial angle β has an increasing trend with compression.

DISCUSSION

The high-pressure behavior of cuprous oxide Cu_2O has attracted broad interests due to their various structures at different *P-T* conditions and its potential applications. Several previous studies

TABLE 1 | Calculated and Observed *d* spacings of a new monoclinic polymorph Cu_2O, as well as the normalized intensity I_{obs} for the *h k l* reflections.

h k l	d_{obs}	d_{cal}	d_{obs}-d_{cal}	$2\theta_{obs}$	$2\theta_{cal}$	$2\theta_{obs}$-$2\theta_{cal}$
200	2.8301	2.8274	0.0027	8.795	8.804	−0.008
010	2.741	2.7407	0.0003	9.082	9.082	−0.001
20-1	2.419	2.4234	−0.0044	10.293	10.275	0.019
011	2.3014	2.3028	−0.0016	10.823	10.815	0.008
002	2.124	2.1233	0.0007	11.728	11.732	−0.004
10-2	2.0315	2.0294	0.0021	12.267	12.277	0.01
210	1.971	1.9679	0.0031	12.642	12.662	−0.02
211	1.7613	1.7569	0.0044	14.157	14.189	−0.033
30-1	—	1.7636	−0.0026	—	14.135	0.021
21-2	1.4741	1.4753	−0.0012	16.932	16.917	0.015
003	1.4138	1.4155	−0.0017	17.656	17.637	0.019
212	—	1.4134	0.0007	—	17.664	−0.008
400	—	1.4137	−0.0003	—	17.66	−0.004
013	1.257	1.2577	−0.0007	19.882	19.871	0.011
11-3	1.2441	1.2422	−0.0019	20.092	20.121	−0.03
312	1.2243	1.2242	0.0001	20.424	20.42	0.004
41-1	—	1.2232	0.0009	—	20.438	−0.014
022	1.1511	1.1514	−0.0003	21.734	21.727	0.007
004	1.061	1.0616	−0.0006	23.603	23.589	0.014
023	0.984	0.9846	−0.0006	25.48	25.465	0.015

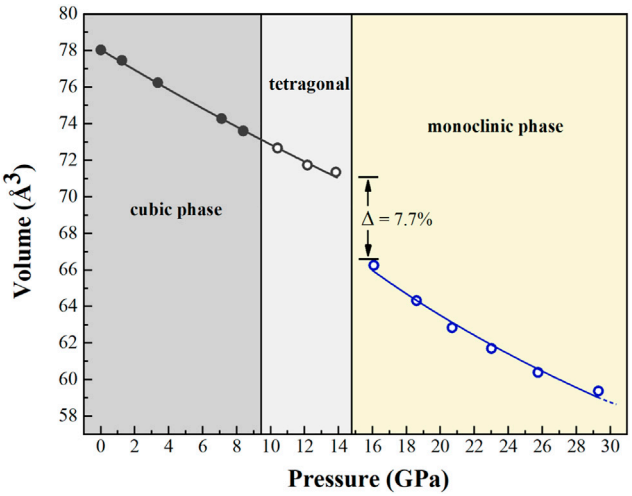

FIGURE 3 | The volume of Cu_2O as a function of pressure. A volume collapse of 7.7% at about 10.4–13.8 GPa, which is the location where the phase transition occurs between the tetragonal and monoclinic phases.

have been published which focus on the phase transitions and decompositions of Cu_2O and its thermodynamic properties as well (Machon et al., 2003; Sinitsyn et al., 2004; Cortona and Mebarki, 2011; Liu et al., 2014; Feng et al., 2017). However, these previous results were unclear about the high-pressure crystal structure of Cu_2O (tetragonal or hexagonal phase) and it is obvious that a large discrepancy of transformation pressure between the cubic and high-pressure phases existed between literatures. In this study, we re-confirmed the phase transition sequence from cubic-to-tetragonal phase occurred between 8.4 and 10.4 GPa using single-crystal XRD, which is significantly more higher than previously estimated (Machon et al., 2003). A new high-pressure phase of Cu_2O was also indexed using Dicvol06 software (Louër and Boultif, 2007). A volume collapse of ~7.7% in the region of 13.8–16.1 GPa was observed during the structural transformation from cubic to monoclinic phase (**Figure 3**). There is no indication of structural decomposition in this case. In addition, it is obvious that a considerable anisotropy in axial compressibility with $\beta_b > \beta_c > \beta_a$ and we found the ratio of zero-pressure axial compressibility is 1.00:1.64:1.45 according to our data. Thus, it can be concluded that the largest anisotropy in compressibility is along the *b* axis, which behaves about twice as compressible than the *a*-axis in the structure (**Figure 4**). Further investigation should be done to investigate the exact high temperature phases of Cu_2O.

In some recent studies, several members of copper chalcogenides, such as Cu_2S and Cu_2Se have been theoretically proposed and experimentally exhibited as the thermoelastic materials (Danilkin et al., 2011; Santamaria-Perez et al., 2014; Zhang et al., 2018; Zimmer et al., 2018; Xue et al., 2019). The high-pressure phase Cu_2O, Cu_2Se and Cu_2S may adopt the same monoclinic structure at different pressure conditions, which indicates that these copper compounds may have a similar crystal chemistry configuration (Santamaria-Perez et al., 2014; Zhang et al., 2018). The structural complexity of Cu_2S have been studied previously, in which two phase transitions occurred at 3.2 and 7.4 GPa from the *P*21/*c* phase to two different monoclinic structures (Santamaria-Perez et al., 2014). Pressure-induced structural transition sequence is also identified in Cu_2Se. The initial low-pressure phase (*C*2/*c*) transformed to phase II and semimetallic phase III at 3.2 GPa, and then followed by a reconstructive transformation to bulk metallic phase IV (*Pca*21) at 7.4 GPa. These mentioned phases could be confidently associated with the electronic state transitions (Zhang et al., 2018; Chuliá-Jordan et al., 2020). As for the copper sulfide, three phase-transitions occurred at 3.2, 7.4 and 26 GPa, respectively, and there is a significant difference of the reported values of bulk modulus, ranging from 72 to 113 GPa (Santamaria-Perez et al., 2014). The determination of the phase stability of such stoichiometric copper oxides under compression will give more insight into possible systematic trends in group copper chalcogenides, and provide a direct comparison with such thermoelastic materials at extreme conditions where their phase behaviors could converge.

CONCLUSION

The high-pressure behaviors of cuprous oxide Cu_2O have been studied by synchrotron-based single-crystal XRD at pressures up to ~30 GPa at 300 K conditions. The initial low-pressure cubic phase transforms to distorted $P4_2/nnm$ phase between 10.4 and 13.8 GPa, and the tetragonal structure persisted at pressure up to ~16 GPa. A new high-pressure phase of Cu_2O (monoclinic phase,

TABLE 2 | Lattice parameters of Cu_2O (cubic, tetragonal and monoclinic phases) at various pressures.

Pressure (GPa)	a (Å)	b (Å)	c (Å)	B	V (Å^3)	Symmetry
0.00001	4.2733(7)	—	—	—	78.04(2)	Cubic
1.2[a]	4.2630(6)	—	—	—	77.47(9)	—
3.4	4.2405(6)	—	—	—	76.25(9)	—
7.1	4.2036(6)	—	—	—	74.28(9)	—
8.4	4.1909(5)	—	—	—	73.61(7)	—
10.4	4.174(2)	4.174(2)	4.171(3)	—	72.67(7)	Tetragonal
12.2	4.157(2)	4.157(2)	4.152(3)	—	71.75(7)	—
13.8	4.147(3)	4.147(3)	4.149(4)	—	71.36(10)	—
16.1	5.696(2)	2.737(1)	4.2568(8)	93.17(3)	66.26(2)	Monoclinic
18.6	5.639(3)	2.704(1)	4.2237(8)	92.98(3)	64.33(2)	—
20.7	5.615(2)	2.675(1)	4.1913(7)	93.08(3)	62.85(2)	—
23.0	5.577(2)	2.661(1)	4.1645(7)	93.24(3)	61.71(2)	—
25.7	5.533(2)	2.647(1)	4.1307(7)	93.47(3)	60.40(2)	—
29.3	5.520(2)	2.630(1)	4.0997(7)	93.60(3)	59.38(2)	—

[a]*Nominal uncertainty in pressure in ±0.1 GPa.*

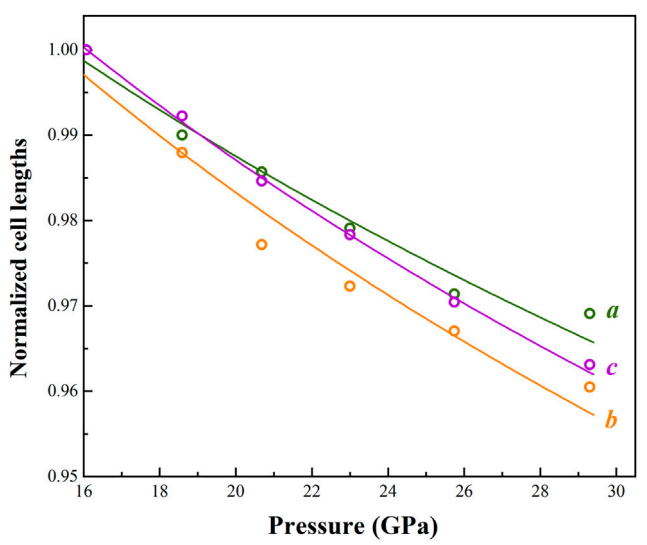

FIGURE 4 | Pressure dependence of normalized cell lengths (a, b and c) of monoclinic phase Cu_2O. EoS fits in the current study are shown by solid curves.

*P*1a or *P*12/*a*1) was obtained at 16.1 GPa at room temperature and the high-pressure elastic properties was firstly measured in this study. It is expected that the three times more compressible high-pressure phase Cu_2O may process some advantages properties than previously thought. The findings contribute to broadening our knowledge of the crystal chemistry of cuprite at high-pressure conditions, thus giving a better understand of thermoelastic materials in the copper chalcogenide system.

DATA AVAILABILITY STATEMENT

The original contributions presented in the study are included in the article/Supplementary Material, further inquiries can be directed to the corresponding author.

AUTHOR CONTRIBUTIONS

FQ and DZ carried out the experiments. FQ, DZ, and SQ performed the data analysis and interpretation. FQ wrote the manuscript. All authors contributed to the discussion of the results and revisions of the manuscript.

FUNDING

This research was supported by the Fundamental Research Funds for the Central Universities (grant no. 590421013) and the National Natural Science Foundation of China (grant no. 42072047). Work performed at GSECARS (Sector 13) of the Advanced photon Source (APS) is supported by the NSF EAR-1634415 and the Department of Energy (DOE) DE-FG02- 94ER1446. The APS at Argonne National Laboratory is supported by the DOE, Office of Science, under Contract No.DE-AC02-06CH11357. Experiments at Sector 13-BM-C of the APS used the PX2 facility, supported by GSECARS and COMPRES under NSF Cooperative Agreement EAR-1661511.

ACKNOWLEDGMENTS

We also thank S.Tkachev for gas loading the diamond cells.

REFERENCES

Angel, R. J., Alvaro, M., and Gonzalez-Platas, J. (2014). EosFit7c and a Fortran Module (Library) for Equation of State Calculations. *Z. Kristallogr.* 229, 405–419. doi:10.1515/zkri-2013-1711

Austin, I. G., and Mott, N. F. (1970). Metallic and Nonmetallic Behavior in Transition Metal Oxides. *Science* 168, 71–77. doi:10.1126/science.168.3927.71

Chuliá-Jordan, R., Santamaría-Pérez, D., Pereira, A. L. J., García-Domene, B., Vilaplana, R., Sans, J. A., et al. (2020). Structural and Vibrational Behavior of Cubic Cu1.80(3)Se Cuprous Selenide, Berzelianite, under Compression. *J. Alloys Compd.* 830, 154646. doi:10.1016/j.jallcom.2020.154646

Cortona, P., and Mebarki, M. (2011). Cu2O Behavior under Pressure: Anab Initiostudy. *J. Phys. Condens. Matter* 23, 045502. doi:10.1088/0953-8984/23/4/045502

Danilkin, S. A., Avdeev, M., Sakuma, T., Macquart, R., and Ling, C. D. (2011). Neutron Diffraction Study of Diffuse Scattering in Cu2−δSe Superionic Compounds. *J. Alloys Compd.* 509, 5460–5465. doi:10.1016/j.jallcom.2011.02.101

Dera, P., Zhuravlev, K., Prakapenka, V., Rivers, M. L., Finkelstein, G. J., Grubor-Urosevic, O., et al. (2013). High Pressure Single-crystal Micro X-ray Diffraction Analysis with GSE_ADA/RSV Software. *High Press. Res.* 33, 466–484. doi:10.1080/08957959.2013.806504

Errandonea, D. (2006). Phase Behavior of Metals at Very High P-T Conditions: A Review of Recent Experimental Studies. *J. Phys. Chem. Sol.* 67, 2017–2026. doi:10.1016/j.jpcs.2006.05.031

Fei, Y., Ricolleau, A., Frank, M., Mibe, K., Shen, G., and Prakapenka, V. (2007). Toward an Internally Consistent Pressure Scale. *Proc. Natl. Acad. Sci.* 104, 9182–9186. doi:10.1073/pnas.0609013104

Feng, W., Ren, W., Yu, J., Zhang, L., Shi, Y., and Tian, F. (2017). High-pressure Phase Transitions of Cu 2 O. *Solid State. Sci.* 74, 70–73. doi:10.1016/j.solidstatesciences.2017.09.011

Hahn, T., Shmueli, U., and Arthur, J. C. W. (1983). *International Tables for Crystallography. Vol. 1*. Dordrecht: Reidel.

Holland, T. J. B., and Redfern, S. A. T. (1997). UNITCELL: a Nonlinear Least-Squares Program for Cell-Parameter Refinement and Implementing Regression and Deletion Diagnostics. *J. Appl. Cryst.* 30, 84. doi:10.1107/S0021889896011673

Khanna, P. K., Gaikwad, S., Adhyapak, P. V., Singh, N., and Marimuthu, R. (2007). Synthesis and Characterization of Copper Nanoparticles. *Mater. Lett.* 61, 4711–4714. doi:10.1016/j.matlet.2007.03.014

Laskowski, R., Blaha, P., and Schwarz, K. (2003). Charge Distribution and Chemical Bonding inCu2O. *Phys. Rev. B* 67, 075102. doi:10.1103/PhysRevB.67.075102

Liu, K., Duan, Y.-F., Lv, D., Wu, H.-B., Qin, L.-X., Shi, L.-W., et al. (2014). Pressure-Induced Cubic-To-Hexagonal Phase Transition in Cu 2 O. *Chin. Phys. Lett.* 31, 117701. doi:10.1088/0256-307X/31/11/117701

Louër, D., and Boultif, A. (2007). Powder Pattern Indexing and the Dichotomy Algorithm. *Z. Kristallogr. Suppl.* 2007, 191–196. doi:10.1524/zksu.2007.2007.suppl_26.191

Machon, D., Sinitsyn, V. V., Dmitriev, V. P., Bdikin, I. K., Dubrovinsky, L. S., Kuleshov, I. V., et al. (2003). Structural Transitions in Cu2O at Pressures up to 11 GPa. *J. Phys. Condens. Matter* 15, 7227–7235. doi:10.1088/0953-8984/15/43/007

Maksimov, E. G. (2000). High-temperature Superconductivity: the Current State. *Phys.-Usp.* 43, 965–990. doi:10.1070/PU2000v043n10ABEH000770

Prescher, C., and Prakapenka, V. B. (2015). DIOPTAS: a Program for Reduction of Two-Dimensional X-ray Diffraction Data and Data Exploration. *High Press. Res.* 35, 223–230. doi:10.1080/08957959.2015.1059835

Qin, F., Wu, X., Zhang, D., Qin, S., and Jacobsen, S. D. (2017). Thermal Equation of State of Natural Ti-Bearing Clinohumite. *J. Geophys. Res. Solid Earth* 122, 8943–8951. doi:10.1002/2017JB014827

Restori, R., and Schwarzenbach, D. (1986). Charge Density in Cuprite, Cu2O. *Acta Crystallogr. Sect B* 42, 201–208. doi:10.1107/S0108768186098336

Rivers, M., Prakapenka, V., Kubo, A., Pullins, C., Holl, C., and Jacobsen, S. (2008). The COMPRES/GSECARS Gas-Loading System for diamond Anvil Cells at the Advanced Photon Source. *Ghpr* 28, 273–292. doi:10.1080/08957950802333593

Santamaria-Perez, D., Garbarino, G., Chulia-Jordan, R., Dobrowolski, M. A., Mühle, C., and Jansen, M. (2014). Pressure-induced Phase Transformations in mineral Chalcocite, Cu2S, under Hydrostatic Conditions. *J. Alloys Compd.* 610, 645–650. doi:10.1016/j.jallcom.2014.04.176

Sinitsyn, V. V., Dmitriev, V. P., Bdikin, I. K., Machon, D., Dubrovinsky, L., Ponyatovsky, E. G., et al. (2004). Amorphization of Cuprite, Cu2O, Due to Chemical Decomposition under High Pressure. *Jetp Lett.* 80, 704–706. doi:10.1134/1.1862798

Toby, B. H. (2001). EXPGUI, a Graphical User Interface forGSAS. *J. Appl. Cryst.* 34, 210–213. doi:10.1107/S0021889801002242

Werner, A., and Hochheimer, H. D. (1982). High-pressure X-ray Study ofCu2O andAg2O. *Phys. Rev. B* 25, 5929–5934. doi:10.1103/PhysRevB.25.5929

Xue, L., Zhang, Z., Shen, W., Ma, H., Zhang, Y., Fang, C., et al. (2019). Thermoelectric Performance of Cu2Se Bulk Materials by High-Temperature and High-Pressure Synthesis. *J. Materiomics* 5, 103–110. doi:10.1016/j.jmat.2018.12.002

Zhang, D., Dera, P. K., Eng, P. J., Stubbs, J. E., Zhang, J. S., Prakapenka, V. B., et al. (2017). High Pressure Single crystal Diffraction at PX̌2. *JoVE* 119, e54660. doi:10.3791/54660

Zhang, Y., Shao, X., Zheng, Y., Yan, L., Zhu, P., Li, Y., et al. (2018). Pressure-induced Structural Transitions and Electronic Topological Transition of Cu2Se. *J. Alloys Compd.* 732, 280–285. doi:10.1016/j.jallcom.2017.10.201

Zimmer, D., Ruiz-Fuertes, J., Morgenroth, W., Friedrich, A., Bayarjargal, L., Haussühl, E., et al. (2018). Pressure-induced Changes of the Structure and Properties of Monoclinic α -chalcocite Cu2S. *Phys. Rev. B* 97, 134111. doi:10.1103/PhysRevB.97.134111

Conflict of Interest: The authors declare that the research was conducted in the absence of any commercial or financial relationships that could be construed as a potential conflict of interest.

Publisher's Note: All claims expressed in this article are solely those of the authors and do not necessarily represent those of their affiliated organizations, or those of the publisher, the editors and the reviewers. Any product that may be evaluated in this article, or claim that may be made by its manufacturer, is not guaranteed or endorsed by the publisher.

frontiers in Earth Science

REVIEW
published: 10 September 2021
doi: 10.3389/feart.2021.732289

Review of Electrical Resistivity Measurements and Calculations of Fe and Fe-Alloys Relating to Planetary Cores

Meryem Berrada and Richard A. Secco*

Department of Earth Sciences, University of Western Ontario, London, ON, Canada

There is a considerable amount of literature on the electrical resistivity of iron at Earth's core conditions, while only few studies have considered iron and iron-alloys at other planetary core conditions. Much of the total work has been carried out in the past decade and a review to collect data is timely. High pressures and temperatures can be achieved with direct measurements using a diamond-anvil cell, a multi-anvil press or shock compression methods. The results of direct measurements can be used in combination with first-principle calculations to extrapolate from laboratory temperature and pressure to the relevant planetary conditions. This review points out some discrepancies in the electrical resistivity values between theoretical and experimental studies, while highlighting the negligible differences arising from the selection of pressure and temperature values at planetary core conditions. Also, conversions of the reported electrical resistivity values to thermal conductivity *via* the Wiedemann-Franz law do not seem to vary significantly even when the Sommerfeld value of the Lorenz number is used in the conversion. A comparison of the rich literature of electrical resistivity values of pure Fe at Earth's core-mantle boundary and inner-core boundary conditions with alloys of Fe and light elements (Si, S, O) does not reveal dramatic differences. The scarce literature on the electrical resistivity at the lunar core suggests the effect of P on a wt% basis is negligible when compared to that of Si and S. On the contrary, studies at Mercury's core conditions suggest two distinct groups of electrical resistivity values but only a few studies apply to the inner-core boundary. The electrical resistivity values at the Martian core-mantle boundary conditions suggest a negligible contribution of Si, S and O. In contrast, Fe-S compositions at Ganymede's core-mantle boundary conditions result in large deviations in electrical resistivity values compared to pure Fe. Contour maps of the reported values illustrate $\rho(P, T)$ for pure Fe and its alloys with Ni, O and Si/S and allow for estimates of electrical resistivity at the core-mantle boundary and inner-core boundary conditions for the cores of terrestrial-like planetary bodies.

Keywords: electrical resistivity, planetary body cores, diamond anvil cell, multi-anvil press, first-principle calculations, dynamical mean field theory, density-functional theory, shock compression

OPEN ACCESS

Edited by:
Xi Liu,
Peking University, China

Reviewed by:
Liwei Deng,
Shenzhen Technology University, China
Zhixue Du,
Chinese Academy of Sciences (CAS), China

****Correspondence:***
Meryem Berrada
mberrada@uwo.ca

Specialty section:
This article was submitted to Earth and Planetary Materials, a section of the journal Frontiers in Earth Science

Received: *28 June 2021*
Accepted: *24 August 2021*
Published: *10 September 2021*

Citation:
Berrada M and Secco RA (2021) Review of Electrical Resistivity Measurements and Calculations of Fe and Fe-Alloys Relating to Planetary Cores. Front. Earth Sci. 9:732289. doi: 10.3389/feart.2021.732289

INTRODUCTION

The current interest in direct measurements and modelling of electrical resistivity (ρ) originates mainly from an interest in heat flow modelling of planetary cores. For terrestrial-like planetary bodies that contain predominantly Fe cores, the applications are thermal evolution of the core, which includes freezing of an inner core and sustenance of a dynamo. To model core thermal evolution, the adiabatic heat flow is needed and is normally calculated via the thermal conductivity (k). Although ρ and k of metals are directly related through electron transfer of charge and energy, respectively, the following quote indicates the tolerance for variation in each of these properties in relation to our understanding of core processes. "*A factor of two or so uncertainty in ρ does not appear critical to dynamo theory but it has a strong impact on calculations of the thermal regime of the core.*" (Stacey and Anderson, 2001). The literature on ρ of pure Fe is rich and the values are scattered while the reported data on Fe-alloys is more scarce but less dispersed. The inconsistencies in measurements and modelling may be the result of different techniques in addition to the range of pressures and temperatures attributed to planetary cores. Much of the total work has been carried out in the past decade and **Figure 1** shows the cumulative number of papers published on ρ of pure Fe and Fe-alloys during the past half-century. At the time of writing this article, the four studies labelled on **Figure 1** combined for more than 1,000 citations and are viewed as responsible for the increased rate of activity following their publication. This review attempts to summarize both older and recent results to identify a range of reliable and representative values for ρ of the cores of terrestrial-like planetary bodies composed of pure Fe or Fe-alloys.

A general formulation of the core adiabatic heat flow is described as:

$$q_{ad} = -k_c \frac{\alpha g T}{C_p} \tag{1}$$

where k_c is k of the core, α is thermal expansion coefficient, g is gravitational acceleration, T is temperature at the top of the core, and C_p is heat capacity at constant pressure (P). Direct measurements of k are difficult to make at core-relevant P and T. In contrast, direct measurements of electrical conductivity (σ), which is inversely proportional to ρ, are achievable with relatively high accuracy. The two variables may be related through the electronic component of k (k_e) with the Wiedemann-Franz Law (WFL), where L is the Lorenz number:

$$k_e = LT\sigma = LT/\rho \tag{2}$$

Thermal conductivity is controlled by electrons and phonons, but the phonon contribution is negligible in metals and metallic alloys (Klemens and Williams, 1986). The appropriate values of the Lorenz number for specific compositions at relevant T are not well constrained. The theoretical value, the Sommerfeld value ($L_0 = 2.44 \cdot 10^{-8}$ W·Ω·K^{-2}), has been shown to account for more than 99% of k_e for Fe, suggesting that its use at high T and $P < 6$ GPa is reasonable (Secco, 2017). While $L > L_0$ for Fe-Si alloys at high T and low P (Secco, 2017), calculations at Earth core P, T conditions have shown that $L < L_0$ (de Koker et al., 2012; Xu et al., 2018). The following relationship was developed from measurements of the Seebeck coefficient of Fe up to 6 GPa and 2,100 K (Secco, 2017):

$$\left[\frac{dL}{dP}\right]_{melt\ boundary,\ <5\ GPa} = \frac{\rho k_e}{K_T T}\left\{\frac{1}{3} - \frac{K_T}{T}\left(\frac{dT}{dP}\right)_{melt\ boundary,\ <5\ GPa}\right\} = -3.98 \cdot 10^{-10}\frac{W\Omega}{K^2 GPa} \tag{3}$$

where K_T is isothermal bulk modulus. For metals in general, ρ is governed by the scattering rate of conduction electrons. Similarly, the Lorenz number has been shown to be both lower and higher than L_0 depending on the state and composition of the system (Pozzo et al., 2012; Pozzo et al., 2013; Pozzo et al., 2014; Pozzo and Alfè, 2016a; Pozzo and Alfè, 2016b; Pourovskii et al., 2020). The scattering rate of conduction electrons is affected by electron-phonon, electron-magnon, and electron-electron interactions. Electrical resistivity is proportional to the inverse of the electron mean free path (d), which is proportional to the amplitudes of atomic vibrations (A) and thus proportional to T:

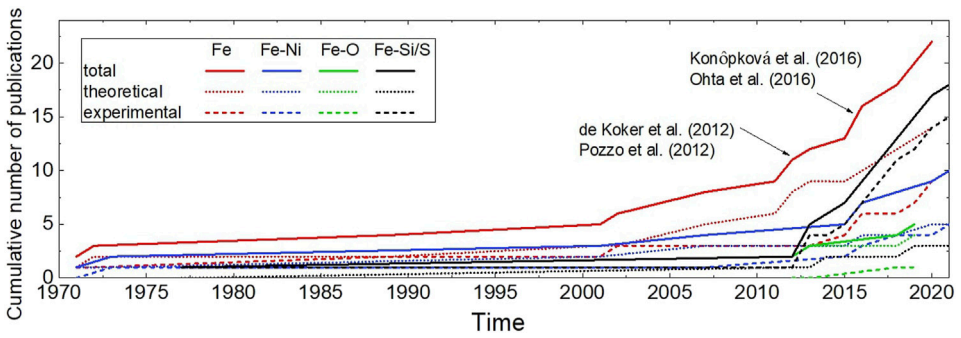

FIGURE 1 | Cumulative number of publications on theoretical and experimental methods of estimating ρ of Fe, Fe-Ni, Fe-O and Fe-Si and S alloys at the core conditions of Earth, Moon, Mercury, Mars, and Ganymede.

$$\rho \propto \frac{1}{d} \propto A^2 \propto T \tag{4}$$

Electron-phonon interactions are electron scattering caused by lattice vibrations and are relatively negligible at low T. At high T, the occupation of phonon density of states shifts toward higher energy states which increases the frequency of collisions with conduction electrons. Electron-magnon interactions, or spin-disorder scattering, is only relevant in ferromagnetic metals such as Fe and their ferromagnetic alloys. This interaction increases scattering as a function of T^2 up to the Curie T (T_c) and dominates ρ up to approximately 300 K. In Fe-alloys, the interaction of electron-lattice defects (including impurities) also affects the scattering rate of conduction electrons. The increased lattice defects cause electron structure perturbations and shorter electron mean free paths, which results in a larger ρ. The interactions between electrons and lattice defects dominate over the electron-phonon, electron-magnon and electron-electron interactions at low T. Overall, the net effect of T is to increase ρ, while ρ decreases with P as the decreased amplitude of lattice vibrations increases the electron mean free path. The Ioffe-Regel criterion argues that the growth of resistivity is reduced with T increase, i.e. saturates, as the electron mean free path approaches the interatomic distance (Mooij, 1973; Wiesmann et al., 1977; Gurvitch, 1981). Bohnenkamp et al. (2002) estimated a saturation value of 1.68 μΩm for Fe at 1 atm and up to 1,663 K, while there are variations in the saturation value of Fe-Si alloys at high P (Kiarasi and Secco, 2015; Gomi et al., 2016). Gomi et al. (2013) were the first to propose the idea of resistivity saturation for Fe at Earth core conditions however recent work (Zhang et al., 2020) provides contradictory results and suggests resistivity saturation behavior was an experimental artifact.

METHODS OF ELECTRICAL RESISTIVITY DETERMINATION

Theory: First-Principles Calculations

Initially meant to describe the diffusion of gases in the atmosphere, Boltzmann (1894) developed the following equation that considers the electronic band structure, phonon dispersion and electron-phonon interactions:

$$\rho = \frac{\pi \Omega k_B T}{N(\varepsilon_F) V_F^2} \lambda_{tr} \tag{5}$$

where $N(\varepsilon_F)$ is the electronic density of states per atom per spin at the Fermi energy (ε_F) level, k_B is the Boltzmann constant, Ω is the unit cell volume, V_F is the Fermi velocity, and λ_{tr} is the transport coefficient. This work was followed by the introduction of the Free Electron model by Sommerfeld (1928), based on the classical Drude model of electrical conduction (Drude, 1900a; Drude, 1900b) and Fermi-Dirac statistics describing the distribution of particles over energy states. The model predicts σ from the electron density, the mean free time (time between collisions), and the electron charge. The model includes many relations, including the Wiedemann-Franz law, the Seebeck coefficient of the thermoelectric effect and the shape of the electronic density of states function. In their analysis of Earth's magnetic field variations, Elsasser (1946) estimated the ρ of a pure Fe core from the theory of electronic conductivity, which states that σ is inversely proportional to the absolute T and directly proportional to the square of the Debye temperature (Θ_D).

$$\rho \propto \Theta_D^{-2} \tag{6}$$

The Debye temperature is proportional to the sound velocity and the acoustic phonon cut-off frequency and inversely proportional to volume (Kittel, 2005). Ziman (1960) later described the Nearly-Free Electron model, which is based on the behavior of electrons, ions, and holes. In the Free Electron model, all energy states from 0 to ∞ are allowed, whereas the Nearly-Free Electron model allows for weak perturbations of electrons by periodic potential ions. Following this idea, Ziman (1961) developed a theory for the behavior of liquid metals. This model was modified by Evans et al. (1971) to include a transition matrix term, introducing a more complex method of calculating ρ of a metallic liquid for metals that have empty d-band states in to which s-conduction electrons may jump (s-d transitions):

$$\rho = \frac{3\pi\Omega_0}{e^2 \hbar V_F^2} \int_0^1 d\left(\frac{q}{2K_F}\right) * 4\left(\frac{q}{2K_F}\right) * a(q) * \left| t\left(\frac{q}{2K_F}\right)\right|^2 \tag{7}$$

where e is the electron charge, K_F is the radius of the Fermi surface, $q = K - K'$ relates to the scattering angle of the Fermi surface, Ω_0 is the atomic volume of the liquid, $a(q)$ is the structure factor, $\hbar$ is the modified Planck constant, and $t(K, K')$ is the transition matrix that describes the scattering cross-section related to s-electron to d-band (s-d) scattering. While this formulation focuses on the liquid state of a metal, Mott (1972) and Mott (1980) derived a relationship for the solid state of a metal. Mott's theory considers the thermal and impurity contributions, as well as a magnetic contribution in ferromagnetic metals. The theory describes the relationship between ρ and the area of the Fermi surface (S_F). The relationship can be written as follows:

$$\rho = \frac{12\pi^3 \hbar}{S_F e^2 d} \tag{8}$$

The more complex, and commonly used, Kubo-Greenwood formula (Kubo, 1957; Greenwood, 1958) describes the frequency dependent electron conductivity and yields the linear contribution to the current response. The T dependence of ρ, which is related to electron-phonon interactions, is described by the Bloch–Grüneisen equation. Combined with the Bloch–Grüneisen equation for ρ as a function of volume (V) and T, the Kubo–Greenwood equation can be written as follows:

$$\rho(V,T) = \rho_{0R}\left[\frac{V}{V_R}\right]^a + \rho_{1R}\left[\frac{V}{V_R}\right]^b \frac{T}{T_R} \tag{9}$$

where a and b are constants relating to the volume dependence of the vibrational frequencies, the subscript R refers to the reference state, and ρ_{0R} and ρ_{1R} are composition-dependent model parameters (de Koker et al., 2012). The electronic structure of

a system can be investigated *via* Density-Functional Theory (DFT), which mainly describes the potential energies of a system. The DFT approach investigates an approximate solution to the Schrödinger equation in 3D based on the electron density, which results in solutions for ion-electron, ion-ion, and electron-electron potential energies (Argaman and Makov, 2000). Often used in combination with DFT, the dynamical mean field theory (DMFT) is a powerful numerical approximation of the potential of a many-particle system, such as electrons in solids. The complex many-particle system is studied by reducing it to a simpler single-particle system with an external mean field. The external field essentially accounts for the other particles in addition to the interactions and local quantum fluctuations that would occur in the many-particle system (Vollhardt et al., 2012). Drchal et al. (2019) and Korell et al. (2019) investigated the effects of magnetism on the electronic properties of metals via the Kubo-Greenwood equation along with DFT and the Tight-Binding Linear Muffin-Tin Orbital method (a method of calculating short-range transitions between electrons in s-, d- and f- orbitals), respectively. Korell et al. (2019) suggested that spin polarization must be accounted for in order to reconcile the first-principle calculations of ρ with measurements. In addition to drawing a similar conclusion, Drchal et al. (2019) suggested that the contributions of the various scattering mechanisms (caused by electron-phonon interactions, electron-magnon interactions, electron-electron interactions, and electron-lattice defects) are comparable but not additive. Through these first-principle calculations which require values of the thermal properties at a reference P and T, theoretical studies are able to estimate ρ of any metal or metal-alloys.

Experiments

Static: Multi-Anvil Press

Static experiments are typically carried out in a multi-anvil press. A typical multi-anvil press uses hydraulic pumps to drive uniaxially a hydraulic ram to compress a pressure cell located at the center of an arrangement of tungsten carbide (WC) anvils. In the 3000-ton press at the University of Western Ontario for example, there are three steel wedges on the bottom and three wedges on the top part of the pressure module. The wedges provide a nest for eight truncated WC cubes that house and converge on an octahedral pressure cell assembly. The octahedral cell may vary in size depending on the truncation edge length (TEL) of the WC cubes. The TEL may vary from 3 to 25 mm, and the smallest sizes are used to reach higher P, albeit on smaller sample volumes. The octahedral pressure cells are usually composed of Magnesium Oxide (MgO) which provides a balance between machinability, low k and hardness that allows for efficient conversion of applied force to the sample inside. With compression, the octahedral cell extrudes out between the WC cubes creating gaskets. Similarly, other multiple anvil apparatus designs such as the cubic anvil press, which consists of six WC anvils that compress a cubic pressure cell assembly made typically of the mineral pyrophyllite, creates gaskets as the cell extrudes out between the anvils. The insulating material, furnace, sample, and electrodes are placed inside the cell, and arranged co-axially in a hole connecting two opposite faces. Elevated temperatures are generated by Joule heating of an electrically resistant furnace, typically made of graphite, lanthanum chromite or rhenium foil, surrounding the sample. The electrical resistance (R) of the sample is measured with a four-wire method, where a pair of thermocouple wires is placed at each end of the sample. Each pair acts as a temperature sensor, while opposite pairs are assigned as potential and current leads in a switchable circuit configuration. The electrical resistivity is then calculated using the following equation which combines Ohm's law and Pouillet's law:

$$\boldsymbol{\rho} = \frac{\Delta \boldsymbol{E}}{\boldsymbol{I}} \cdot \frac{\boldsymbol{A}}{\boldsymbol{l}} \tag{10}$$

where ΔE is the voltage drop across the sample, I is the input current, A is the cross-sectional area of a wire-shaped sample and l the length of the sample. The general experimental methods for multi-anvil apparatuses are described in more detail by Liebermann (2011) and Ito (2015).

Static: Diamond-Anvil Cell Experiments

A Diamond-Anvil Cell (DAC) consists of two opposing gem-quality diamonds that enable the compression of small ($\sim 10^{-4}$ mm^3 scale) samples placed between the two diamond culets. Applying moderate force generates high pressures due to the small diameter, typically 50–250 μm, of the culet. Considering that P is applied uniaxially, a metal gasket with a hole drilled to form the sample chamber provides lateral support. A pressure-transmitting medium such as a gas (Ne, Ar, He, N_2) in the sample chamber must be added to obtain hydrostatic pressure but for high T experiments a solid medium (SiO_2, KCl, Al_2O_3, KBr, NaCl) is often used. The system is therefore translucent and allows for the use of XRD to determine the crystallographic structure of the sample. The two main pressure scales are the equation of state of a reference material and the shift in ruby fluorescence lines, although the latter is less reliable at high T. The equation of state describes the relationship between P, T, and V. Measurements of changes in V are compared with a known V-P relation in order to determine the experimental P. The second pressure scale relies on the P-dependent shift in fluorescence wavelength of an irradiated ruby included in the sample chamber. The sample is insulated from the gasket by adding a layer of insulating material, such as Al_2O_3. High temperatures can be achieved with single or double-sided laser heating or by internal resistive heating of a metal element, which may be the sample itself. Resistive heating allows for the precise measurement of T with thermocouples but is limited by the oxidization of diamond in air at approximately 973 K. Laser heating can achieve much higher T (up to 7000 K), although large T gradients can exist and care is needed to locate the sample measurements in a relatively uniform T-field. A common method for measuring the sample resistance in DAC experiments is the Van der Pauw method. This method is used for samples of arbitrary shape, as long as the sample is approximately two-dimensional such as a sheet or foil. Four electrodes are connected to the perimeter of the sample. Two opposite electrodes serve as potential leads, which can be machined within the same foil as the sample or carefully

connected manually and fixed by applying pressure. The ρ of the sample at a particular P can be calculated as follows:

$$\boldsymbol{\rho} = \boldsymbol{\rho}_0\left(\frac{\boldsymbol{V}}{\boldsymbol{V}_0}\right)^{\frac{1}{3}}\frac{\boldsymbol{R}}{\boldsymbol{R}_0} \tag{11}$$

where the subscript zero refers to the ambient conditions. The experimental methods for DAC are described in more detail by Mao and Mao (2007) and Anzellini and Boccato (2020).

Dynamic: Shock Compression Experiments

Shock compression is a dynamic method of generating high pressures which can be used in conjunction with an experimental configuration that allows determination of the physical properties of a sample, usually conducted in a vacuum. This apparatus consists of using compressed gas and/or gunpowder to launch a metallic projectile onto a stationary sample. The collision generates a strong shock wave that results in simultaneous high P and high T across the sample. The projectile, typically referred to as a flyer plate and made of W or Fe, accelerates to the desired velocities on the order of a few km/s (Bi et al., 2002). A high P, T conductivity zone propagates through the sample under shock compression. The σ of the sample can be measured by contact or contactless methods. The contactless method requires the remote probing of the sample by optical and electromagnetic field sources, which results in values of the impact velocity of the flyer and shock velocity. The arrival of the shock waves generates two electromotive forces that relate to the product of σ and thickness of sample (Gilev, 2011). The contact method requires typically four electrodes placed in contact with the sample. Two electrodes provide the voltage measurements while the other two are used to input constant current. The interface temperatures are usually measured with an optical pyrometer (Gilev, 2011). The most fundamental shock wave characteristic of the sample is its principal Hugoniot curve, which is formed by the locus of shock states along a compression path from initial P, T, and density. The P, T and density properties at the final state are obtained using a standard impedance matching method (Bi et al., 2002). In both methods, σ can be calculated from:

$$\boldsymbol{\sigma_F} = (\Delta \boldsymbol{E}_0/\Delta \boldsymbol{E_F})(\boldsymbol{V}_0/\boldsymbol{V}_F)\boldsymbol{\sigma}_0 \tag{12}$$

where the subscripts 0 and F refer to the initial and final states, respectively, and V is the specific volume. The experimental methods for shock compression experiments are described in more detail by Ahrens (2007) and Asimow (2015).

ELECTRICAL RESISTIVITY OF THE CORES OF TERRESTRIAL-TYPE BODIES

Earth

It is widely accepted that the Earth's core composition must be composed of Fe, Ni and some light elements in order to satisfy the core density (Birch, 1961; Birch, 1964; Jeanloz, 1979; Mao et al., 1990). Approximately 10 wt% of light elements is expected in the outer core (Poirier, 1994; Litasov and Shatskiy, 2016). In the inner core, approximately 3–8 wt% of light elements has been suggested (Alfè et al., 2007; Badro et al., 2007; Mao et al., 2012). In addition to approximately 5–10 wt% Ni in the core, light elements include C, H, Si, O and S (Poirier, 1994; Stixrude et al., 1997; Li and Fei, 2003; Alfè et al., 2007). Accordingly, the ρ of multiple Fe binary, ternary and even quaternary alloys must be investigated.

Gardiner and Stacey (1971) used available ρ measurements of liquid Fe from the literature to investigate the effects of T, P, and composition. They reported ρ of 0.25 μΩm at 2,500 K and 3,000 km, which corresponds to the Core-Mantle Boundary (CMB). Similarly, they reported 0.69 μΩm at 5,500 K and 5,000 km, which corresponds to the Inner-Core boundary (ICB). These extrapolations were achieved by applying a P-dependence of ρ of solid Fe (Bridgman, 1957) to measurements of liquid Fe at 1 atm (Baum et al., 1967), as shown below:

$$\boldsymbol{\rho_P}(\boldsymbol{T}) = \boldsymbol{\rho}_0(\boldsymbol{T})\left(\frac{\boldsymbol{\Theta}_{\boldsymbol{D}_0}}{\boldsymbol{\Theta}_{\boldsymbol{D_P}}}\right)^2\frac{\boldsymbol{D_P}}{\boldsymbol{D}_0} \tag{13}$$

where the subscript P refers to the final pressure, the subscript 0 refers to zero pressure, and D is density. Shock wave experiments by Keeler and Royce (1971) reported a similar value of 0.67 μΩm at 140 GPa, which corresponds to CMB conditions. However, it has been suggested by Bi et al. (2002) that the previous shock compression experiments above 50 GPa underestimated ρ due to the shunting effect of epoxy, which is used to fill gaps between the sample and insulator. Bi et al. (2002) conducted shock compression measurements of σ of Fe up to 208 GPa, corrected for the shunting effect, and suggested a value for ρ of 0.69 μΩm at conditions near the CMB (2,010 K, 101 GPa) and 1.31 μΩm for conditions near the ICB (5,220 K, 208 GPa). Although these values represent a correction to previously underestimated values, they remain lower than the values reported by Jain and Evans (1972). Jain and Evans (1972) carried out first-principle calculations using the Nearly-Free Electron model and reported ρ of a pure Fe core between 1.00 and 2.00 μΩm. These higher values are in agreement with direct measurements by Secco and Schloessin (1989), who used a large-volume press to measure ρ of Fe up to 7 GPa and above the melting T. The similarities in their measurements with calculations of the density of state functions at low and high P suggest ρ of an Fe solvent is probably between 1.2 and1.5 μΩm at outer core conditions.

A theory was developed by Stacey and Anderson (2001) suggesting a constant ρ along the melting boundary of pure metals such as Fe, based on a cancelling of the decreasing effects of P on ρ by the increasing effects of T on ρ. The description of their analysis, rooted mainly in thermo-elastic considerations, begins with the theory of electronic conductivity, as mentioned earlier by Elsasser (1946), while also considering the electron energy. According to the Free-Electron model and the approximation of the electron energy at the Fermi surface, the total energy varies with volume as $V^{-2/3}$. This term is multiplied by the inverse square of the Debye T in **Equation 6** to calculate ρ. Stacey and Anderson (2001) then extrapolated ρ of Fe at 140 GPa (Matassov, 1977) and 2,180 K (Anderson, 1998) to core

temperatures and reported values of 1.22 μΩm at CMB and 1.12 μΩm at ICB, in agreement with earlier estimates (Jain and Evans, 1972; Secco and Schloessin, 1989; Stacey and Anderson, 2001). Stacey and Loper (2007) revised the theory of constant ρ along the melting boundary and suggested that the constant behavior only applies to electronically simple metals with filled d-bands such as Cu but not Fe. They reported a revised ρ of Fe of 3.62 μΩm at the CMB and 4.65 μΩm at the ICB, higher than the values reported thus far. Experiments on several simple metals showed the ρ invariance prediction of Stacey and Loper (2007) to be over-simplified as ρ of Cu (Ezenwa et al., 2017), Ag (Littleton et al., 2018), Au (Berrada et al., 2018), all decrease on their pressure-dependent melting boundaries whereas Zn (Ezenwa and Secco, 2017a), Co (Ezenwa and Secco, 2017b), Ni (Silber et al., 2017) and Fe (Silber et al., 2018; Yong et al., 2019) all show invariant ρ along the melting boundary. Similarly, Davies (2007) revised the results of Stacey and Anderson (2001) and Bi et al. (2002) by correcting for *T* at the top of the core (~4,023 K, 135 GPa), which suggested a ρ of 1.25–1.9 μΩm for Fe at CMB conditions.

First-principle calculations using the Boltzmann equation suggested ρ of 0.75 μΩm for solid ε-Fe at ICB conditions (Sha and Cohen, 2011), while using the Kubo–Greenwood equation via the Bloch–Grüneisen equation on liquid Fe suggested a ρ of ~0.61–0.69 μΩm at core conditions (de Koker et al., 2012). These results are comparable with first-principle calculations of transport properties based on DFT on liquid Fe alloy mixtures by Pozzo et al. (2012) who reported a value of 0.64 μΩm at the ICB, and 0.73–0.74 μΩm at the CMB. Soon after this work, Pozzo et al. (2013) used first-principle simulations from DFT calculations with the Kubo-Greenwood relation to obtain *k* while ρ was independently calculated from σ. The appropriate Lorenz number for liquid Fe ($2.47–2.51{\cdot}10^{-8}$ WΩ K^{-2}) was then calculated using the Wiedemann-Franz law. Their results also showed 0.64 μΩm for Fe at the ICB, and 0.747 μΩm at the CMB. First-principle calculations combined with molecular dynamic simulations on solid Fe by Pozzo et al. (2014) suggested lower values of 0.50–0.53 μΩm at ICB conditions. Pozzo and Alfè (2016a) extended the set of calculations of core ρ of ε-Fe by Pozzo et al. (2014) to lower temperatures in order to investigate the *T* dependence of ρ. Their results suggested that ρ increases linearly with *T* and eventually saturates at high *T*, implying ρ of Fe of ~0.72 μΩm not far from CMB conditions (4,350 K, 97 GPa) and ~0.54 μΩm at Earth's center (6,350 K, 365 GPa), comparable to previous results mentioned above. This study is also in agreement with DAC experiments up to 70 GPa and 300 K by Gomi and Hirose (2015), who suggested values of 0.537 (+0.049/−0.077) μΩm and 0.431 (+0.058/−0.095) μΩm at CMB (3,750 K, 135 GPa) and ICB (4971 K, 330 GPa) conditions respectively. In contrast, extrapolations of DAC measurements from 26 to 51 GPa up to 2,880 K, assuming resistivity saturation suggested the ρ of Fe is 0.404 (+0.065/−0.097) μΩm at CMB conditions (Ohta et al., 2016). However, in the first study to measure *k* of Fe at CMB conditions, Konôpková et al. (2016) measured the propagation of heat pulses across Fe foils in a DAC, up to 130 GPa and 3,000 K, and then modelled the *T* and *P* dependences of ρ. They derive ρ of Fe of 3.7 ± 1.5 μΩm at the outer core. Although in agreement with the high values reported by Stacey and Loper (2007), this value is higher than the saturation resistivity of 1.43 μΩm suggested by Xu et al. (2018). Xu et al. (2018) computed the electron-phonon and electron-electron contributions to the ρ of solid ε-Fe, from first-principle calculations and molecular dynamics. They suggested values of 0.998 μΩm and 1.008 μΩm at ICB (6,000 K, 330 GPa) and CMB (4,000 K, 136 GPa) respectively. Their results also suggested that previous DAC data (Ohta et al., 2016) may have overestimated the saturation effect. Zhang et al. (2020) proposed that the saturation effect observed at high *T* by Ohta et al. (2016) should be considered an experimental artifact due to the incorrect positioning of the laser over the sample during heating and inaccurate geometries of the four-probe method. First, the misalignment of the laser during heating generates a large *T* gradient across the sample. The ρ measurements at high *T* are then dominated by the colder regions, leading to lower ρ values. Secondly, the measurement uncertainties are expected to be significantly larger than the reported values considering the small size of the sample compared to the location of the electrodes. The geometries of the assembly essentially result in a two-probe method. While considering these key factors, Zhang et al. (2020) used first-principle calculations to compare with their ρ measurements of ε-Fe up to ~170 GPa and ~3,000 K in a laser heated DAC using the Van der Pauw method. Their analysis suggested a ρ of 0.80 ± 0.05 μΩm at CMB conditions (4,000 K, 136 GPa). Values obtained from DAC measurements extrapolated based on the resistivity saturation model (Gomi and Hirose, 2015; Ohta et al., 2016) are thus expected to be almost doubled according to the results of Zhang et al. (2020). However, these results remain lower than those extrapolated from multi-anvil press measurements (Secco and Schloessin, 1989; Yong et al., 2019). For example, the reported value from Yong et al. (2019) is 1.6× higher than that from Zhang et al. (2020). While Yong et al. (2019) reported measured values of ρ of Fe on the liquid side of the melting boundary, their reported value for ρ at the CMB was linearly extrapolated to 200 GPa based on the *P*-dependency observed between 14–24 GPa. Zhang et al. (2020) assumed a 10% increase resistivity on melting but only extrapolated from 133 to 136 GPa. In general, the differences in values for ρ at the CMB reported from multi-anvil and DAC experimental studies may arise from uncertainties from large extrapolations, from predispositions specific to each method such as errors in sample geometries, temperature homogeneity of heated sample region, lack of sample symmetry, possible thermoelectric effects and other parasitic voltages, etc.

Silber et al. (2018) reported an invariant behavior of Fe ρ at ~1.2 μΩm, from direct measurements in a multi-anvil press up to 12 GPa and at liquid *T*. A similar method was used by Yong et al. (2019), who carried out static experiments in a 3000-ton multi-anvil press from 14–24 GPa into the liquid. Their results suggested an invariant ρ of liquid Fe of 1.20 ± 0.02 μΩm along the melting boundary. However, a statistical linear regression of their measurements, in order to account for the effect of *P*, suggested a slight deviation from invariant behavior to 1.28 ± 0.09 μΩm along the melting boundary of Fe at 200 GPa.

Wagle and Steinle-Neumann (2018) focused on the behavior of liquid Fe from first-principle calculations based on Ziman's theory on liquid metals. Combining their ICB value of 0.58 μΩm for ε-Fe with the literature values of liquid Fe-Si/S alloys (de Koker et al., 2012; Pozzo et al., 2014), ρ of outer core is expected to be up to 36% larger than that of the inner core. In contrast, estimations of pure Fe from DFT and molecular dynamics suggested almost no increase between ICB and CMB conditions, from 0.60 ± 0.27 μΩm to 0.67 ± 0.27 respectively (Wagle et al., 2019). Recent DFT simulations by Pourovskii et al. (2020) accounted for electron-electron interactions at high *T* and suggested an inner core ρ of 0.637 μΩm for pure Fe, in general agreement with the lower values mentioned above. Pourovskii et al. (2020) applied DFT and DMFT to Fe and concluded that thermal disorder suppresses the non-Fermi-liquid behavior of bcc Fe which reduces electron-electron scattering at high *T*. The variations among pure Fe results seem to range between 0.25 μΩm (Gardiner and Stacey, 1971) and 3.7 ± 1.5 μΩm (Konôpková et al., 2016), and may not simply be attributed to the method used.

The thermal properties of Fe-Ni alloys show similar variations. Gardiner and Stacey (1971) also estimated ρ of Fe with up to 25 wt% of light element (Ni, S, Si, MgO). Their results indicate an upper bound of 2.77 μΩm at CMB conditions and 6.03 μΩm at ICB conditions. Direct measurements at 1 atm up to ~1,373 K by Johnston and Strens (1973) show comparable results. Assuming ρ at core pressures is smaller than that at 1 atm, Johnston and Strens (1973) suggested that ρ should not exceed 2.0 μΩm for Fe-10 wt% Ni-2.6 wt% C-15 wt% S (hereinafter referred to as Fe10Ni2.6C15S) at core pressures. Stacey and Anderson (2001) predicted the addition of 23 wt% and 15 wt% Si (or Fe23Ni15Si) to increase ρ to 2.12 μΩm at CMB and 2.02 μΩm at ICB, in agreement with Johnston and Strens (1973). Davies (2007) also reported ρ in the range of 2.15–2.8 μΩm for Fe23Ni15Si at CMB conditions. In contrast, DAC experiments combined with the Bloch–Grüneisen equation suggested values of 0.675 μΩm for ε-Fe10Ni, 1.26 (+0.05/−0.17) μΩm for ε-Fe5Ni4Si and 1.77 (+0.05/−0.25) μΩm for ε-Fe5Ni8Si at CMB conditions (4,000 K, 140 GPa) (Zhang et al., 2021). Gomi and Hirose (2015) suggested similar ρ values for Fe-Ni with up to 13.4 wt % of light elements (O, Si, S, C) of 0.53–1.19 μΩm at CMB and 0.39–0.96 μΩm at ICB. Similarly, Ohta et al. (2016) combined their DAC measurements with Matthiessen's rule and the resistivity saturation model to infer ρ of Fe11.9Ni13.4Si of 0.869 (+0.154/−0.216) μΩm at 140 GPa and 3,750 K. Gomi et al. (2016) estimated the ρ of Fe12Ni15Si (or $Fe_{65}Ni_{10}Si_{25}$) between 1.12 and 1.16 μΩm at 4,000–5,500 K and 156–175 GPa from the Kubo–Greenwood formula. As expected from additional impurity scattering, the previous values of Fe-alloys (Gomi and Hirose, 2015; Gomi et al., 2016) are greater than that of pure Fe (Ohta et al., 2016) using similar methods. First-principle electronic band structure calculations of Fe-alloys accounting for the saturation theory suggested values ranging from 0.58–0.74 μΩm for Fe-(5.4 to 31.6 wt%)Ni at CMB conditions (Gomi and Yoshino, 2018). In agreement with these studies, Zidane et al. (2020) also used first-principle calculations based on the Kubo-Greenwood relation and reported values of 0.62–1.22 μΩm for Fe-Ni with 2.7–37.7 wt% light elements (O, Si, S) at ICB conditions (5,500 K, 360 GPa).

The results of Gomi and Yoshino (2018) also suggested values ranging from 0.71–0.88 μΩm for Fe-(1.6 to 11.7 wt%)O at CMB conditions. Similarly, de Koker et al. (2012) reported a range of 0.67–0.82 μΩm for Fe-O alloys at core conditions, while Pozzo et al. (2012) also reported a value of ~0.80 μΩm for Fe-O-S/Si (2.7–3.5 wt% O and wt% S/Si between 9.1 and 11.4) at the ICB and 0.90 μΩm at the CMB. Wagle et al. (2019) reported ρ values in very good agreement with de Koker et al. (2012) for the same alloys. Their results suggested that at ICB conditions, ρ is 0.65 ± 0.24 μΩm and 0.71 ± 0.27 μΩm, while at the CMB conditions ρ is 0.74 ± 0.24 μΩm and 0.81 ± 0.27 μΩm, for Fe3.9O (or Fe_7O) and Fe8.7O (or Fe_3O) respectively (Wagle et al., 2019). Similarly, Pozzo et al. (2013) reported a calculated ρ of ~0.79 μΩm for Fe2.7O6Si (or $Fe_{0.82}O_{0.08}Si_{0.10}$) and ~0.80 μΩm for Fe4.6O4.9Si (or $Fe_{0.79}O_{0.13}Si_{0.08}$) at the ICB, not unlike the direct calculations of resistivity for Fe-O-S/Si by Pozzo et al. (2012). They also report a Lorenz number for liquid Fe-alloys varying from 2.17 to $2.24{\cdot}10^{-8}$ $W\Omega K^{-2}$ from the Wiedemann-Franz law (Pozzo et al., 2013).

The recent DAC experiments by Zhang et al. (2021) suggested a value of 1.00 μΩm for ε-Fe1.8Si at CMB conditions. Gomi and Yoshino (2018) considered a greater Si content and reported values ranging from 0.71–1.13 μΩm for Fe-(2.8 to 18.8 wt%)Si and 0.72–0.94 μΩm for Fe-(3.1 to 20.9 wt%)S at CMB conditions. The first-principle calculations and molecular dynamics simulations on Fe4.5Si (or $Fe_{0.92}Si_{0.08}$) and Fe3.9Si (or $Fe_{0.93}Si_{0.07}$) suggested ρ of 0.65–0.66 μΩm at the ICB (Pozzo et al., 2014). The agreement with the reported values of Fe3.9O (de Koker et al., 2012) and Fe (Keeler and Royce, 1971) suggested the contribution of Si and O to the total ρ at inner core conditions may not be significant. It has been shown though at lower pressures that increasing Si content from 2 to 17 wt% increases ρ (Berrada et al., 2020), yet Wagle et al. (2019) reported lower values than Zhang et al. (2021) for a higher Si content. At CMB and ICB conditions, ρ of Fe6.7Si (or Fe_7Si) is calculated to be 0.81 ± 0.5 μΩm and 0.73 ± 0.5 μΩm, while that of Fe14.4Si (or Fe_3Si) is 1.02 ± 0.5 μΩm and 0.92 ± 0.5 μΩm (Wagle et al., 2019). Wagle et al. (2019) also revised previous estimates by Wagle et al. (2018) of Fe7.6S (or Fe_7S) and Fe16.1S (or Fe_3S) and reported values of 0.82 ± 0.22 μΩm and 1.01 ± 0.42 μΩm at CMB conditions, and 0.75 ± 0.22 μΩm and 0.95 ± 0.42 μΩm at ICB conditions, respectively. Gomi et al. (2013) estimated that ρ of ε-Fe13.2Si (or $Fe_{78}Si_{22}$) is 1.02 (+0.04/−0.11) μΩm at the CMB and 0.820 (+0.054/−0.131) μΩm at the ICB. Their results are in very good agreement with Wagle et al. (2019) and were extrapolated from a combination of DAC measurements up to 100 GPa and first-principle calculations while considering the effect of ρ saturation. Silber et al. (2019) conducted direct measurements of ρ of Fe4.5Si from 3 to 9 GPa and up to liquid *T* and postulated that the ρ of liquid Fe alloyed with light elements remains unchanged from that of Fe at inner core conditions, but the variation in *T* at the CMB suggested that ρ could increase up to ~1.50 μΩm. In only the second study to measure experimentally *k* of a composition in the Fe system at Earth's core conditions, Hsieh et al. (2020) used a pulsed laser

TABLE 1 | Electrical resistivity values of Fe at Earth's CMB (4,000 K, 136 GPa) and ICB (5,000 K, 330 GPa) conditions determined by different methods.

Composition	ρ_{CMB} (μΩm)	CMB conditions	ρ_{ICB} (μΩm)	ICB conditions	Method (variable)	References
Fe	*0.25*	2,500 K, 3,000 km	*0.69*	5,500 K, 5,000 km	[a]Calculations (ρ)	Gardiner and Stacey (1971)
Fe	0.67	140 GPa	—	—	Shock compression (ρ)	Keeler and Royce (1971)
Fe	*1.00*	—	*2.00*	—	Calculations (ρ)	Jain and Evans (1972)
Fe	*1.2–1.5*	—	—	—	Multi-anvil press (ρ)	Secco and Schloessin (1989)
Fe	1.22	3,750 K, 135 GPa	1.12	4,971 K, 330 GPa	Calculations (ρ)	Stacey and Anderson (2001)
Fe	0.69	2,010 K, 101 GPa	1.31	5,220 K, 208 GPa	Shock compression (σ)	Bi et al. (2002)
Fe	3.62	3739 K	4.65	5,000 K	Calculations (*k*)	Stacey and Loper (2007)
Fe	1.25–1.9	4023 K, 135 GPa	—	—	calculations (ρ)	Davies (2007)
ε-Fe	—	—	**0.75**	5,000 K, 330 GPa	Calculations (ρ)	Sha and Cohen (2011)
Fe	*0.69*	—	*0.61*	—	Calculations (ρ)	de Koker et al. (2012)
Fe	*0.73–0.74*	4,039–4186 K	*0.64*	5,500–5,700 K	Calculations (σ)	Pozzo et al. (2012)
Fe	*0.747*	4630 K, 124 GPa	*0.64*	6,350 K, 328 GPa	Calculations (σ)	Pozzo et al. (2013)
Fe	0.537 (+0.049/−0.077)	3750 K, 135 GPa	0.431 (+0.058/−0.095)	4,971 K, 330 GPa	DAC (ρ)	Gomi and Hirose (2015)
Fe	0.404 (+0.065/−0.097)	3750 K, 140 GPa	—	—	DAC (ρ)	Ohta et al. (2016)
ε-Fe	**0.72**	—	**0.54**	—	Calculations (ρ)	Pozzo and Alfè (2016a)
Fe	*3.7 ± 1.5*	3,000 K, 130 GPa	—	—	DAC (*k*)	Konôpková et al. (2016)
ε-Fe	**1.008**	4,000 K, 136 GPa	**0.998**	6,000 K, 330 GPa	Calculations (ρ)	Xu et al. (2018)
ε-Fe	—	—	**0.58**	—	Calculations (ρ)	Wagle and Steinle-Neumann (2018)
Fe	*1.28 ± 0.09*	—	—	—	Multi-anvil press (ρ)	Yong et al. (2019)
Fe	*0.67 ± 0.27*	130 GPa	*0.60 ± 0.27*	330 GPa	Calculations (ρ)	Wagle et al. (2019)
ε-Fe	**0.80 ± 0.05**	4,000 K, 136 GPa	—	—	DAC (ρ)	Zhang et al. (2020)
Fe	—	—	0.637	—	Calculations (ρ)	Pourovskii et al. (2020)

The ρ values associated with studies that have reported k *values are obtained via the Wiedemann-Franz law with the Sommerfeld value for the Lorenz number.*
[a]*This method refers to first principles theoretical calculations.*
Values specific to liquid Fe are in red, those specific to solid Fe are in ***blue****, while unspecified values are in black. Compositions specific to the hcp phase of Fe are denoted by ε.*

method with a DAC to measure *k* of Fe-Si alloys up to 144 GPa and 3,300 K. Calculations of ρ using the Wiedemann-Franz law, with the Sommerfeld value of the Lorenz number, and extrapolations to high *T* suggested approximately 4.6 μΩm (or 20 $Wm^{-1} K^{-1}$) at ~136 GPa and 3,750 K for ε-Fe8.7Si (or $Fe_{0.85}Si_{0.15}$) (Hsieh et al., 2020). Hsieh et al. (2020) note that the discrepancy with previously mentioned results may be caused by the assumptions made by studies that did not directly measure *k*. Both the modeled T-dependence of ρ and the use of the Sommerfeld value of the Lorenz number at high *P* and *T* lead to underestimates of *k* at Earth's core conditions. Shock compression experiments by Matassov (1977) on Fe-Si alloys up to 140 GPa and 2,700 K suggested a ρ of 1.12 μΩm for an Fe33.5Si core, which is within previously reported values from shock wave measurements. As mentioned earlier, this value may be underestimated due to the shunting effect of epoxy above 50 GPa (Bi et al., 2002). The results of de Koker et al. (2012) also suggested a lower range of 0.74–1.03 μΩm for Fe-Si alloys at core conditions. Similar to the results of de Koker et al. (2012), DAC measurements up to 60 GPa and 300 K indicate ρ values for Fe9Si of 0.6–1.3 μΩm at the CMB (Seagle et al., 2013). Their measurements were extrapolated to CMB conditions using a model of ρ as a function of *T*, *V*, and Debye temperature. These results are in agreement with measurements in a cubic-anvil press up to 5 GPa and 2,200 K, indicating ρ of Fe17Si in the range of 0.90–0.94 μΩm at outer core conditions (Kiarasi, 2013). In comparison, Suehiro et al. (2017) reported CMB values of approximately 0.699 μΩm for Fe12.8S (or $Fe_{80.8}S_{19.2}$), 0.741 μΩm for Fe6.1Si6.7S (or $Fe_{79.7}Si_{10.3}S_{10}$), and 0.784 μΩm for Fe13.5Si (or $Fe_{77.5}Si_{22.5}$). Suehiro et al. (2017) carried out measurements in a laser-heated DAC up to 110 GPa and 300 K and used Matthiessen's Rule and the saturation resistivity value of 1.68 μΩm, to obtain ρ of Fe-Si-S alloys at core conditions. Thus, the contribution of S to the ρ of Fe-alloys is reported to be weaker than that of Si. Gomi and Hirose (2015) proposed higher ρ values for Fe13.5Si of 1.02 (+0.04/−0.13) μΩm and 0.820 (+0.055/−0.130) μΩm at the CMB and ICB, respectively. These higher values are in agreement with Zhang et al. (2018), who applied their model of *k* to Fe13.5Si and reported ρ values of 0.92 μΩm at CMB conditions (4,050 K, 136 GPa). Recently, the saturation resistivity of ε-Fe-Si alloys was further investigated in an internally heated DAC up to 117 GPa and 3,120 K (Inoue et al., 2020). Results show that the saturation resistivity of ε-Fe-Si alloys is comparable to that of pure Fe at ~100 GPa (Inoue et al., 2020). They obtained ρ values for ε-Fe12.7Si of 1.040 (+0.126/−0.212) μΩm and 0.775 (+0.150/-0.231) μΩm at ICB

TABLE 2 | Electrical resistivity values of Fe-Ni alloys at Earth's CMB (4,000 K, 136 GPa) and ICB (5,000 K, 330 GPa) conditions determined by different methods.

Composition	ρ_{CMB} (μΩm)	CMB conditions	ρ_{ICB} (μΩm)	ICB conditions	Method (variable)	References
ε-Fe5Ni4Si	**1.26 (+0.05/–0.17)**	4,000 K, 140 GPa	—	—	DAC (ρ)	Zhang et al. (2021)
ε-Fe5Ni8Si	**1.77 (+0.05/–0.25)**		—			
Fe5.4Ni	0.58	—	—	—	DAC (ρ)	Gomi and Yoshino (2018)
ε-Fe10Ni	**0.675**	4,000 K, 140 GPa	—	—	DAC (ρ)	Zhang et al. (2021)
Fe10Ni2.6C15S	*2*	—	—	—	Meas. at 1 atm (σ)	Johnston and Strens (1973)
Fe10.7Ni	0.615 (+0.050/–0.084)	3,750 K, 135 GPa	0.494 (+0.061/–0.104)	4,971 K, 330 GPa	DAC (ρ)	Gomi and Hirose (2015)
Fe10.9Ni2.7Si	—	—	0.62	5,500 K, 360 GPa	[a]Calculations (ρ)	Zidane et al. (2020)
Fe10.9Ni3.1S	—		0.67			
Fe11.1Ni1.6O	—		0.70			
Fe.11.3Ni9.7S	—		0.97			
Fe11.5Ni8.6Si	—		1.00			
Fe11.5Ni12.8S	0.758 (+0.049/–0.099)	3,750 K, 135 GPa	0.601 (+0.061/–0.118)	4,971 K, 330 GPa	DAC (ρ)	Gomi and Hirose (2015)
Fe11.9Ni13.4Si	1.04 (+0.04/–0.10)		0.844 (+0.054/–0.129)			
Fe11.9Ni13.4Si	0.869 (+0.154/–0.216)	3,750 K, 140 GPa	—	—	DAC (ρ)	Ohta et al. (2016)
Fe11.9Ni5.1O	—	—	1.04	5,500 K, 360 GPa	Calculations (ρ)	Zidane et al. (2020)
Fe12Ni15Si	1.12–1.16	4,000–5,500 K, 156–175 GPa	—	—	Calculations (ρ)	Gomi et al. (2016)
Fe12.1Ni15.1Si	—	—	1.16	5,500 K, 360 GPa	Calculations (ρ)	Zidane et al. (2020)
Fe12.7Ni8.4O	0.781 (+0.049/–0.100)	3,750 K, 135 GPa	0.619 (+0.061/–0.120)	4,971 K, 330 GPa	DAC (ρ)	Gomi and Hirose (2015)
Fe12.9Ni9.2O	—	—	1.12	5,500 K,	Calculations (ρ)	Zidane et al. (2020)
Fe13.2Ni37.7S	—		1.10	360 GPa		
Fe13.9Ni8.9C	1.10 (+0.04/–0.09)	3,750 K, 135 GPa	0.908 (+0.051/–0.127)	4,971 K, 330 GPa	DAC (ρ)	Gomi and Hirose (2015)
Fe13.9Ni34.7Si	—	—	1.22	5,500 K,	Calculations (ρ)	Zidane et al. (2020)
Fe16.3Ni23.3O	—		1.02	360 GPa		
Fe16.9Ni11.8S	—		1.06			
Fe23Ni15Si	2.12	3,750 K, 135 GPa	2.02	4,971 K, 330 GPa	Calculations (ρ)	Stacey and Anderson (2001)
Fe23Ni15Si	2.15–2.8	4,023 K, 135 GPa	—	—	Calculations (ρ)	Davies (2007)
Fe-25Ni,S,Si,MgO	*2.77*	2,500 K, 3,000 km	*6.03*	5,500 K, 5,000 km	Calculations (ρ)	Gardiner and Stacey (1971)
Fe51.6Ni	0.74	4,000–5,500 K	—	—	DAC (ρ)	Gomi and Yoshino (2018)

The ρ values associated with studies that have reported k *values are obtained* via *the Wiedemann-Franz law with the Sommerfeld value for the Lorenz number.*
[a]*This method refers to first principles theoretical calculations.*
Values specific to liquid Fe are in red, those specific to solid Fe are in ***blue****, while unspecified values are in black. Compositions specific to the hcp phase of Fe are denoted by ε.*

(3,760 K, 135 GPa) and CMB (5,120 K, 330 GPa) respectively. All values discussed above are summarized in **Tables 1**–**4**. The variations in ρ, organized in terms of composition, are visualized in **Figure 2**.

A large quantity of theoretically- and experimentally-based estimates are considered for the ρ of a terrestrial core of pure Fe. In general, ρ values of Fe are centered about 1.05 and 1.08 μΩm at the CMB and ICB, respectively, without considering the high values (>3 μΩm) from Stacey and Loper (2007) and Konôpková et al. (2016). The high values reported in the theoretical work of Stacey and Loper (2007) and very challenging experimental work of Konôpková et al. (2016) can hardly be explained by the selection of P and T values since they are similar to those reported by the studies reporting lower ρ values. However, the values reported by Konôpková et al. (2016) are direct measurements of k, which include the phonon contribution. Their values are thus expected to be higher than measurements or calculations of k_e, although such a large discrepancy (3.5× higher than the average) cannot be explained by currently understood physics of the relative contributions of electron and phonon components of k in metals. The average ρ of Fe-Ni alloys is

TABLE 3 | Electrical resistivity values of Fe-O alloys at Earth's CMB (4,000 K, 136 GPa) and ICB (5000 K, 330 GPa) conditions determined by different methods.

Composition	ρ_{CMB} (μΩm)	CMB conditions	ρ_{ICB} (μΩm)	ICB conditions	Method (variable)	References
Fe1.6O	0.71	4,000–5,500 K	—	—	DAC (ρ)	Gomi and Yoshino (2018)
Fe11.7O	0.88		—			
Fe2.7O6Si	—	—	*0.79*	5,500 K, 328 GPa	[a]Calculations (ρ)	Pozzo et al. (2013)
Fe (2.7–3.5)O with 9.1 < S/Si < 11.4	*0.9*	4,039–4186 K	*0.8*	5,500–5,700 K	Calculations (σ)	Pozzo et al. (2012)
Fe3.9O	*0.75*	—	*0.67*	—	Calculations (ρ)	de Koker et al. (2012)
Fe3.9O	*0.74 ± 0.24*	130 GPa	*0.65 ± 0.24*	330 GPa	Calculations (ρ)	Wagle et al. (2019)
Fe4.6O4.9Si	—	—	*0.8*	5,500 K, 328 GPa	Calculations (ρ)	Pozzo et al. (2013)
Fe8.7O	*0.82*	—	*0.73*	—	Calculations (ρ)	de Koker et al. (2012)
Fe8.7O	*0.81 ± 0.29*	—	*0.71 ± 0.29*	—	Calculations (ρ)	Wagle et al. (2019)

The ρ values associated with studies that have reported k *values are obtained* via *the Wiedemann-Franz law with the Sommerfeld value for the Lorenz number.*
[a]*This method refers to first principles theoretical calculations.*
Values specific to liquid Fe are in red, while unspecified values are in black.

TABLE 4 | Electrical resistivity values of Fe-Si/S alloys at Earth's CMB (4000 K, 136 GPa) and ICB (5000 K, 330 GPa) conditions determined by different methods.

Composition	ρ_{CMB} (μΩm)	CMB conditions	ρ_{ICB} (μΩm)	ICB conditions	Method (variable)	References
ε-Fe1.8Si	**1.00**	4000 K, 140 GPa	—	—	DAC (ρ)	Zhang et al. (2021)
Fe2.8Si	0.71	4,000–5500 K	—	—	DAC (ρ)	Gomi and Yoshino (2018)
Fe3.1S	0.72		—			
Fe (3.9–4.5)Si	—	—	**0.65–66**	3750 K, 135 GPa	[a]Calculations (σ)	Pozzo et al. (2014)
Fe4.5Si	*1.5*	4,000–4500 K	—	—	Multi-anvil press (ρ)	Silber et al. (2019)
Fe6.1Si6.7S	0.741	—	—	—	DAC (σ)	Suehiro et al. (2017)
Fe7Si	*0.82*	—	*0.74*	—	Calculations (ρ)	de Koker et al. (2012)
Fe7Si	*0.81 ± 0.5*	130 GPa	*0.73 ± 0.5*	330 GPa	Calculations (ρ)	Wagle et al. (2019)
Fe7.6S	*0.82 ± 0.22*		*0.75 ± 0.22*			
ε-Fe8.7Si	**4.6**	3,300 K, 144 GPa	—	—	DAC (k)	Hsieh et al. (2020)
Fe9Si	**0.6–1.3**	—	—	—	DAC (ρ)	Seagle et al. (2013)
ε-Fe12.7Si	**0.775 (+0.150/–0.231)**	5,120 K, 330 GPa	**1.040 (+0.126/–0.212)**	3,760 K, 135 GPa	DAC (ρ)	Inoue et al. (2020)
Fe12.8S	0.699	—	—	—	DAC (σ)	Suehiro et al. (2017)
ε-Fe13.2Si	**1.02 (+0.04/–0.11)**	3,750 K, 135 GPa	**0.820 (+0.054/–0.131)**	4,971 K, 330 GPa	DAC (ρ)	Gomi et al. (2013)
Fe13.5Si	0.784	—	—	—	DAC (σ)	Suehiro et al. (2017)
Fe13.5Si	0.92	4,050 K, 136 GPa	—	—	DAC (ρ)	Zhang et al. (2018)
Fe13.5Si	1.02 (+0.04/–0.13)	3,750 K, 135 GPa	0.820 (+0.055/–0.130)	4,971 K, 330 GPa	DAC (ρ)	Gomi & Hirose (2015)
Fe14.4Si	*1.03*	—	*0.92*	—	Calculations (ρ)	de Koker et al. (2012)
Fe14.4Si	*1.02 ± 0.5*	130 GPa	*0.91 ± 0.5*	330 GPa	Calculations (ρ)	Wagle et al. (2019)
Fe16.1S	*1.01 ± 0.42*		*0.95 ± 0.42*			
Fe17Si	0.90–0.94	—	—	—	Multi-anvil press (ρ)	Kiarasi (2013)
Fe18.8Si	1.13	4,000–5,500 K	—	—	DAC (ρ)	Gomi and Yoshino (2018)
Fe20.9S	0.94		—			
Fe33.5Si	1.12	2,180 K, 140 GPa	—	—	Shock compression (σ)	Matassov (1977)

The ρ values associated with studies that have reported k *values are obtained* via *the Wiedemann-Franz law with the Sommerfeld value for the Lorenz number.*
[a]*This method refers to first principles theoretical calculations.*
Values specific to liquid Fe are in red, those specific to solid Fe are in ***blue****, while unspecified values are in black. Compositions specific to the hcp phase of Fe are denoted by ε.*

1.35 and 1.22 μΩm at the CMB and ICB respectively, without considering the high value from Gardiner and Stacey (1971) at ICB conditions. The theoretical work of Gardiner and Stacey (1971) reported the highest values corresponding to the estimated ρ of Fe-25Ni,S,Si,MgO. The reported data on Fe-Ni alloys are scattered and a clear relationship between light element content and ρ, or even between theoretical and experimental methods, cannot be readily seen. The average ρ of Fe-O alloys is 0.80 and 0.74 μΩm at the CMB and ICB respectively. Theoretical and experimental ρ values of Fe-Si/S alloys are centered about 1.08 and 0.83 μΩm at the CMB and ICB respectively, without considering the high value from Hsieh et al. (2020) at ICB conditions. Indeed, the ρ value for Fe8.7Si (Hsieh et al., 2020) is expected to be higher than that of Fe7.6Si (Wagle et al., 2019) but lower than that of Fe9Si (Seagle et al., 2013) and higher Si content alloys. The averages

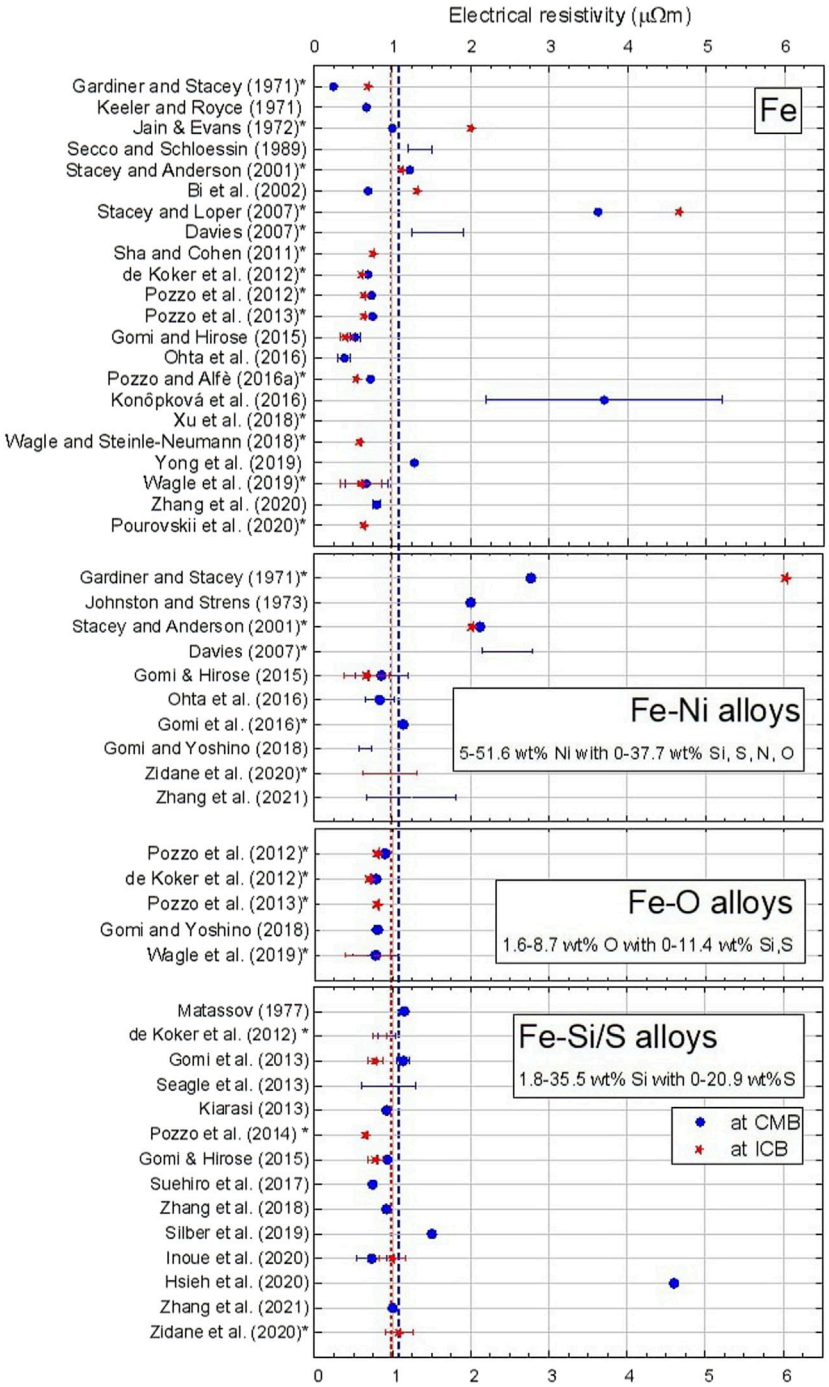

FIGURE 2 | Combined values of ρ from the literature applied to Earth's core presented in date order. The blue dashed line represents the average values (without values > 3 μΩm) at the CMB, while the red dashed line represents the average values at the ICB. The average of all reported values at CMB (4,000 K, 136 GPa) conditions is 1.07 μΩm, and that at ICB (5,000 K, 330 GPa) is 0.97 μΩm. The * denotes theoretical studies. Repeated references indicate different compositions.

of all studies reporting values for Earth are 1.07 and 0.97 μΩm at CMB and ICB conditions, respectively. Higher *P* and lower light element content generally result in a lower ρ for a given core composition, while high *T* acts to increase ρ. Yet, the consistently greater averages at CMB conditions, which consider a higher light element content and lower *P*, suggested that the effects of light element content and *P* dominate over the effects of *T*.

Moon

A combination of the lunar seismic profiles (Weber et al., 2011) and sound wave velocity measurements of Fe-alloys

TABLE 5 | Electrical resistivity values of Fe and Fe-alloys according to different methods, at the lunar CMB.

Composition	ρ_{CMB} (μΩm)	CMB conditions	Method (variable)	References
Fe	1.23–1.31	1,687–1,800 K, 4.9 GPa	Multi-anvil press (ρ)	Silber et al. (2018)
Fe	**0.66**	1,700 K, 4.5 GPa	Multi-anvil press (ρ)	Pommier (2018)
Fe5S	**2.15**			
Fe15.6P	<1.65	1,773 K, 4.5–5.5 GPa	Multi-anvil press (ρ)	Yin et al. (2019)
FexSi (x = 2–17)	1.17–1.66	1,600 K, 5–7 GPa	Multi-anvil press (ρ)	Berrada et al. (2020)

*The ρ values associated with studies that have reported k values are obtained via the Wiedemann-Franz law with the Sommerfeld value for the Lorenz number. Values specific to solid Fe are in **blue**, while unspecified values are in black.*

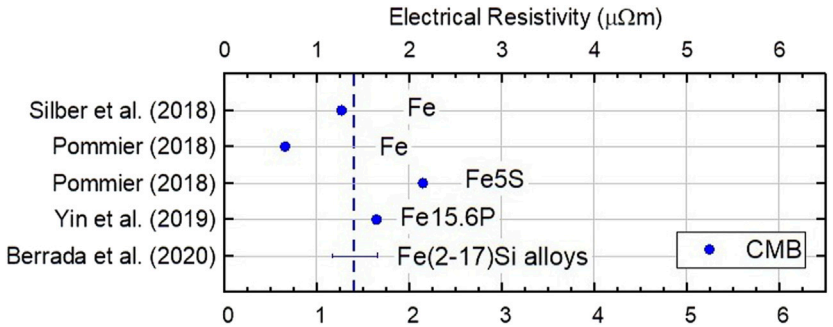

FIGURE 3 | Combined values of ρ from the literature applied to the Moon's core presented in date order. The blue dashed line represents the average values at the CMB. The average of all reported values at CMB (1,687–1,800 K, 4.5 GPa) conditions is 1.40 μΩm. Repeated references indicate different compositions.

(Antonangeli et al., 2015) indicates that the Moon is currently composed of a liquid outer core and solid inner core. The exact amount and nature of light element(s) in the core is not constrained but S, C, and Ni are expected (Wieczorek et al., 2006; Steenstra and van Westrenen, 2017). The presence of Si in the lunar core is also considered possible since the lunar Si isotope composition suggests a mantle composition similar to Earth's (Armytage et al., 2012; Nazarov et al., 2012; de Meijer et al., 2013; Zambardi et al., 2013). Szurgot (2017) reported at least 2.7 wt% Si in the lunar core when considering the uncompressed density of the Moon.

The calculated k of Fe (25–50 W m^{-1} K^{-1}) by Anderson (1998) and Stacey and Anderson (2001) have been commonly used in thermal evolution models of the lunar dynamo (Stegman et al., 2003; Zhang et al., 2013; Evans et al., 2014; Laneuville et al., 2014; Scheinberg et al., 2015; Laneuville et al., 2018). However, the corresponding ρ via the Wiedemann-Franz law varies from study to study due to the large variations in T assigned to the lunar CMB. Direct resistivity measurements of Fe in a multi-anvil press from 3–12 GPa and into the liquid state suggested ρ of 1.23–1.31 μΩm on the core side of the CMB (1,687–1,800 K, 4.9 GPa) (Silber et al., 2018). Using a similar method, Pommier (2018) measured ρ in a multi-anvil apparatus up to 10 GPa and over a wide range of T. Their results suggested a value of 0.66 μΩm, or slightly more than half of the value measured by Silber et al. (2018). Also, Pommier (2018) reported a ρ of 2.15 μΩm for Fe5S at 4.5 GPa and 1,700 K. According to their results, the effect of S, even for such a small wt%, is not negligeable. Recently, Yin et al. (2019) reported measurements of ρ of Fe35.7P (or FeP), Fe21.7P (or Fe_2P) and Fe15.6P (or Fe_3P) in a multi-anvil press at 3.2 GPa. These authors include P as a possible light element in the lunar core considering its large solubility in liquid Fe and Fe-S alloys (Zaitsev et al., 1995; Stewart and Schmidt, 2007). Their results indicate that ρ of Fe35.7P is approximately four times that of Fe. Yin et al. (2019) conclude that ρ is expected to be lower than 1.65 μΩm for a lunar core with Fe15.6P. In addition, the direct measurements of Berrada et al. (2020) constrained the ρ of Fe-Si alloys (2, 8.5, 17 wt% Si) between 1.17–1.66 μΩm at the top of the lunar outer core (1,600 K, 5–7 GPa). These studies have all used a multi-anvil apparatus with a four-wire measurement method to measure ρ. The values discussed in this section are summarized in **Table 5** and the variations in ρ are visualized in **Figure 3**.

Although the exact identity and amount of light elements in the lunar core is not constrained, to our knowledge, only few studies have reported ρ values to the relevant P and T conditions of the lunar core. At CMB conditions, the measured ρ of Fe15.6P is lower than that reported for Fe-Si alloys (up to 17 wt% Si) and Fe5S, suggesting the effect of P on the core ρ is relatively negligible. The reported Fe-alloys show greater ρ than that of Fe, as expected considering the additional scattering mechanism caused by electron-impurity interactions. The average of all studies reporting values at CMB conditions is 1.40 μΩm.

Mercury

Our understanding of the light element content of Mercury is mainly based on solar-system chemical abundances, models based on the compositions of Earth and the Moon, and data returned from the MESSENGER X-ray spectrometer (Harder and Schubert, 2001; McCubbin et al., 2012). Early estimates of the

TABLE 6 | Electrical resistivity values of Fe and Fe-alloys according to different methods, at Mercury's CMB and ICB conditions.

Composition	ρ_{CMB} (μΩm)	CMB conditions	ρ_{ICB} (μΩm)	ICB conditions	Method (variable)	References
γ-Fe	**0.44**	1800–2,000 K, 5–7 GPa	**0.36**	2,200–2,500 K, 36 GPa	Multi-anvil press (ρ)	Deng et al. (2013)
γ-Fe	—	—	**1.08–2.44**	2,200–2,500 K, 40 GPa	DAC (ρ)	Konôpková et al. (2016)
Fe	*1.044*	1,823 K, 5.5 GPa	—	—	Multi-anvil press (ρ)	Secco (2017)
Fe	—	—	0.87 ± 0.10	1,900 K, 5 GPa	Multi-anvil press (ρ)	Silber et al. (2018)
Fe	**1.18**–*1.24*	1,880 K, 5 GPa	—	—	Multi-anvil press (ρ)	Ezenwa and Secco (2019)
Fe8.5Si	*1.40–1.44*	1,600–2100 K, 5–7 GPa	—	—	Multi-anvil press (ρ)	Berrada et al. (2021)
Fe10Si	0.35	2,000 K, 6 GPa	—	—	Multi-anvil press (ρ)	Pommier et al. (2019)
Fe8Si3S	0.33		—			
Fe33.5Si	0.49		—			
Fe36.5S	8.01	1,300 K, 8 GPa	—	—	Multi-anvil press (σ)	Manthilake et al. (2019)

The ρ values associated with studies that have reported k *values are obtained via the Wiedemann-Franz law with the Sommerfeld value for the Lorenz number. Values specific to liquid Fe are in red, those specific to solid Fe are in* ***blue****, while unspecified values are in black. Compositions specific to the fcc phase of Fe are denoted by γ.*

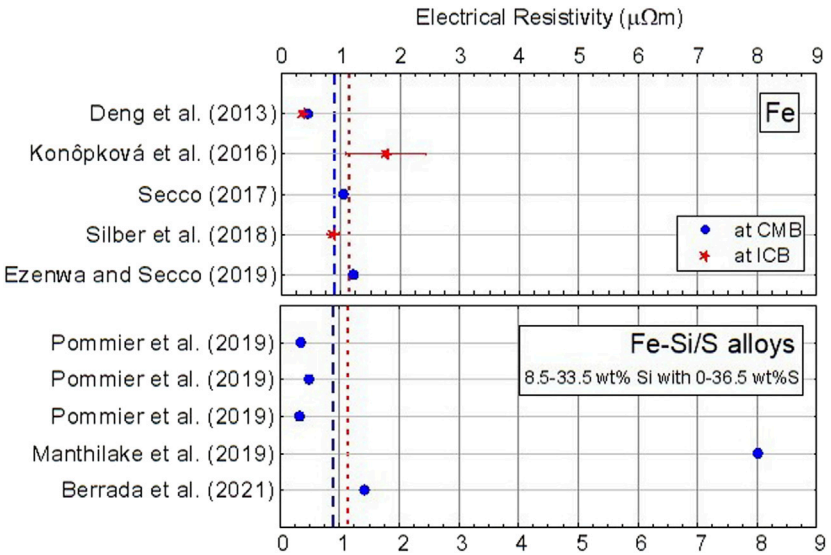

FIGURE 4 | Combined values of ρ from the literature applied to Mercury's core presented in date order. The blue dashed line represents the average values at the CMB, while the red dashed line represents the average values at the ICB. The average of all reported values at CMB (1,900 K, 5 GPa) conditions is 0.88 μΩm, and that at ICB (2,200–2,500 K, 36 GPa) is 1.12 μΩm.

core composition of Mercury suggest ~99 wt% is metal (Fe, Ni, Co) and ~1 wt% is Fe36.5S (or FeS) (Morgan and Anders, 1980). Nittler et al. (2017) has argued a Si-bearing core with perhaps some small amounts of S and C, while Rivoldini et al. (2009) suggest a minimum of 5 wt% S. Various thermal evolution models consider an Fe-Si core with uncertainty on the exact Si composition (Knibbe and van Westrenen, 2017; Knibbe and van Westrenen, 2018). Estimates of Si content range between 5 and 25 wt% Si (Malavergne et al., 2010; Chabot et al., 2014), although recent studies propose that 10.5 wt% Si provides the best modelling results of the core's elastic property and geodesy data (Terasaki et al., 2019; Steinbrügge et al., 2021).

Early models of Mercury's core formation generally consider k of 40–43 W m^{-1} K^{-1}, which correspond to 1.06–1.15 μΩm, at 1,880 K for a core of mainly Fe with 1–5 wt% S (Stevenson et al., 1983; Christensen, 2006; Tosi et al., 2013). Thermal evolution models by Knibbe and van Westrenen (2018) considered a range of k from 30 to 60 W m^{-1} K^{-1} for an Fe-Si core with T between 1,800–2,200 K, which corresponds to 0.73–1.79 μΩm *via* the Wiedemann-Franz law. In contrast, direct measurements of ρ of γ-Fe at 5, 7 and 15 GPa into the liquid state in a multi-anvil press suggested values of ~0.36 μΩm and ~0.44 μΩm at ICB (2,200–2500 K, 36 GPa) and CMB (1800–2000 K, 5–7 GPa) conditions respectively (Deng et al., 2013). The direct measurements of ρ for γ-Fe at Mercury core temperatures in a laser-heated DAC suggested values of 1.08–2.44 μΩm (or 35 ± 10 W m^{-1} K^{-1}) at 2,200–2,500 K and ~40 GPa (Konôpková et al., 2016). Considering the variations in the Lorenz number with T, Secco (2017) reported ρ for Fe of 1.044 μΩm at 1,823 K and 5.5 GPa. Silber et al. (2018) used direct ρ measurements of Fe from 3–12 GPa and up to liquid T and suggested a value of 0.87 ± 0.10 μΩm for Fe at CMB conditions (1,900 K, 5 GPa). Ezenwa

and Secco (2019) revised previous measurements of ρ of Fe at Mercury's CMB conditions (1,880 K, 5 GPa) to 1.18 μΩm on the solid side just before melting and 1.24 μΩm on the liquid side. Berrada et al. (2021) reported higher ρ values of Fe8.5Si between 1.40–1.44 μΩm at CMB conditions (1,600–2,100 K, 5–7 GPa) from measurements in a multi-anvil press up to 24 GPa and above the liquid *T*. Similarly, Pommier et al. (2019) conducted direct measurements in a multi-anvil apparatus up to 10 GPa and over a wide range of *T*. Their results suggested approximately 0.35 μΩm for Fe10Si, 0.49 μΩm for Fe33.5Si, and 0.33 μΩm for Fe8Si3S at CMB conditions (2,000 K, 6 GPa). In contrast, Manthilake et al. (2019) reported σ data from resistance measurements of Fe36.5S, which convert to 8.01 μΩm near CMB conditions (1,300 K, 8 GPa). This result is significantly larger that of any composition reported in the literature thus far at similar *P* and *T* conditions. The values discussed in this section are summarized in **Table 6** and the variations in ρ are visualized in **Figure 4**.

Reported theoretical and experimental values of the ρ of Fe applied to Mercury's CMB and ICB conditions show an important disagreement. Deng et al. (2013) reported lower values (~35% less) than those reported by Konôpková et al. (2016), Secco (2017), Silber et al. (2018), and Ezenwa and Secco (2019). Such a discrepancy is not negligible when calculating q_{ad} at the top of the outer core. The direct *k* measurements by Konôpková et al. (2016) convert to similar ρ values to the direct ρ measurements by Secco (2017), Silber et al. (2018) and Ezenwa and Secco (2019). The values reported for Fe-Si/S alloys also show two distinct trends. Berrada et al. (2021) reported higher values than those by Pommier et al. (2019), although Pommier (2018) considered a higher light element content (up to 33.5 wt% Si). Indeed, the light element content is expected to increase the scattering contribution and thus the measured ρ. The values reported by Pommier (2018) are consistent with the lower ρ values for Fe reported by Deng et al. (2013) and Konôpková et al. (2016). Similarly, the values reported by Berrada et al. (2021) are consistent with the high ρ of Fe values reported by Secco (2017), Silber et al. (2018),and Ezenwa and Secco (2019). The averages of all studies reporting values for Mercury are 0.88 and 1.12 μΩm at CMB and ICB conditions, respectively, without considering the high values (>3 μΩm) from Manthilake et al. (2019). Although all the reported data at the ICB consist only of pure Fe measurements, the average ρ at ICB conditions is greater than that at CMB conditions which considers Fe-alloys. This contrast with the observations at Earth's core conditions could be explained by the strong effect of *T* over the effects of light elements and *P* at Mercury's core conditions, although further studies are necessary to draw reliable conclusions.

Mars

The chemical composition of the Martian core is presumed to be Fe14.2S based on analyses of Martian meteorites (Wänke et al., 1988). Laser-heated DAC experiments and *in-situ* X-ray diffraction confirm the phase stability of Fe36.5S at core conditions (Kavner et al., 2001). Thermal evolution models also consider a core primarily composed of Fe with 6–8 wt% Ni, and 10–17 wt% S, in addition to containing lower amounts of O, C, H and P (Rivoldini et al., 2011).

Stevenson et al. (1983) investigated core evolution models of Mars by combining theories of geomagnetism and fluid dynamics. In their model, the value of *k* of Fe used for Earth, Mercury, Mars and Venus is 40 W m^{-1} K^{-1}, which corresponds to 1.15 μΩm at 1,880 K (Stevenson et al., 1983). Thermal evolution models based on measurements by Anderson (1998) suggested a range of 43–88 W m^{-1} K^{-1} at Martian CMB conditions (25 GPa, 1,800 K) (Nimmo and Stevenson, 2000). Using the Wiedemann-Franz law, this suggested ρ values for Fe ranging from 0.50–1.02 μΩm, which are lower than previously mentioned. In fact, Deng et al. (2013) estimated ρ of γ-Fe to be at most 0.40 μΩm at the outermost part of the Martian core (2,000 K, 24 GPa) based on their measurements at 7 GPa. Recent measurements by Silber et al. (2018) reported ρ of Fe of 1.7 μΩm at CMB conditions (1,770 K, 23 GPa), higher than previously reported. Similar experiments by Ezenwa and Yoshino (2021) in a multi-anvil apparatus from 14 to 22.5 GPa and above the liquid *T*, estimated ρ of 0.68 ± 0.03 μΩm at CMB conditions (2,106 K, 23 GPa). The measurements by Ezenwa and Yoshino (2021) are in agreement with first-principle calculations of pure Fe reporting values from 0.74 ± 0.29 μΩm to 0.75 ± 0.29 at the ICB and CMB respectively (Wagle et al., 2019). Wagle et al. (2019) also calculated the ρ of Fe3.9O, Fe8.7O, Fe7.6S, Fe16.1S, Fe6.7Si, and Fe14.4Si at the Martian ICB and CMB conditions, as reported in **Table 7**. Direct measurements of ρ up to 110 GPa at 300 K suggested values from 1.064 μΩm at the CMB to 0.952 μΩm at the center of an Fe15S (or $Fe_{77.7}S_{22.3}$) core (Suehiro et al., 2017). The values discussed in this section are summarized in **Table 7** and the variations in ρ are visualized in **Figure 5**.

The literature on ρ values at Martian core conditions is insufficient to determine a reasonable value at CMB and ICB conditions. While both Deng et al. (2013) and Silber et al. (2018) reported values for solid Fe, the value reported by Deng et al. (2013) is in best agreement with the reported values of liquid Fe (Wagle et al., 2019; Ezenwa and Yoshino, 2021). However, Silber et al. (2018) considered lower *T* values at the CMB than Ezenwa and Yoshino (2021). Their measured ρ is therefore expected to be lower than that of Ezenwa and Yoshino (2021), although the opposite is observed. Within the results of Wagle et al. (2019), the effect of O in increasing ρ seems to be less than that of Si and S, although all alloys seems to be in agreement within uncertainty. The values for an Fe15S (Suehiro et al., 2017) are in agreement with those of Fe16.1S (Wagle et al., 2019). The average of all studies reporting values at CMB conditions is 0.95 μΩm, while that at ICB conditions is 0.93 μΩm. The greater average at CMB conditions relative to ICB conditions is comparable to that observed at Earth's core conditions.

Ganymede

The presence of Fe36.5S in meteorites indicates that S is probably a major light element in Ganymede's core (Krot, 2005). Hydrogen is also a light element candidate considering that a layer of H_2O in Ganymede's interior has been proposed (Anderson et al., 1996).

TABLE 7 | Electrical resistivity values of Fe and Fe-alloys according to different methods, at the Martian CMB (1,770 K, 23 GPa) and ICB (2,000 K, 40 GPa) conditions.

Composition	ρ_{CMB} (μΩm)	CMB conditions	ρ_{ICB} (μΩm)	ICB conditions	Method (variable)	References
γ-Fe	0.4	2,000 K, 24 GPa	—	—	Multi-anvil press (ρ)	Deng et al. (2013)
Fe	1.7	1,770 K, 23 GPa	—	—	Multi-anvil press (ρ)	Silber et al. (2018)
Fe	*0.68 ± 0.03*	2,106 K, 23 GPa	—	—	Multi-anvil press (ρ)	Ezenwa and Yoshino (2021)
Fe	*0.75 ± 0.29*	23 GPa	*0.74 ± 0.29*	40 GPa	[a]Calculations (ρ)	Wagle et al. (2019)
Fe3.9O	*0.83 ± 0.25*		*0.87 ± 0.25*			
Fe8.7O	*0.95 ± 0.32*		*0.92 ± 0.32*			
Fe6.7Si	*0.92 ± 0.55*		*0.91 ± 0.55*			
Fe14.4Si	*1.16 ± 0.42*		*1.14 ± 0.42*			
Fe7.6S	*0.88 ± 0.25*		*0.87 ± 0.25*			
Fe16.1S	*1.07 ± 0.42*		*1.06 ± 0.42*			
Fe15S	1.064	—	0.952	—	DAC (ρ)	Suehiro et al. (2017)

The ρ values associated with studies that have reported k values are obtained via the Wiedemann-Franz law with the Sommerfeld value for the Lorenz number.
[a]*This method refers to first principles theoretical calculations.*
Values specific to liquid Fe are in red, while unspecified values are in black. Compositions specific to the fcc phase of Fe are denoted by γ.

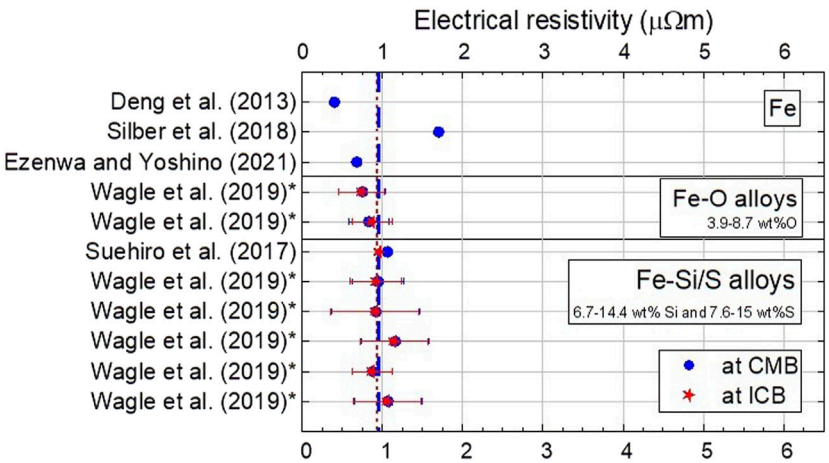

FIGURE 5 | Combined values of ρ from the literature applied to Mars' core presented in date order. The blue dashed line represents the average values at the CMB, while the red dashed line represents the average values at the ICB. The average of all reported values at CMB (1770 K, 23 GPa) conditions is 0.95 μΩm, and that at ICB (2,000 K, 40 GPa) is 0.93 μΩm. The * denotes theoretical studies. Repeated references indicate different compositions.

TABLE 8 | Electrical resistivity values of Fe and Fe-alloys according to different methods, at Ganymede's CMB.

Composition	ρ_{CMB} (μΩm)	CMB conditions	ρ_{ICB} (μΩm)	ICB conditions	Method (variable)	References
Fe	1.2	1,500 K, 5.9 GPa	—	—	Multi-anvil press (ρ)	Silber et al. (2018)
Fe	—	—	**1.17**–*1.38*	2,200 K, 9 GPa	Multi-anvil press (ρ)	Ezenwa and Secco (2019)
Fe	**0.59**	1,400 K, 4.5 GPa	—	—	Multi-anvil press (ρ)	Pommier (2018)
Fe5S	**2.23**					
Fe20S	**4.32**					
Fe36.5S	8.01	1,300 K, 8 GPa	—	—	Multi-anvil press (σ)	Manthilake et al. (2019)
Fe36.5S	4.12 ± 0.07	1,411 K, 5 GPa	—	—	Multi-anvil press (ρ)	Littleton et al. (2021)

Values specific to liquid Fe are in red, those specific to solid Fe are in ***blue****, while unspecified values are in black.*

Although the exact composition is not constrained, the light element content is greatly dependent on the core size and oxidation state of the interior during differentiation. The CMB conditions are expected to be near 2,000 K and 7 GPa in the case of a low (1 wt%) S content, while near 1,400 K and 5 GPa in the case of a near eutectic (36.5 wt%) S content (Hauck et al., 2006; Bland et al., 2008; Kimura et al., 2009).

Silber et al. (2018) measured ρ of Fe at 1.20 μΩm at 1,500 K (Shibazaki et al., 2011) and 5.9 GPa (Hussmann et al., 2007), while a considerably lower value of 0.59 μΩm is proposed by

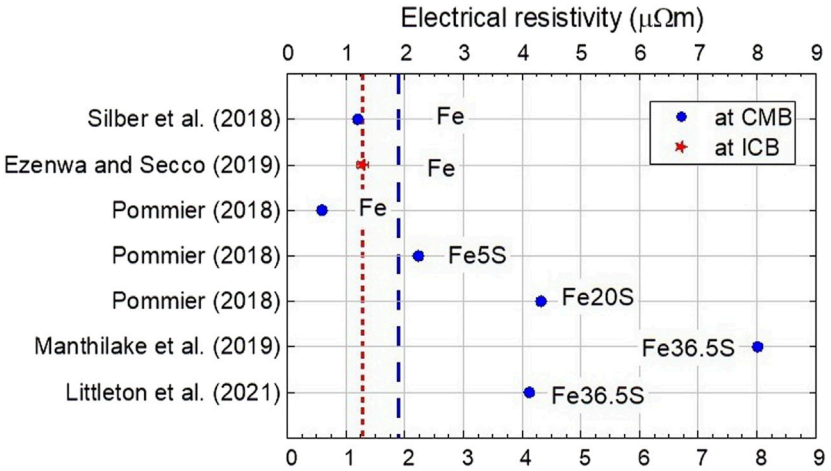

FIGURE 6 | Combined values of ρ from the literature applied to Ganymede's core presented in date order. The blue dashed line represents the average values at the CMB, while the red dashed line represents the average at the ICB. The average of all reported values at CMB (1,400–2000 K, 5–7 GPa) conditions is 1.90 μΩm, and that at the ICB (2,200 K, 9 GPa) is 1.28 μΩm. Repeated references indicate different compositions.

Pommier (2018) at 1,400 K and 4.5 GPa. Similar to the measurements by Silber et al. (2018), Ezenwa and Secco (2019) estimated values of 1.17 μΩm and 1.38 μΩm on the solid and liquid sides of the ICB (2,200 K, 9 GPa) respectively. Regardless of the variation in these Fe results, adding S is expected to increase ρ, in agreement with the direct measurements of Pommier (2018). Pommier (2018) reported values of 2.23 μΩm for Fe5S at 1,880 K and 4.5 GPa, and 4.32 μΩm for Fe20S at 1,400 K and 4.5 GPa. To our knowledge, only two studies have reported measurements of Fe36.5S at the relevant *P* and *T* conditions. First, the results of Manthilake et al. (2019) applied to Ganymede's conditions suggest 8.01 μΩm near CMB. In contrast, direct ρ measurements of Fe36.5S, from 2 to 5 GPa and up to 1,785 K in a multi-anvil press, suggested a value of 4.13 ± 0.07 μΩm at CMB conditions (1,411 K, 5 GPa) (Littleton et al., 2021). The values discussed in this section are summarized in **Table 8** and the variations in ρ are visualized in **Figure 6**.

As with the other small planetary bodies reviewed, the available literature is scarce and insufficient to distinguish a reasonable value for ρ at core conditions. Overall, the addition of S impurity scattering increases ρ as expected. However, ρ of Fe36.5S as measured by Littleton et al. (2021) is greater than that of Fe20S (Pommier, 2018). Pressure is expected to decrease ρ, yet the ρ of Fe36.5S from Manthilake et al. (2019) at 8 GPa is almost double that from Littleton et al. (2021) at 5 GPa. Although total *k* measurements include the phonon contribution to conductivity, it likely does not explain the extent of the disagreement between these two studies. The average of all studies reporting values at CMB conditions is 1.90 μΩm, larger than that at the other planetary bodies reviewed, while the average at ICB conditions is 1.28 μΩm.

CONTOUR MAPS OF ρ(*P*, *T*)

Figure 7 illustrates contour maps generated from the available literature on ρ for Fe, Fe-Ni alloys, Fe-O alloys and Fe-Si/S alloys, without excluding high values (>3 μΩm). The contour maps suggest ρ(*P*, *T*) is unique for each composition, and can hardly be defined by a linear function of *P* and *T*. The rich literature on Fe at Earth's and Mercury's CMB and ICB conditions produce an accurate contour map at the relevant *P* and *T*. Similarly, the contour map results of the ρ of Fe at the lunar and Martian CMB consist of the mean of the few reported values. However, Fe-Ni alloys were only reported at *P* and *T* conditions relevant to Earth's core. Thus, the contour map results for Fe-Ni alloys for the Moon, Mercury, Mars, and Ganymede's cores are unreliable extrapolations. The contour map of Fe-Ni alloys suggest ρ at low *P* and *T* is considerably higher than the values reported at high *P* and *T*. This would mean the effect of decreasing *P*, which acts to increase ρ, dominates over the effect of decreasing *T*, which acts to decrease ρ. In the same idea, ρ of Fe-O alloys was only reported at Earth's and Mars' core conditions, which implies the most reliable areas of the contour map are within those *P* and *T* boundaries. The contour map of Fe-Si/S alloys is in agreement with the reported data at the planetary core conditions of Earth, Moon, Mercury, Mars and Ganymede. The advantage of the contour maps is that they take into account the various *P* and *T* values used for the planetary core conditions and allow for a general estimate at a specific *P* and *T* combination. For example, the contour map of Fe-Si/S shows ρ of ~1.70 μΩm at the lunar CMB (at 1,750 K which is the mid-*T* range, and 4.5 GPa), while the average of reported values is 1.66 μΩm without considering the differences in *P* and *T* conditions.

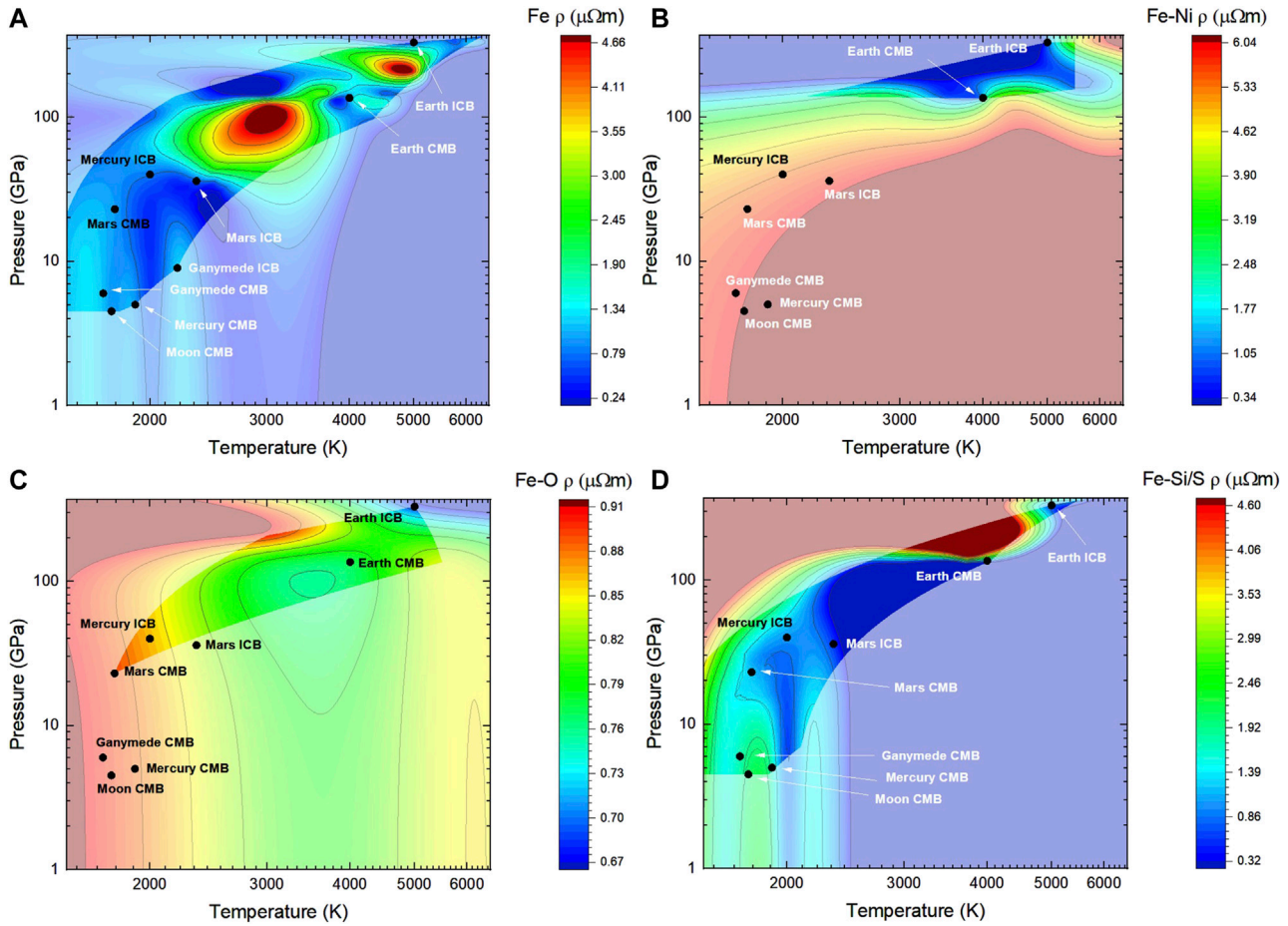

FIGURE 7 | 3D visualization of the reported ρ with *P* and *T* of **(A)** Fe, **(B)** Fe-Ni alloys, **(C)** Fe-O alloys, and **(D)** Fe-Si/S alloys. Studies that did not state the exact *P*, *T* conditions for Earth's CMB and ICB are placed at 4,000 K and 136 GPa, and 5,000 K and 330 GPa, respectively. Similarly, the lunar CMB is placed at 1,750 K (which is the mid-*T* range of 1,687–1,800 K) and 4.5 GPa. Mercury's CMB and ICB are placed at 1,900 K and 5 GPa, and 2,350 K (which is the mid-*T* range of 2,200–2,500 K) and 36 GPa, respectively. The Martian CMB and ICB are placed at 1,770 K and 23 GPa, and 2,000 K and 40 GPa, respectively. Ganymede's CMB is located at 1,700 K (which is the mid-*T* range of 1,400–2,000 K) and 6 GPa (which is the mid-*P* range of 5–7 GPa), while the ICB is at 2,200 K and 9 GPa. The areas encompassing the reported data are in full colour, while the faded colors are areas of extrapolations.

DISCUSSION

The interest in determining q_{ad} is namely motivated by thermal evolution modelling. Direct measurements of thermal properties, and in particular *k*, of metals and metal-alloys at planetary core conditions are challenging and extrapolations from relatively low *P* and *T* conditions are not always consistent. Experimental progress made so far in measuring *k* at core conditions is very promising and future studies are needed to establish conclusively this important core property. The available literature on ρ at Earth's core conditions is focused on pure Fe, while a few studies have considered various light elements and a range of concentrations. Results suggest that the ρ of Fe-alloys at Earth's CMB and ICB does not significantly deviate from that of pure Fe. The scarce literature on ρ at the lunar core suggest the effect of P is negligible when compared to that of Si and S at similar wt%. On the contrary, the effect of Si and S at Mercury's core conditions remains unclear as the literature seems to be divided into two distinct groups of ρ, with ~35% difference. At the Martian core, the ρ of Fe-alloys are within the variations of ρ for pure Fe. In contrast, the reported ρ of Fe-S alloys at Ganymede's CMB conditions show a great deviation from pure Fe measurements. Overall, the calculated ρ from the reported *k* values via the Wiedemann-Franz law, with the Sommerfeld value for *L*, do not significantly vary from direct measurements of ρ. Results from first-principle calculations are within the variations of those from direct measurements from multi-anvil press, DAC and shock compression experiments. Although ρ values depend on the *P* and *T*, the variations in the selection of *P* and *T* at the planetary core conditions among the literature seem to have a negligible effect on the average ρ values. The contour maps provide an interpolation of ρ as a function of *P* and *T* within the boundaries of the reported values.

Further experimental research on ρ should focus on different light element compositions, particularly in Fe with multi-light element alloys, in order to constrain reliably ρ for

likely core compositions at planetary core conditions. A larger data set on measurements of k will be needed to verify both theoretically determined values of the Lorenz number at extreme conditions of P and T for pure Fe and its many alloys as well as to substantiate the use of ρ data to calculate k. Calculations that account for spin polarization and the effects of magnetism on the electron scattering have recently been developed and further progress in this area to quantify this important contribution to electrical and thermal properties at planetary core conditions is likely.

It is clear there is much to be done in the area of ρ and k property determination for application to thermal modelling of terrestrial-like planetary bodies in our Solar System. However, an even greater challenge appearing on the horizon is for similar studies to be carried out at the even greater P, T conditions of terrestrial-type exoplanets where the internal pressures are an order of magnitude higher than in Earth. Studies of those systems, which are currently in the nascent stages of characterizing equation of state and other structure-related characteristics of Fe (Smith et al., 2018) and Fe alloys (Wicks et al., 2018), will then turn to interior modelling of heat flow and core dynamics to understand dynamos in super-Earths, which will require knowledge of ρ and k behavior over much greater P, T space.

AUTHOR CONTRIBUTIONS

MB is responsible for the formal analysis, writing and editing. RS is responsible for supervision, reviewing, editing, and funding.

FUNDING

This work was supported by funds to RS from the Natural Sciences and Engineering Research Council of Canada (grant number 2018-05021).

ACKNOWLEDGMENTS

We are very grateful to Dr. Gerd Steinle-Neumann and Dr. Monica Pozzo for their insightful comments on the manuscript and to two reviewers for their constructive comments.

REFERENCES

Ahrens, T. J. (2007). "Shock Wave Experiments," in *Encyclopedia of Geomagnetism and Paleomagnetism*. Editors D. Gubbins and E. Herrero-Bervera (Dordrecht: Springer Netherlands), 912–920.

Alfè, D., Gillan, M. J., and Price, G. D. (2007). Temperature and Composition of the Earth's Core. *Contemp. Phys.* 48 (2), 63–80. doi:10.1080/00107510701529653

Anderson, J. D., Lau, E. L., Sjogren, W. L., Schubert, G., and Moore, W. B. (1996). Gravitational Constraints on the Internal Structure of Ganymede. *Nature* 384 (6609), 541–543. doi:10.1038/384541a0

Anderson, O. L. (1998). The Grüneisen Parameter for Iron at Outer Core Conditions and the Resulting Conductive Heat and Power in the Core. *Phys. Earth Planet. Interiors* 109 (3), 179–197. doi:10.1016/s0031-9201(98)00123-x

Antonangeli, D., Morard, G., Schmerr, N. C., Komabayashi, T., Krisch, M., Fiquet, G., et al. (2015). Toward a mineral Physics Reference Model for the Moon's Core. *Proc. Natl. Acad. Sci.* 112 (13), 3916–3919. doi:10.1073/pnas.1417490112

Anzellini, S., and Boccato, S. (2020). A Practical Review of the Laser-Heated Diamond Anvil Cell for University Laboratories and Synchrotron Applications. *Crystals* 10 (6), 459. doi:10.3390/cryst10060459

Argaman, N., and Makov, G. (2000). Density Functional Theory: An Introduction. *Am. J. Phys.* 68 (1), 69–79. doi:10.1119/1.19375

Armytage, R. M. G., Georg, R. B., Williams, H. M., and Halliday, A. N. (2012). Silicon Isotopes in Lunar Rocks: Implications for the Moon's Formation and the Early History of the Earth. *Geochimica et Cosmochimica Acta* 77, 504–514. doi:10.1016/j.gca.2011.10.032

Asimow, P. D. (2015). "Dynamic Compression," in *Treatise on Geophysics*. Editor G. Schubert Second Edition (Oxford: Elsevier), 393–416. doi:10.1016/b978-0-444-53802-4.00050-6

Badro, J., Fiquet, G., Guyot, F., Gregoryanz, E., Occelli, F., Antonangeli, D., et al. (2007). Effect of Light Elements on the Sound Velocities in Solid Iron: Implications for the Composition of Earth's Core. *Earth Planet. Sci. Lett.* 254 (1), 233–238. doi:10.1016/j.epsl.2006.11.025

Baum, B., Gel'd, P., and Tyagunov, G. (1967). Resistivity of Ferrosilicon Alloys in the Temperature Range 800–1700 C. *The Phys. Met. Metallography* 24 (181), 52–57. doi:10.1016/0016-2361(73)90012-4

Berrada, M., Secco, R. A., and Yong, W. (2021). Adiabatic Heat Flow in Mercury's Core from Electrical Resistivity Measurements of Liquid Fe-8.5 wt%Si to 24 GPa. *Earth Planet. Sci. Lett.* 568, 117053. doi:10.1016/j.epsl.2021.117053

Berrada, M., Secco, R. A., and Yong, W. (2018). Decreasing Electrical Resistivity of Gold along the Melting Boundary up to 5 GPa. *High Press. Res.* 38 (4), 367–376. doi:10.1080/08957959.2018.1493476

Berrada, M., Secco, R. A., and Yong, W. (2020). Electrical Resistivity Measurements of Fe-Si with Implications for the Early Lunar Dynamo. *J. Geophys. Res. Planets* 125 (7), e2020JE006380. doi:10.1029/2020je006380

Bi, Y., Tan, H., and Jing, F. (2002). Electrical Conductivity of Iron under Shock Compression up to 200 GPa. *J. Phys. Condensed Matter* 14 (44), 10849–10854. doi:10.1088/0953-8984/14/44/389

Birch, F. (1961). Composition of the Earth's Mantle. *Geophys. J. Int.* 4 (Suppl. ment_1), 295–311. doi:10.1111/j.1365-246x.1961.tb06821.x

Birch, F. (1964). Density and Composition of Mantle and Core. *J. Geophys. Res.* 69 (20), 4377–4388. 1896-1977. doi:10.1029/jz069i020p04377

Bland, M. T., Showman, A. P., and Tobie, G. (2008). The Production of Ganymede's Magnetic Field. *Icarus* 198 (2), 384–399. doi:10.1016/j.icarus.2008.07.011

Bohnenkamp, U., Sandström, R., and Grimvall, G. (2002). Electrical Resistivity of Steels and Face-Centered-Cubic Iron. *J. Appl. Phys.* 92 (8), 4402–4407. doi:10.1063/1.1502182

Boltzmann, L. (1894). Zur Integration der Diffusionsgleichung bei variabeln Diffusionscoefficienten. *Ann. Phys.* 289 (13), 959–964. doi:10.1002/andp.18942891315

Bridgman, P. W. (1957). Effects of pressure on binary alloys. VI. Systems for the most part of dilute Úlloys of high melting metals. *Proc. Am. Acad. Arts. Sci.* 84, 179–216.

Chabot, N. L., Wollack, E. A., Klima, R. L., and Minitti, M. E. (2014). Experimental Constraints on Mercury's Core Composition. *Earth Planet. Sci. Lett.* 390, 199–208. doi:10.1016/j.epsl.2014.01.004

Christensen, U. R. (2006). A Deep Dynamo Generating Mercury's Magnetic Field. *Nature* 444 (7122), 1056–1058. doi:10.1038/nature05342

Davies, G. F. (2007). Mantle Regulation of Core Cooling: A Geodynamo without Core Radioactivity? *Phys. Earth Planet. Interiors* 160 (3), 215–229. doi:10.1016/j.pepi.2006.11.001

de Koker, N., Steinle-Neumann, G., and Vlcek, V. (2012). Electrical Resistivity and thermal Conductivity of Liquid Fe Alloys at High P and T, and Heat Flux in Earth's Core. *Proc. Natl. Acad. Sci.* 109 (11), 4070–4073. doi:10.1073/pnas.1111841109

de Meijer, R. J., Anisichkin, V. F., and van Westrenen, W. (2013). Forming the Moon from Terrestrial Silicate-Rich Material. *Chem. Geology.* 345, 40–49. doi:10.1016/j.chemgeo.2012.12.015

Deng, L., Seagle, C., Fei, Y., and Shahar, A. (2013). High Pressure and Temperature Electrical Resistivity of Iron and Implications for Planetary Cores. *Geophys. Res. Lett.* 40 (1), 33–37. doi:10.1029/2012gl054347

Drchal, V., Kudrnovský, J., Wagenknecht, D., and Turek, I. (2019). Alloy Disorder and Fluctuating Magnetic Moments in the Earth's Core. *J. Magnetism Magn. Mater.* 475, 767–771. doi:10.1016/j.jmmm.2018.11.112

Drude, P. (1900a). Zur Elektronentheorie der Metalle. *Ann. Phys.* 306 (3), 566–613. doi:10.1002/andp.19003060312

Drude, P. (1900b). Zur Elektronentheorie der Metalle; II. Teil. Galvanomagnetische und thermomagnetische Effecte. *Ann. Phys.* 308 (11), 369–402. doi:10.1002/andp.19003081102

Elsasser, W. M. (1946). Induction Effects in Terrestrial Magnetism Part II. The Secular Variation. *Phys. Rev.* 70 (3-4), 202–212. doi:10.1103/physrev.70.202

Evans, A. J., Zuber, M. T., Weiss, B. P., and Tikoo, S. M. (2014). A Wet, Heterogeneous Lunar interior: Lower Mantle and Core Dynamo Evolution. *J. Geophys. Res. Planets* 119 (5), 1061–1077. doi:10.1002/2013je004494

Evans, R., Greenwood, D. A., and Lloyd, P. (1971). Calculations of the Transport Properties of Liquid Transition Metals. *Phys. Lett. A* 35 (2), 57–58. doi:10.1016/0375-9601(71)90543-3

Ezenwa, I. C., and Secco, R. A. (2017a). Constant Electrical Resistivity of Zn along the Melting Boundary up to 5 GPa. *High Press. Res.* 37 (3), 319–333. doi:10.1080/08957959.2017.1340473

Ezenwa, I. C., and Secco, R. A. (2019). Fe Melting Transition: Electrical Resistivity, Thermal Conductivity, and Heat Flow at the Inner Core Boundaries of Mercury and Ganymede. *Crystals* 9 (7). doi:10.3390/cryst9070359

Ezenwa, I. C., and Secco, R. A. (2017b). Invariant Electrical Resistivity of Co along the Melting Boundary. *Earth Planet. Sci. Lett.* 474, 120–127. doi:10.1016/j.epsl.2017.06.032

Ezenwa, I. C., Secco, R. A., Yong, W., Pozzo, M., and Alfè, D. (2017). Electrical Resistivity of Solid and Liquid Cu up to 5 GPa: Decrease along the Melting Boundary. *J. Phys. Chem. Sol.* 110, 386–393. doi:10.1016/j.jpcs.2017.06.030

Ezenwa, I. C., and Yoshino, T. (2021). Martian Core Heat Flux: Electrical Resistivity and thermal Conductivity of Liquid Fe at Martian Core P-T Conditions. *Icarus* 360, 114367. doi:10.1016/j.icarus.2021.114367

Gardiner, R. B., and Stacey, F. D. (1971). Electrical Resistivity of the Core. *Phys. Earth Planet. Interiors* 4 (5), 406–410. doi:10.1016/0031-9201(71)90022-7

Gilev, S. D. (2011). Measurement of Electrical Conductivity of Condensed Substances in Shock Waves (Review). *Combust Explos Shock Waves* 47 (4), 375–393. doi:10.1134/s0010508211040010

Gomi, H., Hirose, K., Akai, H., and Fei, Y. (2016). Electrical Resistivity of Substitutionally Disordered Hcp Fe-Si and Fe-Ni Alloys: Chemically-Induced Resistivity Saturation in the Earth's Core. *Earth Planet. Sci. Lett.* 451, 51–61. doi:10.1016/j.epsl.2016.07.011

Gomi, H., and Hirose, K. (2015). Electrical Resistivity and thermal Conductivity of Hcp Fe-Ni Alloys under High Pressure: Implications for thermal Convection in the Earth's Core. *Phys. Earth Planet. Interiors* 247, 2–10. doi:10.1016/j.pepi.2015.04.003

Gomi, H., Ohta, K., Hirose, K., Labrosse, S., Caracas, R., Verstraete, M. J., et al. (2013). The High Conductivity of Iron and thermal Evolution of the Earth's Core. *Phys. Earth Planet. Interiors* 224, 88–103. Article. doi:10.1016/j.pepi.2013.07.010

Gomi, H., and Yoshino, T. (2018). Impurity Resistivity of Fcc and Hcp Fe-Based Alloys: Thermal Stratification at the Top of the Core of Super-earths. *Front. Earth Sci.* 6 (217). Original Research. doi:10.3389/feart.2018.00217

Greenwood, D. A. (1958). The Boltzmann Equation in the Theory of Electrical Conduction in Metals. *Proc. Phys. Soc.* 71 (4), 585–596. doi:10.1088/0370-1328/71/4/306

Gurvitch, M. (1981). Ioffe-Regel Criterion and Resistivity of Metals. *Phys. Rev. B* 24 (12), 7404–7407. doi:10.1103/physrevb.24.7404

Harder, H., and Schubert, G. (2001). Sulfur in Mercury's Core? *Icarus* 151 (1), 118–122. doi:10.1006/icar.2001.6586

Hauck, S. A., Aurnou, J. M., and Dombard, A. J. (2006). Sulfur's Impact on Core Evolution and Magnetic Field Generation on Ganymede. *J. Geophys. Res. Planets* 111 (E9). doi:10.1029/2005je002557

Hsieh, W.-P., Goncharov, A. F., Labrosse, S., Holtgrewe, N., Lobanov, S. S., Chuvashova, I., et al. (2020). Low thermal Conductivity of Iron-Silicon Alloys at Earth's Core Conditions with Implications for the Geodynamo. *Nat. Commun.* 11 (1), 3332. doi:10.1038/s41467-020-17106-7

Hussmann, H., Sotin, C., and Lunine, J. I. (2007). "Interiors and Evolution of Icy Satellites," in *Treatise on Geophysics*. Editor G. Schubert (Amsterdam: Elsevier), 509–539. doi:10.1016/b978-044452748-6.00168-1

Inoue, H., Suehiro, S., Ohta, K., Hirose, K., and Ohishi, Y. (2020). Resistivity Saturation of Hcp Fe-Si Alloys in an Internally Heated diamond Anvil Cell: A Key to Assessing the Earth's Core Conductivity. *Earth Planet. Sci. Lett.* 543, 116357. doi:10.1016/j.epsl.2020.116357

Ito, E. (2015). "Multi-Anvil Cells and High Pressure Experimental Methods," in *Treatise on Geophysics Mineral Physics*. Editors R. B.G. Schubert and A. Dziewonski Second edition (Elsevier), 233–261. doi:10.1016/b978-0-444-53802-4.00035-x

Jain, A., and Evans, R. (1972). Calculation of the Electrical Resistivity of Liquid Iron in the Earth's Core. *Nat. Phys. Sci.* 235 (61), 165–167. doi:10.1038/physci235165a0

Jeanloz, R. (1979). Properties of Iron at High Pressures and the State of the Core. *J. Geophys. Res.* 84 (B11), 6059–6069. doi:10.1029/jb084ib11p06059

Johnston, M. J. S., and Strens, R. G. J. (1973). Electrical Conductivity of Molten FeNiSC Core Mix. *Phys. Earth Planet. Interiors* 7 (2), 219–222. doi:10.1016/0031-9201(73)90013-7

Kavner, A., Duffy, T. S., and Shen, G. (2001). Phase Stability and Density of FeS at High Pressures and Temperatures: Implications for the interior Structure of Mars. *Earth Planet. Sci. Lett.* 185 (1), 25–33. doi:10.1016/s0012-821x(00)00356-3

Keeler, R. N., and Royce, E. B. (1971). Shock Waves in Condensed Media. *Phys. High Energ. Density*, 51–150.

Kiarasi, S. (2013). *High Pressure-Temperature Electrical Resistivity Experiments on Fe-Si Alloys Bearing on Conductive Heat Flow at the Top of the Outer Core [electronic Resource]*. London, Ontario: School of Graduate and Postdoctoral Studies, University of Western Ontario.

Kiarasi, S., and Secco, R. A. (2015). Pressure-induced Electrical Resistivity Saturation of Fe17Si. *Phys. Status Solidi B* 252 (9), 2034–2042. doi:10.1002/pssb.201552029

Kimura, J., Nakagawa, T., and Kurita, K. (2009). Size and Compositional Constraints of Ganymede's Metallic Core for Driving an Active Dynamo. *Icarus* 202 (1), 216–224. doi:10.1016/j.icarus.2009.02.026

Kittel, C. (2005). *Introduction to Solid State Physics*. 8th ed. New York: J. Wiley.

Klemens, P. G., and Williams, R. K. (1986). Thermal Conductivity of Metals and Alloys. *Int. Met. Rev.* 31 (1), 197–215. doi:10.1179/imtr.1986.31.1.197

Knibbe, J. S., and van Westrenen, W. (2017). *Mercury's Thermal Evolution and Magnetic Field Generation with an Fe-Si Core Paper Presented at the 48th Lunar and Planetary Science Conference*. The Woodlands, Texas. LPI Contribution No. 1964, id. 1094.

Knibbe, J. S., and van Westrenen, W. (2018). The thermal Evolution of Mercury's Fe-Si Core. *Earth Planet. Sci. Lett.* 482, 147–159. doi:10.1016/j.epsl.2017.11.006

Konôpková, Z., McWilliams, R. S., Gómez-Pérez, N., and Goncharov, A. F. (2016). Direct Measurement of thermal Conductivity in Solid Iron at Planetary Core Conditions. *Nature* 534 (7605), 99–101. doi:10.1038/nature18009

Korell, J. A., French, M., Steinle-Neumann, G., and Redmer, R. (2019). Paramagnetic-to-Diamagnetic Transition in Dense Liquid Iron and its Influence on Electronic Transport Properties. *Phys. Rev. Lett.* 122 (8), 086601. doi:10.1103/PhysRevLett.122.086601

Krot, A. N. (2005). Classification of Meteorites. *Meteorites, Comets, and Planets*, 83–142. doi:10.1007/978-3-642-65863-1_2

Kubo, R. (1957). Statistical-Mechanical Theory of Irreversible Processes. I. General Theory and Simple Applications to Magnetic and Conduction Problems. *J. Phys. Soc. Jpn.* 12 (6), 570–586. doi:10.1143/jpsj.12.570

Laneuville, M., Taylor, J., and Wieczorek, M. A. (2018). Distribution of Radioactive Heat Sources and Thermal History of the Moon. *J. Geophys. Res. Planets* 123 (12), 3144–3166. doi:10.1029/2018je005742

Laneuville, M., Wieczorek, M. A., Breuer, D., Aubert, J., Morard, G., and Rückriemen, T. (2014). A Long-Lived Lunar Dynamo Powered by Core Crystallization. *Earth Planet. Sci. Lett.* 401, 251–260. doi:10.1016/j.epsl.2014.05.057

Li, J., and Fei, Y. (2003). "2.14 - Experimental Constraints on Core Composition," in *Treatise on Geochemistry*. Editors H. D. Holland and K. K. Turekian (Oxford: Pergamon), 1–31.

Liebermann, R. C. (2011). Multi-anvil, High Pressure Apparatus: a Half-century of Development and Progress. *High Press. Res.* 31 (4), 493–532. doi:10.1080/08957959.2011.618698

Litasov, K. D., and Shatskiy, A. F. (2016). Composition of the Earth's Core: A Review. *Russ. Geology. Geophys.* 57 (1), 22–46. doi:10.1016/j.rgg.2016.01.003

Littleton, J. A. H., Secco, R. A., and Yong, W. (2018). Decreasing Electrical Resistivity of Silver along the Melting Boundary up to 5 GPa. *High Press. Res.* 38 (2), 99–106. doi:10.1080/08957959.2018.1435786

Littleton, J. A. H., Secco, R. A., and Yong, W. (2021). Electrical Resistivity of FeS at High Pressures and Temperatures: Implications of Thermal Transport in the Core of Ganymede. *J. Geophys. Res. Planets* 126 (5), e2020JE006793. doi:10.1029/2020je006793

Malavergne, V., Toplis, M. J., Berthet, S., and Jones, J. (2010). Highly Reducing Conditions during Core Formation on Mercury: Implications for Internal Structure and the Origin of a Magnetic Field. *Icarus* 206 (1), 199–209. doi:10.1016/j.icarus.2009.09.001

Manthilake, G., Chantel, J., Monteux, J., Andrault, D., Bouhifd, M. A., Bolfan Casanova, N., et al. (2019). Thermal Conductivity of FeS and its Implications for Mercury's Long-Sustaining Magnetic Field. *J. Geophys. Res. Planets* 124 (9), 2359–2368. doi:10.1029/2019je005979

Mao, H.-K., and Mao, W. L. (2007). "Theory and Practice: Diamond-Anvil Cells and Probes for High-P-T Mineral Physics Studies," in *Treatise on Geophysics*. Editor G. Schubert Second Edition (Oxford: Elsevier), 263–291. doi:10.1016/b978-0-444-53802-4.00036-1

Mao, H. K., Wu, Y., Chen, L. C., Shu, J. F., and Jephcoat, A. P. (1990). Static Compression of Iron to 300 GPa and Fe0.8Ni0.2alloy to 260 GPa: Implications for Composition of the Core. *J. Geophys. Res.* 95 (B13), 21737–21742. doi:10.1029/jb095ib13p21737

Mao, Z., Lin, J.-F., Liu, J., Alatas, A., Gao, L., Zhao, J., et al. (2012). Sound Velocities of Fe and Fe-Si alloy in the Earth's Core. *Proc. Natl. Acad. Sci.* 109 (26), 10239–10244. doi:10.1073/pnas.1207086109

Matassov, G. (1977). *The Electrical Conductivity of Iron-Silicon Alloys at High Pressures and the Earth's Core*. University of California.

McCubbin, F. M., Riner, M. A., Vander Kaaden, K. E., and Burkemper, L. K. (2012). Is Mercury a Volatile-Rich Planet? *Geophys. Res. Lett.* 39 (9), L09202. doi:10.1029/2012gl051711

Mooij, J. H. (1973). Electrical Conduction in Concentrated Disordered Transition Metal Alloys. *Phys. Stat. Sol. (A)* 17 (2), 521–530. doi:10.1002/pssa.2210170217

Morgan, J. W., and Anders, E. (1980). Chemical Composition of Earth, Venus, and Mercury. *Proc. Natl. Acad. Sci.* 77 (12), 6973–6977. doi:10.1073/pnas.77.12.6973

Mott, N. F. (1980). LIQUID AND AMORPHOUS METALS. *J. Phys. Colloques* 41 (C8), C1–7. doi:10.1051/jphyscol:1980801

Mott, N. F. (1972). The Electrical Resistivity of Liquid Transition Metals. *Phil. Mag.* 26 (6), 1249–1261. doi:10.1080/14786437208220339

Nazarov, M. A., Demidova, S. I., Anosova, M. O., Kostitsyn, Y. A., Ntaflos, T., and Brandstaetter, F. (2012). Native Silicon and Iron Silicides in the Dhofar 280 Lunar Meteorite. *Petrology* 20 (6), 506–519. doi:10.1134/s0869591112060021

Nimmo, F., and Stevenson, D. J. (2000). Influence of Early Plate Tectonics on the thermal Evolution and Magnetic Field of Mars. *J. Geophys. Res.* 105 (E5), 11969–11979. doi:10.1029/1999je001216

Nittler, L. R., Chabot, N. L., Grove, T. L., and Peplowski, P. N. (2017). "The Chemical Composition of Mercury," in *Mercury: The View after MESSENGER* (Cambridge University Press).

Ohta, K., Kuwayama, Y., Hirose, K., Shimizu, K., and Ohishi, Y. (2016). Experimental Determination of the Electrical Resistivity of Iron at Earth's Core Conditions. *Nature* 534 (7605), 95–98. doi:10.1038/nature17957

Poirier, J.-P. (1994). Light Elements in the Earth's Outer Core: A Critical Review. *Phys. Earth Planet. Interiors* 85 (3), 319–337. doi:10.1016/0031-9201(94)90120-1

Pommier, A. (2018). Influence of Sulfur on the Electrical Resistivity of a Crystallizing Core in Small Terrestrial Bodies. *Earth Planet. Sci. Lett.* 496, 37–46. doi:10.1016/j.epsl.2018.05.032

Pommier, A., Leinenweber, K., and Tran, T. (2019). Mercury's thermal Evolution Controlled by an Insulating Liquid Outermost Core? *Earth Planet. Sci. Lett.* 517, 125–134. doi:10.1016/j.epsl.2019.04.022

Pourovskii, L. V., Mravlje, J., Pozzo, M., and Alfè, D. (2020). Electronic Correlations and Transport in Iron at Earth's Core Conditions. *Nat. Commun.* 11 (1), 4105. doi:10.1038/s41467-020-18003-9

Pozzo, M., and Alfè, D. (2016b). "Electrical Resistivity Saturation of Solid Iron at Earth's Core Conditions from Density Functional Theory," in *AGU Abstract DI13A-2356* (San Francisco, CA): AGU Fall Meeting).

Pozzo, M., and Alfè, D. (2016a). Saturation of Electrical Resistivity of Solid Iron at Earth's Core Conditions. *SpringerPlus* 5 (1), 256. doi:10.1186/s40064-016-1829-x

Pozzo, M., Davies, C., Gubbins, D., and Alfè, D. (2012). Thermal and Electrical Conductivity of Iron at Earth's Core Conditions. *Nature* 485 (7398), 355–358. doi:10.1038/nature11031

Pozzo, M., Davies, C., Gubbins, D., and Alfè, D. (2014). Thermal and Electrical Conductivity of Solid Iron and Iron-Silicon Mixtures at Earth's Core Conditions. *Earth Planet. Sci. Lett.* 393, 159–164. doi:10.1016/j.epsl.2014.02.047

Pozzo, M., Davies, C., Gubbins, D., and Alfè, D. (2013). Transport Properties for Liquid Silicon-Oxygen-Iron Mixtures at Earth's Core Conditions. *Phys. Rev. B* 87 (1), 014110. doi:10.1103/physrevb.87.014110

Rivoldini, A., Van Hoolst, T., Verhoeven, O., Mocquet, A., and Dehant, V. (2011). Geodesy Constraints on the interior Structure and Composition of Mars. *Icarus* 213 (2), 451–472. doi:10.1016/j.icarus.2011.03.024

Rivoldini, A., Van Hoolst, T., and Verhoeven, O. (2009). The interior Structure of Mercury and its Core Sulfur Content. *Icarus* 201 (1), 12–30. doi:10.1016/j.icarus.2008.12.020

Scheinberg, A., Soderlund, K. M., and Schubert, G. (2015). Magnetic Field Generation in the Lunar Core: The Role of Inner Core Growth. *Icarus* 254, 62–71. doi:10.1016/j.icarus.2015.03.013

Seagle, C. T., Cottrell, E., Fei, Y., Hummer, D. R., and Prakapenka, V. B. (2013). Electrical and thermal Transport Properties of Iron and Iron-Silicon alloy at High Pressure. *Geophys. Res. Lett.* 40 (20), 5377–5381. doi:10.1002/2013gl057930

Secco, R. A., and Schloessin, H. H. (1989). The Electrical Resistivity of Solid and Liquid Fe at Pressures up to 7 GPa. *J. Geophys. Res.* 94 (B5), 5887–5894. doi:10.1029/jb094ib05p05887

Secco, R. A. (2017). Thermal Conductivity and Seebeck Coefficient of Fe and Fe-Si Alloys: Implications for Variable Lorenz Number. *Renew. Energ.* 113, 23–34. doi:10.1016/j.pepi.2017.01.005

Sha, X., and Cohen, R. E. (2011). First-principles Studies of Electrical Resistivity of Iron under Pressure. *J. Phys. Condens. Matter* 23 (7), 075401. doi:10.1088/0953-8984/23/7/075401

Shibazaki, Y., Ohtani, E., Terasaki, H., Tateyama, R., Sakamaki, T., Tsuchiya, T., et al. (2011). Effect of Hydrogen on the Melting Temperature of FeS at High Pressure: Implications for the Core of Ganymede. *Earth Planet. Sci. Lett.* 301 (1), 153–158. doi:10.1016/j.epsl.2010.10.033

Silber, R. E., Secco, R. A., and Yong, W. (2017). Constant Electrical Resistivity of Ni along the Melting Boundary up to 9 GPa. *J. Geophys. Res. Solid Earth* 122 (7), 5064–5081. doi:10.1002/2017jb014259

Silber, R. E., Secco, R. A., Yong, W., and Littleton, J. A. H. (2018). Electrical Resistivity of Liquid Fe to 12 GPa: Implications for Heat Flow in Cores of Terrestrial Bodies. *Sci. Rep.* 8 (1), 10758. doi:10.1038/s41598-018-28921-w

Silber, R. E., Secco, R. A., Yong, W., and Littleton, J. A. H. (2019). Heat Flow in Earth's Core from Invariant Electrical Resistivity of Fe-Si on the Melting Boundary to 9 GPa: Do Light Elements Matter? *J. Geophys. Res. Solid Earth* 124 (6), 5521–5543. doi:10.1029/2019jb017375

Smith, R. F., Fratanduono, D. E., Braun, D. G., Duffy, T. S., Wicks, J. K., Celliers, P. M., et al. (2018). Equation of State of Iron under Core Conditions of Large Rocky Exoplanets. *Nat. Astron.* 2 (6), 452–458. doi:10.1038/s41550-018-0437-9

Sommerfeld, A. (1928). Zur Elektronentheorie der Metalle auf Grund der Fermischen Statistik. *Z. für Physik* 47 (1), 1–32. doi:10.1007/bf01391052

Stacey, F. D., and Anderson, O. L. (2001). Electrical and thermal Conductivities of Fe–Ni–Si alloy under Core Conditions. *Phys. Earth Planet. Interiors* 124 (3), 153–162. doi:10.1016/s0031-9201(01)00186-8

Stacey, F. D., and Loper, D. E. (2007). A Revised Estimate of the Conductivity of Iron alloy at High Pressure and Implications for the Core Energy Balance. *Phys. Earth Planet. Interiors* 161 (1), 13–18. doi:10.1016/j.pepi.2006.12.001

Steenstra, E. S., and van Westrenen, W. (2017). "Sulfides in the Moon," in *Encyclopedia of Lunar Science*. Editor B. Cudnik (Cham: Springer International Publishing), 1–6. doi:10.1007/978-3-319-05546-6_119-1

Stegman, D. R., Jellinek, A. M., Zatman, S. A., Baumgardner, J. R., and Richards, M. A. (2003). An Early Lunar Core Dynamo Driven by Thermochemical Mantle Convection. *Nature* 421 (6919), 143–146. doi:10.1038/nature01267

Steinbrügge, G., Dumberry, M., Rivoldini, A., Schubert, G., Cao, H., Schroeder, D. M., et al. (2021). Challenges on Mercury's Interior Structure Posed by the New Measurements of its Obliquity and Tides. *Geophys. Res. Lett.* 48 (3), e2020GL089895. doi:10.1029/2020gl089895

Stevenson, D. J., Spohn, T., and Schubert, G. (1983). Magnetism and thermal Evolution of the Terrestrial Planets. *Icarus* 54 (3), 466–489. doi:10.1016/0019-1035(83)90241-5

Stewart, A. J., and Schmidt, M. W. (2007). Sulfur and Phosphorus in the Earth's Core: The Fe-P-S System at 23 GPa. *Geophys. Res. Lett.* 34 (13), L13201. doi:10.1029/2007gl030138

Stixrude, L., Wasserman, E., and Cohen, R. E. (1997). Composition and Temperature of Earth's Inner Core. *J. Geophys. Res.* 102 (B11), 24729–24739. doi:10.1029/97jb02125

Suehiro, S., Ohta, K., Hirose, K., Morard, G., and Ohishi, Y. (2017). The Influence of Sulfur on the Electrical Resistivity of Hcp Iron: Implications for the Core Conductivity of Mars and Earth. *Geophys. Res. Lett.* 44 (16), 8254–8259. doi:10.1002/2017gl074021

Szurgot, M. (2017). *Uncompressed Density of the Moon, Lunar Mantle and Core*. Budapest, Hungary: Analytical Methods Applied to Earth. Paper presented at the Workshop on Modern.

Terasaki, H., Rivoldini, A., Shimoyama, Y., Nishida, K., Urakawa, S., Maki, M., et al. (2019). Pressure and Composition Effects on Sound Velocity and Density of Core-Forming Liquids: Implication to Core Compositions of Terrestrial Planets. *J. Geophys. Res. Planets* 124 (8), 2272–2293. doi:10.1029/2019je005936

Tosi, N., Grott, M., Plesa, A.-C., and Breuer, D. (2013). Thermochemical Evolution of Mercury's interior. *J. Geophys. Res. Planets* 118 (12), 2474–2487. doi:10.1002/jgre.20168

Vollhardt, D., Byczuk, K., and Kollar, M. (2012). "Dynamical Mean-Field Theory," in *Strongly Correlated Systems*. Editors M. F. Avella, (Berlin, Heidelberg: Springer), 171. doi:10.1007/978-3-642-21831-6_7

Wagle, F., Steinle-Neumann, G., and de Koker, N. (2019). Resistivity Saturation in Liquid Iron–Light-Element Alloys at Conditions of Planetary Cores from First Principles Computations. *Comptes Rendus Geosci.* 351 (2), 154–162. doi:10.1016/j.crte.2018.05.002

Wagle, F., Steinle-Neumann, G., and de Koker, N. (2018). Saturation and Negative Temperature Coefficient of Electrical Resistivity in Liquid Iron-Sulfur Alloys at High Densities from First-Principles Calculations. *Phys. Rev. B* 97 (9), 094307. doi:10.1103/physrevb.97.094307

Wagle, F., and Steinle-Neumann, G. (2018). Electrical Resistivity Discontinuity of Iron along the Melting Curve. *Geophys. J. Int.* 213 (1), 237–243. doi:10.1093/gji/ggx526

Wänke, H., Dreibus, G., Runcorn, S. K., Turner, G., and Woolfson, M. M. (1988). Chemical Composition and Accretion History of Terrestrial Planets. *Phil. Trans. R. Soc. Lond. A.* 325 (1587), 545–557. doi:10.1098/rsta.1988.0067

Weber, R. C., Lin, P.-Y., Garnero, E. J., Williams, Q., and Lognonné, P. (2011). Seismic Detection of the Lunar Core. *Science* 331 (6015), 309–312. doi:10.1126/science.1199375

Wicks, J. K., Smith, R. F., Fratanduono, D. E., Coppari, F., Kraus, R. G., Newman, M. G., et al. (2018). Crystal Structure and Equation of State of Fe-Si Alloys at Super-earth Core Conditions. *Sci. Adv.* 4 (4), eaao5864. doi:10.1126/sciadv.aao5864

Wieczorek, M. A., Jolliff, B. L., Khan, A., Pritchard, M. E., Weiss, B. P., Williams, J. G., et al. (2006). The Constitution and Structure of the Lunar Interior. *Rev. Mineralogy Geochem.* 60 (1), 221–364. doi:10.2138/rmg.2006.60.3

Wiesmann, H., Gurvitch, M., Lutz, H., Ghosh, A., Schwarz, B., Strongin, M., et al. (1977). Simple Model for Characterizing the Electrical Resistivity inA−15Superconductors. *Phys. Rev. Lett.* 38 (14), 782–785. doi:10.1103/physrevlett.38.782

Xu, J., Zhang, P., Haule, K., Minar, J., Wimmer, S., Ebert, H., et al. (2018). Thermal Conductivity and Electrical Resistivity of Solid Iron at Earth's Core Conditions from First Principles. *Phys. Rev. Lett.* 121 (9), 096601. doi:10.1103/PhysRevLett.121.096601

Yin, Y., Zhai, K., Zhang, B., and Zhai, S. (2019). Electrical Resistivity of Iron Phosphides at High-Pressure and High-Temperature Conditions with Implications for Lunar Core's Thermal Conductivity. *J. Geophys. Res. Solid Earth* 124 (6), 5544–5556. doi:10.1029/2018jb017157

Yong, W., Secco, R. A., Littleton, J. A. H., and Silber, R. E. (2019). The Iron Invariance: Implications for Thermal Convection in Earth's Core. *Geophys. Res. Lett.* 46 (20), 11065–11070. doi:10.1029/2019gl084485

Zaitsev, A. I., Dobrokhotova, Z. V., Litvina, A. D., and Mogutnov, B. M. (1995). Thermodynamic Properties and Phase Equilibria in the Fe-P System. *J. Chem. Soc. Faraday Trans.* 91 (4), 703–712. doi:10.1039/FT9959100703

Zambardi, T., Poitrasson, F., Corgne, A., Méheut, M., Quitté, G., and Anand, M. (2013). Silicon Isotope Variations in the Inner Solar System: Implications for Planetary Formation, Differentiation and Composition. *Geochimica et Cosmochimica Acta* 121, 67–83. doi:10.1016/j.gca.2013.06.040

Zhang, C., Lin, J. F., Liu, Y., Feng, S., Jin, C., Hou, M., et al. (2018). Electrical Resistivity of Fe-C Alloy at High Pressure: Effects of Carbon as a Light Element on the Thermal Conductivity of the Earth's Core. *J. Geophys. Res. Solid Earth* 123 (5), 3564–3577. doi:10.1029/2017jb015260

Zhang, N., Parmentier, E. M., and Liang, Y. (2013). A 3-D Numerical Study of the thermal Evolution of the Moon after Cumulate Mantle Overturn: The Importance of Rheology and Core Solidification. *J. Geophys. Res. Planets* 118 (9), 1789–1804. doi:10.1002/jgre.20121

Zhang, Y., Hou, M., Liu, G., Zhang, C., Prakapenka, V. B., Greenberg, E., et al. (2020). Reconciliation of Experiments and Theory on Transport Properties of Iron and the Geodynamo. *Phys. Rev. Lett.* 125 (7), 078501. doi:10.1103/PhysRevLett.125.078501

Zhang, Y., Hou, M., Driscoll, P., Salke, N. P., Liu, J., Greenberg, E., et al. (2021). Transport Properties of Fe-Ni-Si Alloys at Earth's Core Conditions: Insight into the Viability of thermal and Compositional Convection. *Earth Planet. Sci. Lett.* 553, 116614. doi:10.1016/j.epsl.2020.116614

Zidane, M., Salmani, E. M., Majumdar, A., Ez-Zahraouy, H., Benyoussef, A., and Ahuja, R. (2020). Electrical and thermal Transport Properties of Fe-Ni Based Ternary Alloys in the Earth's Inner Core: An Ab Initio Study. *Phys. Earth Planet. Interiors* 301, 106465. doi:10.1016/j.pepi.2020.106465

Ziman, J. M. (1961). A Theory of the Electrical Properties of Liquid Metals. I: The Monovalent Metals. *Phil. Mag.* 6 (68), 1013–1034. doi:10.1080/14786436108243361

Ziman, J. M. (1960). *Electrons and Phonons; the Theory of Transport Phenomena in Solids*. Oxford: Clarendon Press.

Conflict of Interest: The authors declare that the research was conducted in the absence of any commercial or financial relationships that could be construed as a potential conflict of interest.

Publisher's Note: All claims expressed in this article are solely those of the authors and do not necessarily represent those of their affiliated organizations, or those of the publisher, the editors and the reviewers. Any product that may be evaluated in this article, or claim that may be made by its manufacturer, is not guaranteed or endorsed by the publisher.

frontiers in Earth Science

ORIGINAL RESEARCH
published: 05 November 2021
doi: 10.3389/feart.2021.749896

Influence of Saline Fluids on the Electrical Conductivity of Olivine Aggregates at High Temperature and High Pressure and Its Geological Implications

Wenqing Sun[1], *Lidong Dai*[1,2,3]*, *Haiying Hu*[1,3]*, *Jianjun Jiang*[1,2], *Mengqi Wang*[1,4], *Ziming Hu*[1,4] and *Chenxin Jing*[1,4]

[1]Key Laboratory of High-temperature and High-pressure Study of the Earth's Interior, Institute of Geochemistry, Chinese Academy of Sciences, Guiyang, China, [2]United Laboratory of High-Pressure Physics and Earthquake Science, Institute of Earthquake Forecasting, Chinese Earthquake Administration, Beijing, China, [3]Shandong Provincial Key Laboratory of Water and Soil Conservation and Environmental Protection, College of Resources and Environment, Linyi University, Linyi, China, [4]University of Chinese Academy of Sciences, Beijing, China

OPEN ACCESS

Edited by:
Jean-louis Vigneresse,
Université de Lorraine, France

Reviewed by:
Yongsheng Huang,
Tohoku University, Japan
Yu Nishihara,
Ehime University, Japan

***Correspondence:**
Lidong Dai
dailidong@vip.gyig.ac.cn
Haiying Hu
huhaiying@vip.gyig.ac.cn

Specialty section:
This article was submitted to Geochemistry, a section of the journal Frontiers in Earth Science

Received: 30 July 2021
Accepted: 21 October 2021
Published: 05 November 2021

Citation:
Sun W, Dai L, Hu H, Jiang J, Wang M, Hu Z and Jing C (2021) Influence of Saline Fluids on the Electrical Conductivity of Olivine Aggregates at High Temperature and High Pressure and Its Geological Implications. Front. Earth Sci. 9:749896. doi: 10.3389/feart.2021.749896

The electrical conductivities of hydrous olivine (Ol) aggregates and Ol–H_2O, Ol–NaCl–H_2O (salinity: 1–21 wt%; fluid fraction: 5.1–20.7 vol%), Ol–KCl–H_2O (salinity: 5 wt%; fluid fraction: 10.9–14.0 vol%) and Ol–$CaCl_2$–H_2O systems (salinity: 5 wt%; fluid fraction: 10.7–13.7 vol%) were measured at 2.0–3.0 GPa and 773–1073 K using a multi-anvil apparatus. The electrical conductivity of saline fluid-bearing olivine aggregates slightly increases with increasing pressure and temperature, and the electrical conductivities of both hydrous and saline fluid-bearing samples are well described by an Arrhenius relation. The dihedral angle of the saline fluids is approximately 50° in the Ol–NaCl–H_2O system with 5 wt% NaCl and 5.1 vol% fluids, which implies that the fluids were interconnected along grain boundaries under the test conditions. The electrical conductivities of the Ol–NaCl–H_2O system with 5 wt% NaCl and 5.1 vol% fluids are ~two to four orders of magnitude higher than those of hydrous olivine aggregates. The salinity and fluid fraction moderately enhance the sample electrical conductivities owing to the interconnectivity of the saline fluids. The activation enthalpies of the electrical conductivities for the Ol–NaCl–H_2O systems range from 0.07 to 0.36 eV, and Na^+, Cl^-, H^+, OH^-, and soluble ions from olivine are proposed to be the main charge carriers. For a fixed salinity and fluid fraction, the electrical conductivities of the Ol–NaCl–H_2O system resemble the Ol–KCl–H_2O system but are slightly higher than that of the Ol–$CaCl_2$–H_2O system. The Ol–NaCl–H_2O system with a salinity of ~5 wt% NaCl and fluid fraction larger than 1.8 vol% can be employed to reasonably explain the origin of the high-conductivity anomalies observed in mantle wedges.

Keywords: olivine, saline fluids, fluid fraction, electrical conductivity, high pressure, high-conductivity anomaly

INTRODUCTION

Electrical conductivities of geological materials at high temperatures and pressures in combination with magnetotelluric data can be used to infer the material compositions and thermodynamic conditions of the Earth's interior (Vallianatos, 1996; Heise et al., 2019). Previous field magnetotelluric results confirmed that high-conductivity layers (HCLs), as the special weak zones, are widely distributed in the Earth's interior (McGary et al., 2014; Selway, 2015; Hata et al., 2017). Typically, the HCLs have a characteristic of abnormally low velocity on the basis of seismic sounding data (Selway and O'Donnell, 2019; Manthilake et al., 2021a). The electrical conductivities of geological samples at high temperatures and high pressures are required to invert the MT profiles. Numerous studies have therefore investigated the conductivity of the dominant geological materials in the Earth's interior (Reynard et al., 2011; Saltas et al., 2013, 2020; Manthilake et al., 2015, 2016; Dai and Karato, 2020). Dehydration, metasomatism, and magmatism processes are considerably more active in subduction zones than in the stable continental lithosphere. The dehydration products of hydrous minerals (e.g., amphibole, lawsonite etc.) have been proposed to be the main origin of the high-conductivity anomalies in subduction zones (Manthilake et al., 2015; Hu et al., 2018). However, the dehydration products of typical hydrous minerals are present throughout the subduction tunnel and therefore widely distributed between the transitional interface of the subducted slab and mantle wedge. The aqueous fluid dehydration products migrate upward to the mantle wedge, as do silicate and carbonate melts from subduction zone magmatism (Wang et al., 2020). Aqueous fluids and melts have thus been inferred to be plausible candidates for the origin of the high-conductivity and low-velocity anomalies in mantle wedge regions (Pommier and Evans, 2017; Vargas et al., 2019; Manthilake et al., 2021c). Silicate/carbonate melts with or without aqueous fluids form and converge in regions at sufficiently high temperature; however, aqueous fluids as an independent fluid phase can be stable in regions with temperatures below the rock matrix solidus. The high-conductivity anomalies have been shown to occur in relatively cold subduction zones, which might be caused by the presence of aqueous fluids (Pommier and Evans, 2017). Previous studies of fluid inclusions in deep Earth rocks and high-temperature and high-pressure experiments have demonstrated that aqueous fluids with some form of volatile and salt species are abundant in subduction zones (Carter et al., 2015; Huang et al., 2019; Lacovino et al., 2020). NaCl-bearing aqueous fluids have been proposed to be the most significant saline fluid in subduction environments because Na^+ and Cl^- are the most dominant ions in most saline fluid inclusions (Morikawa et al., 2016). Free water, as the solvent of saline fluids, dominantly forms by the dehydration of hydrous minerals in subduction slabs (Manthilake et al., 2015; Hu et al., 2018). Saline ions (Na^+ and Cl^-) in aqueous fluids are released from subduction slabs during dehydration and metasomatism (Reynard, 2016; Förster et al., 2019; Manthilake et al., 2021b). Numerous studies have attributed the origin of the high-conductivity anomalies in the mid-lower crust and some subduction zones to the distribution of NaCl-bearing aqueous fluids along the grain boundaries of silicate minerals (Shimojuku et al., 2012, 2014; Guo et al., 2015; Sinmyo and Keppler, 2017; Li et al., 2018; Sun et al., 2020). However, the effect of saline fluids on the electrical conductivity of silicate minerals in mantle wedge regions remains poorly constrained.

Olivine (Ol) is the dominant rock-forming mineral of the Earth's upper mantle with a volume percentage of ~63% (Ringwood, 1982; Lin et al., 2013). The Ol–NaCl–H_2O system is therefore a relevant representation of the composition of wet regions in the uppermost mantle, e.g., mantle wedges of subduction zones. Although numerous studies have reported the high-pressure electrical conductivity of olivine single crystals and polycrystalline aggregates (Dai et al., 2010; Dai and Karato, 2014a; Dai and Karato, 2014b; Dai and Karato, 2014c; Dai and Karato, 2014d; Dai and Karato, 2020), the detailed Ol–NaCl–H_2O system has not been previously reported under high-temperature and high-pressure conditions. In addition to the effects of pressure and oxygen fugacity, the molar percentages of magnesium and iron in synthetic olivine also exert a significant effect on the electrical conductivity of anhydrous samples at high temperatures and pressures (Dai and Karato, 2014b). Water is another crucial factor that can enhance the electrical conductivity of olivine and its high-pressure polymorphs at high temperatures and pressures by several orders of magnitude (Dai and Karato, 2009; Dai and Karato, 2014b). Previous geophysical field observations of the electrical conductivity in the asthenosphere, including the high and highly anisotropic conductivity regions, have been attributed to the high water contents, which is consistent with geochemical models based of the reported electrical conductivity values of anisotropic hydrous single-crystal olivine (Dai and Karato, 2014a). The olivine in geologically active regions is hydrous owing to the existence of aqueous fluids from the dehydration of hydrous minerals. Hydrogen-related point defects can significantly enhance the conductivity of olivine; thus hydrous olivine is a possible candidate for the origin for the high-conductivity anomalies in the upper mantle (Dai and Karato, 2014a). However, the electrical conductivity of hydrous olivine at its maximum probable water content (~1,000 ppm) in the mantle wedge region is approximately 10^{-1} S/m (Dai and Karato, 2014b), whereas the center of the semi-ellipsoidal HCL shapes in mantle wedges show maximum conductivities of ~1 S/m, which gradually decrease to approximately 10^{-2} S/m at the edges (McGary et al., 2014; Hata et al., 2017). The presence of hydrous olivine may therefore generate conductivities in the range of ~10^{-2}–10^{-1} S/m (Dai and Karato, 2014b), but cannot be employed to interpret conductivities in the range of ~10^{-1}–1 S/m. It is possible that interconnected saline fluids can be employed to interpret the high conductivities of ~10^{-1}–1 S/m in some HCLs of mantle wedges, in which interconnected saline fluid-bearing peridotite is surrounded by hydrous peridotite with or without disconnected saline fluids. Huang et al. (2019) recently demonstrated that NaCl-bearing aqueous fluids might be interconnected in mantle wedges. The electrical conductivities of clinopyroxene (Cpx)–NaCl–H_2O, plagioclase (Pl)–NaCl–H_2O,

albite (Ab)–NaCl–H_2O and pure NaCl-bearing saline fluid systems have been previously investigated (Guo et al., 2015; Li et al., 2018; Guo and Keppler, 2019; Sun et al., 2020), but the electrical conductivity of saline fluid-bearing olivine aggregates has not been reported. Although saline fluids exert a dominant control over the conductivities of saline fluid-bearing mineral aggregates, the mineral species still play a significant role in the system conductivity as a whole (Guo et al., 2015; Li et al., 2018; Sun et al., 2020). The conductivities of saline fluids in mineral–NaCl–H_2O systems calculated using theoretical models (e.g., Hashin–Shtrikman upper model (HS^+) and cube model) were reported to be substantially lower than those of pure NaCl-bearing aqueous fluids (Sinmyo and Keppler, 2017; Li et al., 2018; Guo and Keppler, 2019; Sun et al., 2020). This implies that the dissolution of silicate minerals into saline fluids significantly affects the conductivities of the aqueous fluids, and the distribution characteristics and channel morphology of the aqueous fluids on the mineral boundaries might influence the conductivity of saline fluid-bearing mineral aggregates to some extent. An accurate determination of the electrical conductivity of saline fluid-bearing olivine aggregates is therefore difficult to precisely estimate using the HS^+ and cube theoretical models based on the conductivity of hydrous olivine aggregates and pure saline fluids. *In-situ* measurements of the electrical conductivity of saline fluid-bearing polycrystalline olivine are therefore required to interpret the origin of the high-conductivity anomalies in mantle wedges.

In the present study, the electrical conductivity of olivine aggregates mixed with saline fluids (solute: NaCl, KCl and $CaCl_2$) was measured *in-situ* over a pressure range of 2.0–3.0 GPa and temperature range of 773–1073 K. The effects of temperature, pressure, salinity, fluid fraction, and ionic species on electrical conductivity were explored in detail. Three representative saline fluid-bearing systems (Ol–NaCl–H_2O, Ol–KCl–H_2O, and Ol–$CaCl_2$–H_2O) were comprehensively compared over the investigated pressure and temperature range. The results are applied to discuss the possible geological implications of the electrical conductivities of saline fluid-bearing olivine aggregates at high temperature and pressure.

EXPERIMENTAL METHODS

Sample Preparation

The natural, fresh and pure olivine with a gem-grade single crystal grain was collected from Damaping village, Wanquan County, Zhangjiakou City, Hebei Province, China. The chemical compositions of the olivine were tested using an electron probe microanalyzer (EPMA) at the State Key Laboratory of Ore Deposit Geochemistry, Chinese Academy of Science (CAS), Guiyang, China. The molar Fe/(Fe + Mg) ratio was 9.3%, which is very similar to that for San Carlos olivine (10%) (**Supplementary Table S1**). As described in supplementary material in detail, the samples of hydrous olivine aggregates, Ol–H_2O and Ol–NaCl/KCl/$CaCl_2$–H_2O systems were precisely prepared. For the saline fluid-bearing olivine aggregates, the salinity and fluid fraction ranges were 0–21 wt% and 5.1–20.7 vol%, respectively. The detailed salinity and fluid fraction values of the saline fluid-bearing olivine aggregates are listed in **Table 1**. High-temperature-resistant quartz glass sleeves (SiO_2 content: ~100 wt%) with a 3-mm inner diameter, 6-mm outer diameter and 4-mm height were employed as the sample capsules. Although the reaction of quartz and olivine can take place at high temperatures and pressures and produce a very thin pyroxene-bearing layer, the contribution to the bulk conductivity could be negligible because the conductivity of pyroxene is much lower than that of interconnected fluid phases (Huang et al., 2021). Two Au stoppers were applied to seal the top and bottom of the sample capsule using a small amount of silver colloid.

Impedance Spectra Measurements

Sample assembly for the *in-situ* measurement of electrical conductivity was displayed in **Supplementary Figure S1**. The high-temperature and high-pressure conditions were provided using a YJ–3000t cubic multi-anvil apparatus at the Key Laboratory of High-Temperature and High-Pressure Study of the Earth's Interior, Institute of Geochemistry, CAS, Guiyang, China. The target pressure was achieved using a slow compression rate of 0.5 GPa/h to avoid damaging the quartz sleeve. Once reaching the target pressure, the temperature was rapidly increased to 1073 K. Our measurement results have shown that the resistance of saline fluid-bearing polycrystalline olivine dramatically increases with time to values greater than 1 MΩ at 1073 K when the quartz sleeve sample capsule is damaged. However, the quartz sleeves remained undamaged in the successful runs and the low resistance values of the saline fluid-bearing systems only slightly increased with time. This is because saline fluids might weakly diffuse to the exterior of the sample capsule when the aqueous fluids and olivine grains have approximately equilibrated. At a given pressure, the impedance spectra were firstly collected continuously at the highest temperature of 1073 K, and the spectra gradually reached stable after ~30 min. It reflected that the saline fluids gradually diffused along olivine grain boundaries, and finally it reached a uniform distribution of fluid in the sample. Meanwhile, a very small amount of olivine is dissolved into the saline fluids with time. At a fixed temperature, pressure and volume fraction, the electrical conductivities of olivine–NaCl–H_2O systems slightly decreased due to the loss of saline fluids. In order to avoid the inevitable influence of the loss of saline fluids, at the highest measurement point of 1073 K, the olivine–NaCl–H_2O system was kept a relatively longer time in order to reach an equilibrium state by continuously checking the variation of impedance spectroscopy of sample. After that, a decreasing temperature cycle from 1073 to 773 K was chosen to quickly measure the electrical conductivity of sample at the temperature interval of 50 K. Due to the small solubility of olivine in the saline fluids, the change of the geometry of the olivine grain boundaries was feeble (Macris et al., 2003). We proposed that the distribution of saline fluids was dominated by the salinities and volume fractions of fluids, and the grain sizes and geometries of olivine grains. And thus, the textures of the olivine–NaCl–H_2O systems were almost stable, and the very slight change of texture due to the dissolution

TABLE 1 | Thermodynamic parameters for the electrical conductivities of hydrous olivine aggregates, the Ol–H_2O system, and saline fluid-bearing olivine aggregates with various salinities and fluid fractions at 2.0 GPa and 773–1073 K, except for runs a and b, which were conducted at 2.5 and 3.0 GPa, respectively.

Sample	Salinity (wt%)	Fluid fraction (vol%)	Log σ_0 (S/m)	ΔH (eV)	R^2 (%)
Hydrous Ol	0	0	2.62 ± 0.49	0.97 ± 0.09	95.13
Ol–H_2O	0	10.9	–0.11 ± 0.03	0.36 ± 0.01	99.90
Ol–NaCl–H_2O	1	14.5	0.02 ± 0.05	0.18 ± 0.01	98.44
Ol–NaCl–H_2O	5	5.1	0.35 ± 0.23	0.36 ± 0.04	92.38
Ol–NaCl–H_2O	5	9.9	–0.90 ± 0.06	0.07 ± 0.01	89.05
Ol–NaCl–H_2O	5	13.7	0.70 ± 0.12	0.27 ± 0.02	96.15
Ol–NaCl–H_2O	5	18.0	1.50 ± 0.08	0.36 ± 0.02	98.97
Ol–NaCl–H_2O	5	20.3	1.53 ± 0.23	0.33 ± 0.04	91.44
Ol–NaCl–H_2O	9	13.7	0.95 ± 0.08	0.23 ± 0.01	98.01
Ol–NaCl–H_2O	9	20.7	0.59 ± 0.02	0.10 ± 0.00	99.34
Ol–NaCl–H_2O^a	9	20.7	0.57 ± 0.01	0.09 ± 0.00	99.59
Ol–NaCl–H_2O^b	9	20.7	0.48 ± 0.02	0.07 ± 0.00	98.82
Ol–NaCl–H_2O	13	10.9	0.58 ± 0.11	0.18 ± 0.02	93.04
Ol–NaCl–H_2O	17	10.9	0.42 ± 0.17	0.12 ± 0.03	73.63
Ol–NaCl–H_2O	17	13.9	1.30 ± 0.10	0.23 ± 0.02	96.13
Ol–NaCl–H_2O	21	10.6	0.96 ± 0.10	0.20 ± 0.02	94.98
Ol–NaCl–H_2O	21	13.2	1.50 ± 0.07	0.25 ± 0.01	98.37
Ol–KCl–H_2O	5	10.9	0.03 ± 0.12	0.20 ± 0.01	93.36
Ol–KCl–H_2O	5	14.0	0.32 ± 0.06	0.15 ± 0.01	96.64
Ol–$CaCl_2$–H_2O	5	10.7	0.21 ± 0.10	0.28 ± 0.02	97.35
Ol–$CaCl_2$–H_2O	5	13.7	–0.20 ± 0.05	0.11 ± 0.01	96.67

of olivine in the saline fluids cannot affect the conductivities of the olivine–NaCl–H_2O systems. The fluid fraction of the aqueous fluid-bearing system remained mostly stable during the impedance spectra measurements, with less than 10% error of the fluid fraction in the aqueous fluid-bearing system, and the salinity remained unchanged during the experiments. The impedance spectra of the aqueous fluid-bearing system were continuously collected twice at a given temperature, and the two measured resistances were similar. This supports that the impedance spectra of the aqueous fluid-bearing system were collected during a relatively stable state. It is worthily mentioned that the reaction of quartz and olivine can take place at high temperatures and pressures, and a very thin pyroxene-bearing layer might be produced. However, the contribution of the thin pyroxene-bearing layer to the bulk conductivity could be negligible because the conductivity of pyroxene is much lower than that of interconnected fluid phases (Huang et al., 2021). Stable impedance spectra of hydrous polycrystalline olivine were collected using a similar process to that for the aqueous fluid-bearing system. The detailed thermodynamic conditions of the runs are listed in **Table 1**. The errors of the experimental pressures and temperatures were ±0.2 GPa and ±10 K, respectively.

Post-Experiment Sample Analysis

The chemical compositions of the recovered olivine for the olivine–NaCl–H_2O system with 5 wt% salinity and 20.3 vol% volume fraction were measured by EPMA. The chemical compositions of olivine were similar before and after the electrical conductivity measurements, as shown in **Supplementary Table S1**. The internal structures of the recovered samples were also observed using a scanning electron microscope (SEM) at the Center for Lunar and Planetary Sciences, Institute of Geochemistry, CAS, Guiyang, China. The SEM images show that the boundaries of the large olivine grains were curved and smooth, and small ellipsoidal olivine grains were distributed in the triangular spaces between the large olivine grains. A corrosion border is clearly visible on the olivine grains and numerous small circular holes are observed in the grain interiors (**Figure 1**). These phenomena reflect the strong dissolution and corrosion of olivine by the saline fluids at high temperature and pressure. Furthermore, the median dihedral angle of the saline fluids in of the Ol–NaCl–H_2O system with 5 wt% NaCl and 5.1 vol% fluids was found to be 50° (**Supplementary Figure S2**). The detail relevant analysis process was described in the supplementary material.

RESULTS

The representative impedance spectra of the Ol–H_2O and Ol–NaCl–H_2O systems comprise two parts: an approximate semicircle in the high-frequency region (10^6–10^3 Hz), and an additional tail in the low-frequency region (10^3–10^{-1} Hz) (**Figure 2**). Previous relevant studies have shown that the high-frequency semicircle reflects the conduction process of the bulk sample (Guo et al., 2015; Sinmyo and Keppler, 2017), and the low-frequency tail might correspond to an electrode effect (Tyburczy and Roberts, 1990). A comparison of the impedance spectra of the Cpx–NaCl–H_2O system suggests that inductive reactance did not appear for all of the saline fluid-bearing systems (Sun et al., 2020). For all of the hydrous olivine, Ol–H_2O system and Ol–NaCl–H_2O system samples, the bulk resistances were obtained by fitting the impedance spectra. The equivalent circuit

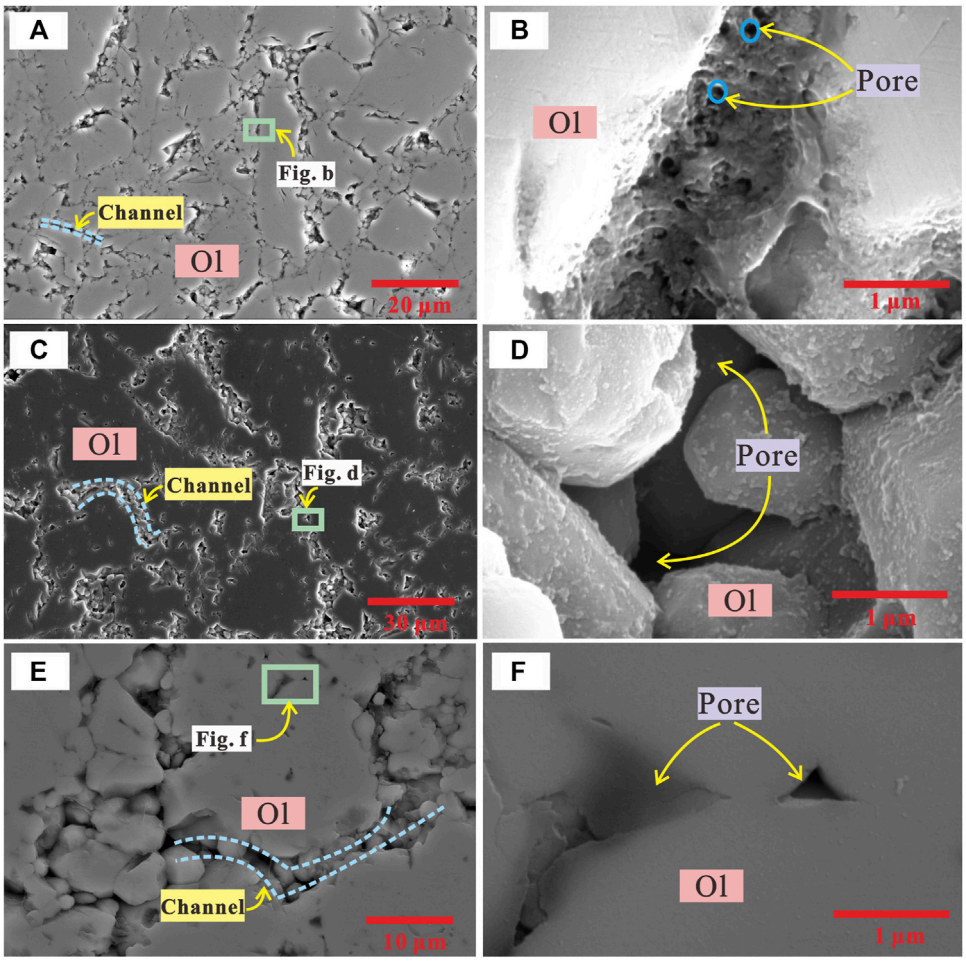

FIGURE 1 | Scanning electron microscope images of the recovered samples of saline fluid-bearing olivine aggregates after electrical conductivity measurements. **(A)** and **(B)** show the Ol–NaCl–H_2O system with a salinity of 5 wt% and fluid fraction of 13.7 vol%, **(C)** and **(D)** show the Ol–$CaCl_2$–H_2O system with a salinity of 5 wt% and fluid fraction of 10.7 vol%, and **(E)** and **(F)** show the Ol–NaCl–H_2O system with a salinity of 5 wt% and fluid fraction of 18.0 vol%. The saline fluids are uniformly distributed on the olivine grain boundaries, and the cross-sections of pores occupied by saline fluids contain triangular, elliptical, and irregular shapes. Fluid channels formed in the shattered zones among the large olivine grains.

of the impedance spectra comprises a series connection of R_S–CPE_S and R_E–CPE_E, where R_S and CPE_S represent the sample resistance and sample constant–phase element, respectively, and R_E and CPE_E indicate the resistance and constant–phase element for the interaction of the charge carrier with the electrode. The R_S errors were caused by the weak diffusion of aqueous fluids and fitting errors of the impedance spectra. Our evaluation indicates that the sample resistance errors were less than 10%. The calculation formula for the electrical conductivity (σ) is given as:

$$\sigma = G/R \tag{1}$$

where G is the sample geometric constant calculated based on L/S, in which L is the sample height (m) and S is the cross-sectional area of the electrodes (m^2), and R is the fitting resistance (Ω) of the sample.

The results show that the conductivity of the Ol–NaCl–H_2O system with 9 wt% salinity and 20.7 vol% volume fraction slightly increases with increasing pressure (**Figure 3**). This indicates that pressure has a weakly positive effect on the conductivity of saline fluid-bearing olivine aggregates. A comparison of the relationship between temperature and electrical conductivity of hydrous olivine aggregates shows that the positive temperature effect is substantially weaker on the conductivities of the Ol–H_2O and Ol–NaCl–H_2O systems, as shown in **Figure 4**. In comparison with the thermodynamic conditions (T and P), the salinity and fluid fraction have a much more significant effect on the olivine aggregate conductivities. The electrical conductivity of the Ol–NaCl–H_2O system moderately increases with increasing salinity and fluid fraction (**Figures 4**, **5**).

The median dihedral angle (50°) for the Ol–NaCl–H2O system with 5 wt% NaCl, and 5.1 vol% saline fluids is less than 60°, which

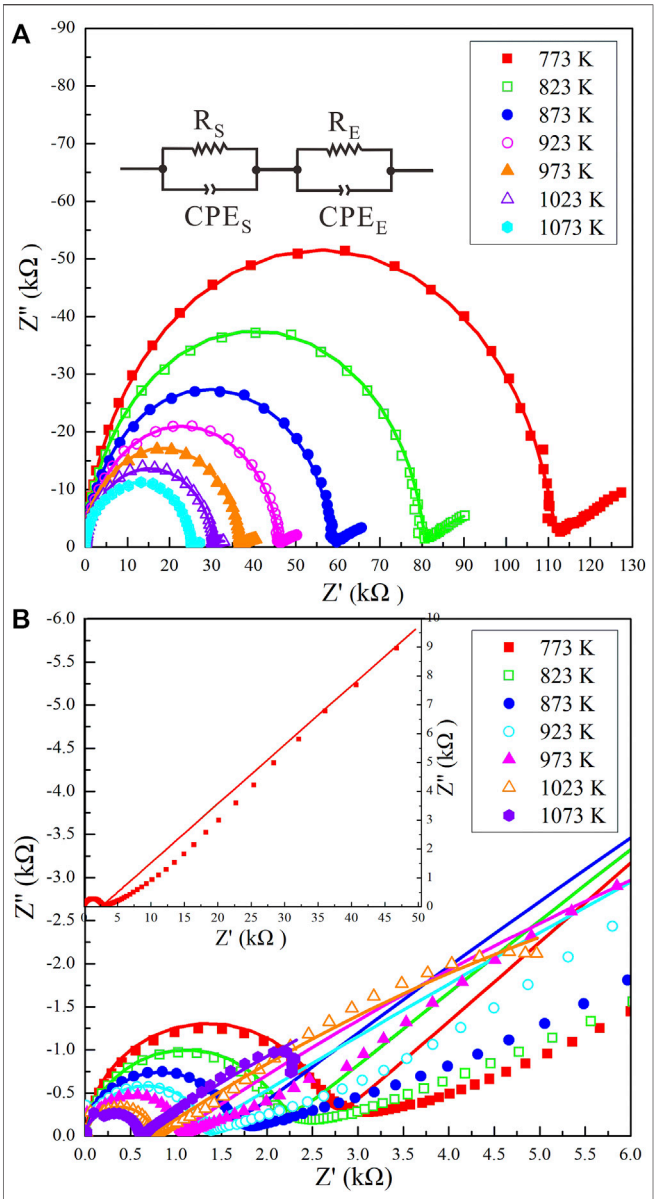

FIGURE 2 | Representative complex impedance spectra for **(A)** the Ol–H_2O system with a fluid fraction of 10.9 vol% and **(B)** the Ol–NaCl–H_2O system with a salinity of 5 wt% and fluid fraction of 17.8 vol% at 2.0 GPa and 773–1073 K. The equivalent circuit for the impedance spectra of the Ol–H_2O and Ol–NaCl–H_2O systems comprises a series connection of R_S–CPE_S and R_E–CPE_E, where R_S and CPE_S represent the sample resistance and sample constant–phase element, respectively, and R_E and CPE_E indicate the resistance and constant–phase element for the interaction of the charge carrier with the electrode.

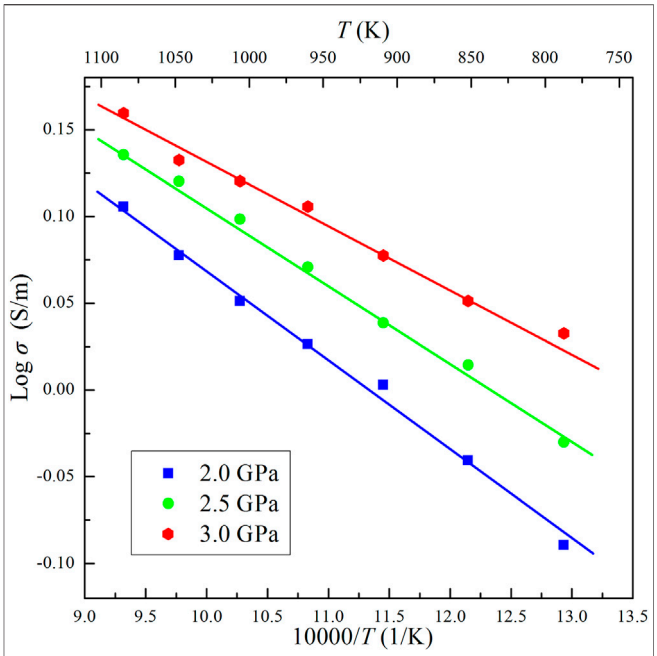

FIGURE 3 | Electrical conductivities of the Ol–NaCl–H_2O system with a salinity of 9 wt% and fluid fraction of 20.7 vol% at 2.0–3.0 GPa and 773–1073 K.

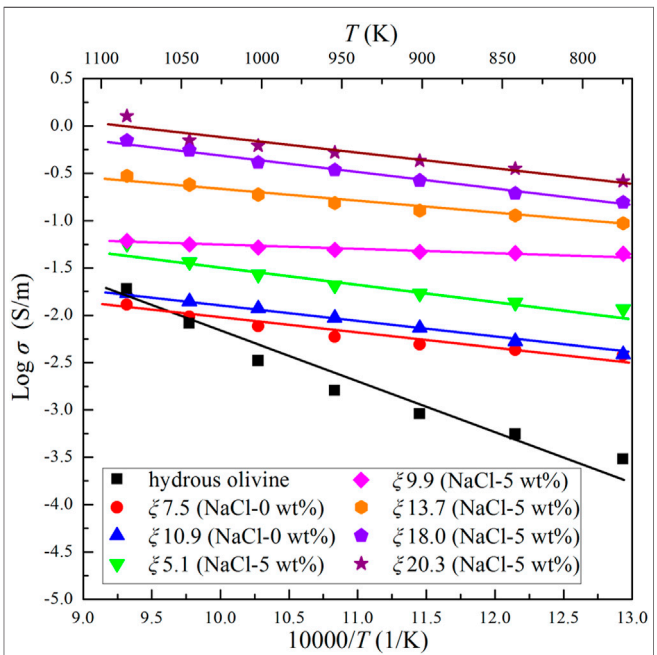

FIGURE 4 | Electrical conductivities of hydrous olivine aggregates and the Ol–NaCl–H_2O system with a salinity of 0–5 wt% and fluid fraction of 5.1–20.3 vol% at 2.0 GPa and 773–1073 K.

indicates that the saline fluids were interconnected in the systems where fluid fractions were substantially higher than 5.1 vol% (Bulau, 1982; Holness, 1995). The conductivities of the olivine aggregates with interconnected saline fluids do not regularly increase with increasing salinity and fluid fraction (**Figures 4**, **5**). The conductivity of the Ol–NaCl–H_2O system is similar to that of the Ol–KCl–H_2O system under similar salinity and fluid fraction conditions, but slightly higher than that of the Ol–$CaCl_2$–H_2O system (**Figure 6**). The activation enthalpy of the electrical conductivity of the saline fluid-bearing olivine

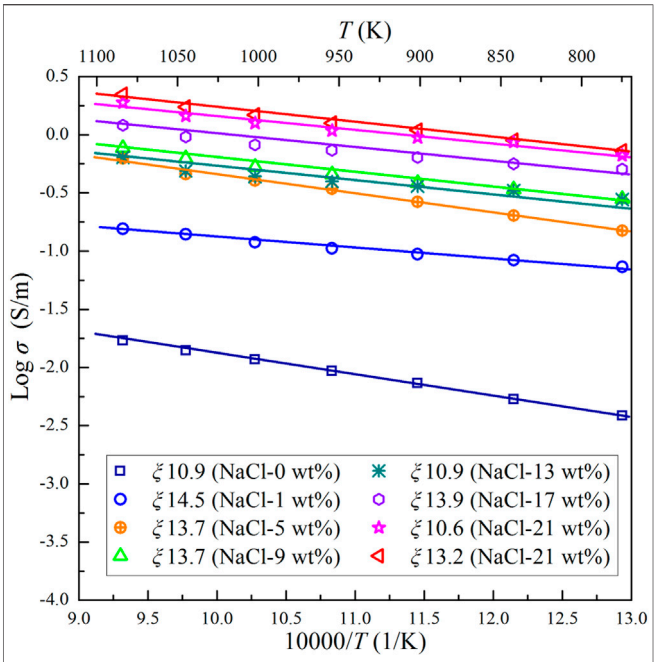

FIGURE 5 | Electrical conductivities of the Ol–NaCl–H_2O system with a salinity of 0–21 wt% and fluid fraction of 10.9–14.5 vol% at 2.0 GPa and 773–1073 K.

aggregates provides a crucial thermodynamic parameter that reveals the difficulty level for potential charge carriers to migrate in the samples. At a given pressure, the logarithmic electrical conductivities of the samples and reciprocal temperatures conform to approximate linear relations (**Figures 4–6**). The activation enthalpies of the conductivities of saline fluid-bearing olivine aggregates can thus be obtained by the following modified Arrhenius relation:

$$\mathrm{Log}\sigma = \mathrm{Log}\sigma_0 + \frac{-\Delta H}{\mathrm{Log\,e\,k}}\frac{1}{T} \quad (2)$$

where σ (S/m) denotes the sample conductivity, σ_0 is a fitting constant, k is the Boltzmann constant, T is temperature (K) and ΔH is the activation enthalpy for the sample conductivity. We calculated the activation enthalpies of the hydrous olivine aggregates, Ol–H_2O and Ol–NaCl/KCl/$CaCl_2$–H_2O systems based on **Eq. 2** and the slopes of the linear fitting relation for the logarithmic conductivities and reciprocal temperatures (details given in **Table 1**). The activation enthalpy of hydrous olivine aggregates (0.97 eV) is substantially higher than those for the Ol–H_2O and Ol–NaCl/KCl/$CaCl_2$–H_2O systems (0.07–0.36 eV) owing to the different conduction mechanisms that operate at high temperatures and pressures.

Disscussion

Effect of Temperature and Pressure on Conductivity

Temperature and pressure, which are crucial thermodynamic conditions of the Earth's interior, affect the electrical conductivity of most minerals, rocks, melts and aqueous fluids to varying degrees. Temperature and pressure fundamentally constrain the species, molar concentration and mobility of thermally activated charge carriers in materials and further influence the bulk conductivity. The conductivity of hydrous olivine aggregate is highly sensitive to temperature and increases by approximately two orders of magnitude upon increasing the temperature from 773 to 1073 K at 2 GPa (**Figure 4**). The effect of temperature on the conductivities is closely related to the activation enthalpy, which is directly constrained by the conduction mechanism in the samples. The conductivities and temperatures of hydrous olivine aggregates conform to an Arrhenius relation under the conditions of 2.0 GPa and 773–1073 K. The activation enthalpy for the conductivity of hydrous olivine aggregates is 0.97 eV and hydrogen-related point defects are proposed to be the dominant charge carriers (Dai and Karato, 2014a, 2020). This value is substantially lower than that from the model of Karato (1990) (1.50 eV), but similar to that from Dai and Karato, 2014b (0.82 eV). Huang et al. (2005) proposed that the electrical conductivity of hydrous olivine is related to the migration of free protons produced by an ionization reaction:

$$(2\mathrm{H})_{\mathrm{M}}^{\times} \rightleftharpoons \mathrm{H}_{\mathrm{M}}^{-} + \mathrm{H}^{\bullet} \quad (3)$$

where $(2\mathrm{H})_{\mathrm{M}}^{\times}$ represents two hydrogen ions at an M-site, $\mathrm{H}_{\mathrm{M}}^{'}$ is a proton trapped at the M-site vacancy, and $\mathrm{H}^{\bullet}$ is a free proton. For hydrous olivine with a fixed water content, the molar concentration and migration rate of the free proton might increase with increasing temperature. The temperature effect on the conductivity of hydrous olivine is also substantially weaker than that for dry olivine, where small polaron is the

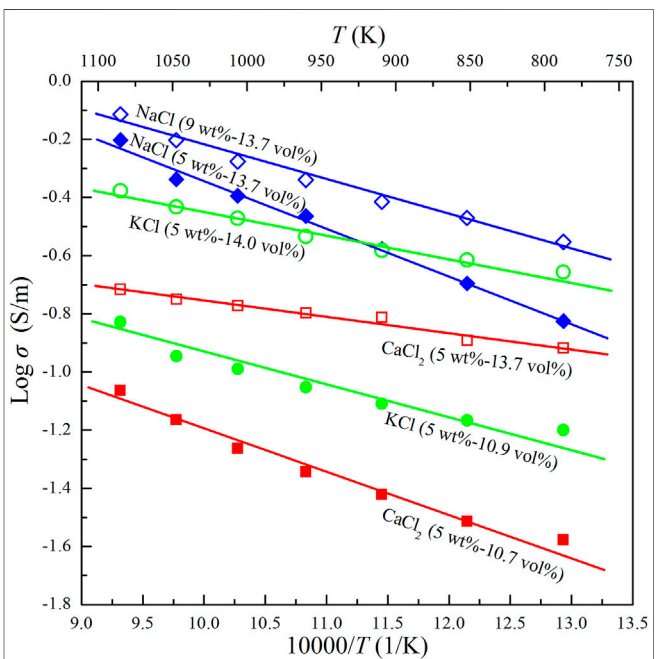

FIGURE 6 | Electrical conductivities of the Ol–NaCl–H_2O, Ol–KCl–H_2O and Ol–$CaCl_2$–H_2O systems with various salinity and fluid fraction conditions at 2.0 GPa and 773–1073 K.

dominant charge carrier, owing to the different conduction mechanisms (Dai and Karato, 2014b). For the Ol–NaCl/KCl/$CaCl_2$–H_2O systems, the conductivities slightly increase with increasing temperature and conform to an Arrhenius relation. The effect of temperature on the conductivities of the Ol–NaCl/KCl/$CaCl_2$–H_2O systems is considerably weaker than that for hydrous olivine aggregates at 2.0 GPa and 773–1073 K (**Figures 4–6**). This is because of the lower activation enthalpies (0.07–0.36 eV) for the dominant charge carriers of the Ol–NaCl/KCl/$CaCl_2$–H_2O systems. The electrical conductivity of olivine aggregates with interconnected aqueous fluids is dominantly constrained by the conductivities of the aqueous fluids. Free ions of $Na^+/K^+/Ca^{2+}$, Cl^-, H^+, and OH^- have been proposed to be the dominant charge carriers for olivine aggregates with interconnected saline fluids. According to the previous studies, the dissociation ratios of NaCl in the fluid phase of Ol–NaCl–H_2O systems were estimated to be ~95–100% under the conditions of 2.0–3.0 GPa and 773–1073 K (Manning, 2013). It was implied that the dissociation ratios of NaCl were very high, and thus the Na^+ and Cl^- might be the most dominant charge carriers in the Ol–NaCl–H_2O systems. In addition, Macris et al. (2003) reported that the solubility of olivine in the saline aqueous fluid is much higher than that of pure water, and decreases the dihedral angle simultaneously. As shown in **Figure 1**, corrosion borders are widely distributed on the olivine grains of the recovered samples. The conductivities of saline fluid-bearing olivine aggregates were measured from the highest temperature (1073 K) to the lowest temperature (773 K); thus, the olivine content dissolved in the aqueous fluids was approximately the same over the full temperature region in each experiment. The ionic groups from the reaction of olivine and saline fluids at high temperatures and pressures participate in the conduction process to some extent. The effect of pressure on the conductivity of dry and hydrous olivine has been previously reported to have a slightly negative correlation (Dai et al., 2010; Dai and Karato, 2014d). In this study, the electrical conductivity of saline fluid-bearing olivine aggregates is found to slightly increase with increasing pressure. As shown in **Figure 3**, the electrical conductivity of the Ol–NaCl–H_2O system with a salinity of 9 wt% and fluid fraction of 20.7 vol% increased by 0.05–0.15 orders of magnitude with increasing pressure from 2 to 3 GPa. According to previous studies, the conductivity of NaCl-bearing aqueous fluids weakly increases with pressure between 1 and 4 GPa and 773–1073 K (Guo and Keppler, 2019). The weak positive pressure effect on the conductivity of the Ol–NaCl–H_2O system is thus due to the presence of interconnected saline fluids. At a certain temperature, the saline fluids on the boundary of olivine particles become more interconnected with increasing pressure. The pressure might also increase the rate of salt decomposition in the aqueous fluids, and the molar concentration of the charge carriers in the fluids thus increase correspondingly. These might be the primary causes for the positive effect of pressure on the conductivity of the Ol–NaCl–H_2O system.

Effect of Salinity and Fluid Fraction on Conductivity

Salinity directly affects the conductivity of saline fluids, and the fluid fraction significantly influences the interconnectivity of the fluids in the matrix. The salinity and fluid fraction are thus closely related to the conductivity of saline fluid-bearing olivine aggregates. The median dihedral angle for the saline fluids of the Ol–NaCl–H_2O system with a salinity of 5 wt% and fluid fraction of 5.1 vol% is 50°, which indicates that the saline fluids were interconnected on the polycrystalline olivine boundaries (**Supplementary Figure S2**). The dihedral angles of the Ol–(NaCl)–H_2O system are found to be higher than those of the Pl–NaCl–H_2O and Cpx–NaCl–H_2O systems and dehydration products of lawsonite (**Supplementary Figure S3**). This might imply that aqueous fluids in the uppermost mantle are more difficult to interconnect than those in the mid-to lower crust and interfaces of subduction slabs. It's should be noted that pressure and temperature affect the dihedral angles for the aqueous fluids in the polycrystalline silicate minerals to some extent (Yoshino et al., 2007), but the dihedral angles for the aqueous fluids-bearing systems might be dominated by the mineral constituent and the salinity and fluid fraction of the saline fluids. As shown in **Figure 5**, the conductivities of the Ol–NaCl–H_2O system with a salinity of 1 wt% and fluid fraction of 14.5 vol% are ~1–1.5 orders magnitudes higher than those of the Ol–H_2O system with the fluid fraction of 10.9 vol%. However, the conductivities of the Ol–NaCl–H_2O system with a salinity of 5 wt% and fluid fraction of 13.7 vol% are only ~0.2–0.5 orders magnitudes higher than those of the Ol–H_2O system with a salinity of 1 wt% and fluid fraction of 14.5 vol%. This implies that a small quantity of salt can dramatically enhance the conductivity of the Ol–H_2O system owing to the sharp increase of charge carrier concentrations in the aqueous fluids. The molar concentration of Na^+ and Cl^- increases with increasing salinity and accordingly enhances the conductivity of the Ol–NaCl–H_2O system. However, the decomposition ratio of the solute might decrease with increasing salinity at a certain temperature and pressure; thus the conductivity of saline fluid-bearing olivine aggregates does not proportionately increase with increasing salinity (0–21 wt%). **Supplementary Figure S4** shows the logarithmic conductivity values versus salinity for the Ol–NaCl–H_2O system with similar fluid fractions (10.9–14.5 vol%). The conductivity of the Ol–NaCl–H_2O system dramatically increases with increasing salinity in the lower salinity range (< 17 wt%), but remains nearly unchanged in the higher salinity range (17–21 wt%). It should be noted that the conductivity of the Ol–NaCl–H_2O system with a salinity of 13 wt% and fluid fraction of 10.9 vol % is slightly lower than that of the Ol–NaCl–H_2O system with a salinity of 9 wt% and fluid fraction of 13.7 vol% at 2 GPa and 873–1073 K. We propose that the degree to which the fluid fraction influences the conductivity of saline fluid-bearing olivine aggregates is more significant than that of salinity when salinities are sufficiently high (>9 wt%). Salinity might also influence the solubility of olivine in saline fluids, which would explain the different activation enthalpies of the various saline fluid-bearing olivine aggregates (**Table 1**). Previous studies

TABLE 2 | Electrical conductivities (S/m) of saline fluids with various NaCl contents in the Ol–NaCl–H_2O, Cpx–NaCl–H_2O, Pl–NaCl–H_2O, Ab–NaCl–H_2O, and Qtz–NaCl–H_2O systems, and NaCl solutions calculated on the basis of the HS^+ and cube models at high temperatures and pressures.

Sample	*p* (GPa)	*T* (K)	Model	Salinity (wt%)									
				~0.6	1	5	~5.5	9	9.7	10.5	17	20	21
Ol–NaCl–H_2O	2.0	1,073	HS^+	–	0.76	3.5	–	4.32	–	–	10.61	–	13.11
			Cube	–	1.56	6.7	–	8.22	–	–	19.95	–	24.71
Cpx–NaCl–H_2O[a]	1.0	873	HS^+	–	–	3.7	–	–	–	15.0	–	16.3	–
			Cube	–	–	6.9	–	–	–	28.3	–	31.1	–
Pl–NaCl–H_2O[b]	1.0	800	HS^+	–	0.36	–	–	–	2.29	–	–	–	15.33
			Cube	–	0.45	–	–	–	2.40	–	–	–	15.95
Ab–NaCl–H_2O[c]	1.0	800	HS^+	–	–	–	15.5	–	–	55	–	–	–
			Cube	–	–	–	16	–	–	58	–	–	–
Qtz–NaCl–H_2O[d]	1.0	800	HS^+	–	–	1.4	–	–	–	–	20	–	
			Cube	–	–	1.4	–	–	–	–	21	–	–
NaCl solution[e]	2.0	1,073	–	7.74	–	–	59.1	–	–	–	–	–	–

Note: data of a, b, c, d and e were from Sun et al. (2020), Li et al. (2018), Guo et al. (2015), Shimojuku et al. (2014) and Guo and Keppler (2019), respectively.

have shown that the solubility of quartz and albite in NaCl–H_2O fluids decreases with increasing salinity, whereas the solubility of diopside in NaCl–H_2O fluids positively relates to salinity (Newton and Manning, 2000; Shmulovich et al., 2001). According to the research of Macris et al. (2003), the solubility of olivine in the saline aqueous fluid is much higher than that of pure water, which increases the concentration of dissolved component and decreases the dihedral angle simultaneously. We propose that the dissolution of olivine in saline fluids might play an important role in the conductivity of the Ol–NaCl–H_2O system. The logarithmic conductivity of the Ol–NaCl–H_2O system with a salinity of 5 wt% linearly relates to the logarithmic fluid fractions (**Supplementary Figure S5**). The bulk conductivity and fluid fraction thus conform to Archie's law (Archie, 1942):

$$\sigma_{\mathrm{bulk}} = \mathrm{c}\boldsymbol{\Phi}^{\mathrm{n}}\sigma_f \tag{4}$$

where σ_{bulk} and σ_f are the conductivities of the Ol–NaCl–H_2O systems and saline fluids, respectively, Φ is the fluid fraction, and as well as c and n are constants, respectively. Upon increasing the temperature from 773 to 1073 K, n increases from 2.34 to 4.12. This reflects that the conductivity of the Ol–NaCl–H_2O system significantly increases with increasing fluid fraction, and the fluid fraction has a more significant influence on conductivity at higher temperatures. The electrical conductivity of aqueous fluids (σ_f) distributed in the interspaces of the olivine aggregates remains unclear and is difficult to directly measure in the Ol–NaCl–H_2O system. The conductivity of interconnected aqueous fluids distributed in the solid matrix can be calculated based on the HS^+ model and cube model (Hashin and Shtrikman, 1962; Waff, 1974). According to the HS^+ model, the electrical conductivity of the aqueous fluids in the Ol–NaCl–H_2O system is calculated by:

$$\sigma_{\mathrm{b}} = \sigma_{\mathrm{f}} + \frac{1-\boldsymbol{\Phi}}{\frac{1}{\sigma_{\mathrm{s}}-\sigma_{\mathrm{f}}} - \frac{\boldsymbol{\Phi}}{3\sigma_{\mathrm{f}}}} \tag{5}$$

where σ_{b}, σ_{s} and σ_{f} are the conductivities of the Ol–NaCl–H_2O system, hydrous olivine aggregates and saline fluids, respectively. The mathematical formula for the cube model is expressed as:

$$\sigma_{\mathrm{b}} = \left(1-(1-\boldsymbol{\Phi})^{2/3}\right)\sigma_{\mathrm{f}} \tag{6}$$

We apply our experimental data to calculate the conductivity of aqueous fluids using **Eq. 5**, **Eq. 6**. As shown in **Table 2**, the conductivities of NaCl–H_2O fluids calculated from the HS^+ and cube models are substantially lower than experimental data reported by Sinmyo and Keppler (2017) and Guo and Keppler (2019). A similar phenomenon was reported by Guo et al. (2015), Li et al. (2018) and Sun et al. (2020). This discrepancy might be mainly caused by the compositional differences between the pure NaCl–H_2O fluids and aqueous fluids in the Ol–NaCl–H_2O system. For aqueous fluids in the Ol–NaCl–H_2O system, Na^+ and Cl^- have been proposed to be the dominant charge carriers and a small quantity of H^+, OH^- and soluble ions from olivine slightly enhance the conductivity, whereas tiny particles of silicate minerals in the aqueous fluids might dramatically impede charge carrier migration. The degree of NaCl dissociation might decrease owing to the presence of olivine aggregates. Furthermore, the true distribution of aqueous fluids in the systems possibly differs from those for the ideal HS^+ and cube models. Aqueous fluids are distributed in a variety of pathways, such as on mineral surfaces, spherical holes, triple junctions and local channels. Although the hydrodynamic pressure of the fluids is relatively homogeneous, the geometric shapes of the local aggregation fluids are constrained by the sizes and shapes of the olivine grains. In addition, the olivine has faceted interfaces due to its anisotropy, which could affect the fluid connectivity even with a low dihedral angle (Price et al., 2006), resulting in a more tortuous network of fluid. Notably, it is inevitable that a slow fluid movement from the temperature gradient of sample capsule is also of the possible effect on the measured conductivity results of the NaCl–H_2O and Ol–NaCl–H_2O systems.

Comparison With Previous Studies

The electrical conductivity of hydrous olivine aggregates determined in this study (~$10^{-3.5}$–$10^{-1.25}$) is similar to that reported by Dai and Karato, 2014b, and the iron contents of the two hydrous olivine aggregates are very similar (**Figure 7**). This supports that the water content in our olivine is similar to that in the olivine from Dai and Karato, 2014b (130 ppm). The

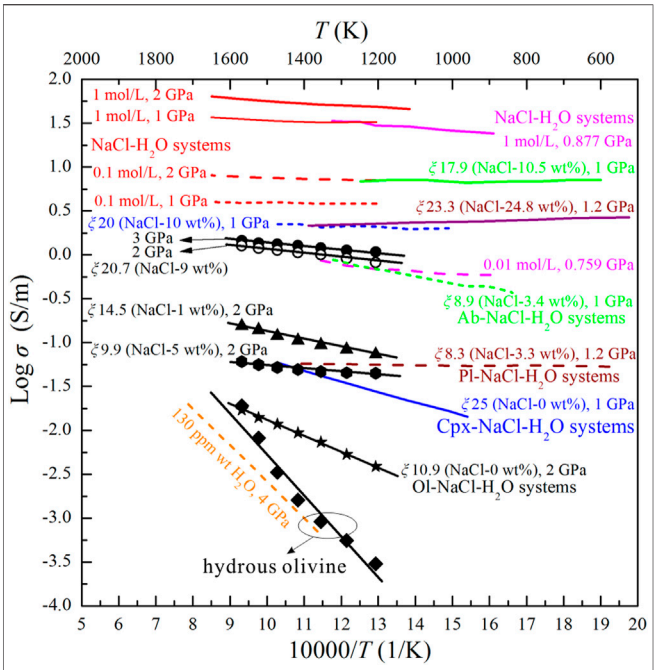

FIGURE 7 | Electrical conductivities of hydrous olivine aggregates and the Ol–H_2O and Ol–NaCl–H_2O systems in this study and relevant systems from previous studies. The dashed orange line indicates the conductivities of the hydrous olivine aggregates (Dai and Karato, 2014b). The purple five-pointed star indicates the conductivity of saline fluids-bearing forsterite aggregates (Huang et al., 2021). The solid and dashed blue lines indicate the conductivities of the Cpx–H_2O and Cpx–NaCl–H_2O systems (Sun et al., 2020), respectively. The dashed and solid brown lines indicate the conductivities of the Pl–NaCl–H_2O systems (Li et al., 2018). The dashed and solid green lines indicate the conductivities of the Ab–NaCl–H_2O systems (Guo et al., 2015). The red and pink lines indicate the conductivities of NaCl–H_2O systems (Sinmyo and Keppler, 2017; Guo and Keppler, 2019). The relationships between the logarithmic conductivities of the various hydrous olivine aggregates and saline fluid-bearing systems and reciprocal temperature are distinguished in different colors.

presence of pure water dramatically enhances the conductivity of olivine aggregates at lower temperature, but the conductivity of the Ol–H_2O system is similar to those of hydrous olivine aggregates with increasing temperature. The effect of saline fluids on the conductivity of olivine aggregates is substantially more significant than that of pure water (**Figure 7**). As shown in **Figure 7**, we compared the electrical conductivities of iron-free forsterite–fluid system from Huang et al. (2021) and the conductivities of iron-bearing olivine–fluid system from the present study. It was shown that the conductivity of iron-free forsterite–fluid system was moderately higher than that of iron-bearing olivine–fluid system at the same salinity and similar fluid fractions. And thus, the existence of iron in the olivine might be obstructive to the interconnectivity of saline fluids. The influence of aqueous fluids on the various silicate mineral aggregates also differs to some extent. The conductivity of olivine aggregates with interconnected pure water (10.9 vol%) is approximately one order of magnitude lower than that of clinopyroxene aggregates with 25 vol% pure water. In comparison with the electrical conductivity of Cpx–NaCl–H_2O system with a salinity of 10 wt% and fluid fraction of 20 vol%, the conductivity of Ol–NaCl–H_2O system with a salinity of 9 wt% and fluid fraction of 20.7 vol% is slightly lower. Under similar salinity and fluid fraction conditions, the conductivity of the Ol–NaCl–H_2O system is slightly lower than that of the Pl–NaCl–H_2O system, but dramatically lower than that of the Ab–NaCl–H_2O system (**Figure 7**). For example, the conductivity of the Ol–NaCl–H_2O system with a salinity of 5 wt% and fluid fraction of 9.9 vol% is slightly lower than that of the Pl–NaCl–H_2O system with a salinity of 3.3 wt% and fluid fraction of 8.3 vol%, but approximately 1.5 orders of magnitude lower than that of the Ab–NaCl–H_2O system with a salinity of 3.4 wt% and fluid fraction of 8.9 vol% (Guo et al., 2015; Li et al., 2018). The interconnected saline fluids thus dominantly constrain the conductivity of saline fluid-bearing silicate mineral aggregates, but the silicate minerals still play a significant role in the electrical properties of the systems. This is because the conductivities of various silicate minerals, (e.g., olivine, clinopyroxene, plagioclase and albite) differ under a given temperature and pressure condition. The various dissolution mechanisms and solubilities of different silicate minerals in saline fluids might therefore significantly affect the species and migration speed of the charge carriers in the fluids. Furthermore, the distribution characteristics of saline fluids in the interspaces of the solid matrix might be closely related to the grain size and shape, viscosity, defect concentration, and solubility of the minerals in the saline fluids-bearing systems. The electrical conductivity of the Ol–NaCl–H_2O system slightly increases with increasing pressure. A similar effect of pressure on the conductivity of the NaCl–H_2O system was reported by Guo and Keppler (2019). Salinity significantly affects the conductivity of the NaCl–H_2O system at high temperatures and pressures (Sinmyo and Keppler, 2017; Guo and Keppler, 2019), and further influences the conductivity of saline fluid-bearing rocks. The electrical conductivity of the Ol–NaCl–H_2O system with a salinity of 9 wt% and fluid fraction of 20.7 vol% is similar to that of the NaCl–H_2O system with a molar concentration of 0.01 mol/L (salinity: ~0.059 wt%), and approximately one order of magnitude lower than that of the NaCl–H_2O system with a molar concentration of 0.1 mol/L (salinity: ~0.58 wt%). Furthermore, the conductivity of the NaCl–H_2O system with a molar concentration of 1 mol/L (salinity: ~5.5 wt%) is substantially higher than that of the silicate mineral–NaCl–H_2O system with higher salinities (>5.7 wt%) (**Figure 7**). We propose that the dissolution of silicate minerals into the saline fluids might affect the conductivities of the aqueous fluids to some extent, and the hydrological regime in the silicate rocks dramatically affects the conductivities of fluid–rock systems. The measured conductivities of pure saline fluids are therefore significantly different from the calculated conductivities of saline fluids in silicate mineral–NaCl–H_2O systems based on the HS^+ and cube models.

Electrical conductivities of the Ol–NaCl–H_2O systems were the latest measuring results at the various thermodynamic conditions of 2.0–3.0 GPa and 773–1073 K. Effects of temperature and pressure on the conductivities of the

Ol–NaCl–H_2O systems were very slight, but salinity and fluid fraction are important influence factors on the conductivities. Electrical conductivities of the Ol–NaCl–H_2O systems were compared with the conductivities of the Ol–KCl–H_2O and Ol–$CaCl_2$–H_2O systems with a certain salinity and fluid fraction. It was shown that the conductivities of the Ol–NaCl–H_2O systems were close to those of the Ol–KCl–H_2O systems, but moderately higher than the Ol–$CaCl_2$–H_2O systems at the similar salinities and fluid fractions. Although the formation mechanism and evolution low for the saline fluids in the mantle wedges have not been researched in detail, the previous studies have proposed that NaCl is the dominant salt in the saline fluids based on the material compositions of the inclusion fluids in the mantle xenoliths (Kawamoto et al., 2013; Morikawa et al., 2016; Huang et al., 2019). And thus, the presence of NaCl fluids might be the origin of the high-conductivity anomalies in the mantle wedges. It's important to constrain the volume fractions of the saline fluids in the high-conductivity layers of the mantle wedges.

Geophysical Implications

Subduction zones are the most active geological environments on Earth, where various geological processes lead to complex material compositions and structural characteristics. Magnetotelluric profiles indicate that high-conductivity geological bodies are widely distributed in the mantle wedges of subduction zones. Various hypotheses regarding the origin for the high-conductivity anomalies have been proposed based on field geological investigations and high-temperature and high-pressure experiments (Dai and Karato, 2014a; Manthilake et al., 2015; Guo et al., 2017; Hu et al., 2018; Li et al., 2018). In subduction zones, the dehydration products of hydrous minerals, which contain residual minerals and aqueous fluids, are located along the interface between the subduction slab and mantle wedge. Owing to the wide distribution of aqueous fluids in mantle wedges (Peslier et al., 2017), hydrogen-related defects are likely to exist in nominally anhydrous minerals (Karato, 1990), causing a significant increase of the electrical conductivity in relevant regions (Dai and Karato, 2014b). According to the magnetotelluric profiles, the unusually high electrical conductivities of the high-conductivity layers in the mantle wedges were ~10^{-2}–1 S/m (Yamaguchi et al., 2009; Burd et al., 2013; McGary et al., 2014; Hata et al., 2017). The largest conductivity of hydrous San Carlos olivine with 0.1 wt% H_2O (close to the solubility of water in olivine) is approximately 10^{-1} S/m under the uppermost mantle conditions (Dai and Karato, 2014b), and thus the unusually high electrical conductivities of ~10^{-2}–10^{-1} S/m in the high-conductivity layers of the mantle wedges can be interpreted by the conductivities of hydrous peridotite. However, the unusually high conductivities of 10^{-1}–1 S/m in the mantle wedges were higher than the largest conductivity of hydrous peridotite (10^{-1} S/m), indicating that the conductivities of hydrous peridotite cannot interpret the unusually high electrical conductivities of 10^{-1}–1 S/m in the mantle wedges. Therefore, it's possible that the interconnected saline fluids cause the high-conductivity anomalies with the conductivities of ~10^{-1}–1 S/m in the mantle wedges.

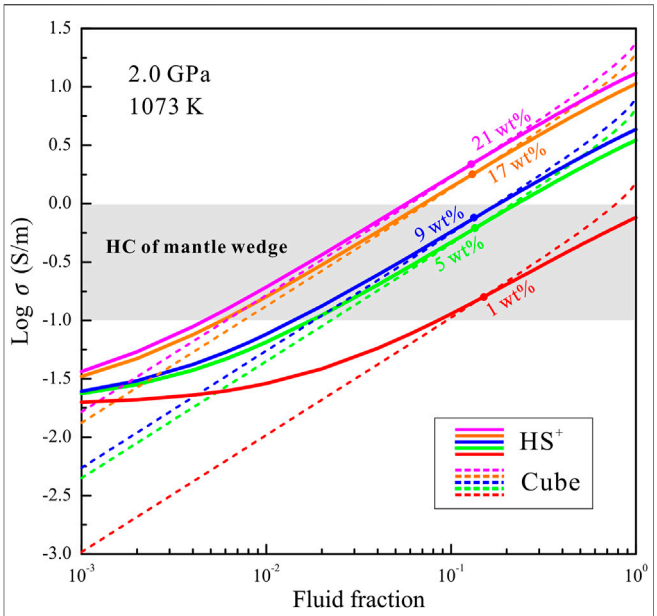

FIGURE 8 | Electrical conductivities of the Ol–NaCl–H_2O systems with constant salinity (1, 5, 9, 17, and 21 wt%) and various fluid fractions (0.1–100 vol%) based on the HS^+ and cube models at 2.0 GPa and 1073 K. The electrical-conductivity region (0.1–1 S/m) of the high-conductivity layers in the mantle wedges of subduction zones is indicated by a gray rectangle (Yamaguchi et al., 2009; Burd et al., 2013; McGary et al., 2014; Hata et al., 2017). The solid and dashed color curves represent the conductivities from the HS^+ and cube models, respectively.

Hydrous minerals (e.g., chlorite, epidote, serpentine, phengite) in subducting plates are transported into the Earth's deep interior, and subsequent dehydration reactions are triggered under the dehydration thermodynamic conditions of high temperatures and pressures (Zheng, 2019). A large proportion of free water released from hydrous minerals migrates upwards to a certain depth within the mantle wedges. A certain amount of solutes dissolve into the free water during the compositional differentiation of free water and residual minerals. The presence of NaCl-bearing aqueous fluids has been determined to be a significant cause of the high-conductivity anomalies in the middle to lower crust of subduction zones (Guo et al., 2015; Sinmyo and Keppler, 2017; Li et al., 2018; Guo and Keppler, 2019; Sun et al., 2020). The question of whether or not saline fluids are present and interconnected in the mantle wedges of subduction zones has been long debated. Huang et al. (2019) recently demonstrated that interconnected NaCl-bearing aqueous fluids are present in mantle wedges based on high-temperature and high-pressure experiments. This was an important discovery, which implies that NaCl-bearing aqueous fluids might cause the high-conductivity anomalies in the mantle wedges. Fluid fraction and salinity are significant factors that influence the conductivities of HCLs that might be caused by saline fluids. To quantitatively constrain the origin of the high-conductivity anomalies related to NaCl-bearing aqueous fluids in mantle wedges, we compare the conductivities of the HCLs in mantle wedges and NaCl-bearing aqueous fluids with

various salinities and fluid fractions. Magnetotelluric profiles indicate that the highest conductivities of the HCLs in most mantle wedges are close to 1 S/m (Yamaguchi et al., 2009; Burd et al., 2013; McGary et al., 2014; Hata et al., 2017). The conductivities of ellipsoidal HCLs gradually decrease from core to edge. In regions with aqueous fluids, the lattice water in nominally anhydrous minerals should be saturated. The presence of hydrous olivine can be employed to interpret the origin of HCLs with conductivities on the order of 10^{-2}–10^{-1} S/m (Dai and Karato, 2014b), but regions with conductivities of 10^{-1}–1 S/m are possibly related to saline fluids. The conductivities of the Ol–NaCl–H_2O system with various fluid fractions (0.1–100 vol%) and salinities (1–21 wt %) were calculated based on the HS^+ and cube models, as shown in **Figure 8**. The effects of temperature and pressure on the conductivities of the interconnected saline fluid-bearing olivine aggregates are very limited; thus the calculated conductivities are obtained based on the experimental data at 2.0 GPa and 1073 K. In the conductivity range of 10^{-1}–1 S/m, the conductivities of the Ol–NaCl–H_2O system estimated from the HS^+ and cube models at a certain salinity and fluid fraction differ slightly. This discrepancy might be caused by differences of the fluid distribution in the ideal cube and HS^+ models and real Ol–NaCl–H_2O system. For the Ol–NaCl–H_2O system with a certain salinity and electrical conductivity, the real fluid fractions are close to the average fluid fractions obtained from the HS^+ and cube models. The fluid fractions in the HCLs can be approximated by combining the electrical conductivities of HCLs in mantle wedges and those of the Ol–NaCl–H_2O system at a certain salinity. For the lower bound of conductivity (10^{-1} S/m) in the HCLs, the fluid fractions of the Ol–NaCl–H_2O system with a salinity of 1, 5, 9, 17 and 21 wt% are 9.0, 1.8, 1.5, 0.7 and 0.5 vol%, respectively. For the upper bound of conductivity (1 S/m) in the HCLs, the fluid fractions of the Ol–NaCl–H_2O system with a salinity of 5, 9, 17 and 21 wt% are 21.9, 17.9, 6.9 and 5.9 vol%, respectively. For the Ol–NaCl–H_2O system with a salinity of 1 wt%, the fluid fraction employed to interpret the upper bound for the high conductivities (1 S/m) is close to 100 vol%. The presence of the Ol–NaCl–H_2O system with a salinity of ~1 wt% can therefore not be the origin of the HCLs in mantle wedges. The original salinities of the aqueous fluids from the dehydration of subduction slabs are proposed to be 0.5–2.0 wt% NaCl (Li and Hermann, 2015). However, the salinity of the saline fluids measured in a peridotite xenolith from a mantle wedge was reported to be 5.1 ± 1.0 wt% NaCl (Kawamoto et al., 2013). In addition, the NaCl contents in slab-derived aqueous fluids that upwell up to forearc regions are close to 6.6 wt% (Morikawa et al., 2016). The higher salinities might be caused by the chromatographic fractionation during the hydration reaction of the mantle wedge after the fluid is released from the subduction slab (Huang et al., 2019). According to all of these above-mentioned evidences, it makes clear that the salinities of most stable aqueous fluids in the mantle wedges are close to 5.0 wt%. The Ol–NaCl–H_2O systems with the salinity of ~5.0 wt% and fluid fractions larger than 1.8 vol% might thus be the origin of the HCLs in mantle wedges.

CONCLUSION

Pressure and temperature play a relatively minor role on the electrical conductivity of olivine aggregates with interconnected saline fluids. The conductivity of saline fluid-bearing olivine aggregates slightly increases with the rise of temperature and pressure. The salinity and fluid fraction significantly affect the conductivity of saline fluid-bearing olivine aggregates at 2.0 GPa and 773–1073 K. At a fixed salinity and fluid fraction condition, the conductivity of the Ol–NaCl–H_2O system is similar to that of the Ol–KCl–H_2O system, but slightly higher than that of the Ol–$CaCl_2$–H_2O system. The electrical conductivity of the Ol–NaCl–H_2O system with interconnected saline fluids is constrained by the conductivity of NaCl-bearing saline fluids. For the Ol–NaCl–H_2O system, the dominant charge carriers are proposed to be Na^+, Cl^-, H^+, OH^-, and soluble ions from olivine. The activation enthalpies of charge carriers in the Ol–NaCl–H_2O systems are 0.07–0.36 eV, which are substantially lower than that of hydrous olivine aggregates (0.97 eV). Under a similar salinity and fluid fraction condition, our presently obtained electrical conductivity of the Ol–NaCl–H_2O system is slightly lower than those of other previous saline fluid-bearing systems (Cpx–NaCl–H_2O, Pl–NaCl–H_2O, and Al–NaCl–H_2O). The conductivities of saline fluids in the Ol–NaCl–H_2O system and other systems calculated using theoretical models (HS^+ and cube) differ to some extent and are substantially lower than the measured conductivities of saline fluids. The dissolution of olivine and other silicate minerals is proposed to dramatically reduce the conductivity of saline fluids distributed on the boundaries of silicate mineral aggregates. The distribution characteristics of saline fluids in olivine or other silicate mineral aggregates significantly influence the conductivities of saline fluid-bearing mineral aggregates. The salinity of stable saline fluids in mantle wedges is close to 5 wt% NaCl, and fluid fractions larger than 1.8 vol% can be employed to interpret the high-conductivity anomalies in mantle wedges based on the magnetotelluric result and calculated conductivities of the Ol–NaCl–H_2O system.

DATA AVAILABILITY STATEMENT

The datasets presented in this study can be found in online repositories. The names of the repository/repositories and accession number(s) can be found in the article/ **Supplementary Material**.

AUTHOR CONTRIBUTIONS

LD designed the project. WS and LD wrote the initial draft of the work and the final paper. LD, HH and WS contributed in

interpreting the results. WS, JJ, MW, ZH, CJ performed and interpreted the high-pressure electrical conductivity experiments and scanning electron microscope images.

FUNDING

This research was financially supported by the NSF of China (42072055, 41774099, 41772042, and 42002043), Youth Innovation Promotion Association of CAS (Grant No. 2019390), Special Fund of the West Light Foundation of CAS, the Foundation of the Key Laboratory of Earthquake Forecasting and United Laboratory of High-Pressure Physics and Earthquake Science, the Institute of Earthquake Forecasting, Chinese Earthquake Administration and as well as Special Fund from Shandong Provincial Key Laboratory of Water and Soil Conservation and Environmental Protection.

SUPPLEMENTARY MATERIAL

The Supplementary Material for this article can be found online at: https://www.frontiersin.org/articles/10.3389/feart.2021.749896/full#supplementary-material

REFERENCES

Archie, G. E. (1942). The Electrical Resistivity Log as an Aid in Determining Some Reservoir Characteristics. *Trans. Am. Inst. Min. Metall. Pet. Eng. Inc.* 146, 54–62. doi:10.2118/942054-G

Bulau, J. R. (1982). Intergranular Fluid Distribution in Olivine–Liquid basalt Systems. PhD dissertation. New Haven, Connecticut: Yale University.

Burd, A. I., Booker, J. R., Mackie, R., Pomposiello, C., and Favetto, A. (2013). Electrical Conductivity of the Pampean Shallow Subduction Region of Argentina Near 33 S: Evidence for a Slab Window. *Geochem. Geophys. Geosyst.* 14, 3192–3209. doi:10.1002/ggge.20213

Carter, M. J., Zimmerman, M. E., and Teyssier, C. (2015). The Fate of Fluid Inclusions during High-Temperature Experimental Deformation of Olivine Aggregates. *J. Geophys. Res. Solid Earth* 120, 3077–3095. doi:10.1002/2014JB011782

Dai, L., and Karato, S.-i. (2009). Electrical Conductivity of Wadsleyite at High Temperatures and High Pressures. *Earth Planet. Sci. Lett.* 287, 277–283. doi:10.1016/j.epsl.2009.08.012

Dai, L., and Karato, S.-i. (2014a). High and Highly Anisotropic Electrical Conductivity of the Asthenosphere Due to Hydrogen Diffusion in Olivine. *Earth Planet. Sci. Lett.* 408, 79–86. doi:10.1016/j.epsl.2014.10.003

Dai, L., and Karato, S.-i. (2014b). Influence of FeO and H on the Electrical Conductivity of Olivine. *Phys. Earth Planet. Interiors* 237, 73–79. doi:10.1016/j.pepi.2014.10.006

Dai, L., and Karato, S.-i. (2014d). Influence of Oxygen Fugacity on the Electrical Conductivity of Hydrous Olivine: Implications for the Mechanism of Conduction. *Phys. Earth Planet. Interiors* 232, 57–60. doi:10.1016/j.pepi.2014.04.003

Dai, L., and Karato, S.-i. (2014c). The Effect of Pressure on the Electrical Conductivity of Olivine under the Hydrogen-Rich Conditions. *Phys. Earth Planet. Interiors* 232, 51–56. doi:10.1016/j.pepi.2014.03.010

Dai, L., and Karato, S. i. (2020). Electrical Conductivity of Ti-Bearing Hydrous Olivine Aggregates at High Temperature and High Pressure. *J. Geophys. Res. Solid Earth* 125, e2020JB020309. doi:10.1029/2020JB020309

Dai, L., Li, H., Li, C., Hu, H., and Shan, S. (2010). The Electrical Conductivity of Dry Polycrystalline Olivine Compacts at High Temperatures and Pressures. *Mineral. Mag.* 74, 849–857. doi:10.1180/minmag.2010.074.5.849

Förster, M. W., Foley, S. F., Marschall, H. R., Alard, O., and Buhre, S. (2019). Melting of Sediments in the Deep Mantle Produces saline Fluid Inclusions in Diamonds. *Sci. Adv.* 5, eaau2620. doi:10.1126/sciadv.aau2620

Guo, H., and Keppler, H. (2019). Electrical Conductivity of NaCl-Bearing Aqueous Fluids to 900 °C and 5 GPa. *J. Geophys. Res. Solid Earth* 124, 1397–1411. doi:10.1029/2018JB016658

Guo, X., Li, B., and Ni, H. W. (2017). Electrical Conductivity of Hydrous Andesitic Melts Pertinent to Subduction Zones. *J. Geophys. Res. Solid Earth* 122, 1777–1788. doi:10.1002/2016JB013524

Guo, X. Z., Yoshino, T., and Shimojuku, A. (2015). Electrical Conductivity of Albite–(quartz)–Water and Albite–Water–NaCl Systems and its Implication to the High Conductivity Anomalies in the continental Crust. *Earth Planet. Sci. Lett.* 412, 1–9. doi:10.1016/j.epsl.2014.12.021

Hashin, Z., and Shtrikman, S. (1962). A Variational Approach to the Theory of the Effective Magnetic Permeability of Multiphase Materials. *J. Appl. Phys.* 33, 3125–3131. doi:10.1063/1.1728579

Hata, M., Uyeshima, M., Handa, S., Shimoizumi, M., Tanaka, Y., Hashimoto, T., et al. (2017). 3-D Electrical Resistivity Structure Based on Geomagnetic Transfer Functions Exploring the Features of Arc Magmatism beneath Kyushu, Southwest Japan Arc. *J. Geophys. Res. Solid Earth* 122, 172–190. doi:10.1002/2016JB013179

Heise, W., Ogawa, Y., Bertrand, E. A., Caldwell, T. G., Yoshinura, R., Ichihara, H., et al. (2019). Electrical Resistivity Imaging of the Inter-plate Coupling Transition at the Hikurangi Subduction Margin, New Zealand. *Earth Planet. Sci. Lett.* 524, 115710. doi:10.1016/j.epsl.2019.115710

Holness, M. B. (1995). The Effect of Feldspar on quartz–H_2O–CO_2 Dihedral Angles at 4 Kbar, with Consequences for the Behaviour of Aqueous Fluids in Migmatites. *Contrib. Mineral. Petrol.* 118, 356–364. doi:10.1007/s004100050020

Hu, H. Y., Dai, L. D., Li, H. P., Sun, W. Q., and Li, B. S. (2018). Effect of Dehydrogenation on the Electrical Conductivity of Fe-Bearing Amphibole: Implications for High Conductivity Anomalies in Subduction Zones and continental Crust. *Earth Planet. Sci. Lett.* 498, 27–37. doi:10.1016/j.epsl.2018.06.003

Huang, X. G., Xu, Y. S., and Karato, S. I. (2005). Water Content of the Mantle Transition Zone from the Electrical Conductivity of Wadsleyite and Ringwoodite. *Nature* 434, 746–749. doi:10.1038/nature03426

Huang, Y. S., Guo, H. H., Nakatani, T., Uesugi, K., Nakamura, M., and Keppler, H. (2021). Electrical Conductivity in Texturally Equilibrated Fluid-Bearing Forsterite Aggregates at 800°C and 1 GPa: Implications for the High Electrical Conductivity Anomalies in Mantle Wedges. *J. Geophys. Res. Solid Earth* 126, e2020JB021343. doi:10.1029/2020JB021343

Huang, Y. S., Nakatani, T., Nakamura, M., and McCammon, C. (2019). Saline Aqueous Fluid Circulation in Mantle Wedge Inferred from Olivine Wetting Properties. *Nat. Commun.* 10, 5557. doi:10.1038/s41467-019-13513-7

Karato, S. I. (1990). The Role of Hydrogen in the Electrical Conductivity of the Upper Mantle. *Nature* 347, 272–273. doi:10.1038/347272a0

Kawamoto, T., Yoshikawa, M., Kumagai, Y., Mirabueno, M. H. T., Okuno, M., and Kobayashi, T. (2013). Mantle Wedge Infiltrated with saline Fluids from Dehydration and Decarbonation of Subducting Slab. *Proc. Natl. Acad. Sci. USA* 110, 9663–9668. doi:10.1073/pnas.1302040110

Lacovino, K., Guild, M. R., and Till, C. B. (2020). Aqueous Fluids Are Effective Oxidizing Agents of the Mantle in Subduction Zones. *Contrib. Mineral. Petrol.* 175, 36. doi:10.1007/s00410-020-1673-4

Li, H., and Hermann, J. (2015). Apatite as an Indicator of Fluid Salinity: an Experimental Study of Chlorine and Fluorine Partitioning in Subducted Sediments. *Geochim. Cosmochim. Acta* 166, 267–297. doi:10.1016/j.gca.2015.06.029

Li, P., Guo, X. Z., Chen, S. B., Wang, C., Yang, J. L., and Zhou, X. F. (2018). Electrical Conductivity of the Plagioclase–NaCl–Water System and its Implication for the High Conductivity Anomalies in the Mid-lower Crust of Tibet Plateau. *Contrib. Mineral. Petrol.* 173, 1–12. doi:10.1007/s00410-018-1442-9

Lin, J. F., Speziale, S., Mao, Z., and Marquardt, H. (2013). Effects of the Electronic Spin Transitions of Iron in Lower Mantle Minerals: Implications for Deep

Mantle Geophysics and Geochemistry. *Rev. Geophys.* 51, 244–275. doi:10.1002/rog.20010

Macris, C. A., Newton, R. C., Wykes, J., Pan, R. G., and Manning, C. E. (2003). Diopside, Enstatite and Forsterite Solubilities in H_2O and H_2O-NaCl Solutions at Lower Crustal and Upper Mantle Conditions. *Geochim. Cosmochim. Acta* 279, 119–142. doi:10.1016/j.gca.2020.03.035

Manning, C. E. (2013). Thermodynamic Modeling of Fluid-Rock Interaction at Mid-crustal to Upper-Mantle Conditions. *Rev. Mineral. Geochem.* 76, 135–164. doi:10.2138/rmg.2013.76.5

Manthilake, G., Bolfan-Casanova, N., Novella, D., Mookherjee, M., and Andrault, D. (2016). Dehydration of Chlorite Explains Anomalously High Electrical Conductivity in the Mantle Wedges. *Sci. Adv.* 2, e1501631. doi:10.1126/sciadv.1501631

Manthilake, G., Chantel, J., Guignot, N., and King, A. (2021a). The Anomalous Seismic Behavior of Aqueous Fluids Released during Dehydration of Chlorite in Subduction Zones. *Minerals* 11, 70. doi:10.3390/min11010070

Manthilake, G., Koga, K. T., Peng, Y., and Mookherjee, M. (2021b). Halogen Bearing Amphiboles , Aqueous Fluids , and Melts in Subduction Zones : Insights on Halogen Cycle from Electrical Conductivity. *J. Geophys. Res. Solid Earth* 126, e2020JB021339. doi:10.1029/2020JB021339

Manthilake, G., Mookherjee, M., Bolfan-Casanova, N., and Andrault, D. (2015). Electrical Conductivity of Lawsonite and Dehydrating Fluids at High Pressures and Temperatures. *Geophys. Res. Lett.* 42, 7398–7405. doi:10.1002/2015GL064804

Manthilake, G., Mookherjee, M., and Miyajima, N. (2021c). Insights on the Deep Carbon Cycle from the Electrical Conductivity of Carbon-Bearing Aqueous Fluids. *Sci. Rep.* 11, 3745. doi:10.1038/s41598-021-82174-8

McGary, R. S., Evans, R. L., Wannamaker, P. E., Elsenbeck, J., and Rondenay, S. (2014). Pathway from Subducting Slab to Surface for Melt and Fluids beneath Mount Rainier. *Nature* 511, 338–340. doi:10.1038/nature13493

Morikawa, N., Kazahaya, K., Takahashi, M., Inamura, A., Takahashi, H. A., Yasuhara, M., et al. (2016). Widespread Distribution of Ascending Fluids Transporting Mantle Helium in the Fore-Arc Region and Their Upwelling Processes: Noble Gas and Major Element Composition of Deep Groundwater in the Kii Peninsula, Southwest Japan. *Geochim. Cosmochim. Acta* 182, 173–196. doi:10.1016/j.gca.2016.03.017

Newton, R. C., and Manning, C. E. (2000). Quartz Solubility in H_2O–NaCl and H_2O–CO_2 Solutions at Deep Crust–Upper Mantle Pressures and Temperatures: 2–15 Kbar and 500–900°C. *Geochim. Cosmochim. Acta* 64, 2993–3005. doi:10.1016/S0016-7037(00)00402-6

Peslier, A. H., Schönbächler, M., Busemann, H., and Karato, S. I. (2017). Water in the Earth's interior: Distribution and Origin. *Space Sci. Rev.* 212, 743–810. doi:10.1007/s11214-017-0387-z

Pommier, A., and Evans, R. L. (2017). Constraints on Fluids in Subduction Zones from Electromagnetic Data. *Geosphere* 13, 1026–1041. doi:10.1130/GES01473.1

Price, J. D., Wark, D. A., Watson, E. B., and Smith, A. M. (2006). Grain-scale Permeabilities of Faceted Polycrystalline Aggregates. *Geofluids* 6, 302–318. doi:10.1111/j.1468-8123.2006.00149.x

Reynard, B. (2016). Mantle Hydration and Cl-Rich Fluids in the Subduction Forearc. *Prog. Earth Planet. Sci.* 3, 9. doi:10.1186/s40645-016-0090-9

Reynard, B., Mibe, K., and de Moortèle, B. Van. (2011). Electrical Conductivity of the Serpentinised Mantle and Fluid Flow in Subduction Zones. *Earth Planet. Sci. Lett.* 307, 387–394. doi:10.1016/j.epsl.2011.05.013

Ringwood, A. E. (1982). Phase Transformations and Differentiation in Subducted Lithosphere: Implications for Mantle Dynamics, basalt Petrogenesis and Crustal Evolution. *J. Geol.* 90, 611–643. doi:10.1086/628721

Saltas, V., Chatzistamou, V., Pentari, D., Paris, E., Triantis, D., Fitilis, I., et al. (2013). Complex Electrical Conductivity Measurements of a KTB Amphibolite Sample at Elevated Temperatures. *Mater. Chem. Phys.* 139, 169–175. doi:10.1016/j.matchemphys.2013.01.016

Saltas, V., Pentari, D., and Vallianatos, F. (2020). Complex Electrical Conductivity of Biotite and Muscovite Micas at Elevated Temperatures: A Comparative Study. *Minerals* 13, 3513. doi:10.3390/ma13163513

Selway, K. (2015). Negligible Effect of Hydrogen Content on Plate Strength in East Africa. *Nat. Commun.* 8, 543–546. doi:10.1038/NGEO2453

Selway, K., and O'Donnell, J. P. (2019). A Small, Unextractable Melt Fraction as the Cause for the Low Velocity Zone. *Earth Planet. Sci. Lett.* 517, 117–124. doi:10.1016/j.epsl.2019.04.012

Shimojuku, A., Yoshino, T., and Yamazaki, D. (2014). Electrical Conductivity of Brine-Bearing Quartzite at 1 GPa: Implications for Fluid Content and Salinity of the Crust. *Earth Planets Space* 66, 2. doi:10.1186/1880-5981-66-2

Shimojuku, A., Yoshino, T., Yamazaki, D., and Okudaira, T. (2012). Electrical Conductivity of Fluid-Bearing Quartzite under Lower Crustal Conditions. *Phys. Earth Planet. Inter.* 198–199, 1–8. doi:10.1016/j.pepi.2012.03.007

Shmulovich, K., Graham, C., and Yardley, B. (2001). Quartz, Albite and Diopside Solubilities in H_2O–NaCl and H_2O–CO_2 Fluids at 0.5–0.9 GPa. *Contrib. Mineral. Petrol.* 141, 95–108. doi:10.1007/s004100000224

Sinmyo, R., and Keppler, H. (2017). Electrical Conductivity of NaCl-Bearing Aqueous Fluids to 600°C and 1 GPa. *Contrib. Mineral. Petrol.* 172, 4. doi:10.1007/s00410-016-1323-z

Sun, W. Q., Dai, L. D., Li, H. P., Hu, H. Y., Jiang, J. J., and Wang, M. Q. (2020). Electrical Conductivity of Clinopyroxene–NaCl–H_2o System at High Temperatures and Pressures: Implications for High-Conductivity Anomalies in the Deep Crust and Subduction Zone. *J. Geophys. Res. Solid Earth* 125, e2019JB019093. doi:10.1029/2019JB019093

Tyburczy, J. A., and Roberts, J. J. (1990). Low Frequency Electrical Response of Polycrystalline Olivine Compacts: Grain Boundary Transport. *Geophys. Res. Lett.* 17, 1985–1988. doi:10.1029/GL017i011p01985

Vallianatos, F. (1996). Magnetotelluric Response of a Randomly Layered Earth. *Geophys. J. Int.* 125, 577–583. doi:10.1111/j.1365-246X.1996.tb00020.x

Vargas, J. A., Meqbel, N. M., Ritter, O., Brasse, H., Weckmann, U., Yáñez, G., et al. (2019). Fluid Distribution in the central Andes Subduction Zone Imaged with Magnetotellurics. *J. Geophys. Res. Solid Earth* 124, 4017–4034. doi:10.1029/2018JB016933

Waff, H. S. (1974). Theoretical Considerations of Electrical Conductivity in a Partially Molten Mantle and Implications for Geothermometry. *J. Geophys. Res. Solid Earth Planets* 79, 4003–4010. doi:10.1029/JB079i026p04003

Wang, J. T., Takahashi, E., Xiong, X. L., Chen, L. L., Li, L., Suzuki, T., et al. (2020). The Water-Saturated Solidus and Second Critical Endpoint of Peridotite: Implications for Magma Genesis within the Mantle Wedge. *J. Geophys. Res. Solid Earth* 125, e2020JB019452. doi:10.1029/2020JB019452

Yamaguchi, S., Uyeshima, M., Murakami, H., Sutoh, S., Tanigawa, D., Ogawa, T., et al. (2009). Modification of the Network-MT Method and its First Application in Imaging the Deep Conductivity Structure beneath the Kii Peninsula, Southwestern Japan. *Earth Planet. Sci. Lett.* 61, 957–971. doi:10.1186/BF03352946

Yoshino, T., Nishihara, Y., and Karato, S. (2007). Complete Wetting of Olivine Grain Boundaries by a Hydrous Melt Near the Mantle Transition Zone. *Earth Planet. Sci. Lett.* 256, 466–472. doi:10.1016/j.epsl.2007.02.002

Zheng, Y. F. (2019). Subduction Zone Geochemistry. *Geosci. Front.* 10, 1223–1254. doi:10.1016/j.gsf.2019.02.003

Conflict of Interest: The authors declare that the research was conducted in the absence of any commercial or financial relationships that could be construed as a potential conflict of interest.

Publisher's Note: All claims expressed in this article are solely those of the authors and do not necessarily represent those of their affiliated organizations, or those of the publisher, the editors, and the reviewers. Any product that may be evaluated in this article, or claim that may be made by its manufacturer, is not guaranteed or endorsed by the publisher.

frontiers in Earth Science

ORIGINAL RESEARCH
published: 26 January 2022
doi: 10.3389/feart.2021.833405

Effect of Thermoelastic Properties of the Pyrope-Almandine Solid Solutions on the Entrapment Pressure of Garnet-Related Elastic Geobarometer

Bo Li[1,2,3], Junjie Jiang[4], Jingui Xu[5], Sergey N. Tkachev[6], Zhilin Ye[2,3], Shijie Huang[2,3], Weihua Guo[1], Yongjun Zeng[1], Vitali B. Prakapenka[6], Dawei Fan[2] and Wenge Zhou[2]*

[1]Research Institute of Petroleum Exploration & Development-Northwest (NWGI), PetroChina, Lanzhou, China, [2]Key Laboratory of High-Temperature and High-Pressure Study of the Earth's Interior, Institute of Geochemistry, Chinese Academy of Sciences, Guiyang, China, [3]University of Chinese Academy of Sciences, Beijing, China, [4]Basic Geological Survey Institute of Jiangxi Geological Survey Institute, Nanchang, China, [5]Hawaii Institute of Geophysics and Planetology, School of Ocean and Earth Science and Technology, University of Hawaii at Manoa, Honolulu, HI, United States, [6]Center for Advanced Radiation Sources, University of Chicago, Chicago, IL, United States

OPEN ACCESS

Edited by:
Lidong Dai,
Institute of geochemistry (CAS), China

Reviewed by:
Dayong Tan,
The Institute of Advanced Science Facilities, China
Dongzhou Zhang,
University of Hawaii at Manoa, United States

***Correspondence:**
Dawei Fan
fandawei@vip.gyig.ac.cn

Specialty section:
This article was submitted to Earth and Planetary Materials, a section of the journal Frontiers in Earth Science

Received: *11 December 2021*
Accepted: *21 December 2021*
Published: *26 January 2022*

Citation:
Li B, Jiang J, Xu J, Tkachev SN, Ye Z, Huang S, Guo W, Zeng Y, Prakapenka VB, Fan D and Zhou W (2022) Effect of Thermoelastic Properties of the Pyrope-Almandine Solid Solutions on the Entrapment Pressure of Garnet-Related Elastic Geobarometer. Front. Earth Sci. 9:833405. doi: 10.3389/feart.2021.833405

The pyrope (Prp)–almandine (Alm) solid solutions are the most fundamental garnet components on the Earth, and both the quartz inclusions in garnet (QuiG) barometry and the garnet inclusions in diamond barometry need to be constrained by the thermoelastic parameters of Prp-Alm solid solution garnets. Here, we report the thermoelastic properties of a series of synthetic Prp-Alm solid solutions based on the high-pressure and high-temperature (*HP–HT*) *in situ* synchrotron single-crystal x-ray diffraction (SCXRD) experiments up to ~20 GPa and 700 K, using diamond anvil cell (DAC). Fitting the SCXRD data by the Birch-Murnaghan equation of state (BM-EoS) and the thermal-pressure EoS, we obtain the thermoelastic parameters of Prp-Alm solid solution garnets, including bulk modulus (K_0), its pressure derivative (K'_0), and the thermal expansion coefficient (α_0). The K_0 along the Prp-Alm solid solution changes linearly with Prp content within their uncertainties and can be expressed by K_0 (GPa) = 181.0(8) – 0.11(1) X_{prp} ($R^2 = 0.91$, X_{prp} is the Prp mole fraction and K'_0 fixed at 4). Our result indicates that the compressibility of the Prp-Alm solid solution increases with the increasing Prp content. However, the thermal expansion coefficient of Prp-Alm solid solution at ambient pressure shows a non-linear trend with Prp content and can be expressed by α_0 (10^{-5} K^{-1}) = 2.7 (1) + 3.0 (5) X_{Prp} – 3.2 (4) X^2_{Prp} ($R^2 = 0.985$). It shows that the Prp-Alm solid solution with intermediate composition has a larger thermal expansion coefficient than those close to the endmembers at ambient conditions. Furthermore, we also evaluated the influence of thermoelastic properties of the Prp-Alm solid solution on the entrapment pressure (P_e) estimation for two types of elastic geobarometers. Our results indicate that the garnet component may significantly influence entrapment pressure, and among the thermoelastic parameters of garnet, the thermal expansion coefficient has the main effect on the estimation of P_e.

Keywords: pyrope-almandine solid solution, elastic geobarometer, equation of state, high pressure and high temperature, diamond anvil cell

INTRODUCTION

Diamond is the only direct sample obtained from inaccessible portions of Earth (Nestola et al., 2019) and the subduction zone metamorphism controls many global geochemical cycles and the lithosphere (Ashley et al., 2016). Estimating the pressure and temperature of these minerals or rocks provides fundamental data for studying many such geological processes, but their determination remains extremely controversial (Bebout, 2007; Tajčmanová et al., 2021). To date, various methods have been developed to address the geological history of rocks. Previous studies have used mineral–mineral equilibrium based on Gibbs free energy minimization or partitioning major or trace elements between phases to recover these geological processes (De Capitani and Petrakakis, 2010; Holland and Powell, 2011). Despite advances in analytical techniques, geothermobarometers still suffer from problems due to alteration processes, such as the erasure of peak metamorphic mineral assemblages (e.g., Korsakov et al., 2009; Jamtveit et al., 2016), chemical re-equilibration, diffusion, and kinetic limitations (e.g., Anzolini et al., 2019; Gonzalez et al., 2019). Additionally, part of the difficulty in determining the pressure of rocks is the lack of typical pressure-dependent mineral equilibria, especially for the diamond-inclusion system (Ashley et al., 2016; Nestola et al., 2017).

Ideally, geobarometers should yield accurate pressure estimates using only commonly found minerals and not be susceptible to significant resetting during exhumation. Recently, an alternative method based on the mechanical equilibrium between entrapped mineral inclusions (e.g., quartz and garnet) and host mineral (e.g., garnet and diamond) has received significant attention and could vastly expand the range of barometers available to petrologists (e.g., Enami et al., 2007; Kohn, 2014; Milani et al., 2015; Cisneros et al., 2020). Inclusions encapsulated in host minerals such as garnet or diamond have different elastic properties; they produce a residual pressure (P_{inc}) following exhumation, thereby allowing us to determine the entrapment pressure (Rosenfeld and Chase, 1961; Zhang, 1998). The P_{inc} and the equations of state (EoS) of the host-inclusion system can be used to calculate unique P–T curves (called isomekes) along which the pressure of the host and the inclusion are equal despite the changes in P–T conditions. Detailed discussions of this application are given by Angel et al. (2015) and Gonzalez et al. (2019).

Much of the previous work has focused on the factors affecting the calculation accuracy of the elastic geobarometer, such as the viscosity/plasticity relaxation properties of the inclusions (Zhong et al., 2020), the elastic anisotropy of minerals (Murri et al., 2018; Mazzucchelli et al., 2019), and the non-ideal geometry of inclusions (Mazzucchelli et al., 2018). Moreover, precisely determining the P_{inc} in inclusions has attracted many studies, as measured by x-ray diffractometry (Angel et al., 2014b) or Raman spectroscopy (Enami et al., 2007; Korsakov et al., 2009; Ashley et al., 2016; Murri et al., 2018; Bonazzi et al., 2019). However, researchers rarely explored the effect of thermoelastic parameters of minerals in entrapment pressure (P_e) calculations, which is crucial to improving elastic geobarometry precision (Angel et al., 2015; Moulas et al., 2020). Only Angel et al. (2015) considered the influence of thermoelastic parameters of diamond in determining the pressure of formation of diamond-inclusion systems. Moreover, as garnet rarely has a homogeneous composition, Moulas et al. (2020) considered the possible propagation of errors caused by the uncertainty of garnet composition in entrapment pressure (P_e) calculations. Therefore, in this study, we evaluated the influence of the thermoelastic parameters of the concerned minerals on the calculated results of the two types of elastic geobarometers, garnet (inclusion)–diamond (host) system and quartz (inclusion)–garnet (host) system (QuiG). The garnet–diamond system is very appropriate for estimating the formation pressure of diamond because the garnet is the most abundant occurring inclusion mineral in the diamond (Milani et al., 2015). Similarly, QuiG is also suitable for geobarometers because quartz is highly compressible relative to garnet, and the garnet host can maintain a large stress difference caused by changes in P–T conditions (Ashley et al., 2016). In these two types of elastic geobarometers, diamond and quartz are generally virtually pure endmember, and their thermoelastic parameters have been accurately determined (Angel et al., 2015; Angel et al., 2017a). However, the effect of composition of garnet on its thermoelastic parameters is still not very clear (Fan et al., 2017; Fan et al., 2018; Xu et al., 2019).

Garnet has cubic symmetry with $Ia\,\overline{3}\,d$. The structure of garnet $X_3^{2+}Y_2^{3+}Si_3O_{12}$ consists of a mixed framework of corner-sharing SiO_4 tetrahedra and YO_6 octahedra, with XO_8 triangular dodecahedron lying in between (Geiger, 2013) (**Supplementary Figure S1**). Garnet is flexible in accommodating a variety of cations with different ionic radii. Generally, divalent cations (e.g., Mg^{2+}, Fe^{2+}, Ca^{2+}, Mn^{2+}) occupy the X-site while trivalent cations (e.g., Al^{3+}, Fe^{3+}, Cr^{3+}) occupy the Y-site. Natural garnet usually does not exist as pure endmember components but form solid solutions through element partitioning (Fan et al., 2015). Summary and analysis of garnet compositions from the global major ultra-high-pressure metamorphic (UHPM) rocks and kimberlites indicate that garnet is mainly composed of pyrope (Prp, $Mg_3Al_2Si_3O_{12}$), almandine (Alm, $Fe_3Al_2Si_3O_{12}$), and grossular (Grs, $Ca_3Al_2Si_3O_{12}$) with some other endmember components like spessartine (Sps, $Mn_3Al_2Si_3O_{12}$) and andradite (Adr, $Ca_3Fe_2^{3+}Si_3O_{12}$) (Zhang et al., 2010; Kosman et al., 2016; Riches et al., 2016; Broadwell et al., 2019; Cruciani et al., 2019; Xu et al., 2019; Liu et al., 2020). In addition, the modal abundance of Prp and Alm can reach ~70% and become higher with the increasing of the metamorphic pressure.

Understanding the thermoelastic properties of garnet, especially the Prp-Alm solid solution, is not only important to model the structure of the subducted slab but also a primary step in quantifying the P–T conditions of subduction and exhumation (Bass et al., 2008; Ashley et al., 2014). There are already extensive studies about the thermoelastic properties of Prp and Alm endmember component (Zhang L. et al., 1998; Gwanmesia et al., 2006; Fan et al., 2009; Li et al., 2011; Zou et al., 2012; Arimoto et al., 2015; Chantel et al., 2016; Hu et al., 2016; Fan et al., 2019b; Hartwig and Galkin, 2021). However, there is still a lack of tight constraints on the variation behavior of thermoelastic

parameters developed when Prp-Alm solid solution is varying with composition (Takahashi and Liu, 1970; Huang and Chen, 2014; Milani et al., 2015). It is known that, for different mineral compositions, a variety of different cations incorporated in the garnets will affect their thermoelastic properties (Zhang et al., 1999; Kuang et al., 2019). In the 1970s, Takahashi and Liu (1970) conducted the pressure–volume (*P–V*) EoS study on four garnet samples with different compositions (Prp_{100}, $Prp_{60}Alm_{31}$, $Prp_{22}Alm_{72}$, and Alm_{100}) up to 32.8 GPa using single-crystal x-ray diffraction (SCXRD) and diamond anvil cell (DAC). They inferred that the bulk modulus (K_0) of the Prp-Alm solid solution decreases with the increasing Alm content. However, the conclusion from Takahashi and Liu (1970) needs to be further verified because they did not use any gasket in their high-pressure SCXRD experiments, which may significantly influence their experimental results. Similarly, Huang and Chen (2014) also performed the *P–V* EoS study on three synthetic Prp-Alm solid solutions ($Prp_{83}Alm_{17}$, $Prp_{54}Alm_{46}$, and $Prp_{30}Alm_{70}$) up to ~21 GPa using *in situ* XRD combined with DAC, but obtained the opposite conclusion from Takahashi and Liu (1970), that is, the K_0 increases with the increasing Alm content. Furthermore, Huang and Chen (2014) also obtained the relationship between the K_0 of the Prp-Alm solid solutions and Alm content: K_0 = 170.5 (2.6) + 0.12 (4) X_{Alm} (X_{Alm} is the mole fraction of Alm). Subsequently, Milani et al. (2015) studied the *P–V* EoS on three synthetic Prp-Alm solid solutions (Prp_{100}, $Prp_{60}Alm_{40}$, and Alm_{100}) and obtained the same conclusion as that of Huang and Chen (2014). Nevertheless, to date, the thermoelastic properties of the Prp-Alm solid solutions at simultaneous high-pressure and high-temperature (*HP–HT*) conditions are still not entirely well constrained.

In this study, we selected eight synthetic Prp-Alm solid solution samples (Prp_9Alm_{91}, $Prp_{23}Alm_{76}$, $Prp_{31}Alm_{68}$, $Prp_{48}Alm_{52}$, $Prp_{57}Alm_{43}$, $Prp_{67}Alm_{32}$, $Prp_{78}Alm_{22}$, and $Prp_{87}Alm_{12}$) for the synchrotron SCXRD measurements up to ~20 GPa and four Prp-Alm solid solution samples ($Prp_{14}Alm_{86}$, $Prp_{31}Alm_{68}$, $Prp_{48}Alm_{52}$, and $Prp_{67}Alm_{32}$) for the synchrotron SCXRD measurements up to ~20 GPa and 700 K. Based on the obtained thermoelastic parameters of the systematic Prp-Alm solid solutions, we discussed the effects of composition (Mg^{2+}-Fe^{2+} substitution) on the thermoelastic parameters of Prp-Alm solid solutions. Finally, we used these results to calculate the P_e in two host-inclusion systems and discussed the effects of the thermoelastic parameters of Prp-Alm-rich garnet on the results of P_e calculations.

SAMPLES AND EXPERIMENTAL METHODS

The single crystals of Prp-Alm solid solutions (Prp_9Alm_{91}, $Prp_{14}Alm_{86}$, $Prp_{23}Alm_{76}$, $Prp_{31}Alm_{68}$, $Prp_{48}Alm_{52}$, $Prp_{57}Alm_{43}$, $Prp_{67}Alm_{32}$, $Prp_{78}Alm_{22}$, and $Prp_{87}Alm_{12}$) used in this study were synthesized at *HP–HT* conditions using a multi-anvil pressure apparatus (YJ-3000t) at the Institute of Geochemistry, Chinese Academy of Sciences, Guiyang, China. The detailed information about the garnet sample synthesis and subsequent compositional and structural analysis are described by Kuang et al. (2019). In general, with the increasing Alm content, the typical size of granular Prp-Alm crystals increases from ~60 μm to more than 100 μm. The Prp-Alm solid solutions with good euhedral crystals, high quality, and without inclusions were selected for the SCXRD experiments. We successively double-side polished our sample pieces to ~20–30 μm thickness, using the 3M diamond lapping films with grain size from coarse to a final 1 μm. The polished platelets were then cleaved into several square pieces of the desired size (~40–60 μm) for SCXRD experiments.

High pressure and room temperature (*HP–RT*) SCXRD experiments were conducted on eight Prp-Alm solid solution samples using three short symmetrical DACs (cell-1: Prp_9Alm_{91}, $Prp_{31}Alm_{68}$, $Prp_{48}Alm_{52}$; cell-2: $Prp_{57}Alm_{43}$, $Prp_{67}Alm_{32}$, $Prp_{78}Alm_{22}$, and $Prp_{87}Alm_{12}$, and cell-3: $Prp_{23}Alm_{76}$). Rhenium (Re) gaskets of ~250 μm thickness were pre-indented to ~65 μm thickness using a pair of 500-μm culet size diamond anvils. Subsequently, a ~300-μm-diameter cylindrical hole was drilled in the pre-indented area as the sample chamber. The selected single-crystal platelets with diameters of ~40–60 μm were then placed into the sample chamber together with gold powder, which served as the pressure standard (Fei et al., 2007). The diffraction patterns of gold were collected before and after sample data collection for each pressure, and the average pressure values were used for the EoS fitting. A small ruby sphere of ~10 μm was also loaded into each DAC sample chamber and used as the pressure indicator during the neon gas-loading. The neon pressure medium was loaded into the sample chamber using the gas-loading system at GeoSoilEnviroCARS (GSECARS) (Rivers et al., 2008). After the neon gas loading, the diameter of the sample chamber was ~220 μm.

HP–HT SCXRD experiments were carried out using an externally heated DAC (EHDAC) equipped with an alumina ceramic heater coiled with two Pt wires of 200 μm in diameter and 48 cm length (Kantor et al., 2012; Fan et al., 2019a). A rhenium foil was used as the gasket material and pre-indented to ~60 μm thickness using a pair of diamond anvils with 500-μm culet size and then a 300-μm-diameter sample chamber was drilled at the center of pre-indentation. The selected single-crystal platelets ($Prp_{14}Alm_{86}$, $Prp_{31}Alm_{68}$, $Prp_{48}Alm_{52}$, and $Prp_{67}Alm_{32}$) with a diameter of ~40 μm were loaded into the sample chamber together with gold powder, which served as the pressure standard at *HP–HT* conditions. For each *P–T* point, the diffraction patterns of gold were collected before and after sample data collection, and the average pressure values were used. Likewise, a small ruby sphere of ~10 μm was loaded as the pressure indicator for the gas-loading with neon as the pressure transmitting medium using the GSECARS gas-loading system. Heating was carried out by a resistance-heating system (Fan et al., 2010). A $Pt_{90}Rh_{10}$-Pt_{100} thermocouple was attached to one of the diamond surfaces, approximately 500 μm away from its culet, and clad with a ceramic adhesive (Resbond 920) for temperature measurements (Kantor et al., 2012). To minimize temperature instability for each heating run, we first heated the sample chamber to an expected temperature and then kept it at this temperature for 15 min. The temperatures of the sample chamber

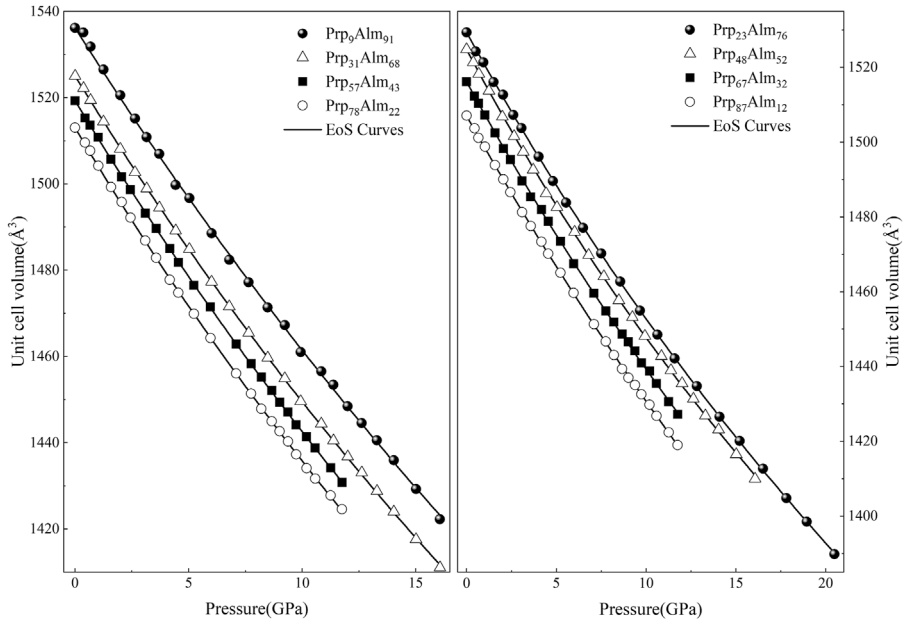

FIGURE 1 | Unit-cell volume compression of pyrope-almandine solid solution garnets at high pressure and room temperature in this study. The error bars of the data points are smaller than the symbols.

were actively stabilized within ±1 K using the temperature-power feedback program with a remotely controlled Tektronix Keithley DC power supply during the experiments (Sinogeikin et al., 2006).

Both of the *HP–RT* and *HP–HT* synchrotron SCXRD experiments were conducted at the 13-BMD beamline of the GeoSoilEnviroConsortium for Advanced Radiation Sources (GSECARS) of Advanced Photon Source (APS), Argonne National Laboratory (ANL). An incident x-ray beam of 0.3344 Å wavelength focused on a $3 \times 7\ \mu m^2$ area was used to determine the unit-cell volume of Prp-Alm solid solution samples in the DACs. Diffraction images were acquired on a stationary Perkin-Elmer area detector. Tilting and rotation of the detector and the sample-to-detector distance were calibrated using ambient LaB_6 as the diffraction standard. Wide and stepped φ-rotation exposure were collected for the single-crystal samples at each loading run, with an exposure time of 2 s/deg. The φ-rotation (the opening angle of the DAC is ±15°) axis was horizontal and perpendicular to the incident x-ray direction. The diffraction images collected at each *P–T* point were analyzed using the GSE_ADA/RSV software (Dera et al., 2013).

RESULTS

Equations of State of Prp-Alm Solid Solutions at High Pressure and Room Temperature

The unit-cell volumes change with pressure at room temperature for eight Prp-Alm solid solution garnets and are presented in **Supplementary Table S1** and **Figure 1**, showing that the unit-cell volumes of Prp-Alm solid solution with increasing pressure garnets decrease systematically. Using the console program EosFit7c (Angel et al., 2014a; Gonzalez-Platas et al., 2016), the EoS parameters, including the room *P–T* volume, the isothermal bulk modulus, and its pressure derivative of these Prp-Alm solid solutions, were refined by fitting their *P–V* data using two different EoSs (Birch-Murnaghan EoS and Vinet EoS).

Birch-Murnaghan equation of state. The *P–V* relations of these Prp-Alm solid solutions have been determined by fitting their *HP–RT* data to the third-order Birch-Murnaghan EoS, which is given in the following form:

$$P = (3/2)K_0\left[\left(\frac{V_0}{V}\right)^{7/3} - \left(\frac{V_0}{V}\right)^{5/3}\right] \times \left[1 + \left(\frac{3}{4}\right)\left(K_0' - 4\right)\left[\left(\frac{V_0}{V}\right)^{2/3} - 1\right]\right], \quad (1)$$

where V_0, K_0, and K'_0 are the unit-cell volume, isothermal bulk modulus, and its pressure derivative at ambient conditions, respectively. We obtained the V_0, K_0, and K'_0 of Prp-Alm solid solutions, as shown in **Table 1**. The refined value of V_0 was within 1σ or so of the measured V_0 by XRD at ambient conditions, indicating the accuracy of the refined results (Angel, 2000). It can be found that the bulk moduli of Prp-Alm solid solutions gradually increase with increasing Alm content, especially when K'_0 was fixed at 4 (**Table 1**). Furthermore, this trend is also in agreement with the conclusion of Huang and Chen (2014) and Milani et al. (2015).

TABLE 1 | Bulk moduli and their first pressure derivative of garnets along the Prp-Alm join.

Composition	V_0 (Å^3)	K_0 (GPa)	K'_0	EoS
Prp_9Alm_{91}	1,537.3 (2)	178.1 (9)	4 (fixed)	BM[a]
	1,537.6 (2)	174 (3)	4.8 (5)	
	1,537.6 (3)	174 (3)	4.8 (5)	Vinet[b]
$Prp_{23}Alm_{76}$	1,529.0 (1)	178.8 (5)	4 (fixed)	BM
	1,528.9 (1)	181 (2)	3.7 (2)	
	1,528.9 (1)	181 (2)	3.8 (3)	Vinet
$Prp_{31}Alm_{68}$	1,525.06 (2)	177.9 (4)	4 (fixed)	BM
	1,525.06 (2)	177 (1)	4.2 (3)	
	1,525.06 (2)	177 (1)	4.2 (2)	Vinet
$Prp_{48}Alm_{52}$	1,524.0 (2)	175.8 (8)	4 (fixed)	BM
	1,524.6 (2)	167 (2)	5.7 (3)	
	1,524.6 (2)	167 (2)	5.8 (3)	Vinet
$Prp_{57}Alm_{43}$	1,519.3 (1)	174.1 (5)	4 (fixed)	BM
	1,519.3 (2)	174 (2)	4.0 (4)	
	1,519.3 (2)	174 (2)	4.0 (4)	Vinet
$Prp_{67}Alm_{32}$	1,516.1 (1)	173.6 (5)	4 (fixed)	BM
	1,516.1 (2)	172 (2)	4.2 (4)	
	1,516.1 (2)	172 (1)	4.3 (4)	Vinet
$Prp_{78}Alm_{22}$	1,513.04 (3)	171.4 (3)	4 (fixed)	BM
	1,513.05 (3)	169 (2)	4.5 (4)	
	1,513.05 (3)	169 (2)	4.6 (4)	Vinet
$Prp_{87}Alm_{12}$	1,507.4 (1)	172.6 (5)	4 (fixed)	BM
	1,507.3 (2)	174 (2)	3.7 (4)	
	1,507.3 (2)	174 (2)	3.7 (4)	Vinet

[a]*BM: Birch-Murnaghan EoS.*
[b]*Vinet: Vinet EoS.*
Numbers in parentheses represent standard deviations.

Vinet equation of state. We also analyzed the *P*–*V* data using the Vinet EoS (Vinet et al., 1986), which is derived from a "universal equation" for solids and is represented as follows:

$$P(V) = 3K_0 y^{-2}(1-y)exp[\eta_0(1-y)], \quad (2)$$

where $y = x^{1/3}$, $x = V/V_0$, and $\eta_0 = (3/2)$ $(K'\ 0\text{-}1)$. Analyses of **Equation 2** yielded V_0, K_0, and K'_0 for the Prp-Alm solid solutions (**Table 1**), which are reasonably consistent with those derived by fitting to the Birch-Murnaghan EoS.

Supplementary Table S2 summarizes the bulk moduli and their pressure derivatives for Prp and Alm endmembers and their solid solutions determined with various experimental techniques. As shown in **Supplementary Table S2**, the K_0 values of Prp endmember from the literature range from 163.7 (17) to 175 (2) GPa. Among them, Milani et al. (2015) reported the least value (163.7 GPa) due to their largest K'_0 value (6.4) than those of other studies (4.3–4.6). There is a trade-off between the bulk modulus and its pressure derivative, which negatively correlates (Gatta et al., 2011). So, we obtained the confidence ellipses of K_0 and K'_0 for pyrope from previous XRD studies, as shown in **Figure 2**. From **Figure 2**, we can see that the previous XRD results of pyrope all fall within the 68.3% (1σ) confidence interval, with mean values of 171 (8) GPa and 4 (2) for K_0 and K'_0, respectively. Meanwhile, the obtained K_0 of pyrope [170.0 (2)–175 (2) GPa] by using Brillouin light spectroscopy (BLS) and ultrasonic interferometry (UI) methods are also consistent with the results from the XRD method (**Supplementary Table S2** and **Figure 2**). For the Alm endmember, the K_0 value [172.6 (15) GPa] obtained by Milani et al. (2015) was also smaller than other XRD results [179 (3)–185 (3) GPa]. The main reason remains that the K'_0 value (5.6) obtained by Milani et al. (2015) is higher than those of other studies (4–4.2). Moreover, Arimoto et al. (2015) reported that the K_0 value [174.2 (12) GPa] of Alm endmember using the UI method is slightly smaller than the result [179 (3) GPa] using the XRD method.

As a comparison, until now, the previous EoS studies on the Prp-Alm solid solutions are relatively limited. Huang and Chen (2014) measured three synthetic Prp-Alm solid solutions ($Prp_{83}Alm_{17}$, $Prp_{54}Alm_{46}$, and $Prp_{30}Alm_{70}$) by the XRD method up to 7, 21, and 19 GPa, respectively. With fixed K'_0 at 4.3, the K_0 obtained for these three samples were 172 (4), 174 (2), and 183 (2) GPa, respectively. Subsequently, Milani et al. (2015) reported a significantly smaller value [167.2 (17) GPa], also using the XRD method for synthetic $Prp_{60}Alm_{40}$. As a consequence, the previous experimental studies indicated that the K_0 range along the Prp-Alm solid solutions from Prp to Alm endmembers is expected to be 163.7 (1)–185 (3) GPa (**Supplementary Table S2**). Our results show that the bulk moduli of our eight Prp-Alm solid solutions (**Table 1**) are within this range. Because the bulk modulus and its pressure derivative have a negative correlation of bulk modulus and its pressure derivative, the K'_0 is permanently fixed at 4 for the following discussion of the relationship between the bulk moduli of Prp-Alm solid solutions and their compositions. **Figure 3** shows the bulk moduli of Prp-Alm solid solutions as a function of composition, and we can observe that the compressibilities of Prp-Alm solid solutions increase with increasing Prp concentrations. Furthermore, by linear fitting of the results in this study, the bulk moduli of the Prp-Alm solid solutions as a function of Prp content can be expressed by K_0 (GPa) = 181.0 (8)–0.11(1) X_{prp} (R^2 = 0.91, K'_0 fixed at 4). It is worth noting that the K_0 of most previous studies are in harmony with our fitting line, except for Milani et al. (2015) (**Figure 3**). It may be attributed to the

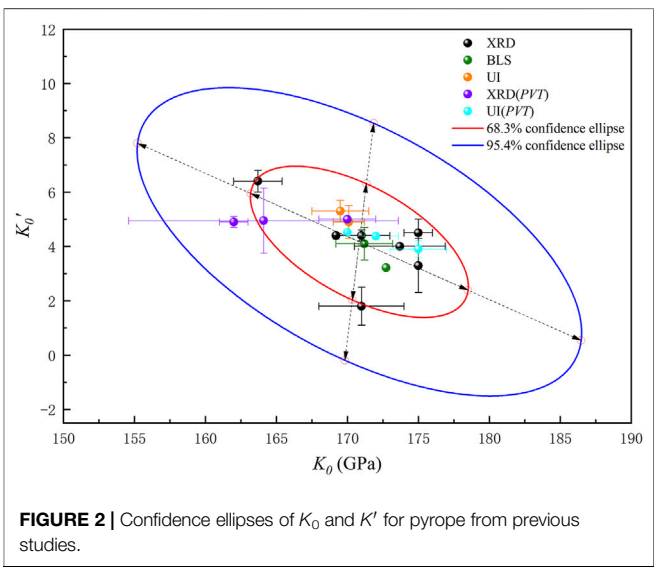

FIGURE 2 | Confidence ellipses of K_0 and K' for pyrope from previous studies.

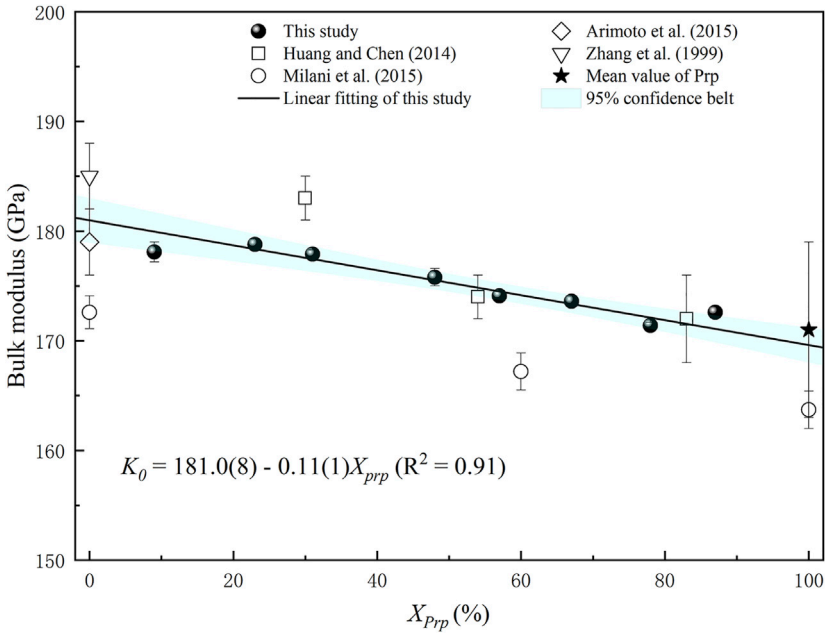

FIGURE 3 | Bulk moduli of pyrope-almandine solid solution garnets as a function of pyrope content.

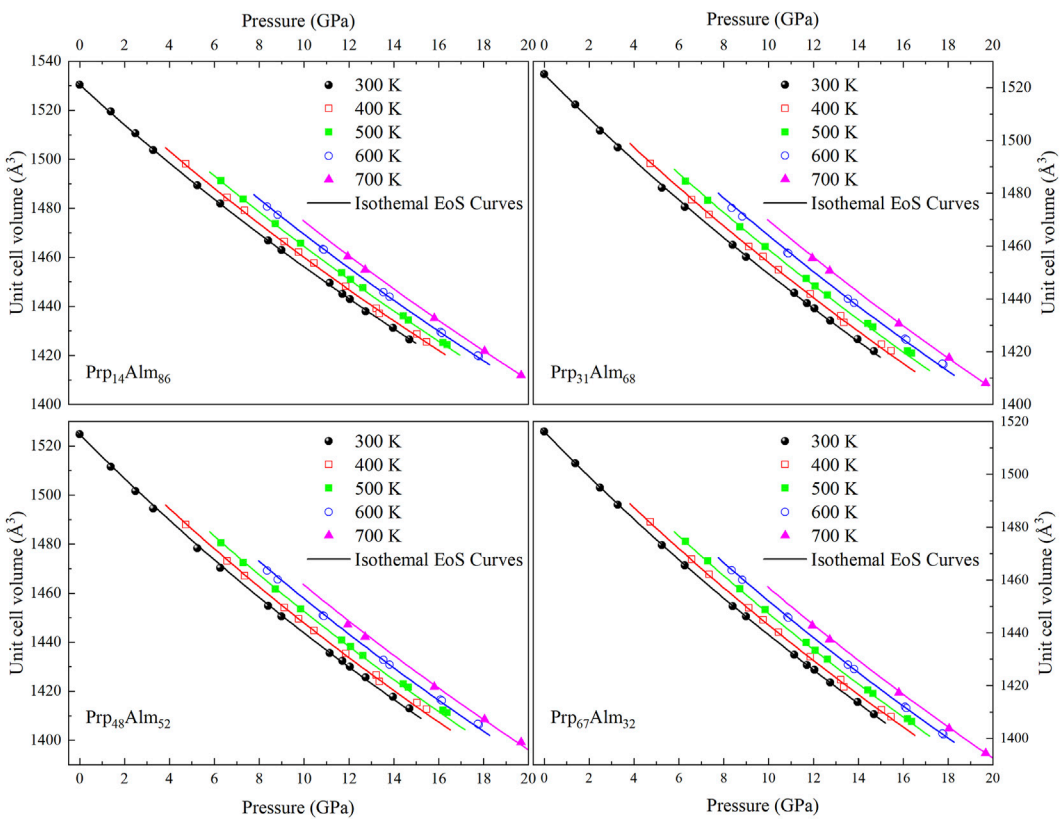

FIGURE 4 | The unit-cell volume of pyrope-almandine solid solution garnet as a function of pressure and temperature. The lines represent the isothermal compression curve from fitting HTBM EoS at 300, 400, 500, 600, and 700 K. The error bars of the data points are smaller than the symbols.

TABLE 2 | Thermoelastic parameters of garnets along the Prp-Alm join, as compared with previous studies.

Composition	V_0 (Å^3)	K_0 (GPa)	K'_0	α_{300} (10^{-5} K^{-1})	θ_E (K)	$\partial K/\partial T$ (GPaK^{-1})	References
$Prp_{14}Alm_{86}$	1,530.5 (1)	184.7 (9)	3.6 (1)	2.95 (5)	560.8	–	This study
	1,530.69 (9)	181.9 (4)	4[a]	3.00 (5)	560.8	–	–
$Prp_{31}Alm_{68}$	1,525.05 (2)	171.6 (6)	5.4 (1)	3.59 (4)	507.2	–	–
	1,525.02 (5)	179.1 (4)	4[a]	3.45 (8)	507.2	–	–
$Prp_{48}Alm_{52}$	1,524.5 (3)	158 (1)	5.6 (2)	3.63 (5)	465.6	–	–
	1,522.5 (2)	169.9 (6)	4[a]	3.37 (6)	465.6	–	–
$Prp_{67}Alm_{32}$	1,516.1 (2)	172 (1)	4.2 (1)	3.30 (4)	406.4	–	–
	1,515.9 (1)	173.8 (4)	4[a]	3.27 (4)	406.4	–	–
Prp_{100}	1,504.64 (4)	–	–	2.543 (5)	–	–	Milani et al. (2015)
Prp_{100}	1,503.1 (5)	170 (2)	5[a]	2.58 (28)	–	–0.020 (3)	Wang et al. (1998)
Prp_{100}	1,500 (2)	167 (3)	4.6[a]	2.89 (33)	–	–0.021 (9)	Zou et al. (2012)
Alm_{100}	1,531.05 (7)	179 (3)	4[a]	3.3 (9)	–	–0.043 (14)	Arimoto et al. (2015)
$Alm_{86}Prp_7Spe_7$	1,539.6 (9)	177 (2)	4[a]	3.1 (7)	–	-0.032 (16)	Fan et al. (2009)

higher K'_0 [5.6 (5)–6.4 (4)] of Milani et al. (2015) than those of others [3.9 (3)–4.61 (14)] (**Supplementary Table S2**).

Equations of State of Prp-Alm Solid Solutions at High Pressure and High Temperature

The unit-cell volumes of $Prp_{14}Alm_{86}$, $Prp_{31}Alm_{68}$, $Prp_{48}Alm_{52}$, and $Prp_{67}Alm_{32}$ at *HP–HT* conditions up to ~19.67 GPa and 700 K are shown in **Supplementary Table S3**. **Figure 4** also shows the pressure–volume–temperature (*P–V–T*) data of these Prp-Alm solid solution samples. In this study, we applied the thermal-pressure model EoS to describe the *P–V–T* behavior of Prp-Alm solid solutions. There are two ways to calculate the *P–V–T* properties of a mineral (as shown in **Figure 1** of Milani et al., 2017). One way to characterize the *P–V–T* behavior of minerals is to describe how the V_{T0}, K_{T0}, and K'_{T0} vary with temperature (at room pressure) and then use these parameters to calculate the isothermal compressibility at the high temperature (as shown by the rough path in **Figure 1** of Milani et al., 2017). A potential weakness of this method is that the variation of K'_{T0} with temperature has rarely been measured, where K'_{T0} should increase slightly with increasing temperature, rather than not change with temperature, as the common assumption. Additionally, this assumption, coupled with the approximation that dK_{T0}/dT is a constant, has often given rise to a non-physical negative coefficient of thermal expansion for many materials at reasonably moderate pressures (Helffrich and Connolly, 2009).

Furthermore, the maximum experimental temperature of only 700 K in this study and the relatively limited number of high-temperature data points make the fitting of the thermal expansion coefficient at high temperatures more inaccurate. Therefore, we employ the concept of thermal pressure (Anderson, 1995) to describe the *P–V–T* behavior of Prp-Alm solid solutions. Then, as shown by the thin path in **Figure 1** of Milani et al., 2017, the *P* at a given *V* and *T* can be expressed as the sum of two terms:

$$P(V,T) = P\left(V, T_{ref}\right) + P_{th}(T), \quad (3)$$

The $P(V, T_{ref})$ is the isothermal EoS for minerals at the reference temperature, up to the volume at *P* and T_{ref}. The thermal-pressure $Pth(T)$ is the pressure generated by raising the temperature from T_{ref} to *T* at a constant volume, which is the isochor of the mineral passing through the final *P–T* point. Details of the employment of a thermal-pressure EoS and any necessity assumptions have been reviewed by Milani et al. (2017). In this study, we used the Birch-Murnaghan isothermal EoS in combination with the Holland and Powell (2011) model of thermal-pressure EoS to determine the thermoelastic parameters of four Prp-Alm solid solutions, as shown in **Table 2**. All described in this study have been performed with the EosFit7c program (Angel et al., 2014a; Gonzalez-Platas et al., 2016). The Einstein temperature, θ_E, of Prp-Alm solid solutions in this study are calculated from the values of the pyrope (320 K) and almandine (400 K) and according to the ideal solution model (Milani et al., 2015). The V_0 and K_{T0} derived from *HP–HT* data were roughly consistent with that from *P–V* data at room temperature, especially as the K'_{T0} was fixed at 4 (**Table 1** and **Table 2**).

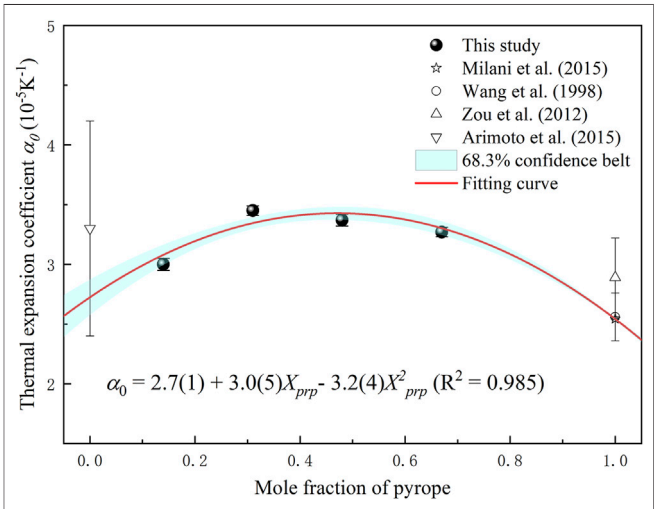

FIGURE 5 | The thermal expansion coefficient of pyrope-almandine solid solution garnet at 300 K as a function of pyrope content.

Figure 5 shows the thermal expansion coefficient at ambient conditions (α_0) of four Prp-Alm solid solutions in this study, combined with the results from previous studies. As shown in

Figure 5, there is a non-linear correlation between α_0 and the Prp content of the Prp-Alm solid solution. The α_0 of Prp-Alm solid solution varies with the composition getting a parabola. At ambient conditions, Prp-Alm solid solution with intermediate composition demonstrates a larger α_0 than the composition close to endmember, the maximum variation in the α_0 from $Prp_{14}Alm_{86}$ to $Prp_{48}Alm_{52}$ is about 23%. The α_0 of the Prp-Alm solid solutions as a function of Prp content can be expressed by α_0 ($10^{-5}K^{-1}$) = 2.7 (1) + 3.0 (5) X_{Prp} − 3.2 (4) X^2_{Prp} (R^2 = 0.985).

DISCUSSION

Mg^{2+}-Fe^{2+} Substitution Effect on Bulk Moduli of Prp-Alm Solid Solutions

Among previous studies about the compositional effect on bulk modulus of different mineral groups, minerals with Mg^{2+}-Fe^{2+} solid solutions have been extensively investigated because of their importance in understanding the composition and dynamic property of the Earth's interior (Takahashi and Liu, 1970; Zhang J. et al., 1998; Zhang et al., 1999; Speziale et al., 2004; Huang and Chen, 2014). The Fe and Mg component dependence of bulk modulus in mantle minerals is interesting for modeling the mineralogical composition of the mantle and mineral crystal chemistry. Anderson and Anderson (1970) proposed a simple bulk modulus (K_0)–volume (V_0) systematics, where K_0V_0 = constant. However, for most of the ferromagnesian silicates and carbonates that have been studied so far, the bulk modulus appears to increase with increasing Fe content, such as garnet (Huang and Chen, 2014), olivine (Speziale et al., 2004), and siderite (Zhang J. et al., 1998), which is inconsistent with bulk modulus–volume systematics. To sum up, it is necessary to understand the Mg^{2+}-Fe^{2+} substitution effect on the bulk modulus of garnet.

Figure 3 shows the bulk moduli of Prp-Alm solid solutions as functions of compositions in this study and compared with those of previous studies. Mg^{2+}-Fe^{2+} substitution results in a nearly linear decrease of the bulk modulus. The reduction of bulk moduli from Prp_9Alm_{91} to $Prp_{87}Alm_{12}$ is ~3%, mainly consistent with the ~6% decrease from $Prp_{30}Alm_{70}$ to $Prp_{83}Alm_{17}$ reported by Huang and Chen (2014).

The bulk moduli of minerals are mainly controlled by their constituent polyhedral compressibilities, primarily determined by the mean cation–oxygen bond length in the polyhedral (Hazen et al., 1994). Many previous high-pressure studies have shown that the SiO_4 tetrahedrons of silicate minerals are essentially rigid units (Robinson et al., 1971; Zhang et al., 1997; Xu et al., 2017). The selected bond distances of Prp-Alm solid solutions at the ambient condition (data from Kuang et al., 2019) as functions of composition are shown in **Figure 6**. Inspection of **Figure 6** demonstrates that the $d_{<M\text{-}O>}$ (M is the divalent cations in X-site) decreases significantly with the increasing Prp content, mainly due to the smaller effective ionic radius of Mg^{2+} (0.89 Å) in eightfold coordination than that of Fe^{2+}(0.92 Å) (Shannon, 1976). In contrast, the average $d_{<Si\text{-}O>}$ of the SiO_4 tetrahedron and $d_{<Al\text{-}O>}$ of the AlO_6 octahedron change negligibly with increasing Prp mol%. These results imply that the compressibility of the MO_8 dodecahedron mainly controls the bulk modulus of the Prp-Alm solid solution. However, other factors, such as the compressibilities of the SiO_4 tetrahedron and the AlO_6 octahedron, may be secondary important to the bulk modulus of Prp-Alm solid solution.

Besides, this study shows that FeO_8 dodecahedron is less compressible than MgO_8 dodecahedron. Similar conclusions were also obtained about the structures with sixfold coordinated Mg^{2+} and Fe^{2+} cations (Zhang et al., 1997), implying that the bonding character plays an essential role in such anomalous compression, whereas structure type and polyhedral coordination may be less critical. Furthermore, the electronegativity of the element, which describes the ability of an atom to attract electrons, may be an essential factor for the bonding character. The electronegativity of Mg (1.31) is distinctly smaller than that of Fe (1.83) (Allred, 1961), resulting in the less compressible FeO_8 dodecahedron than MgO_8 dodecahedron.

Moreover, Hazen et al. (1994) suggested that the SiO_4 octahedra and AlO_6 tetrahedra framework may also dictate the bulk modulus of garnet. Subsequently, Zhang L. et al. (1998) showed that the kinking degree of the Si-O-Al angle decreased continuously with increasing pressure, and the Si-O-Al angle in Alm is less kinked than that in Prp over the same pressure range (Zhang et al., 1999). Furthermore, the Raman spectroscopy results of Kuang et al. (2019) show that both the stretching motions of Si-O and the rotation motions of SiO_4 decreased linearly with increasing Alm content. Thus, the degree of distortion and rotation of SiO_4 may also affect the bulk moduli of the Prp-Alm solid solutions.

To sum up, the bulk moduli of Prp-Alm solid solutions are primarily governed by the compressibility of MO_8 dodecahedra. The difference in the compressibilities of MO_8 can be attributed to the different effective ionic radius and electronegativities of the Mg and Fe atoms. Also, the kinking degree of the Si-O-Al angle and the distortion and rotation of SiO_4 may affect the bulk moduli of Prp-Alm solid solutions.

Mg^{2+}-Fe^{2+} Substitution Effect on Thermal Expansion Coefficient of Prp-Alm Solid Solutions

Contrary to the effect of Mg^{2+}-Fe^{2+} substitution on the bulk modulus of Prp-Alm solid solutions, the α_0 of Prp-Alm solid solutions varies with the composition forming a parabola. As shown in **Figure 5**, at ambient temperatures, the composition of the Prp-Alm solid solution near the intermediate composition displays a larger thermal expansion coefficient than the composition near the endmember. While the causes of this result are yet to be revealed, we think that the most likely reason is the local arrangement of $Mg^{2+}$and Fe^{2+}. For the garnet, the different-sized divalent cations substitution on the dodecahedral site can make its thermodynamic properties (e.g., volume, enthalpy, entropy, free energy, etc.) deviate from the ideal mixing results (Bosenick et al., 2001; Vinograd et al., 2004; Dachs et al., 2014; Du et al., 2016). Besides, the magnitude of the non-ideal mixing is correlated with the size difference between

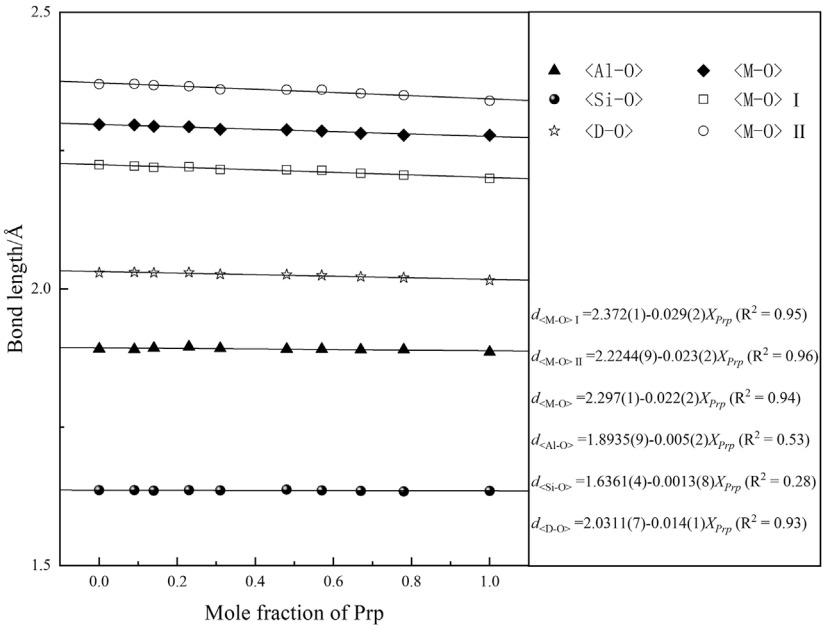

FIGURE 6 | The bond length of the pyrope-almandine solid solution garnet at ambient conditions as a function of pyrope content.

the substituting cations on the dodecahedral site (Geiger and Rossman, 1994). The study on the local structure of the pyrope-grossular garnet solid solution shows that the Mg/Ca substitution can produce significant amounts of short-range order rather than long-range order in garnets (Bosenick et al., 2000). Furthermore, the compositions near $Prp_{50}Grs_{50}$ depart most strongly from random mixing, and all the compositions tend to random disorder at high temperatures. Although the size difference between Mg^{2+} (0.89Å) and Fe^{2+} (0.92Å) is smaller than that between $Mg^{2+}$and Ca^{2+} (1.12 Å) (Shannon, 1976), the influence on the local arrangement by the Mg/Fe substitution cannot be overlooked. It is speculated that local disorder caused by the Mg/Fe substitution is the main reason for a non-linear relationship between thermal expansion coefficient and the composition of the Prp-Alm solid solution.

IMPLICATIONS FOR ELASTIC GEOBAROMETER

It is ordinary to use host-inclusion systems to infer the geological history of a mineral or a rock (Guiraud and Powell, 2006). The history of study on elastic geobarometers can be traced back to the 1980s. Roedder and Bodnar (1980) made the first estimation for the formation pressure of minerals from the fluid inclusions in them. The basic principle is that when the host mineral captures the fluid, it experiences a different *P–T* path than the host mineral because its volume is limited by the space inside the mineral and is subjected to the pressure exerted on it by the host mineral during subsequent changes in temperature and pressure conditions. In turn, this difference and its associated physicochemical properties can be used to estimate the *P–T* conditions experienced by the host mineral. This principle is not only applicable to fluid/melt inclusions but also to other solid mineral inclusions within the mineral that differ from its thermoelastic properties. This method underwent significant developments in the past decade and is gradually gaining the interest of geologists (e.g., Murri et al., 2018; Alvaro et al., 2019; Anzolini et al., 2019; Bonazzi et al., 2019; Gonzalez et al., 2019; Mazzucchelli et al., 2019; Moulas et al., 2020).

The pressure estimation by an elastic geobarometer has some prerequisite assumptions (Bonazzi et al., 2019): (1) The inclusions are in the same pressure environment as the host mineral at the time of capture, and the inclusions fill the vacancies entirely within the host mineral. (2) The host mineral and the inclusions are always reversibly and elastically deformed after capture. In this way, the captured pressure can be estimated by measuring the residual pressure of the inclusions due to the difference in elastic properties between the two minerals under normal temperature and pressure conditions and by combining the equation of the state of the two minerals. In this study, the method for estimating the pressure is based on entrapment isomekes proposed by Angel et al. (2017b). Entrapment isomekes is a single *P–T* path along which the fractional volume change in host and inclusion are equal (Gonzalez et al., 2019). The calculation of P_e was performed with EosFit-Pinc, and the details of this method were described in Angel et al. (2017b).

As mentioned in the introduction section of this study, much of the previous work has focused on the factors affecting the calculation accuracy of the elastic geobarometer except the influence of the thermoelastic parameters of minerals. So, we selected two garnet-related host-inclusion pairs to evaluate the influence of the thermoelastic parameters of the concerned minerals on the calculated results of elastic geobarometers.

TABLE 3 | Room pressure–temperature EoS coefficients for selected minerals (Prp-Alm garnets, diamond and quartz).

Composition	K_0 (GPa)	K'_0	α_{300} (10^{-5} K^{-1})	θ_E (K)	G_0 (GPa)[a]	$\partial G/\partial P$[a]	$\partial G/\partial T$ (GPaK^{-1})[a]	References
Prp_9Alm_{91}	178.1 (9)	4 (fixed)	2.94(6)[b]	574.8[c]	94.6	1.08	–0.013	This study
$Prp_{14}Alm_{86}$	181.9 (4)	4 (fixed)	3.00 (5)	560.8[c]	94.5	1.09	–0.013	—
$Prp_{23}Alm_{76}$	178.8 (5)	4 (fixed)	3.22 (6)[b]	529.6[c]	93.3	1.10	–0.013	—
$Prp_{31}Alm_{68}$	179.1 (4)	4 (fixed)	3.45 (8)	507.2[c]	93.1	1.12	–0.013	—
$Prp_{48}Alm_{52}$	169.9 (6)	4 (fixed)	3.37 (6)	465.6[c]	93.5	1.17	–0.014	—
$Prp_{57}Alm_{43}$	174.0 (2)	4 (fixed)	3.37 (7)[b]	440.4[c]	93.3	1.20	–0.014	—
$Prp_{67}Alm_{32}$	173.8 (4)	4 (fixed)	3.27 (4)	406.4[c]	92.0	1.21	–0.014	—
$Prp_{78}Alm_{22}$	171.6 (2)	4 (fixed)	3.09 (6)[b]	381.6[c]	92.6	1.25	–0.015	—
$Prp_{87}Alm_{12}$	173.5 (2)	4 (fixed)	2.89 (6)[b]	350.4[c]	91.4	1.26	–0.015	—
Prp_{100}	163.7	6.4	2.543 (5)	320	92	1.3	–0.015	Milani et al. (2015)
Alm_{100}[d]	179 (3)	4 (fixed)	3.3 (9)	-	94.9	1.06	–0.0131	Arimoto et al. (2015)
Quartz	62.2798	5.0714	–0.047	—	—	—	—	Angel et al. (2017a)
Diamond	444 (2)	4 (fixed)	0.2672 (3)	1500	535	—	—	Angel et al. (2015)

[a]*Values were calculated by the endmember Prp and Alm result of Arimoto et al. (2015) and Fan et al. (2019b), assuming it is an ideal solid solution.*
[b]*Values were calculated by* α_{300} $(10^{-5}\ K^{-1}) = 2.7\ (1) + 3.0\ (5)\ X_{Prp} - 3.2\ (4)\ X^2_{Prp}$.
[c]*Values were calculated by the endmember Prp and Alm result of Milani et al. (2015), assuming it is an ideal solid solution.*

Quartz is generally a virtually pure endmember, and it is stable over a wide range of metamorphic conditions (Korsakov et al., 2009). Garnet has also served as a central focus of metamorphic studies to discern *P–T* paths because it can store the entire history of metamorphism by its inclusion suites such as quartz, graphite, and rutile (Ague and Carlson, 2013; Baxter et al., 2013; Caddick and Kohn, 2013). Hence, QuiG is considered a particularly useful geobarometer and has been widely used to infer the geological history of the rock from the collisional orogenic belts (Wolfe and Spear, 2018), the subduction complex (Bayet et al., 2018; Alvaro et al., 2019), and ultrahigh-pressure metamorphic complex (Korsakov et al., 2009; Gonzalez et al., 2019; Zhong et al., 2019; Moulas et al., 2020). Similarly, as the primeval samples from inaccessible regions of Earth, diamonds and their inclusions provide direct information of deep Earth's evolution. This information is precious if it can be combined with depth estimates (Anzolini et al., 2019). An estimate of their formative pressure (depth of provenance) can be used to constrain and understand the environment in which they formed. Therefore, the thermoelastic parameters of the minerals play a crucial role in determining the accuracy of the pressure calculation. The garnet, a widespread mineral solid solution in nature, can have varying elastic properties depending on its composition (Du et al., 2015; Fan et al., 2017; Fan et al., 2018; Xu et al., 2019). In most cases, however, the thermoelastic properties used for calculation are the results of the endmember garnet (Milani et al., 2015; Gonzalez et al., 2019; Zhong et al., 2019), or assumed that the solid solution is isotropic and ideal (Johnson et al., 2021). Based on the results of this study, the thermoelastic properties of the Prp-Alm solid solutions may not follow the ideal mode (e.g., **Figure 5**). Therefore, the thermoelastic properties of garnet estimated from the endmember components may cause divergence. It is necessary to discuss the influence of garnet composition on the accuracy of these two elastic geobarometers.

These calculations utilized the thermoelastic coefficients of quartz with a curved α-β transition (Angel et al., 2017a) and the thermoelastic coefficients of the diamond from Angel et al. (2015). The shear modulus and its *P* and *T* derivative of Prp-Alm garnet were calculated by combining the results of the endmembers pyrope and almandine in proportion to their measured abundances, assumed as an ideal solid solution (Arimoto et al., 2015; Fan et al., 2019b). The final full set of thermoelastic coefficients for the P_e estimation are shown in **Table 3**.

Firstly, the uncertainties of the thermoelastic properties of garnets in the QuiG application should be considered. Here, we take the $Prp_{14}Alm_{86}$ garnet to demonstrate the effect of the uncertainties in thermoelastic properties. We chose 0.65 GPa as the P_{inc} obtained by laser Raman spectroscopy for quartz inclusions in garnet from eclogite for our P_e estimation (Zhong et al., 2019). **Supplementary Table S4** lists the calculated P_e for $Prp_{14}Alm_{86}$ considering the uncertainties of the thermoelastic properties. Compared to the bulk modulus, the thermal expansion coefficient in this study has the most considerable effect in calculated P_e (**Figure 7A**). A 1.7% uncertainty in the value of α_0 of garnet

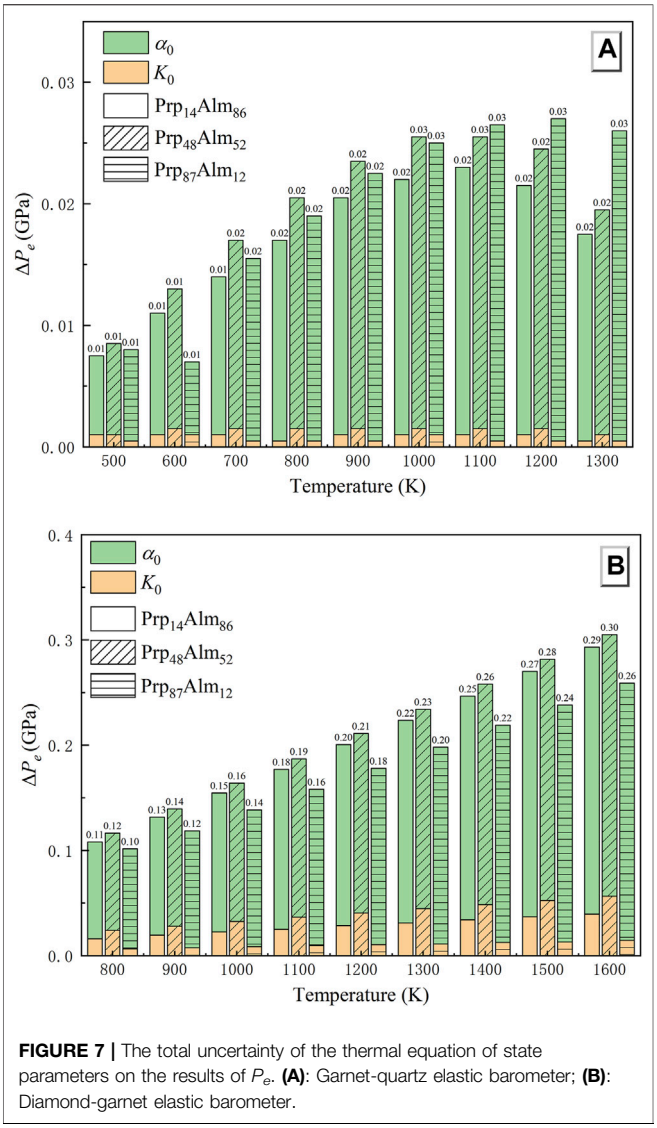

FIGURE 7 | The total uncertainty of the thermal equation of state parameters on the results of P_e. **(A)**: Garnet-quartz elastic barometer; **(B)**: Diamond-garnet elastic barometer.

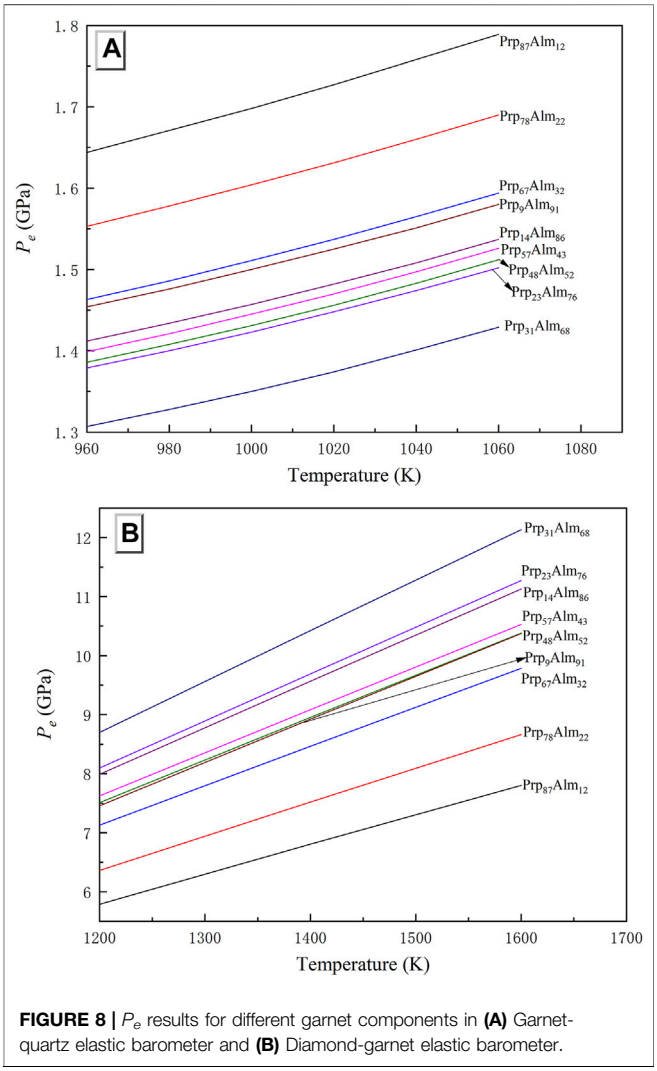

FIGURE 8 | P_e results for different garnet components in **(A)** Garnet-quartz elastic barometer and **(B)** Diamond-garnet elastic barometer.

changes the P_e by ~0.007 GPa at 500 K, and with the temperature rising, it makes the P_e change ~0.016 GPa at 1300 K. The accuracy of bulk modulus obtained in this study has almost no effect on the P_e estimation. A 0.22% uncertainty in the value of K_0 of garnet changes the P_e by only 0.001 GPa. In conclusion, the maximal error caused by the thermoelastic properties of garnet on P_e estimation is less than 0.02 GPa (**Figure 7A**). Besides, as shown in **Figure 7A**, we have calculated the P_e of the other two garnets with different components ($Prp_{48}Alm_{52}$ and $Prp_{87}Alm_{12}$), and the results obtained are consistent with the $Prp_{14}Alm_{86}$.

For the P_e calculations of the diamond–garnet pair, we assume a residual pressure P_{inc} on the garnet inclusion of 0.2 (1) GPa, and we use the thermoelastic properties given in **Table 3**. **Supplementary Table S5** lists the calculated P_e for $Prp_{14}Alm_{86}$. The conclusions drawn from **Supplementary Table S5** and **Figure 7B** are that a 0.22% uncertainty of K_0 may contribute an error of ~0.03 GPa to the calculated P_e. Same as in QuiG, the thermal expansion coefficient in this study has the most considerable effect in the calculated P_e of the diamond–garnet system (**Figure 7B**). A 1.7% uncertainty in the value of α_0 of garnet changes the P_e by ~0.092 GPa at 800 K, and with the temperature rising, it makes the P_e change ~0.254 GPa at 1600 K. The maximal error caused by the thermoelastic properties of garnet in the diamond–garnet system is ~0.3 GPa at 1,600 K (**Figure 7B**). It can be found that for the same garnet composition, the P_e change caused by the uncertainties of its thermoelastic properties is unequal in the two types of elastic geobarometers. The P_e change in the diamond–garnet pair is almost ten times as large as it is in QuiG.

Here, the Pyp-Alm garnets of different compositions (**Table 3**) are used to calculate the P_e, and the results of two elastic geobarometers are shown in **Figures 8A,B**. The effect of garnet composition on the predicted entrapment pressure is relatively large, especially for the diamond–garnet system (**Figure 8B**). At 1,400 K, the different compositions of garnet can cause a variation of P_e up to 4.5 GPa in the diamond–garnet system. In the QuiG, the difference of inferred entrapment pressure may reach ca. 0.35 GPa at 1,060 K. As mentioned

above, this is mainly due to the distinct thermal expansion coefficient among them.

To sum up, even though the procedure of applying an elastic barometer to host-inclusion mineral systems requires several steps that involve various assumptions (Angel et al., 2015), and there are lots of possible factors that could influence the precision and accuracy of calculated P_e value as mentioned above, its advantages could not be ignored. Much previous work suggested that QuiG, and diamond–garnet elastic barometer, may preserve different aspects of garnet history in complex terranes (Wolfe and Spear, 2018; Alvaro et al., 2019; Spear and Wolfe, 2020; Johnson et al., 2021). The advantages of QuiG or other inclusion-based methods are relatively easy to apply and require far less data acquisition than conventional methods. Our results suggest that the entrapment pressure may be significantly influenced by the thermoelastic parameters of garnet, which is selected to have a different component from the research sample, while the thermal expansion coefficient is the main influencing factor for the elastic barometer to P_e estimation, compared with other thermoelastic parameters. Therefore, the effect of the composition of garnet on the P_e estimation could not be ignored. Furthermore, one factor that must not be overlooked is the effect of viscous relaxation, which occurs very rapidly at temperatures >110 K (Moulas et al., 2020) and the preserved P_e may then be a reflection of re-equilibration (Zhong et al., 2020). In the future application of elastic barometer, as the most common garnet component in the Earth, the thermoelastic parameters (especially the thermal expansion coefficient) of the pyrope-almandine-grossular ternary solid solutions must also be considered.

CONCLUSION

In summary, the thermoelastic parameters of systematic Prp-Alm solid solutions were obtained by fitting the P–V–T or P–V data to the EoS and compared with previous studies. The relationship between the bulk moduli of the Prp-Alm solid solutions and Prp content can be expressed as K_0 (GPa) = 181.0 (8) − 0.11 (1) X_{prp} (R^2 = 0.91, K'_0 fixed at 4). Our results demonstrate that the Prp content will decrease the incompressibilities of Prp-Alm solid solutions, which is inconsistent with bulk modulus–volume systematics: K_0V_0 = constant. The possible reasons for this difference may be multiple and complicated. In our view, the most likely reason is the larger compressibility of MgO_8 than that of FeO_8. Also, the kinking degree of the Si-O-Al angle and the degree of distortion and rotation of SiO_4 may affect the compressibilities of the Prp-Alm solid solutions. The thermal expansion coefficient with the component of Prp-Alm solid solution also has a relational expression, α_0 ($10^{-5}K^{-1}$) = 2.7 (1) + 3.0 (5) X_{Prp} − 3.2 (4) X^2_{Prp} (R^2 = 0.985), where the Prp-Alm solid solutions with intermediate composition show a larger coefficient than the endmembers at ambient condition. Furthermore, for two types of elastic geobarometers, we evaluate the correlation of the uncertainties of thermoelastic properties with P_e estimation accuracy. Compared with bulk modulus, the thermal expansion coefficient has the main effect on the estimation of P_e. The P_e change caused by the uncertainties of thermoelastic properties of garnets in the diamond–garnet pair is almost 10 times larger than it is in QuiG. Besides, by calculating P_e with different garnet components, the result suggests that the garnet component may significantly influence entrapment pressure, especially in the diamond–garnet system and the pyrope-almandine-grossular ternary solid solutions EoS must also be considered in the future study.

DATA AVAILABILITY STATEMENT

The original contributions presented in the study are included in the article/**Supplementary Material**, further inquiries can be directed to the corresponding author.

AUTHOR CONTRIBUTIONS

Conceptualization and methodology, DF and WZ; investigation, BL, JX, ST, and VP; sample source, BL and WZ; experimental analysis, BL, JX, DF, and WZ; writing—original draft preparation, BL; writing—review and editing, DF, WZ, JJ, JX, BL, ZY, SH, WG, and YZ; plotting, BL; software, BL and JX. All authors have read and agreed to the published version of the manuscript.

FUNDING

This project was supported by the National Natural Science Foundation of China (Grant Nos. 41802043, U2032118, and 42172048), the Youth Innovation Promotion Association CAS (DF, 2018434), the Chinese Academy of Sciences "Light of West China" Program (2019), the Science and Technology Foundation of Guizhou Province (QKHJC-ZK (2021) ZD042), and the Innovation and Entrepreneurship Funding of High-Level Overseas Talents of Guizhou Province (DF, (2019) 10).

ACKNOWLEDGMENTS

We acknowledge Wei Chen and Yunqian Kuang for the High P–T experiments assistance. The experimental works were conducted at the GeoSoilEnviroCARS (Sector 13), Advanced Photon Source (APS), and Argonne National Laboratory.

SUPPLEMENTARY MATERIAL

The Supplementary Material for this article can be found online at: https://www.frontiersin.org/articles/10.3389/feart.2021.833405/full#supplementary-material

REFERENCES

Ague, J. J., and Carlson, W. D. (2013). Metamorphism as Garnet Sees it: The Kinetics of Nucleation and Growth, Equilibration, and Diffusional Relaxation. *Elements* 9, 439–445. doi:10.2113/gselements.9.6.439

Allred, A. L. (1961). Electronegativity Values from Thermochemical Data. *J. Inorg. Nucl. Chem.* 17, 215–221. doi:10.1016/0022-1902(61)80142-5

Alvaro, M., Mazzucchelli, M. L., Angel, R. J., Murri, M., Campomenosi, N., Scambelluri, M., et al. (2019). Fossil Subduction Recorded by Quartz from the Coesite Stability Field. *Geology* 48, 24–28. doi:10.1130/g46617.1

Anderson, D. L., and Anderson, O. L. (1970). Brief Report: The Bulk Modulus-Volume Relationship for Oxides. *J. Geophys. Res.* 75, 3494–3500. doi:10.1029/JB075i017p03494

Anderson, O. L. (1995). *Equations of State of Solids for Geophysics and Ceramic Science*. New York: Oxford University Press on Demand.

Angel, R. J., Alvaro, M., and Gonzalez-Platas, J. (2014a). EosFit7c and a Fortran Module (Library) for Equation of State Calculations. *Z. Kristallogr Cryst. Mater.* 229, 405–419. doi:10.1515/zkri-2013-1711

Angel, R. J., Alvaro, M., Miletich, R., and Nestola, F. (2017a). A Simple and Generalised P-T-V EoS for Continuous Phase Transitions, Implemented in EosFit and Applied to Quartz. *Contrib. Mineral. Petrol.* 172, 29. doi:10.1007/s00410-017-1349-x

Angel, R. J., Alvaro, M., Nestola, F., and Mazzucchelli, M. L. (2015). Diamond Thermoelastic Properties and Implications for Determining the Pressure of Formation of Diamond-Inclusion Systems. *Russ. Geol. Geophys.* 56, 211–220. doi:10.1016/j.rgg.2015.01.014

Angel, R. J. (2000). Equations of State. *Rev. Mineralogy Geochem.* 41, 35–59. doi:10.2138/rmg.2000.41.2

Angel, R. J., Mazzucchelli, M. L., Alvaro, M., and Nestola, F. (2017b). EosFit-Pinc: A Simple GUI for Host-Inclusion Elastic Thermobarometry. *Am. Mineral.* 102, 1957–1960. doi:10.2138/am-2017-6190

Angel, R. J., Mazzucchelli, M. L., Alvaro, M., Nimis, P., and Nestola, F. (2014b). Geobarometry from Host-Inclusion Systems: The Role of Elastic Relaxation. *Am. Mineral.* 99, 2146–2149. doi:10.2138/am-2014-5047

Anzolini, C., Nestola, F., Mazzucchelli, M. L., Alvaro, M., Nimis, P., Gianese, A., et al. (2019). Depth of Diamond Formation Obtained from Single Periclase Inclusions. *Geology* 47, 219–222. doi:10.1130/g45605.1

Arimoto, T., Gréaux, S., Irifune, T., Zhou, C., and Higo, Y. (2015). Sound Velocities of Fe3Al2Si3O12 Almandine up to 19 GPa and 1700 K. *Phys. Earth Planet. Interiors* 246, 1–8. doi:10.1016/j.pepi.2015.06.004

Ashley, K. T., Caddick, M. J., Steele-Macinnis, M. J., Bodnar, R. J., and Dragovic, B. (2014). Geothermobarometric History of Subduction Recorded by Quartz Inclusions in Garnet. *Geochem. Geophys. Geosyst.* 15, 350–360. doi:10.1002/2013gc005106

Ashley, K. T., Steele-Macinnis, M., Bodnar, R. J., and Darling, R. S. (2016). Quartz-in-garnet Inclusion Barometry under Fire: Reducing Uncertainty from Model Estimates. *Geology* 44, 699–702. doi:10.1130/g38211.1

Bass, J. D., Sinogeikin, S. V., and Li, B. (2008). Elastic Properties of Minerals: A Key for Understanding the Composition and Temperature of Earth's Interior. *Elements* 4, 165–170. doi:10.2113/gselements.4.3.165

Baxter, E. F., Caddick, M. J., and Ague, J. J. (2013). Garnet: Common Mineral, Uncommonly Useful. *Elements* 9, 415–419. doi:10.2113/gselements.9.6.415

Bayet, L., John, T., Agard, P., Gao, J., and Li, J.-L. (2018). Massive Sediment Accretion at ~80 Km Depth along the Subduction Interface: Evidence from the Southern Chinese Tianshan. *Geology* 46, 495–498. doi:10.1130/g40201.1

Bebout, G. E. (2007). Metamorphic Chemical Geodynamics of Subduction Zones. *Earth Planet. Sci. Lett.* 260, 373–393. doi:10.1016/j.epsl.2007.05.050

Bonazzi, M., Tumiati, S., Thomas, J. B., Angel, R. J., and Alvaro, M. (2019). Assessment of the Reliability of Elastic Geobarometry with Quartz Inclusions. *Lithos* 350-351, 105201. doi:10.1016/j.lithos.2019.105201

Bosenick, A., Dove, M. T., and Geiger, C. A. (2000). Simulation Studies on the Pyrope-Grossular Garnet Solid Solution. *Phys. Chem. Minerals* 27, 398–418. doi:10.1007/s002690000088

Bosenick, A., Dove, M. T., Heine, V., and Geiger, C. A. (2001). Scaling of Thermodynamic Mixing Properties in Garnet Solid Solutions. *Phys. Chem. Minerals* 28, 177–187. doi:10.1007/s002690000141

Broadwell, K. S., Locatelli, M., Verlaguet, A., Agard, P., and Caddick, M. J. (2019). Transient and Periodic Brittle Deformation of Eclogites during Intermediate-Depth Subduction. *Earth Planet. Sci. Lett.* 521, 91–102. doi:10.1016/j.epsl.2019.06.008

Caddick, M. J., and Kohn, M. J. (2013). Garnet: Witness to the Evolution of Destructive Plate Boundaries. *Elements* 9, 427–432. doi:10.2113/gselements.9.6.427

Chantel, J., Manthilake, G. M., Frost, D. J., Beyer, C., Ballaran, T. B., Jing, Z., et al. (2016). Elastic Wave Velocities in Polycrystalline Mg3Al2Si3O12-Pyrope Garnet to 24 GPa and 1300 K. *Am. Mineral.* 101, 991–997. doi:10.2138/am-2016-5335

Cisneros, M., Ashley, K. T., and Bodnar, R. J. (2020). Evaluation and Application of the Quartz-Inclusions-In-Epidote Mineral Barometer. *Am. Mineral.* 105, 1140–1151. doi:10.2138/am-2020-7379

Cruciani, G., Franceschelli, M., Scodina, M., and Puxeddu, M. (2019). Garnet Zoning in Kyanite-Bearing Eclogite from Golfo Aranci: New Data on the Early progradeP-Tevolution in NE Sardinia, Italy. *Geol. J.* 54, 190–205. doi:10.1002/gj.3169

Dachs, E., Geiger, C. A., and Benisek, A. (2014). Thermodynamic Mixing Properties and Behavior of Grossular-Spessartine, (Ca Mn1−)3Al2Si3O12, Solid Solutions. *Geochimica et Cosmochimica Acta* 141, 294–302. doi:10.1016/j.gca.2014.06.034

De Capitani, C., and Petrakakis, K. (2010). The Computation of Equilibrium Assemblage Diagrams with Theriak/Domino Software. *Am. Mineral.* 95, 1006–1016. doi:10.2138/am.2010.3354

Dera, P., Zhuravlev, K., Prakapenka, V., Rivers, M. L., Finkelstein, G. J., Grubor-Urosevic, O., et al. (2013). High Pressure Single-Crystal Micro X-Ray Diffraction Analysis with GSE_ADA/RSV Software. *High Press. Res.* 33, 466–484. doi:10.1080/08957959.2013.806504

Du, W., Clark, S. M., and Walker, D. (2016). Excess Mixing Volume, Microstrain, and Stability of Pyrope-Grossular Garnets. *Am. Mineral.* 101, 193–204. doi:10.2138/am-2016-5128

Du, W., Clark, S. M., and Walker, D. (2015). Thermo-Compression of Pyrope-Grossular Garnet Solid Solutions: Non-Linear Compositional Dependence. *Am. Mineral.* 100, 215–222. doi:10.2138/am-2015-4752

Enami, M., Nishiyama, T., and Mouri, T. (2007). Laser Raman Microspectrometry of Metamorphic Quartz: A Simple Method for Comparison of Metamorphic Pressures. *Am. Mineral.* 92, 1303–1315. doi:10.2138/am.2007.2438

Fan, D., Fu, S., Yang, J., Tkachev, S. N., Prakapenka, V. B., and Lin, J.-F. (2019a). Elasticity of Single-Crystal Periclase at High Pressure and Temperature: The Effect of Iron on the Elasticity and Seismic Parameters of Ferropericlase in the Lower Mantle. *Am. Mineral.* 104, 262–275. doi:10.2138/am-2019-6656

Fan, D., Kuang, Y., Xu, J., Li, B., Zhou, W., and Xie, H. (2017). Thermoelastic Properties of Grossular-Andradite Solid Solution at High Pressures and Temperatures. *Phys. Chem. Minerals* 44, 137–147. doi:10.1007/s00269-016-0843-4

Fan, D., Li, B., Chen, W., Xu, J., Kuang, Y., Ye, Z., et al. (2018). Research Progress of the Equation of State for Garnet Minerals. *Chin. J. High Press Phys.* 32, 1–13. doi:10.11858/gywlxb.20170597

Fan, D. W., G. Zhou, W., Liu, C. Q., Liu, Y. G., Wan, F., Xing, Y. S., et al. (2009). The Thermal Equation of State of (Fe0.86Mg0.07Mn0.07)3Al2Si3O12 Almandine. *Mineral. Mag.* 73, 95–102. doi:10.1180/minmag.2009.073.1.95

Fan, D., Xu, J., Lu, C., Tkachev, S. N., Li, B., Ye, Z., et al. (2019b). Elasticity of Single-crystal Low Water Content Hydrous Pyrope at High-Pressure and High-Temperature Conditions. *Am. Mineral.* 104, 1022–1031. doi:10.2138/am-2019-6897

Fan, D., Xu, J., Ma, M., Liu, J., and Xie, H. (2015). P-V-T Equation of State of Spessartine-Almandine Solid Solution Measured Using a Diamond Anvil Cell and *In Situ* Synchrotron X-ray Diffraction. *Phys. Chem. Minerals* 42, 63–72. doi:10.1007/s00269-014-0700-2

Fan, D., Zhou, W., Wei, S., Liu, Y., Ma, M., and Xie, H. (2010). A Simple External Resistance Heating Diamond Anvil Cell and its Application for Synchrotron Radiation X-ray Diffraction. *Rev. Scientific Instr.* 81, 053903. doi:10.1063/1.3430069

Fei, Y., Ricolleau, A., Frank, M., Mibe, K., Shen, G., and Prakapenka, V. (2007). Toward an Internally Consistent Pressure Scale. *Proc. Natl. Acad. Sci.* 104, 9182–9186. doi:10.1073/pnas.0609013104

Gatta, G. D., Merlini, M., Lee, Y., and Poli, S. (2011). Behavior of Epidote at High Pressure and High Temperature: a Powder Diffraction Study up to 10 GPa and 1,200 K. *Phys. Chem. Minerals* 38, 419–428. doi:10.1007/s00269-010-0415-y

Geiger, C. A. (2013). Garnet: A Key Phase in Nature, the Laboratory, and Technology. *Elements* 9, 447–452. doi:10.2113/gselements.9.6.447

Geiger, C., and Rossman, G. (1994). Crystal Field Stabilization Energies of Almandine-Pyrope and Almandine-Spessartine Garnets Determined by FTIR Near Infrared Measurements. *Phys. Chem. Minerals* 21, 516–525. doi:10.1007/BF00203926

Gonzalez, J. P., Thomas, J. B., Baldwin, S. L., and Alvaro, M. (2019). Quartz-in-Garnet and Ti-in-Quartz Thermobarometry: Methodology and First Application to a Quartzofeldspathic Gneiss from Eastern Papua New Guinea. *J. Metamorph. Geol.* 37, 1193–1208. doi:10.1111/jmg.12508

Gonzalez-Platas, J., Alvaro, M., Nestola, F., and Angel, R. (2016). EosFit7-GUI: A New Graphical User Interface for Equation of State Calculations, Analyses and Teaching. *J. Appl. Cryst.* 49, 1377–1382. doi:10.1107/S1600576716008050

Guiraud, M., and Powell, R. (2006). P-V-T Relationships and Mineral Equilibria in Inclusions in Minerals. *Earth Planet. Sci. Lett.* 244, 683–694. doi:10.1016/j.epsl.2006.02.021

Gwanmesia, G. D., Zhang, J., Darling, K., Kung, J., Li, B., Wang, L., et al. (2006). Elasticity of Polycrystalline Pyrope (Mg3Al2Si3O12) to 9GPa and 1000°C. *Phys. Earth Planet. Interiors* 155, 179–190. doi:10.1016/j.pepi.2005.10.008

Hartwig, J., and Galkin, V. (2021). Heat Capacity, Thermal Expansion, and Elastic Parameters of Pyrope. *J. Therm. Anal. Calorim.* 144, 71–79. doi:10.1007/s10973-020-09396-2

Hazen, R. M., Downs, R. T., Conrad, P. G., Finger, L. W., and Gasparik, T. (1994). Comparative Compressibilities of Majorite-Type Garnets. *Phys. Chem. Minerals* 21, 344–349. doi:10.1007/BF00202099

Helffrich, G., and Connolly, J. A. D. (2009). Physical Contradictions and Remedies Using Simple Polythermal Equations of State. *Am. Mineral.* 94, 1616–1619. doi:10.2138/am.2009.3262

Holland, T. J. B., and Powell, R. (2011). An Improved and Extended Internally Consistent Thermodynamic Dataset for Phases of Petrological Interest, Involving a New Equation of State for Solids. *J. Metamorph. Geol.* 29, 333–383. doi:10.1111/j.1525-1314.2010.00923.x

Hu, Y., Wu, Z., Dera, P. K., and Bina, C. R. (2016). Thermodynamic and Elastic Properties of Pyrope at High Pressure and High Temperature by First-Principles Calculations. *J. Geophys. Res. Solid Earth* 121, 6462–6476. doi:10.1002/2016JB013026

Huang, S., and Chen, J. (2014). Equation of State of Pyrope-Almandine Solid Solution Measured Using a Diamond Anvil Cell and *In Situ* Synchrotron X-ray Diffraction. *Phys. Earth Planet. Interiors* 228, 88–91. doi:10.1016/j.pepi.2014.01.014

Jamtveit, B., Austrheim, H., and Putnis, A. (2016). Disequilibrium Metamorphism of Stressed Lithosphere. *Earth-Science Rev.* 154, 1–13. doi:10.1016/j.earscirev.2015.12.002

Johnson, T. A., Cottle, J. M., and Larson, K. P. (2021). Delineation of Multiple Metamorphic Events in the Himalayan Kathmandu Complex, Central Nepal. *J. Metamorph. Geol.* 39 (4), 443–472. doi:10.1111/jmg.12583

Kantor, I., Prakapenka, V., Kantor, A., Dera, P., Kurnosov, A., Sinogeikin, S., et al. (2012). BX90: A New Diamond Anvil Cell Design for X-ray Diffraction and Optical Measurements. *Rev. Scientific Instr.* 83, 125102. doi:10.1063/1.4768541

Kohn, M. J. (2014). "Thermoba-Raman-try": Calibration of Spectroscopic Barometers and Thermometers for mineral Inclusions. *Earth Planet. Sci. Lett.* 388, 187–196. doi:10.1016/j.epsl.2013.11.054

Korsakov, A. V., Perraki, M., Zhukov, V. P., De Gussem, K., Vandenabeele, P., and Tomilenko, A. A. (2009). Is Quartz a Potential Indicator of Ultrahigh-Pressure Metamorphism? Laser Raman Spectroscopy of Quartz Inclusions in Ultrahigh-Pressure Garnets. *Eur. J. Mineral.* 21, 1313–1323. doi:10.1127/0935-1221/2009/0021-2006

Kosman, C. W., Kopylova, M. G., Stern, R. A., Hagadorn, J. W., and Hurlbut, J. F. (2016). Cretaceous Mantle of the Congo Craton: Evidence from Mineral and Fluid Inclusions in Kasai Alluvial Diamonds. *Lithos* 265, 42–56. doi:10.1016/j.lithos.2016.07.004

Kuang, Y., Xu, J., Li, B., Ye, Z., Huang, S., Chen, W., et al. (2019). Crystal-Chemical Properties of Synthetic Almandine-Pyrope Solid Solution by X-Ray Single-Crystal Diffraction and Raman Spectroscopy. *Crystals* 9, 541. doi:10.3390/cryst9100541

Li, L., Weidner, D. J., Brodholt, J., Alfè, D., and Price, G. D. (2011). Ab Initio Molecular Dynamic Simulation on the Elasticity of Mg3Al2Si3O12 Pyrope. *J. Earth Sci.* 22, 169–175. doi:10.1007/s12583-011-0169-6

Liu, Q., Hermann, J., Zheng, S., and Zhang, J. (2020). Evidence for UHP Anatexis in the Shuanghe UHP Paragneiss from Inclusions in Clinozoisite, Garnet, and Zircon. *J. Metamorph. Geol.* 38, 129–155. doi:10.1111/jmg.12515

Mazzucchelli, M. L., Burnley, P., Angel, R. J., Morganti, S., Domeneghetti, M. C., Nestola, F., et al. (2018). Elastic Geothermobarometry: Corrections for the Geometry of the Host-Inclusion System. *Geology* 46, 231–234. doi:10.1130/G39807.1

Mazzucchelli, M. L., Reali, A., Morganti, S., Angel, R. J., and Alvaro, M. (2019). Elastic Geobarometry for Anisotropic Inclusions in Cubic Hosts. *Lithos* 350-351, 105218. doi:10.1016/j.lithos.2019.105218

Milani, S., Angel, R. J., Scandolo, L., Mazzucchelli, M. L., Ballaran, T. B., Klemme, S., et al. (2017). Thermo-Elastic Behavior of Grossular Garnet at High Pressures and Temperatures. *Am. Mineral.* 102, 851–859. doi:10.2138/am-2017-5855

Milani, S., Nestola, F., Alvaro, M., Pasqual, D., Mazzucchelli, M. L., Domeneghetti, M. C., et al. (2015). Diamond-garnet Geobarometry: The Role of Garnet Compressibility and Expansivity. *Lithos* 227, 140–147. doi:10.1016/j.lithos.2015.03.017

Moulas, E., Kostopoulos, D., Podladchikov, Y., Chatzitheodoridis, E., Schenker, F. L., Zingerman, K. M., et al. (2020). Calculating Pressure with Elastic Geobarometry: A Comparison of Different Elastic Solutions with Application to a Calc-Silicate Gneiss from the Rhodope Metamorphic Province. *Lithos* 378-379, 105803. doi:10.1016/j.lithos.2020.105803

Murri, M., Mazzucchelli, M. L., Campomenosi, N., Korsakov, A. V., Prencipe, M., Mihailova, B. D., et al. (2018). Raman Elastic Geobarometry for Anisotropic Mineral Inclusions. *Am. Mineral.* 103, 1869–1872. doi:10.2138/am-2018-6625CCBY

Nestola, F., Jung, H., and Taylor, L. A. (2017). Mineral Inclusions in Diamonds May Be Synchronous but Not Syngenetic. *Nat. Commun.* 8, 14168. doi:10.1038/ncomms14168

Nestola, F., Zaffiro, G., Mazzucchelli, M. L., Nimis, P., Andreozzi, G. B., Periotto, B., et al. (2019). Diamond-Inclusion System Recording Old Deep Lithosphere Conditions at Udachnaya (Siberia). *Sci. Rep.* 9, 1–8. doi:10.1038/s41598-019-48778-x

Riches, A. J. V., Ickert, R. B., Pearson, D. G., Stern, R. A., Jackson, S. E., Ishikawa, A., et al. (2016). *In Situ* Oxygen-Isotope, Major-, and Trace-Element Constraints on the Metasomatic Modification and Crustal Origin of a Diamondiferous Eclogite from Roberts Victor, Kaapvaal Craton. *Geochimica et Cosmochimica Acta* 174, 345–359. doi:10.1016/j.gca.2015.11.028

Rivers, M., Prakapenka, V., Kubo, A., Pullins, C., Holl, C., and Jacobsen, S. (2008). The COMPRES/GSECARS Gas-Loading System for Diamond Anvil Cells at the Advanced Photon Source. *High Press. Res.* 28, 273–292. doi:10.1080/08957950802333593

Robinson, K., Gibbs, G. V., and Ribbe, P. H. (1971). Quadratic Elongation: A Quantitative Measure of Distortion in Coordination Polyhedra. *Science* 172, 567–570. doi:10.1126/science.172.3983.567

Roedder, E., and Bodnar, R. J. (1980). Geologic Pressure Determinations from Fluid Inclusion Studies. *Annu. Rev. Earth Planet. Sci.* 8, 263–301. doi:10.1146/annurev.ea.08.050180.001403

Rosenfeld, J. L., and Chase, A. B. (1961). Pressure and Temperature of Crystallization from Elastic Effects Around Solid Inclusions in Minerals? *Am. J. Sci.* 259, 519–541. doi:10.2475/ajs.259.7.519

Shannon, R. D. (1976). Revised Effective Ionic Radii and Systematic Studies of Interatomic Distances in Halides and Chalcogenides. *Acta Cryst. Sect A.* 32, 751–767. doi:10.1107/s0567739476001551

Sinogeikin, S., Bass, J., Prakapenka, V., Lakshtanov, D., Shen, G., Sanchez-Valle, C., et al. (2006). Brillouin Spectrometer Interfaced with Synchrotron Radiation for Simultaneous X-ray Density and Acoustic Velocity Measurements. *Rev. Scientific Instr.* 77, 103905. doi:10.1063/1.2360884

Spear, F. S., and Wolfe, O. M. (2020). Revaluation of "Equilibrium" P-T Paths from Zoned Garnet in Light of Quartz Inclusion in Garnet (QuiG) Barometry. *Lithos* 372-373, 105650. doi:10.1016/j.lithos.2020.105650

Speziale, S., Duffy, T. S., and Angel, R. J. (2004). Single-Crystal Elasticity of Fayalite to 12 GPa. *J. Geophys. Res.* 109, 1–15. doi:10.1029/2004jb003162

Tajčmanová, L., Manzotti, P., and Alvaro, M. (2021). Under Pressure: High-Pressure Metamorphism in the Alps. *Elements* 17, 17–22. doi:10.2138/gselements.17.1.17

Takahashi, T., and Liu, L.-G. (1970). Compression of Ferromagnesian Garnets and the Effect of Solid Solutions on the Bulk Modulus. *J. Geophys. Res.* 75, 5757–5766. doi:10.1029/JB075i029p05757

Vinet, P., Ferrante, J., Smith, J. R., and Rose, J. H. (1986). A Universal Equation of State for Solids. *J. Phys. C: Solid State. Phys.* 19, L467–L473. doi:10.1088/0022-3719/19/20/001

Vinograd, V. L., Sluiter, M. H. F., Winkler, B., Putnis, A., Hålenius, U., D. Gale, J., et al. (2004). Thermodynamics of Mixing and Ordering in Pyrope - Grossular Solid Solution. *Mineral. Mag.* 68, 101–121. doi:10.1180/0026461046810174

Wang, Y. B., Weidner, D. J., Zhang, J. Z., Gwanrnesia, G. D., and Liebermann, R. C. (1998). Thermal equation of state of garnets along the pyrope-majorite join. *Phys. Earth Planet. Interiors* 105, 59–71. doi:10.1016/S0031-9201(97)00072-1

Wolfe, O. M., and Spear, F. S. (2018). Determining the Amount of Overstepping Required to Nucleate Garnet during Barrovian Regional Metamorphism, Connecticut Valley Synclinorium. *J. Metamorph. Geol.* 36, 79–94. doi:10.1111/jmg.12284

Xu, J., Zhang, D., Dera, P., Zhang, B., and Fan, D. (2017). Experimental Evidence for the Survival of Augite to Transition Zone Depths, and Implications for Subduction Zone Dynamics. *Am. Mineral.* 102, 1516–1524. doi:10.2138/am-2017-5959

Xu, J., Zhang, D., Fan, D., Dera, P. K., Shi, F., and Zhou, W. (2019). Thermoelastic Properties of Eclogitic Garnets and Omphacites: Implications for Deep Subduction of Oceanic Crust and Density Anomalies in the Upper Mantle. *Geophys. Res. Lett.* 46, 179–188. doi:10.1029/2018gl081170

Zhang, H.-F., Zhou, M.-F., Sun, M., and Zhou, X.-H. (2010). The Origin of Mengyin and Fuxian Diamondiferous Kimberlites from the North China Craton: Implication for Palaeozoic Subducted Oceanic Slab-Mantle Interaction. *J. Asian Earth Sci.* 37, 425–437. doi:10.1016/j.jseaes.2009.10.006

Zhang, J., Martinez, I., Guyot, F., and Reeder, R. J. (1998a). Effects of Mg-Fe (Super 2+) Substitution in Calcite-Structure Carbonates; Thermoelastic Properties. *Am. Mineral.* 83, 280–287. doi:10.2138/am-1998-3-411

Zhang, L., Ahsbahs, H., Hafner, S. S., and Kutoglu, A. (1997). Single-Crystal Compression and Crystal Structure of Clinopyroxene up to 10 GPa. *Am. Mineral.* 82, 245–258. doi:10.2138/am-1997-3-402

Zhang, L., Ahsbahs, H., Kutoglu, A., and Geiger, C. A. (1999). Single-Crystal Hydrostatic Compression of Synthetic Pyrope, Almandine, Spessartine, Grossular and Andradite Garnets at High Pressures. *Phys. Chem. Minerals* 27, 52–58. doi:10.1007/s002690050240

Zhang, L., Ahsbahs, H., and Kutoglu, A. (1998b). Hydrostatic Compression and Crystal Structure of Pyrope to 33 GPa. *Phys. Chem. Minerals* 25, 301–307. doi:10.1007/s002690050118

Zhang, Y. (1998). Mechanical and Phase Equilibria in Inclusion–Host Systems. *Earth Planet. Sci. Lett.* 157 (3-4), 209–222. doi:10.1016/S0012-821X(98)00036-3

Zhong, X., Andersen, N. H., Dabrowski, M., and Jamtveit, B. (2019). Zircon and Quartz Inclusions in Garnet Used for Complementary Raman Thermobarometry: Application to the Holsnøy Eclogite, Bergen Arcs, Western Norway. *Contrib. Mineral. Petrol.* 174, 1–17. doi:10.1007/s00410-019-1584-4

Zhong, X., Moulas, E., and Tajčmanová, L. (2020). Post-Entrapment Modification of Residual Inclusion Pressure and its Implications for Raman Elastic Thermobarometry. *Solid Earth* 11, 223–240. doi:10.5194/se-11-223-2020

Zou, Y., Gréaux, S., Irifune, T., Whitaker, M. L., Shinmei, T., and Higo, Y. (2012). Thermal Equation of State of Mg3Al2Si3O12 Pyrope Garnet up to 19 GPa and 1,700 K. *Phys. Chem. Minerals* 39, 589–598. doi:10.1007/s00269-012-0514-z

Conflict of Interest: BL, WG, and YZ were employed by PetroChina.

The remaining authors declare that the research was conducted in the absence of any commercial or financial relationships that could be construed as a potential conflict of interest.

Publisher's Note: All claims expressed in this article are solely those of the authors and do not necessarily represent those of their affiliated organizations, or those of the publisher, the editors, and the reviewers. Any product that may be evaluated in this article, or claim that may be made by its manufacturer, is not guaranteed or endorsed by the publisher.

frontiers in Earth Science

ORIGINAL RESEARCH
published: 03 February 2022
doi: 10.3389/feart.2021.829244

An Efficient Rock Physics Scheme for Estimating Crack Density and Fluid Saturation of Shale Gas Reservoir

Ziran Jiang[1], *Qiaomu Qi*[1,2]*, *Xudong Jiang*[2], *Jikun Meng*[2] *and Xing-Jian Wang*[1]

[1]State Key Laboratory of Oil and Gas Reservoir Geology and Exploitation, Chengdu University of Technology, Chengdu, China, [2]College of Geophysics, Chengdu University of Technology, Chengdu, China

We propose a simple rock physics model for the characterization of elastic properties of shale. The model combines a dual-porosity concept and the effective medium theory for constructing the anisotropic elastic tensor of the multimineral organic-rich shale. Based on the model, we address how to estimate two key shale gas evaluation parameters, i.e., crack density and gas saturation from well-log and seismic data. Application to Wufeng-Longmaxi Shale shows that the estimated crack porosity decreases with increasing burial depth and decreasing clay content. The analysis indicates that the microcracks are mainly developed among clay minerals, which is consistent with the results from mercury injection and SEM imaging experiments. More importantly, we show that the velocity of the Wufeng-Longmaxi Shale is primarily controlled by the crack porosity instead of the total porosity. Both P- and S-wave velocities decrease linearly as the volume of microcrack increases. The fluid substitution analysis shows that the Poisson's ratio and P-impedance of the shale are sensitive to the change of pore-fluid saturation. Based on the above sensitivity analyses, we customize a rock physics template for quantifying crack density, and gas saturation from the shale elastic properties. The interpretation results show that there is an overall good agreement between the measured and predicted petrophysical properties from well-log and seismic data.

Keywords: rock physics, organic-rich shale, elastic property, microcrack, saturation, reservoir characterization, microstructure

OPEN ACCESS

Edited by:
Lidong Dai,
Institute of geochemistry (CAS), China

Reviewed by:
Tongcheng Han,
China University of Petroleum, (Huadong) China
Dawei Fan,
Institute of Geochemistry (CAS), China

***Correspondence:**
Qiaomu Qi
qiaomu_qi@163.com

Specialty section:
This article was submitted to Solid Earth Geophysics, a section of the journal Frontiers in Earth Science

Received: *05 December 2021*
Accepted: *17 December 2021*
Published: *03 February 2022*

Citation:
Jiang Z, Qi Q, Jiang X, Meng J and Wang X-J (2022) An Efficient Rock Physics Scheme for Estimating Crack Density and Fluid Saturation of Shale Gas Reservoir. Front. Earth Sci. 9:829244. doi: 10.3389/feart.2021.829244

1 INTRODUCTION

Quantitative seismic interpretation is the core of shale gas reservoir identification and evaluation. During the exploration stage, seismic data are employed to determine buried depth, thickness, and structural shape of the shale reservoir (Rich and Ammerman, 2010; Bachrach et al., 2014; Jiang et al., 2019). This is followed by applying the inversion technique for mapping the distribution of organic matter content, porosity and this leads to the determination of the favorable area with economical gas potential (Chopra et al., 2012). In the development stage, the seismic technology is used to determine the mechanical and anisotropy characteristics of the reservoir, so as to provide the basis for the deployment of horizontal wells, and well bore design and fracturing stimulation (Goodway et al., 2010; Sena et al., 2011). Understanding the relationship between the elastic and petrophysical properties of shale is fundamental to the geophysical research of shale gas exploration and development. Shale gas reservoir has complex lithologic, pore and structural characteristics. Among them, the compactness caused by low porosity and low permeability is a more obvious

feature of shale gas reservoir (Passey et al., 2010). Former empirical formulas and theoretical rock physics models developed for conventional clastic and carbonate formations may not be applicable for shale gas reservoirs.

A lot of work have been done around the experimental and theoretical investigations of shale elastic properties. Vernik and Nur (1992); Vernik and Liu (1997) measured the elastic anisotropy of Bakken Shale under dry conditions. They analyzed the effects of organic matter content and maturity on rock velocity and anisotropy. They pointed out that the kerogen has a dramatic effect on seismic velocity and the anisotropy of shale is largely controlled by the preferred direction of minerals and micro-fractures. Sondergeld et al. (2000); Sondergeld and Rai (2011) conducted experimental study on the acoustic properties of Kimmeridge Shale and found that the anisotropy of shale increases with increasing organic matter content. The increase of organic matter content will lead to the decrease of density, resulting in the effect opposite to compaction. They also showed that the assumption of weak anisotropy (Thomsen, 1986) cannot be used in the seismic modeling of shale. Domnesteanu et al. (2002); Deng et al. (2009) studied the velocity and attenuation of shale under different saturation and pressure conditions using ultrasonic transmission technique. The experimental results suggest that there is a strong link between the pressure-dependent anisotropy of velocity/attenuation and the pore geometry, connectivity and the response of pore fluid to the propagation direction of the seismic waves. Hornby et al. (1994) combined the self-consistent approximation (SCA) and the differential effective medium (DEM) theories to characterize the seismic elastic properties of Kimmeridge Shale. In the model, clay is treated as the supporting matrix that forms the continuous skeleton of the rock, other minerals such as quartz, feldspar, and pyrite are regarded as isolated inclusions dispersedly distributed in clay. Carcione et al. (2011) used Backus average to evaluate the effect of clay particle orientation on the elastic properties and anisotropy of shale. Guo et al. (2013) developed a seismic petrophysical model of organic-rich shale and investigated the effects of pore shape and mineral composition on the elastic properties of shale.

Organic-rich shale exhibits relatively higher resistivity, higher sonic transit-time and lower density than nonorganic rich sediments (Passey et al., 2010). Tight shale hydrocarbon reservoirs are characterized by total porosity in the range of 3–7% and matrix permeability in the range of micro-to nano-Darcy. The seismic elastic properties of shale are controlled by its own structural characteristics. The key to analyze its seismic elastic properties and influencing factors is to accurately describe the structural characteristics of shale at microscale including the spatial distribution of main constituent minerals, organic matter, and pore structure (Vasin et al., 2013; Luan et al., 2016). Due to the differences in sedimentary history and depositional environment (i.e., stress field change, mineral composition, etc.) of different reservoir rocks, the petrophysical experimental results for specific reservoirs are also regional, and can not be extrapolated arbitrarily (Zhao et al., 2020; Deng et al., 2021). Therefore, it is important to establish site-specific rock physics model to characterize the local elastic properties of shale.

Natural cracks in shale provide necessary fluid conduits for shale gas migration and can greatly enhance the seepage capacity (Guo et al., 2014; Wu et al., 2020). The degree of microcracks contributes to the total porosity which affects the storage capacity of shale reservoir. The evaluation of microcrack volume is of great importance for the exploration and development of shale gas. On the other hand, shale gas saturation is important for predicting reservoir performance in terms of production (Lucier et al., 2011; Qi et al., 2017). Accurate estimation of gas saturation remains as one of the most difficult tasks associated with shale reservoir characterization (Rezaee, 2015; Qi et al., 2021). In order to predict the rock and fluid parameters of gas shale by geophysical methods, it is necessary to establish the relationship between elastic properties and petrophysical parameters. In this work, we address an important issue of estimating two key shale gas evaluation parameters, i.e., crack density and gas saturation from well-log and seismic data. The paper is organized as follows: first, we introduce a simple but effective rock physics modeling scheme for organic-rich shale. Then, we demonstrate how this model can be applied to the inversion of pore structures, fluid substitution, and reservoir characterization with rock physics template. This is followed by the discussion on the novelty and applicability of the model. Finally, we elaborate the main conclusions and set the basis for future works.

2 METHODOLOGY

In this work, we propose a simple anisotropic dual-porosity effective medium model (ADPM) for calculating the elastic property of the organic rich shales. The microstructure of the organic-rich shale can be extremely complex (Vanorio et al., 2008; Uvarova et al., 2014; Qi et al., 2021). The pores of different shapes, such as intergranular pores and microcracks, can develop between or on the edges of the rock matrix minerals such as quartz, and clay. Intraparticle pores of nanoscale can also develop among the organic matter. Despite the complex nature of the shale microstructure, we assume that at any specific logged depth location, the shale porosity system (ϕ_{total}) can be simplified and divided into two spaces: the stiff-pore space (stiff-porosity) and the microcrack space (crack-porosity), i.e.,

$$\phi_{total} = \phi_{stiff} + \phi_{crack}. \tag{1}$$

Stiff porosity (ϕ_{stiff}) and crack porosity (ϕ_{crack}) are defined here as the volumetric fraction of spheres with larger aspect ratio and oblate spheroid inclusions with very small aspect ratio, respectively. The key to our assumption is that we do not consider how the different pore structures fit into the rock frame since their distributions can be arbitrary and are unknown. Later we show that this assumption greatly simplifies the modeling (inversion) procedure and yields results that are consistent with laboratory and field measurements. With the above dual-porosity model, we

propose the following rock physics workflow for modeling shale elastic properties.

First, since different components in the organic-rich shale possess very different stiffness, an accurate mineralogy analysis is crucial for constructing the right rock matrix to start with. First of all, we can obtain the volume fraction of the mineral content in shale from the spectral gamma-ray (well-log) or the X-ray diffraction analysis (core sample). When the exact mineralogy of shale cannot be assessed, simple gamma-ray log can be used to provide an estimate for the volumes of silt and clay in the formation. The mineralogy of the organic-rich shale can be broadly divided into the brittle minerals, clay and kerogen components. The brittle minerals include quartz, carbonate and pyrite whereas the kerogen is the typical soft material. When the volume fractions of each component are determined, we can apply the Voigt-Reuss-Hill average (Mavko et al., 2009) to compute the isotropic effective moduli of the brittle mineral aggregate. Because the shale anisotropy is mainly caused by the lamination of clay and kerogen, we use a three-phase Backus average (Backus, 1962; Vernik and Nur, 1992) to mix the brittle minerals, clay and kerogen. This procedure yields the anisotropic effective moduli of multimineral solid matrix.

The organic-rich shale is typically of low porosity and low permeability with poor pore connectivity. These shales may contain randomly distributed microcracks with crack size below well-log resolution. Theoretical estimates of the effective moduli of the cracked porous shale not only depend on the volume fraction of the inclusions (i.e., cracks and pores) but also the geometric details of shapes and spatial distributions of these inclusions. Several effective medium theories can be used to estimate the effective moduli of the shale. In this work, we use the anisotropic self-consistent approximation (SCA) theory to compute the stiffness tensor of the shale frame. The choice of the SCA model is due to the following consideration. Since the inclusion adding process in the SCA theory is a symmetrical process, it does not identify a specific phase as the host material. This is different for the differential effective medium (DEM) theory. Due to the difference in depositional and diagenetic processes, shale can transits from clay-supporting matrix to quartz-supporting matrix as the burial depth changes (Zhao et al., 2020; Deng et al., 2021). The reservoir section usually contains shales of more than one type. Therefore, we consider the SCA model is more flexible and can adapt to more complex lithologic enviroment. By incorporating the dual-porosity concept into the SCA modeling scheme, the effective stiffness tensor of the shale can be written as

$$C_{eff} = [(1-\phi_{total})C_m Q_m + \phi_{stiff} C_{stiff} Q_{stiff} + \phi_{crack} C_{crack} Q_{crack}] \times [(1-\phi_{total})Q_m + \phi_{stiff} Q_{stiff} + \phi_{crack} Q_{crack}]^{-1}, \quad (2)$$

where,

$$Q_i = [I + G_i (C_i - C_{SCA})]^{-1}, \quad (3)$$

and i represents the matrix (m) or the pore spaces (*stiff*, *crack*), I is the identity tensor. C_i is the stiffness tensor matrix of the i-th phase. G_i is a fourth-rank tensor calculated from the response of an unbounded matrix of the effective medium Eshelby (1957); Mura (1982).

Brown and Korringa (1975) extended the Gassmann's equations and established the model suitable for fluid replacement in anisotropic media such as shale. On the basis of dry shale model, we apply the Brown-Korringa's (BK) equation to compute the stiffness tensor of the saturated shale. In the BK model, the compliance of the saturated shale is given by

$$S^{sat}_{ijkl} = S^{dry}_{ijkl} - \frac{(S^{dry}_{ijaa} - S^{0}_{ijaa})(S^{dry}_{bbkl} - S^{0}_{bbkl})}{(S^{dry}_{ccdd} - S^{0}_{ccdd}) + \phi(\beta_{fl} - \beta_0)}, \quad (4)$$

where S^{dry}_{ijkl} is the effective elastic compliance tensor element of dry rock, S^{sat}_{ijkl} is the effective elastic compliance element of rock saturated with pore fluid, S^{0}_{ijkl} is the effective elastic compliance element of the solid mineral, β_{fl} is the fluid compressibility, and β_0 is the mineral compressibility. The stiffness can be obtained by taking the inverse of the compliance matrix. To model the partially saturated gas shale, we use the Brie's model (Brie et al., 1995) to calculate the effective fluid moduli of a brine and gas mixture. In accordance with the BK model, the compliance of the fluid mixture can be calculated as

$$\beta_{fl} = [(K_w - K_g)(1 - S_g)^e]^{-1}. \quad (5)$$

The fluid compliance depends on the bulk moduli of brine K_w and gas K_g, the gas saturation S_g and an empirical exponent e. The empirical exponent e varies from 1 for patchy saturation to 3.4 for uniform saturation. They provide the upper and lower bounds for the effective bulk modulus of the mixed fluids, respectively. We can substitute the equivalent compliance of brine-gas mixture **(5)** into the BK model **(4)** to replace the empty pores with fluids.

Based on the above anisotropic dual-porosity model, the equivalent elastic tensor of fluid saturated rock can be converted to velocities according to the relationship provided by Thomsen (1986). For a vertical well, the acoustic logging tool records the P- and S-waves traveling perpendicular to the bedding plane, that is parallel to the axis of symmetry of the transversely isotropic shale formations. The expressions for these velocities are

$$V_p = \sqrt{\frac{C_{33}}{\rho}}, \quad (6)$$

$$V_s = \sqrt{\frac{C_{44}}{\rho}}, \quad (7)$$

where C_{33} and C_{44} are the stiffnesses in Voigt notation. ρ is the effective density of the shale, which can be calculated by the volume average of the grain and fluid densities

$$\rho = (1-\phi_{total})\rho_0 + \phi_{total} S_w \rho_w + \phi_{total} S_g \rho_g. \quad (8)$$

To test the effectiveness and applicability of the APDM model, in the following sections, we apply the rock physics model to a suite of analyses including pore type inversion, shear-log prediction, fluid substitution, and seismic reservoir characterization.

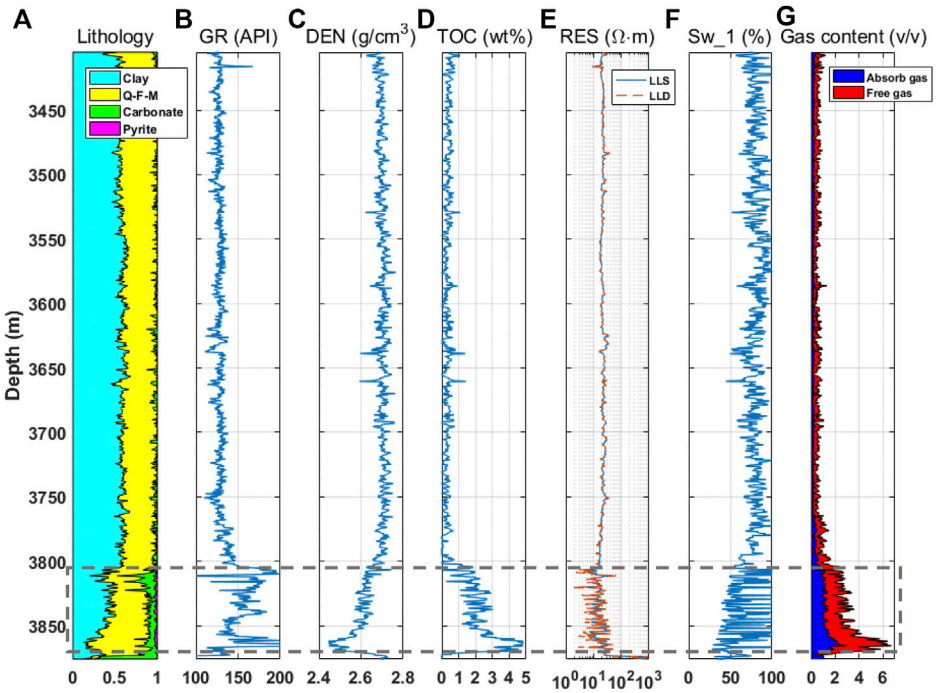

FIGURE 1 | The logging data of Well-Y1 from a shale gas field in Southern Sichuan Basin: **(A)** mineral components; **(B)** gamma-ray; **(C)** density; **(D)** total organic content (TOC); **(E)** shallow (LLS) and deep (LLD) resistivities; **(F)** water saturation evaluated based on resistivity; **(G)** absorb and free gas contents.

3 ROCK PHYSICS ANALYSIS

3.1 Geological Background

We conduct rock physics analysis on the organic-rich shale in the Wufeng-Longmaxi Formation. The Wufeng-Longmaxi Shale are widespread units, and their geologic characteristics are similar to five of the leading shale gas producing basins in North America (Pollastro, 2007; Guo and Liu, 2018; Xu et al., 2019). Therefore, establishing a quantitative characterization model for the Wufeng-Longmaxi Shale would have global impacts. Well-Y1 is a shale gas exploration well located in a shale gas field in Southern Sichuan Basin, China. The section in **Figure 1** is composed of the lower Silurian Longmaxi formation and the upper Ordovician Wufeng formation. The organic-rich shale at the lower part, which shows high gamma and low density, and is the main target layer. The thickness of organic-rich shale in well-Y1 is 67 m, the total organic carbon content (TOC) is 1.8–4.8 wt %, and the thermal maturity is 2.5–3.0. All geological evaluation parameters show that Wufeng-Longmaxi Formation in the work area has superior conditions for shale gas accumulations.

As shown in **Figure 2**, measurements of density, gamma ray, shallow- and deep-resistivities, compressional, and shear velocities are available. The porosity can be calculated based on the density log. In these reservoirs, the total porosity varies from 2 to 10% with an average value of 5%. **Figure 2A** shows that the average values of clay, quartz, and carbonate are 38, 48, and 11%, respectively. Pyrite is also present, ranging from trace amounts to as much as 7%. The quartz is present in the form of silt and siliceous cement. TOC is estimated from resistivity and sonic logs using the method of Passey et al. (1990). The Wufeng-Longmaxi shale reservoir is a typical low-resistivity reservoir as indicated by **Figure 1E**. Conventional resistivity method, such as Archie's equation (Han T.-C. et al., 2021), will lead to overestimation on the water saturation as shown in **Figure 1F**. To overcome this problem, water saturation is estimated using the neutron-density porosity difference method (Qi et al., 2021). **Figure 2D** shows that the corrected water saturation value varies from 18 to 100% in the reservior section. In the rock physics modeling, the bulk moduli and densities of the brine and gas of in-situ pressure and temperature are estimated using the equations of Batzle and Wang (1992). The elastic moduli and densities for the minerals and pore-fluids are presented in **Table 1**.

3.2 Inversion of Different Pore Volume Fractions

The rock physics model provides a nonlinear relation between P- and S-wave velocities and the volume fractions of soft and stiff pores. Using this relation, we can forward calculate the P- and S-wave velocities of rocks based on rock and fluid properties including mineral moduli, porosity, and fluid saturation and pore aspect ratio. Alternatively, we can determine the stiff and soft porosities by matching well-log velocity data with theoretically predicted velocities. Here, we assume that the stiff pores and microcracks are spheroidal inclusions with aspect ratios of 1 and 0.01, respectively. Thus, we keep the pore aspect ratio as constant at all depths in the inversion procedure. The choice of aspect ratio

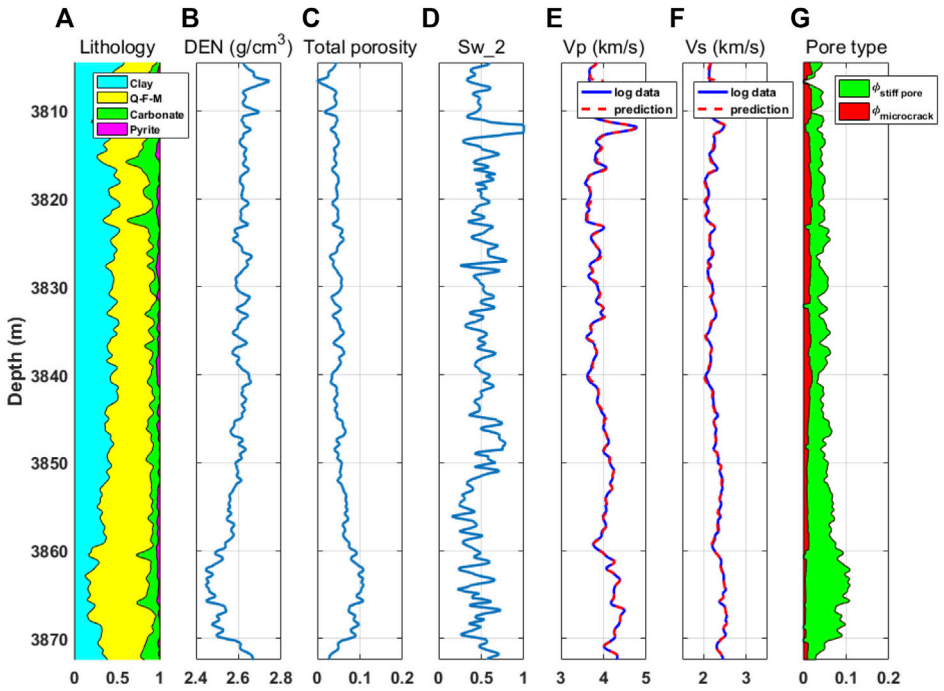

FIGURE 2 | The logging data of the target section in Well-Y1 (this corresponds to the bottom part of the logging data in **Figure 1**): **(A)** mineral components; **(B)** density; **(C)** total porosity; **(D)** water saturation evaluated based on neutron-density method; **(E)** measured and predicted P-wave velocities; **(F)** measured and predicted S-wave velocities; **(G)** porosities of microracks and stiff pores.

TABLE 1 | The bulk, shear moduli and density of the primary minerals and fluids in shale.

	Quartz	Clay	Calcite	Pyrite	Kerogen	Water	Gas
Bulk modulus (GPa)	37	21	77	139	2.9	2.2	0.015
Shear modulus (GPa)	44	7	32	110	2.7	0	0
Density (g/cm^3)	2.65	2.60	2.71	4.93	1.3	1.2	0.42

1 for stiff pore is based on the fact that sphere is the stiffest among all pore shapes. For cracks of small aspect ratio, the key parameter is the crack density $\epsilon = 3\phi_{crack}/4\pi\alpha_{crack}$ (O'Connell and Budiansky, 1974), which is proportional to the crack porosity divided by the aspect ratio. The choice of exact crack aspect ratio value is of secondary importance. We also assume that all cracks have identical shapes, i.e., aspect ratios. In this case, the effect of crack porosity on elastic moduli is equivalent to the crack density (Vernik, 2016). To determine the volume fractions of cracks and stiff pores from sonic-log data, we propose the following objective function

$$Obj = W_p|(V_p^{obs} - V_p^{model})| + W_s|(V_s^{obs} - V_s^{model})|, \quad (9)$$

where V^{obs} and V^{model} are the measured and modelled velocities, respectively. W_p, W_s are the weights, for case that the shear-log is not available, $W_p = 1$, $W_s = 0$ and when both compressional- and shear-logs are available, $W_p = 0.5$, $W_s = 0.5$. By minimizing the objective function **(9)**, ϕ_{crack} and ϕ_{stiff} are jointly inverted from two velocities V_p and V_s. A grid search method can be applied to find the two porosities required to accomplish the velocity match at each well-logging depth. Other formation properties such as mineral component, total porosity and fluid saturation are provided by the well-log data.

The estimated crack and stiff porosities are plotted in **Figure 2G**. We see that the microcracks are well developed in the upper and middle parts of the Wufeng-Longmaxi Shale. As the burial depth increases, the amount of microcracks diminishes and the pore-space is dominated by stiff pores. The average porosities of the crack and stiff pores in the reservoir section are 0.012 and 0.043, respectively. The volume fraction of the stiff pores is 3.6 times of the microcrack overall. **Figures 2E,F** shows the modeled P- and S-wave velocities based on the inverted crack and stiff porosities. There is a satisfactory match between the measured and the modeled velocity. The root-mean-square error (RMSE) for the predicted P- and S-wave velocities are 34.9 m/*s* and 23.4 m/*s*, respectively. The correlation coefficients between the measured and predicted velocities are 0.992 3 for P-wave and 0.991 6 for S-wave. The

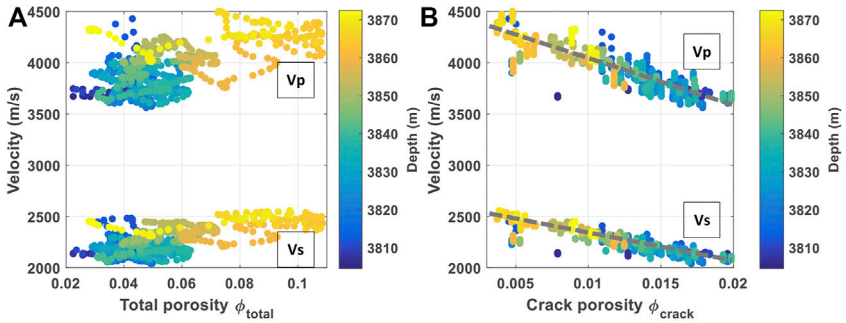

FIGURE 3 | Relationship between the sonic-log velocities and different porosities: **(A)** velocity versus total porosity; **(B)** velocity versus crack porosity.

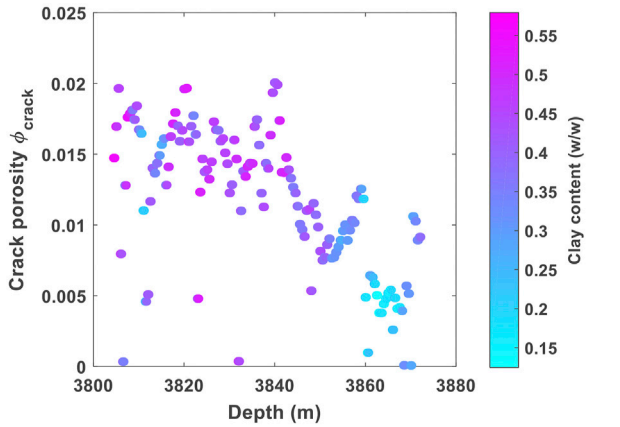

FIGURE 4 | Cross-plot between the crack porosity and burial depth. The data points are color-coded by clay content.

consistent prediction of the two velocity logs shows that the rock physics model is effective for characterizing the elastic behavior of the shale. To further analyze the relationship between the elastic properties of shale and its pore structure, we plot the velocities as functions of different porosities. **Figure 3A** shows that there is a weak dependence of the velocities on the total porosity of the shale. The P-wave velocity increases slowly with increasing total porosity, which is counter-intuitive. The total porosity shows limited influence on the velocities. **Figure 3B** shows the relationship between the velocities and the crack porosity. Interestingly, both P- and S-wave velocities exhibit overall linear correlations with the crack porosity. A linear least-square fit provides the following relations

$$V_p\ (m/s) = -38877\phi_{crack} + 4393, \quad (10)$$

$$V_s\ (m/s) = -22234\phi_{crack} + 2519. \quad (11)$$

The velocities decrease as the volume of microcracks in shale increases. The clear dependence of the velocity on crack porosity shows that the presence of small-aspect-ratio cracks is a key parameter in controlling the elastic property of the Wufeng-Longmaxi Shale.

Figure 4 shows that the development of the microcracks in the Wufeng-Longmaxi Shale generally decreases as burial depth increases. The data points are color-coded by the clay content, as can be seen the crack porosity tends to increase with increasing volume of clay in shale. This observation is consistent with the laboratory results of Sun et al. (2019) who conducted mercury injection experiments to quantify the volume of microcracks in the Longmaxi shale samples. They found that the majority of the microcracks were formed inside the clay particles, followed by those developed in organic matter and brittle minerals (see more details in the discussion section). The SEM images in **Figure 5** reveal the microstructure of the Wufeng-Longmaxi organic-rich shale. In **Figures 5A,B**, the pores between clay platelets or around the edge of rigid particles are shown as elongated, compliant shape. Whereas the intergranular pores, which have a rigid triangular structure, are mainly developed between the quartz minerals as shown in **Figures 5C,D**. Our observation that the microcracks are more likely to develop in the clay is consistent with both the mercury injection statistics and the actual microstructure revealed by the SEM images of the Wufeng-Longmaxi Shale. Once we determine the crack and stiff porosities of the shale formation, a detailed fluid substitution analysis can be carried out at each logged depth. This is discussed in the next section.

3.3 Fluid Substitution Analysis

Fluid substitution is important for examining the sensitivity of the elastic properties to the change of amount of fluids in the pore-space. It directly helps seismic interpreter to determine area with favorable gas potential from cross-plot of seismic attributes. With the calibrated crack and stiff porosity logs, we can conduct fluid substitution for the entire reservoir section based on the dual-porosity model. By assigning different levels of gas saturation S_g to **Eq. 5** and substituting the effective fluid compressibility into Brown-Korringa's equation, we can evaluate the elastic properties of the partially saturated shale. It has been confirmed by studies that due to low permeability and poor pore connectivity, patchy saturation instead of uniform saturation is likely to take place in tight reservoir rocks (Si et al., 2016; Li et al., 2020). We pick the exponent $e = 1$ in Brie's model based on an empirical fit to the data. This corresponds to the upper bound for the velocity-saturation relation in shale.

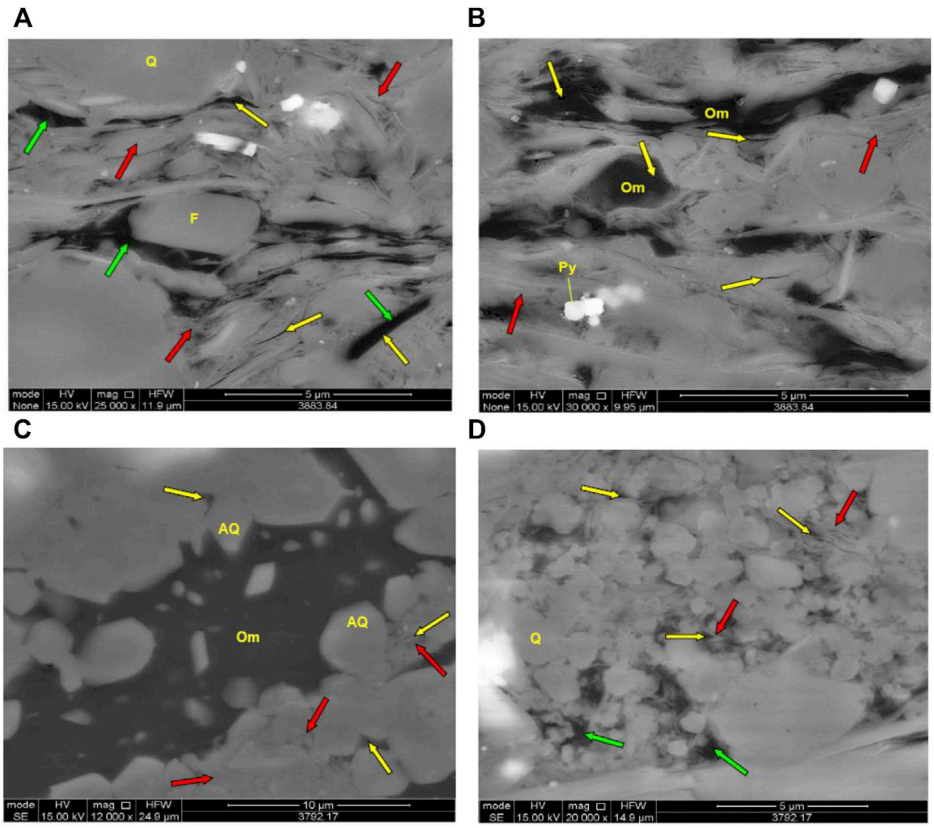

FIGURE 5 | The SEM images showing the microstructure of the Wufeng-Longmaxi Shale: **(A,B)** shows that the pores between clay platelets or around the edge of rigid particles are of elongated, compliant shape; **(C,D)** shows that the intergranular pores, which have a rigid triangular structure, are mainly developed between the quartz minerals.

The water saturation log in **Figure 2D** indicates that the gas saturation in the shale formation varies from 0 to 72% with an average value of 37%. As shown in **Figure 6A**, the corresponding Poisson's ratio varies from 0.25 to 0.36 and the P-impedance varies from $0.95e^4$-$1.2e^4$ g ·m/cm^3 ·s. The red squares in **Figure 6** represent the shale formation with full water saturation. The blue circles in **Figures 6A–D** denote the original well-log data and the formation with gas saturation of 30, 70 and 90%, respectively. For low formation gas saturation, the gas shale shows similar characteristics with the water shale and it is difficult to distinguish them on a Poisson's ratio versus P-impendance cross-plot. When the gas saturation increases to 70%, both the Poisson's ratio, and P-impedance decrease dramatically. For 90% gas saturation, the Poisson's ratio becomes less than 0.25 and the P-impedance reduces by 9%. Overall, with favorable gas saturation larger than 70%, there exists a clear separation between the original, and substituted results on the cross-plot. This indicates that the Wufeng-Longmaxi shale is relatively sensitive to the change of pore fluid saturation. The results suggest that the cross-plot between Poisson's ratio and P-impedance can be useful and applied to seismic inversion results for gas zone identification in the work area.

3.4 Seismic Characterization With Rock Physics Template

Rock physics template (RPT) is an essential tool for mapping the effect of fluids, porosity, and lithology on elastic properties such as P-, S-impedances and V_p/V_s (Avseth et al., 2010; Zhou et al., 2021). Because impedance and V_p/V_s are properties that can be obtained from seismic inversion, RPT allows quantitative interpretation and classification not only of well-logs, but also of seismic data. The main goal is to use the RPT for quantifying two primary properties, i.e., crack density and gas saturation from the well-log and seismic data in the work area. In the last two sections, we have shown that the velocities of the Wufeng-Longmaxi Shale strongly linked to the crack porosity while the Poisson's ratio is sensitive to the fluid saturation. The P-impedance and V_p/V_s can be viewed as proxies for P-wave velocity and Poisson's ratio, respectively. Therefore, we design the RPT so that it outputs a cross-plot between the P-impedance and V_p/Vs for quantitative interpretation. To construct the RPT, we set the crack density and gas saturation as variables in the model and fix other depth-dependent properties to reference values. For example, model parameters such as effective mineral moduli, porosity and fluid properties are defined using the average values in the reservoir section. Thus, for each crack density and gas

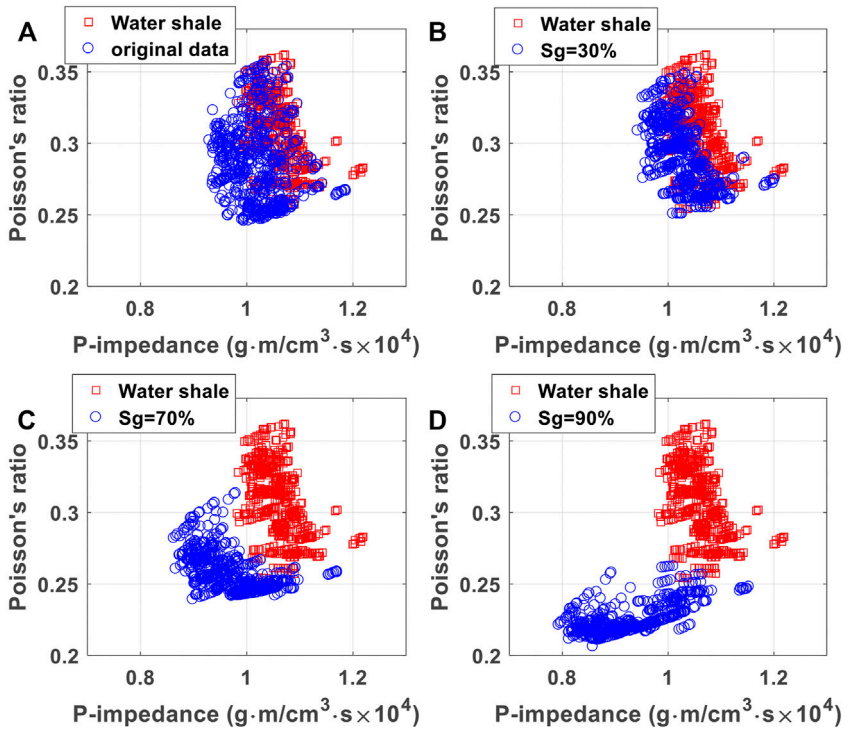

FIGURE 6 | Fluid substitution results of the Wufeng-Longmaxi Formation in well-Y1. The red squares represent the formation with 100% water saturation. The blue circles represent the original well-log data in **(A)** and formations with gas saturations of 30, 70, and 90% in **(B–D)**, respectively.

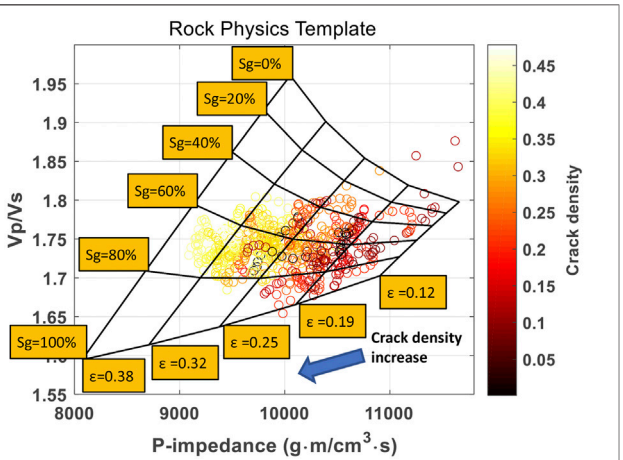

FIGURE 7 | Rock physics template analysis for the interpretation of crack density and gas saturation from cross-plot between the V_p/V_s and P-impedance. The data points are from Well-1 and color-coded by crack density log. The arrow shows the direction of increasing crack density.

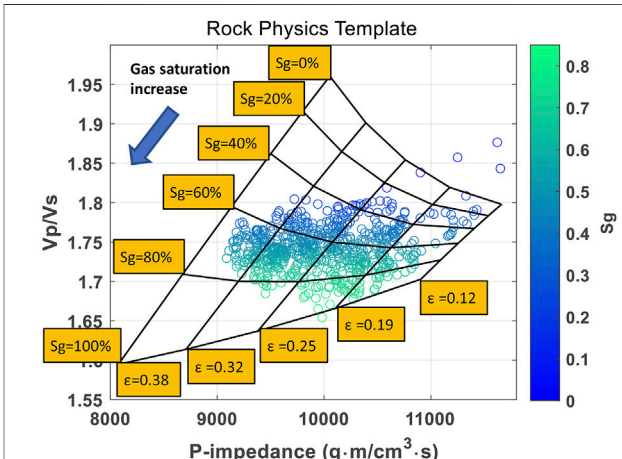

FIGURE 8 | Rock physics template analysis for the interpretation of crack density and gas saturation from cross-plot between the V_p/V_s and P-impedance. The data points are from Well-1 and color-coded by gas saturation log. The arrow shows the direction of increasing gas saturation.

saturation, the template predicts a pair of P-impedance and V_p/V_s.

Figure 7 shows the RPT with the data points color-coded by the well-log crack density. The RPT predicts that at high gas saturation, the V_p/V_s decreases with increasing crack density. When the gas saturation is below 60%, the V_p/V_s increases as crack density increases. The P-impedance decreases with increasing crack density at all saturations. There is a good agreement between the data and the predictions by the RPT.

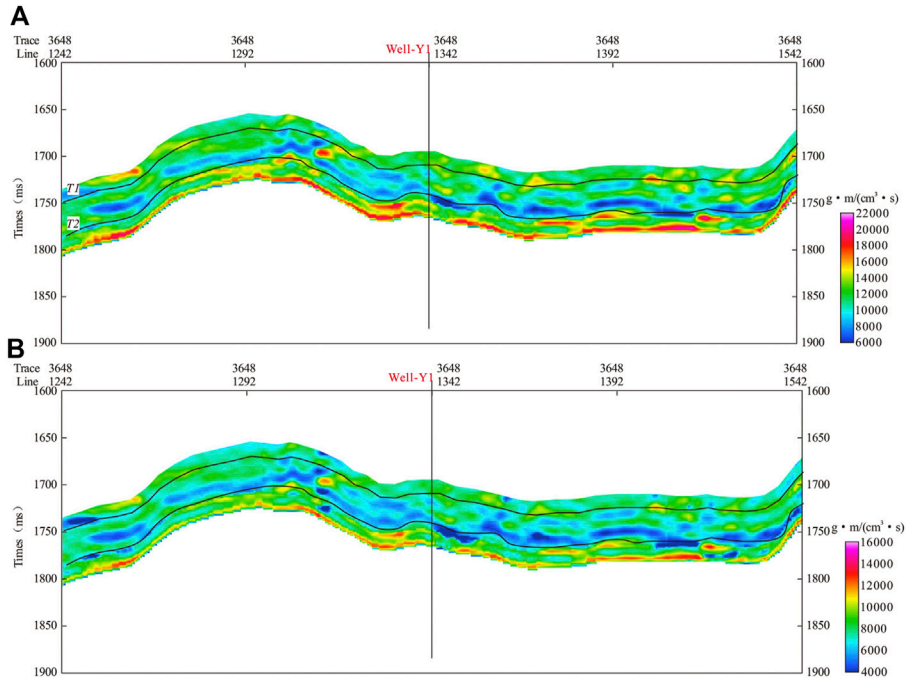

FIGURE 9 | Seismic inversion results of the shale gas field: **(A)** acoustic impedance and **(B)** shear impedance. The location of Well-Y1 is indicated by the black line.

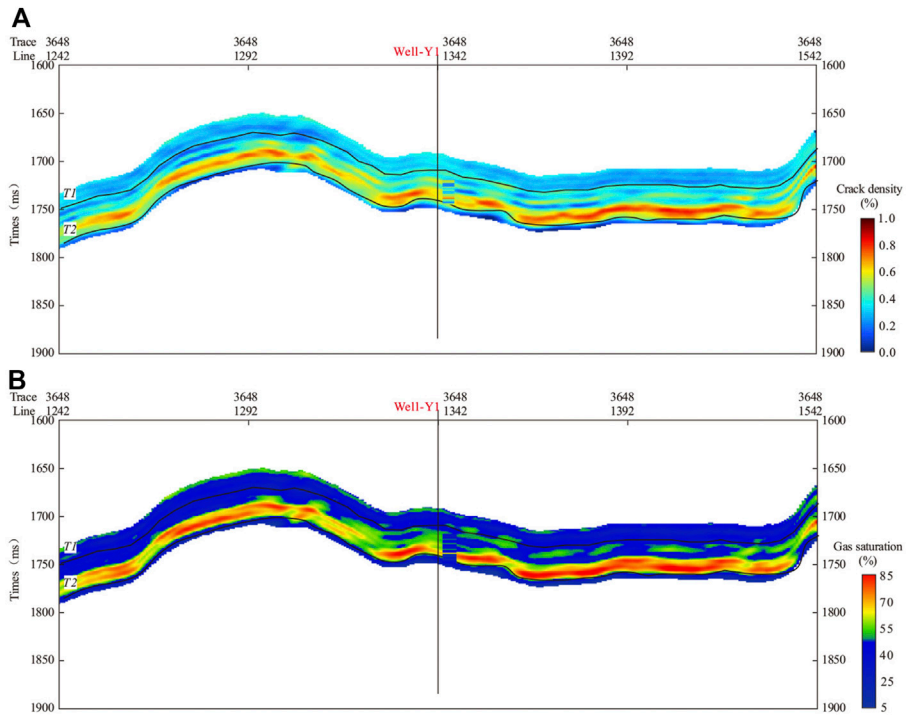

FIGURE 10 | By projecting the inversion results in **Figure 9** onto the rock physics template in **Figures 7**, **8**, we obtain the interpreted sections of **(A)** crack density, and **(B)** gas saturation.

The crack density of the shale formation can be accurately predicted from the RPT analysis. **Figure 8** presents the same RPT with the data points color-coded by the well-log saturation. Again, there is an overall excellent match between the log and predicted saturation values. The interpretation of the well-log data shows the effectiveness and accuracy of the constructed RPT. Next, we apply the RPT to the seismic data and obtain the spatial distribution of the crack density and gas saturation.

To obtain the seismic attributes required for RPT analysis, we perform the pre-stack seismic inversion. In the inversion process, the differences between the seismic amplitudes from different reflection angles are used to obtain the corresponding variation in the shale elastic properties. The pre-stack inversion is based on the Fatti's reflectivity equation in terms of acoustic and shear impedances (Fatti et al., 1994). The inversion results are shown in **Figure 9**. The top and bottom of the shale reservoir are denoted by the horizons *T*1 and *T*2, respectively. The high-quality shale at the bottom of Longmaxi formation in the work area are characterized by low impedance (blue color stripes). We can compute the V_p/V_s by taking the ratio of P- and S-impedance volumes. Similar to the log data analysis, by projecting the seismically-derived V_p/V_s, and P-impedance onto the RPT, we can predict the corresponding crack density and gas saturation. **Figure 10** shows the interpreted sections. The zones of interest can be clearly identified from the interpreted sections. The main target at the lower part of the Wufeng-Longmaxi Formation shows high gas saturation and considerable microcrack concentration. The maps indicate that the lateral distribution of high-quality shale is stable and distributed throughout the region. Such depositional pattern is consistent with the geological studies of this area (Chao et al., 2012; Liu et al., 2013). The difference in the lateral change between crack density and gas saturation can be explained by the fact that the rock and fluid property variations contribute to the change in P- and S-impedances differently (Avseth et al., 2010; Vernik, 2016). The study shows that the RPT based on dual-porosity model is an efficient tool for quantitative interpretation of the well-log and seismic data of the Wufeng-Longmaxi Shale reservoir.

4 DISCUSSION

Based on the dual-porosity model, we proposed an inversion scheme for estimating the volume fractions of different pore structures. Our analysis shows that the majority of the microcracks are formed within the clay minerals, which is consistent with the observation from the SEM images (see **Figure 5**). Sun et al. (2019) carried out a thorough analysis on the correlation between the volume of microcrack and the mineral components in the Longmaxi shale samples based on the electron microscopy and high-pressure mercury injection experiments. The results show that the contribution of clay minerals to the volume of microcracks is the largest, accounting for 70%, followed by the organic matter, and accounting for 24%. The brittle minerals (including quartz, feldspar, and dolomite) contribute to the least volumes of microcracks, accounting for 6%. The experiment also shows that there exists a positive correlation between the volumes of microcrack and clay. This agrees with the sonic-log inversion results based on the dual-porosity model.

The clay minerals reduce the brittleness of shale to a certain extent, this is not in favor of forming the microcracks by mechanical deformation due to tectonic stress (Han et al., 2021b). However, the microcracks can form in terms of small openings between the crystal layers of different clay minerals as revealed from the SEM images (Deng et al., 2021). On the other hand, clays are composed of fine sheet-like particles, they tend to form pores with much smaller aspect ratios than those associated with quartz grains. These pores are very compliant, most of which can be closed by the lithostatic stress at larger burial depth. However, overpressure is a common phenomenon in the shale gas reservoirs of Upper Ordovician Wufeng Formation and Lower Silurian Longmaxi Formation in the southern Sichuan Basin (Gao et al., 2019; Han et al., 2021a). Hydrocarbon generates from organic matter during thermal evolution, which is the main cause for abnormal high pressure in the region. The overpressure reduces the effective stress on reservoir and therefore, the majority of the microcracks still remain open for the Wufeng-Longmaxi Shale. This corroborates with our observation of considerable microcrack growth in well-Y1.

Xu and White (1995) published a velocity model for clay-sand mixtures, which is developed in terms of the Kuster-Toksöz effective medium theory and Gassmann model. In their model, the total pore-space is assumed to consist of pores associated with sand grains, and clays, respectively. The model also assumes that the pores of small aspect ratio are strictly developed in the clays whereas the pores of large aspect ratio only exist among the sand grains. Therefore, for its application one must first determine the volume of sand grain and clay content. In presence of more complex mineral components and microstructures, such as in organic-rich shales, and the classic Wu-White's model may no longer be applicable. Unlike the Xu-White's model, the dual-porosity model proposed in this work does not differentiate how the pore structures fit into the rock frame. Instead, we consider that the microcrack and stiff pores can develop in all mineral components. This assumption greatly simplifies the modeling and inversion procedures. The results as discussed earlier confirms the effectiveness of the dual-porosity model. The pore-volume inversion workflow can serve as fast evaluation tool for assessing the microcrack development in shale reservoir. In this work, the model is applied to the Wufeng-Longmaxi Shale Formation which is of uniform lithology. More future work is needed to examine the applicability of the model for reservoirs with complex lithologies.

5 CONCLUSION

In this work, we propose a simple dual-porosity model for the characterization of elastic properties of shale. The model assumes that the pore-space of shale can be divided into two parts including the pore-spaces of microcracks and stiff pores, respectively. The crack and stiff pore are defined as spheroid

inclusion with contrasting aspect ratios. The dual-porosity concept is incorporated into the anisotropic self-consistent approximation theory for obtaining the effective elastic tensor of the multimineral organic-rich shale. We use the model to analyze the elastic behavior of the Wufeng-Longmaxi Shale in Sichuan Basin, China. We address the important issue of estimating two key shale gas evaluation parameters, i.e., crack density and gas saturation from well-log and seismic data. The main conclusions can be summarized as follows:

1) The log data analysis shows that the estimated crack porosity in Wufeng-Longmaxi Shale exhibits a decreasing trend with increasing burial depths and decreasing clay content. The microcracks are mainly developed between clay minerals, which is consistent with the experimental results and observation from SEM images.

2) The velocities of the Wufeng-Longmaxi Formation is primarily controlled by the crack porosity instead of the total porosity. Both the P- and S-wave velocities show linear decreasing trends with increasing crack porosity in shale.

3) The fluid substitution analysis indicates that the gas shale is sensitive to the change of pore-fluid saturation. We can separate the gas shale from the water shale on a cross-plot between the Poisson's ratio and P-impedance.

4) The rock physics template predicts that at low gas saturation, V_p/V_s increases with increasing crack density whereas at high gas saturation, V_p/V_s decreases with increasing crack density. The well-log crack density and gas saturation can be accurately predicted from the RPT analysis. The interpreted seismic sections show that the high-quality shale at the bottom of Wufeng-Longmaxi Formation is stable and distributed throughout the region.

DATA AVAILABILITY STATEMENT

The original contributions presented in the study are included in the article/Supplementary Material, further inquiries can be directed to the corresponding author.

AUTHOR CONTRIBUTIONS

All authors listed have made a substantial, direct, and intellectual contribution to the work and approved it for submission.

FUNDING

This work is funded by Sichuan International Science and Technology Innovation Cooperation Program (Grant No: 2021YFH0050) and the National Natural Science Foundation of China (Grant No: 41904113).

ACKNOWLEDGMENTS

The authors would like to thank Jixin Deng for providing the SEM image of Wufeng-Longmaxi Shale.

REFERENCES

Avseth, P., Mukerji, T., and Mavko, G. (2010). *Quantitative Seismic Interpretation: Applying Rock Physics Tools to Reduce Interpretation Risk*. New York: Cambridge University Press.

Bachrach, R., Sayers, C. M., Dasgupta, S., Silva, J., and Volterrani, S. (2014). "Recent Advances in the Characterization of Unconventional Reservoirs with Wide-Azimuth Seismic Data," in *SEG Technical Program Expanded Abstracts 2014 (Society of Exploration Geophysicists)*. doi:10.1190/segam2014-0379.1

Backus, G. E. (1962). Long-wave Elastic Anisotropy Produced by Horizontal Layering. *J. Geophys. Res.* 67, 4427–4440. doi:10.1029/jz067i011p04427

Batzle, M., and Wang, Z. (1992). Seismic Properties of Pore Fluids. *Geophysics* 57, 1396–1408. doi:10.1190/1.1443207

Brie, A., Pampuri, F., Marsala, A., and Meazza, O. (1995). "Shear Sonic Interpretation in Gas-Bearing Sands," in *SPE Annual Technical Conference and Exhibition*. Dallas: SPE. doi:10.2118/30595-ms

Brown, R. J. S., and Korringa, J. (1975). On the Dependence of the Elastic Properties of a Porous Rock on the Compressibility of the Pore Fluid. *Geophysics* 40, 608–616. doi:10.1190/1.1440551

Carcione, J. M., Helle, H. B., and Avseth, P. (2011). Source-rock Seismic-Velocity Models: Gassmann versus Backus. *Geophysics* 76, N37–N45. doi:10.1190/geo2010-0258.1

Chao, L., Zaixing, J., Yiting, Y., and Xiaojie, W. (2012). Characteristics of Shale Lithofacies and Reservoir Space of the Wufeng-Longmaxi Formation, Sichuan Basin. *Pet. Exploration Development* 39, 691–698.

Chopra, S., Sharma, R. K., Keay, J., and Marfurt, K. J. (2012). *Shale Gas Reservoir Characterization Workflows*. SEG Technical Program Expanded Abstracts 2012 (Society of Exploration Geophysicists), 1–5. doi:10.1190/segam2012-1344.1

Deng, J., Wang, C., Zhao, Q., Guo, W., Tang, G., and Zhao, J. (2021). Depositional and Diagenetic Controls on Macroscopic Acoustic and Geomechanical Behaviors in Wufeng-Longmaxi Formation Shale. *Front. Earth Sci.* 9, 126. doi:10.3389/feart.2021.617831

Deng, J., Wang, S., and Han, D.-H. (2009). The Velocity and Attenuation Anisotropy of Shale at Ultrasonic Frequency. *J. Geophys. Eng.* 6, 269–278. doi:10.1088/1742-2132/6/3/006

Domnesteanu, P., McCann, C., and Sothcott, J. (2002). Velocity Anisotropy and Attenuation of Shale in Under- and Overpressured Conditions. *Geophys. Prospecting* 50, 487–503. doi:10.1046/j.1365-2478.2002.00329.x

Eshelby, J. D. (1957). The Determination of the Elastic Field of an Ellipsoidal Inclusion, and Related Problems. *Proc. R. Soc. Lond. Ser. A. Math. Phys. Sci.* 241, 376–396. doi:10.1098/rspa.1957.0133

Fatti, J. L., Smith, G. C., Vail, P. J., Strauss, P. J., and Levitt, P. R. (1994). Detection of Gas in sandstone Reservoirs Using AVO Analysis: A 3-D Seismic Case History Using the Geostack Technique. *Geophysics* 59, 1362–1376. doi:10.1190/1.1443695

Gao, J., Zhang, J.-k., He, S., Zhao, J.-x., He, Z.-l., Wo, Y.-j., et al. (2019). Overpressure Generation and Evolution in Lower Paleozoic Gas Shales of the Jiaoshiba Region, China: Implications for Shale Gas Accumulation. *Mar. Pet. Geology.* 102, 844–859. doi:10.1016/j.marpetgeo.2019.01.032

Goodway, B., Perez, M., Varsek, J., and Abaco, C. (2010). Seismic Petrophysics and Isotropic-Anisotropic Avo Methods for Unconventional Gas Exploration. *The Leading Edge* 29, 1500–1508. doi:10.1190/1.3525367

Guo, X., Li, Y., Liu, R., and Wang, Q. (2014). Characteristics and Controlling Factors of Micropore Structures of the Longmaxi Shale in the Jiaoshiba Area, Sichuan Basin. *Nat. Gas Industry B* 1, 165–171. doi:10.1016/j.ngib.2014.11.007

Guo, Z., and Liu, X. (2018). Seismic rock physics characterization of anisotropic shale—a Longmaxi Shale case study. *J. Geophys. Eng.* 15, 512–526.

Guo, Z., Li, X.-Y., Liu, C., Feng, X., and Shen, Y. (2013). A Shale Rock Physics Model for Analysis of Brittleness index, Mineralogy and Porosity in the Barnett Shale. *J. Geophys. Eng.* 10, 025006. doi:10.1088/1742-2132/10/2/025006

Han, T., Yan, H., and Fu, L.-Y. (2021c). A Quantitative Interpretation of the Saturation Exponent in Archie's Equations. *Pet. Sci.* 18, 444–449. doi:10.1007/s12182-021-00547-0

Han, T., Liu, S., Fu, L.-Y., and Yan, H. (2021a). Understanding How Overpressure Affects the Physical Properties of Sandstones. *Geophysics* 86, 1–33. doi:10.1190/geo2020-0776.1

Han, T., Yu, H., and Fu, L.-Y. (2021b). Correlations between the Static and Anisotropic Dynamic Elastic Properties of Lacustrine Shales under Triaxial Stress: Examples from the Ordos Basin, China. *Geophysics* 86, 1–53. doi:10.1190/geo2020-0761.1

Hornby, B. E., Schwartz, L. M., and Hudson, J. A. (1994). Anisotropic Effective-medium Modeling of the Elastic Properties of Shales. *Geophysics* 59, 1570–1583. doi:10.1190/1.1443546

Jiang, Z., Sun, Y., Liu, S., and Lin, K. (2019). Quantitative Identification of Pseudofaults Underlying Igneous Rocks through Wave-Equation-Based Velocity Modeling: A Case Study of the Shuntuoguole Uplift, Tarim Basin, China. *Interpretation* 7, T499–T512. doi:10.1190/int-2018-0107.1

Li, H., Wang, D., Gao, J., Zhang, M., Wang, Y., Zhao, L., et al. (2020). Role of Saturation on Elastic Dispersion and Attenuation of Tight Rocks: An Experimental Study. *J. Geophys. Res. Solid Earth* 125, e2019JB018513. doi:10.1029/2019jb018513

Liu, S., Ma, W., Jansa, L., Huang, W., Zeng, X., and Zhang, C. (2013). Characteristics of the Shale Gas Reservoir Rocks in the Lower Silurian Longmaxi Formation, East Sichuan Basin, China. *Energy Exploration & Exploitation* 31, 187–219. doi:10.1260/0144-5987.31.2.187

Luan, X., Di, B., Wei, J., Zhao, J., and Li, X. (2016). Creation of Synthetic Samples for Physical Modelling of Natural Shale. *Geophys. Prospecting* 64, 898–914. doi:10.1111/1365-2478.12382

Lucier, A. M., Hofmann, R., and Bryndzia, L. T. (2011). Evaluation of Variable Gas Saturation on Acoustic Log Data from the Haynesville Shale Gas Play, NW Louisiana, USA. *The Leading Edge* 30, 300–311. doi:10.1190/1.3567261

Mavko, G., Mukerji, T., and Dvorkin, J. (2009). *The Rock Physics Handbook: Tools for Seismic Analysis of Porous Media*. New York: Cambridge University Press.

Mura, T. (1982). *Micromechanics of Defects in Solids*. Leiden, Netherlands: Martinus Nijhoff.

O'Connell, R. J., and Budiansky, B. (1974). Seismic Velocities in Dry and Saturated Cracked Solids. *J. Geophys. Res.* 79, 5412–5426. doi:10.1029/JB079i035p05412

Passey, Q., Creaney, S., Kulla, J., Moretti, F., and Stroud, J. (1990). A Practical Model for Organic Richness from Porosity and Resistivity Logs. *AAPG Bull.* 74, 1777–1794. doi:10.1306/0c9b25c9-1710-11d7-8645000102c1865d

Passey, Q. R., Bohacs, K., Esch, W. L., Klimentidis, R., and Sinha, S. (2010). "From Oil-Prone Source Rock to Gas-Producing Shale Reservoir–Geologic and Petrophysical Characterization of Unconventional Shale-Gas Reservoirs," in *International Oil and Gas Conference and Exhibition in China*. Beijing, China: SPE.

Pollastro, R. M. (2007). Total petroleum system assessment of undiscovered resources in the giant Barnett Shale continuous (unconventional) gas accumulation, Fort Worth Basin, Texas. *AAPG Bull.* 91, 551–578.

Qi, Q., Fu, L.-Y., Deng, J., and Cao, J. (2021). Attenuation Methods for Quantifying Gas Saturation in Organic-Rich Shale and Tight Gas Formations. *Geophysics* 86, D65–D75. doi:10.1190/geo2020-0291.1

Qi, Q., Müller, T. M., and Pervukhina, M. (2017). Sonic QP/QS Ratio as Diagnostic Tool for Shale Gas Saturation. *Geophysics* 82, MR97–MR103. doi:10.1190/geo2016-0499.1

Rezaee, R. (2015). *Fundamentals of Gas Shale Reservoirs*. Hoboken, NJ: John Wiley & Sons.

Rich, J. P., and Ammerman, M. (2010). "Unconventional Geophysics for Unconventional Plays," in *SPE Unconventional Resources Conference/Gas Technology Symposium*. Pittsburgh: SPE, 1858–1861. doi:10.2118/131779-ms

Sena, A., Castillo, G., Chesser, K., Voisey, S., Estrada, J., Carcuz, J., et al. (2011). Seismic Reservoir Characterization in Resource Shale Plays: Stress Analysis and Sweet Spot Discrimination. *The Leading Edge* 30, 758–764. doi:10.1190/1.3609090

Si, W., Di, B., Wei, J., and Li, Q. (2016). Experimental Study of Water Saturation Effect on Acoustic Velocity of Sandstones. *J. Nat. Gas Sci. Eng.* 33, 37–43. doi:10.1016/j.jngse.2016.05.002

Sondergeld, C. H., and Rai, C. S. (2011). Elastic Anisotropy of Shales. *The leading edge* 30, 324–331. doi:10.1190/1.3567264

Sondergeld, C. H., Rai, C. S., Margesson, R. W., and Whidden, K. J. (2000). "Ultrasonic Measurement of Anisotropy on the Kimmeridge Shale," in *SEG Technical Program Expanded Abstracts 2000* (Tulsa: Society of Exploration Geophysicists), 1858–1861. doi:10.1190/1.1815791

Sun, W., Li, W., Bai, L., and Zhao, H. (2019). Prediction Method of Micro-fracture Development Degree of Shale Reservoir. *Sci. Technology Eng.* 19, 118–123.

Thomsen, L. (1986). Weak Elastic Anisotropy. *Geophysics* 51, 1954–1966. doi:10.1190/1.1442051

Uvarova, Y., Yurikov, A., Pervukhina, M., Lebedev, M., Shulakova, V., Clennell, B., et al. (2014). Microstructural Characterisation of Organic-Rich Shale before and after Pyrolysis. *APPEA J.* 54, 249–258. doi:10.1071/aj13025

Vanorio, T., Mukerji, T., and Mavko, G. (2008). Emerging Methodologies to Characterize the Rock Physics Properties of Organic-Rich Shales. *The Leading Edge* 27, 780–787. doi:10.1190/1.2944163

Vasin, R. N., Wenk, H. R., Kanitpanyacharoen, W., Matthies, S., and Wirth, R. (2013). Elastic Anisotropy Modeling of Kimmeridge Shale. *J. Geophys. Res. Solid Earth* 118, 3931–3956. doi:10.1002/jgrb.50259

Vernik, L., and Liu, X. (1997). Velocity Anisotropy in Shales: A Petrophysical Study. *Geophysics* 62, 521–532. doi:10.1190/1.1444162

Vernik, L., and Nur, A. (1992). Ultrasonic Velocity and Anisotropy of Hydrocarbon Source Rocks. *Geophysics* 57, 727–735. doi:10.1190/1.1443286

Vernik, L. (2016). *Seismic Petrophysics in Quantitative Interpretation*. Tulsa: Society of Exploration Geophysicists.

Wu, J., Yuan, Y., Niu, S., Wei, X., and Yang, J. (2020). Multiscale Characterization of Pore Structure and Connectivity of Wufeng-Longmaxi Shale in Sichuan Basin, China. *Mar. Pet. Geology.* 120, 104514. doi:10.1016/j.marpetgeo.2020.104514

Xu, S., and White, R. E. (1995). A New Velocity Model for clay-sand Mixtures 1. *Geophys. prospecting* 43, 91–118. doi:10.1111/j.1365-2478.1995.tb00126.x

Xu, Z., Shi, W., Zhai, G., Clay, C., Zhang, X., and Peng, N. (2019). A rock physics model for characterizing the total porosity and velocity of shale: A case study in Fuling area, China. *Marine Petrol. Geol.* 99, 208–226.

Zhao, L., Wang, Y., Liu, X., Zhang, J., Liu, Y., Qin, X., et al. (2020). Depositional Impact on the Elastic Characteristics of the Organic Shale Reservoir and its Seismic Application: A Case Study of the Longmaxi-Wufeng Shale in the Fuling Gas Field, Sichuan Basin. *Geophysics* 85, B23–B33. doi:10.1190/geo2019-0326.1

Zhou, X., Ba, J., Santos, J. E., Carcione, J. M., Fu, L.-Y., and Pang, M. (2021). Fluid Discrimination in Ultra-deep Reservoirs Based on a Double Double-Porosity Theory. *Front. Earth Sci.* 9, 288. doi:10.3389/feart.2021.649984

Conflict of Interest: The authors declare that the research was conducted in the absence of any commercial or financial relationships that could be construed as a potential conflict of interest.

Publisher's Note: All claims expressed in this article are solely those of the authors and do not necessarily represent those of their affiliated organizations, or those of the publisher, the editors and the reviewers. Any product that may be evaluated in this article, or claim that may be made by its manufacturer, is not guaranteed or endorsed by the publisher.

frontiers in Earth Science

ORIGINAL RESEARCH
published: 16 February 2022
doi: 10.3389/feart.2022.848954

A Novel Method for Determining Geophone Orientations From Zero-Offset VSP Data Constrained by Scalar Field

Yuyong Yang[1,2], *Qiaomu Qi*[1,2]*, *Huailai Zhou*[1,2] *and Zhengyang Wang*[2]

[1]State Key Laboratory of Oil and Gas Reservoir Geology and Exploitation, Chengdu University of Technology, Chengdu, China, [2]College of Geophysics, Chengdu University of Technology, Chengdu, China

In vertical seismic profile (VSP) acquisition, the orientation of the three-component geophones in a borehole is often not aligned due to random rotation of the wireline receiver array. Knowing the geophone orientation is crucial for rotating the waveforms back to the position where the geophones are assumed to be aligned. This procedure is critical in three-component VSP data processing as it provides the correct wavefields for subsequent VSP data imaging and inversion. For zero-offset or near zero-offset VSP measurements, the direct P-wave propagates nearly vertically, and the horizontal geophones receive only a small fraction of the direct P-wave energy. The first-arrival in the horizontal component data is often of low signal-to-noise ratio (SNR). As a result, it is difficult to apply conventional first-arrival–based methods for obtaining accurate geophone orientations. On the other hand, a seismic event comprising individual waveform would achieve maximum correlation if all corresponding geophones are aligned. The geometric characteristics, that is, the slope and continuity of a seismic event in the vector wavefield are the same with those of the modules of the vector wavefield. The latter, also known as the scalar wavefield, can be used for scanning geophone orientations based on waveform correlation. In this study, we propose to use the scalar field to extract the slope of seismic events. The orientation of the individual geophone was calculated with the constraint of the slope. We use both synthetic and field data to demonstrate the effectiveness and applicability of the proposed method. The results show that the new method can provide wavefields of horizontal component VSP data with much higher accuracy and resolution.

Keywords: geophysical signal processing, seismic waves, vertical seismic profile, geophone orientations, scalar field

OPEN ACCESS

Edited by:
Lidong Dai,
Institute of Geochemistry (CAS), China

Reviewed by:
Shida Sun,
Hebei GEO University, China
Lei Liu,
China Earthquake Administration, China

***Correspondence:**
Qiaomu Qi
Qiaomu_Qi@163.com

Specialty section:
This article was submitted to Solid Earth Geophysics, a section of the journal Frontiers in Earth Science

Received: *05 January 2022*
Accepted: *19 January 2022*
Published: *16 February 2022*

Citation:
Yang Y, Qi Q, Zhou H and Wang Z (2022) A Novel Method for Determining Geophone Orientations From Zero-Offset VSP Data Constrained by Scalar Field. Front. Earth Sci. 10:848954. doi: 10.3389/feart.2022.848954

INTRODUCTION

The orientations of the geophones are hard to control in the borehole, which leads to random rotation of horizontal geophones in the three-component VSP acquisition. A universal coordinate system is required for processing vector field data of different acquisition positions. The inconsistent orientation of geophones not only leads to inconsistent coordinate systems of geophone data but also cause poor continuity of the events of the received vector wavefield (DiSiena et al., 1984). This makes the processing and analysis of VSP data difficult. Accurate information about the orientations of

geophones is critical for transforming the geophone coordinate systems with Z-, X-, and Y-component axes into a consistent acquisition coordinate system with Z-, R- (radial of shot-receiver), and T-component (transverse of shot-receiver) axes (Liu et al., 2003), which is also the foundation of subsequent vector wave separation (Lu et al., 2018, 2019).

In the methods for determining geophone orientation, the most common one is based on the first-arrival of P-wave. In a VSP acquisition, the polarization direction of first-arrival is parallel to the direction of the shot-to-receiver array. Therefore, the direction of the geophone can be determined by analyzing the polarization characteristics of first-arrivals. Methods related to first-arrival include signal correlation (Becquey and Dubesset, 1990; Guevara and Stewart, 2001), matrix transform (Greenhalgh and Mason, 1995; Hendrick and Hearn, 1999; Li and Yuan, 1999; Park et al., 2004), principal component analysis (Michaels 2001), polarization analysis (Knowlton and Spencer, 1996; Oye and Ellsworth, 2005), energy maximization (Lagos and Velis, 2019), and eigenvector and eigenvalue method (Zaręba and Danek, 2018). Menanno et al. (2013) pointed out that the geophone orientation in a walkaround VSP can be estimated more accurately by using a 3D velocity model and allowing for ray bending. The aforementioned methods rely on accurate picking of P-wave first-arrival. The advantages of these methods are fewer data input and fast evaluation. They are commonly suitable for VSP data with strong first-arrivals. However, for zero-offset or near zero-offset VSP measurements, the direct P-wave propagates vertically to the subsurface sediments, leading to weak energy of horizontal components. Furthermore, due to attenuation and dispersion of seismic waves, the amplitude decay of signals becomes more pronounced with increasing depth. In addition, noises in field data may also smear the weak direct P-wave signals. Therefore, in practice, it is difficult to obtain the orientations of geophones by simply analyzing the first-arrival signals.

There also exist a group of methods that do not make use of the first-arrival signals. Zeng and McMechan proposed the relative angle method (Zeng and McMechan, 2006; Katou et al., 2018), where the orientations of the geophones are obtained by averaging the relative azimuths calculated from all shot points. Huo et al. (2021) determined the relative orientations between the sensor pairs by maximizing the waveform coherence along all the traces for the seismic events. These methods are especially suitable for the cases where multiple resources are located at different positions. However, for single-shot data, it is not easy to collect the statistics of relative angles. Grigoli et al. (2012) proposed a complex linear least-squares method to derive relative and absolute geophone orientations. Krieger and Grigoli (2015) used the eigenvectors of a real symmetric matrix to form quaternions and performed coordinate rotation. Zhu et al. (2018) developed a least squares method and combined an attitude and heading reference system for the orientation of all geophones in geographical coordinates. In essence, these methods are used to rotate the signal of one geophone to the coordinate system of another geophone. This requires that the distance between the geophones is much smaller than the wavelength and presence of limited number of geophones so that the time difference between detectors can be ignored. However, when the number of geophones increases, the non-zero time difference can lead to cumulative errors.

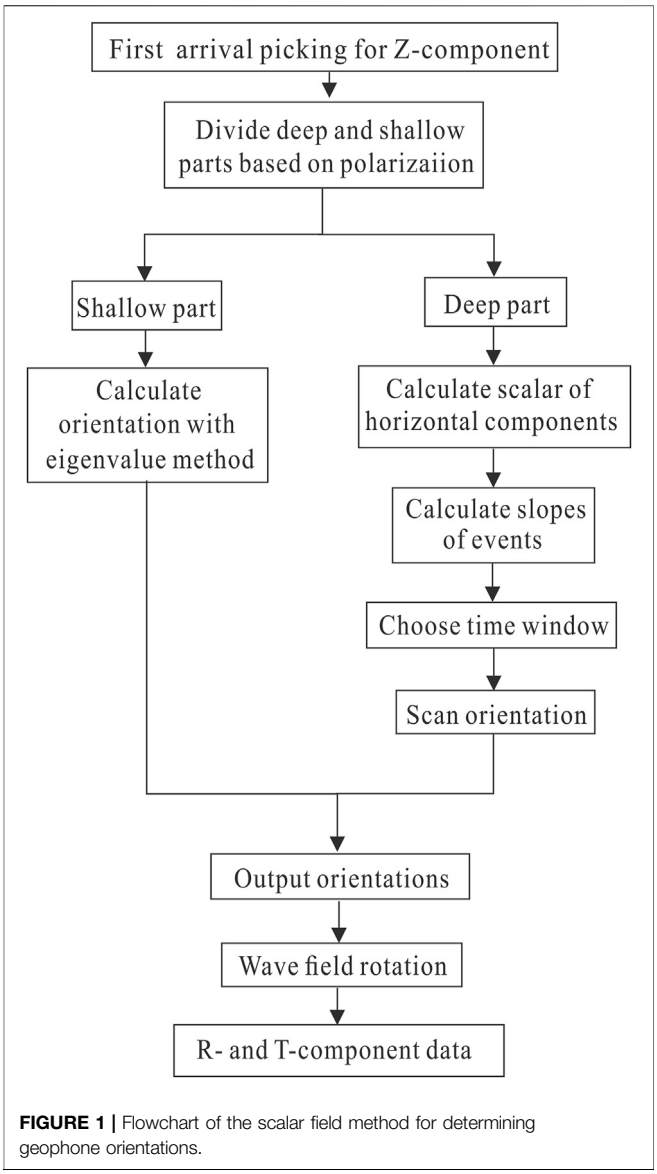

FIGURE 1 | Flowchart of the scalar field method for determining geophone orientations.

On the other hand, the geometric characteristics (slope and continuity) of the seismic events in vector wavefields are consistent with those of scalar fields (i.e., module of vector field). If the geophones are aligned, meaning each component of the geophone points to the same direction, the seismic event would achieve maximum correlation. Therefore, this important information can be used as a constraint to scan the orientations of geophones based on waveform correlation. In this study, we propose to divide the shot gather data into shallow and deep parts because in the shallow part, the P-waves travel a shorter distance and experience less attenuation. For this situation, the direct first-arrivals can still be evident and applied to determine geophone orientations. In the deep part, based on the scalar field of the horizontal component, the slopes of events are obtained.

TABLE 1 | Parameters of the model.

Layer	P-wave velocity (*m*/*s*)	S-wave velocity (*m*/*s*)	Density (kg/m^3)	Thickness (*m*)
1	1,000	525	1,565	400
2	2,500	1,450	2,200	300
3	3,000	1,730	2,200	100
4	3,500	2,020	2,275	700

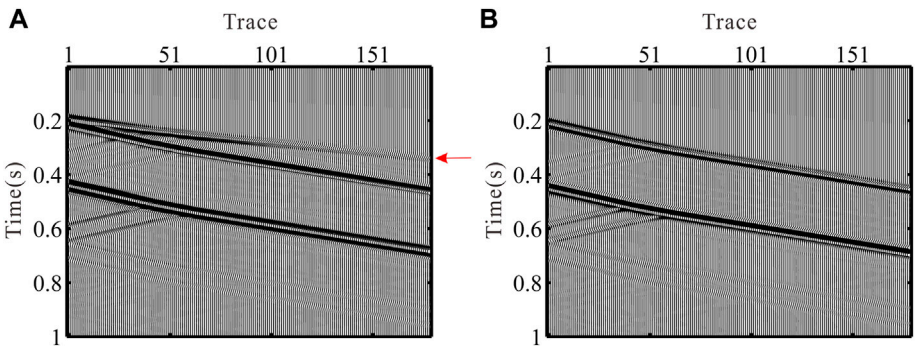

FIGURE 2 | Synthetic VSP data without noises and the geophones are aligned. **(A)** X-component. **(B)** Y-component.

With the constraint of this attribute, we extract the accurate orientations of geophones. This is followed by reconstructing the correct horizontal component wavefields. Both synthetic and field VSP data were used to demonstrate the applicability of the proposed method.

METHODS

Orientation Determination Based on First-Arrival Eigenvalue Method

Signals received by the geophone at shallow depth show the characteristics of approximate linear polarization. This is because with shorter travel distance, the first-arrival amplitude experiences less attenuation and hence, the signal-to-noise ratio (SNR) is high. The conventional eigenvalue methods that use first-arrivals can be directly used to calculate the geophone orientations. First, we need to determine the average value within the time window of first-arrivals. This can be achieved by using the following equations:

$$\begin{cases} \overline{x_i(t)} = \frac{1}{N}\sum_{t=t_{fi}-wt}^{t_{fi}+wt} x_i(t) \\ \overline{y_i(t)} = \frac{1}{N}\sum_{t=t_{fi}-wt}^{t_{fi}+wt} y_i(t) \end{cases}. \tag{1}$$

Then, a covariance matrix is created as follows:

$$M = \begin{bmatrix} \sum_{t=t_{fi}-wt}^{t_{fi}+wt}\left(x_i(t)-\overline{x_i(t)}\right)^2 & \sum_{t=t_{fi}-wt}^{t_{fi}+wt}\left(x_i(t)-\overline{x_i(t)}\right)\left(y_i(t)-\overline{y_i(t)}\right) \\ \sum_{t=t_{fi}-wt}^{t_{fi}+wt}\left(x_i(t)-\overline{x_i(t)}\right)\left(y_i(t)-\overline{y_i(t)}\right) & \sum_{t=t_{fi}-wt}^{t_{fi}+wt}\left(y_i(t)-\overline{y_i(t)}\right)^2 \end{bmatrix}, \tag{2}$$

where x_i(t) and y_i(t) are original signals of x and y components, t_{fi} is the first-arrival at the *i*th geophone, and *wt* is the half-length of the time window. The largest eigenvector of the covariance matrix **Eq. 2** is associated with the polarization direction and represents the deflection angle. The ratio of the minimum and maximum eigenvalues is the polarizability (Jolliffe, 1986). Therefore, the R- and T-component data can be calculated based on the deflection angle αs follows:

$$\begin{bmatrix} R_i(t) \\ T_i(t) \end{bmatrix} = \begin{bmatrix} sin\,\alpha_s & cos\,\alpha_s \\ -cos\,\alpha_s & sin\,\alpha_s \end{bmatrix} \begin{bmatrix} x_i(t) \\ y_i(t) \end{bmatrix}. \tag{3}$$

Orientation Scanning Constrained by Scalar Field

For deep geophones, it is difficult to determine the geophone orientation through the first-arrivals with low signal-to-noise ratio. The vector wavefield comprising X- and Y-components cannot reflect the slope and continuity of events due to random geophone orientations. However, the module of the vector wavefield, that is, the scalar wavefield is independent of the geophone orientations. This feature enables the scalar field of horizontally polarized waves (mainly S-wave and possibly P-wave) to reflect the characteristics of the slope and continuity of the events.

In the first step, we calculate the scalar field by taking the modules of the horizontally polarized wave, that is, the *i*th horizontal components $x_i(t)$ and $y_i(t)$:

$$S_i(t) = \sqrt{x_i(t)^2 + y_i(t)^2}. \tag{4}$$

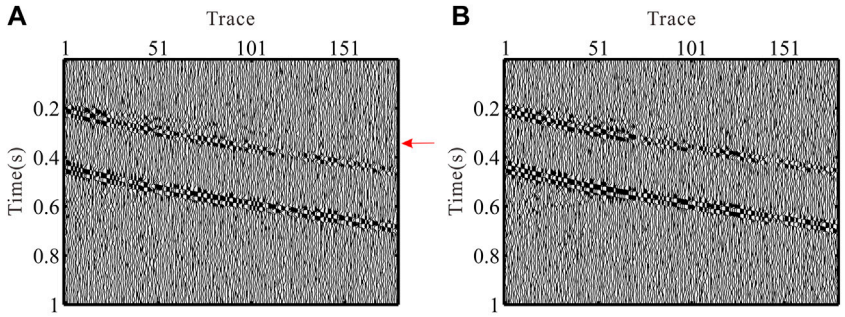

FIGURE 3 | Synthetic VSP data with noises and random geophone rotations. **(A)** X- and **(B)** Y-component.

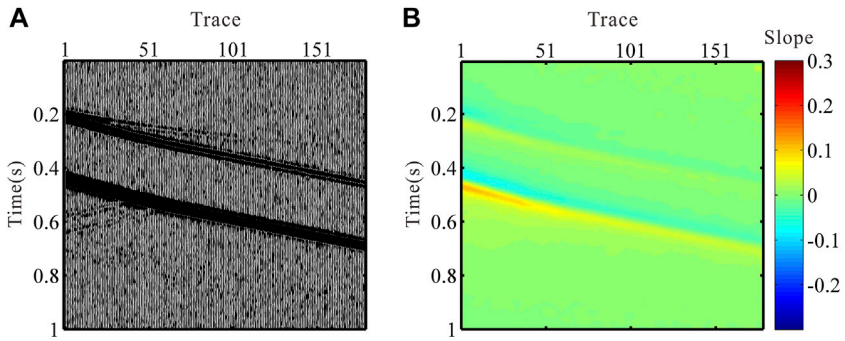

FIGURE 4 | (A) Scalar field of the horizontal components of synthetic VSP data and **(B)** corresponding slope of the scalar field.

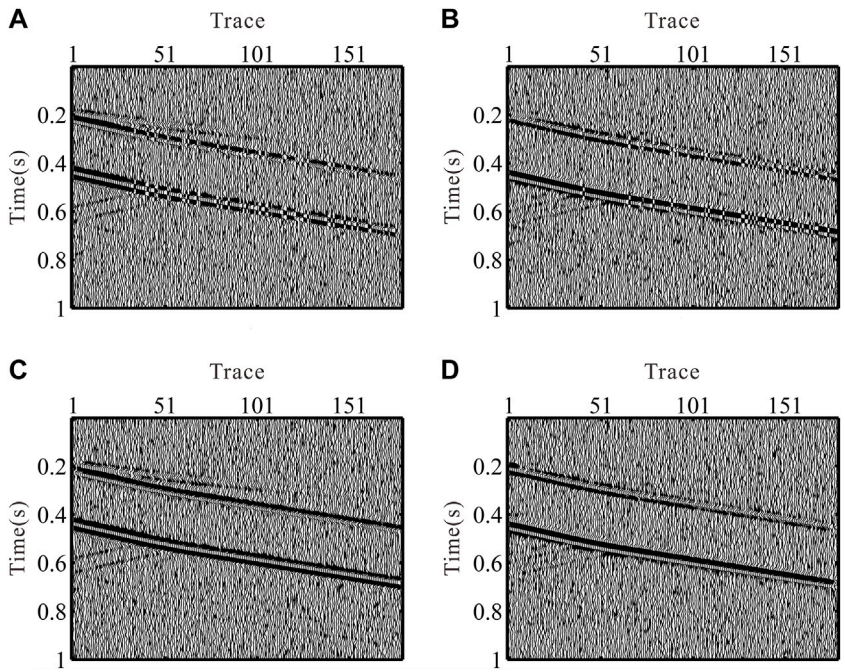

FIGURE 5 | (A) R- and **(B)** T-component VSP data generated by the largest eigenvector of covariance matrix **(C).** R- and **(D)** T-component generated by the proposed method.

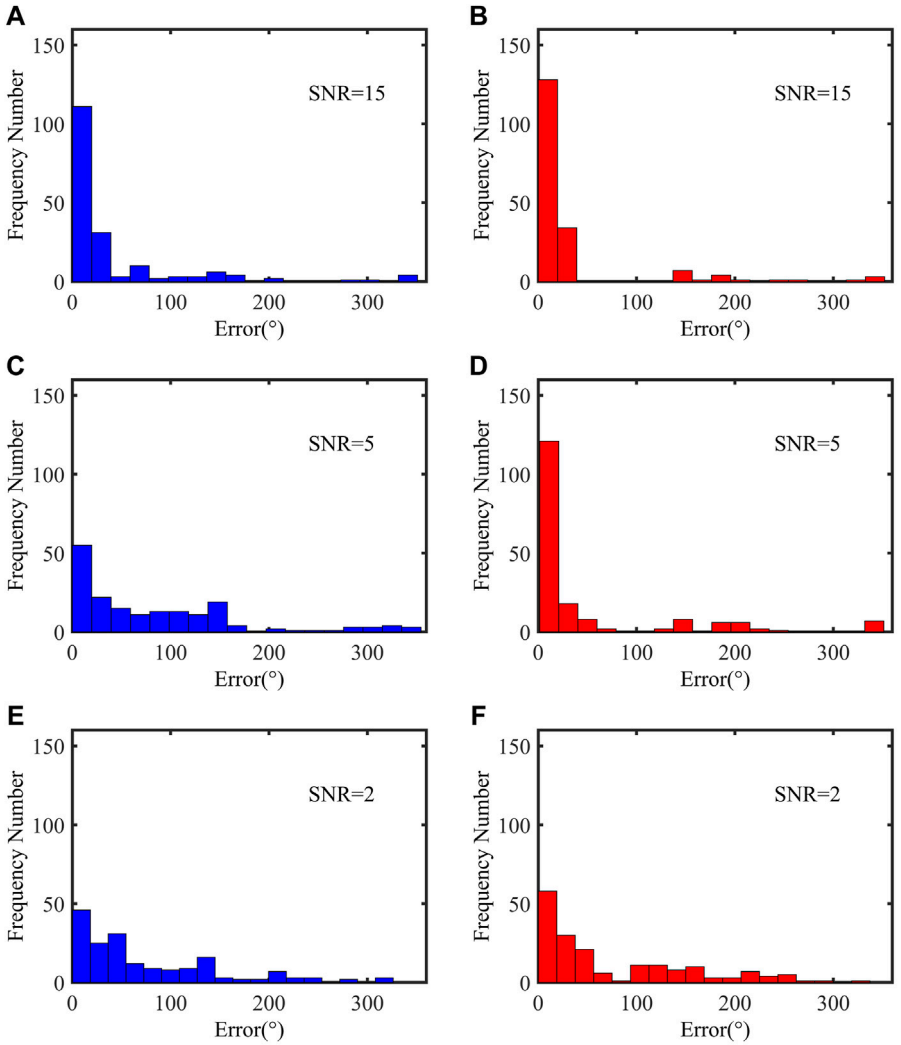

FIGURE 6 | Errors in orientation results of all geophones for the synthetic data. The SNRs of **(A–B)**, **(C–D)**, and **(E–F)** are 15, 5, and 2dB. The left column shows the results obtained from the eigenvalue method, and the right column shows the results obtained using the scalar field method.

The seismic events associated with the scalar field of the horizontal components are usually continuous. The corresponding slope indicates the apparent velocity of the seismic wave. The slope can be used as a constraint for scanning geophone orientation. A fast method to calculate the slope of events is to use the negative ratio of the x- and t-direction (i.e., time-depth domain) scalar field data with Hilbert and inverse Fourier transformations (Liu et al., 2015):

$$k_{i,t} = tan\,\sigma_{i,t} \approx tan\left(-\frac{FFT^{-1}\left[H_{HT}(x)_{i,t}\right]}{FFT^{-1}\left[H_{HT}(t)_{i,t}\right]} \right), \tag{5}$$

where σ is the dip angle of events. The next step is to choose an appropriate time window for orientation scanning. It is unnecessary to choose the slope of all sampling points as the constraint because this increases computation cost. Instead, it can be optimized by selecting the time window where the sample point attains maximum correlation in the scalar field. The correlation between trace i and previous M traces can be calculated by

$$C_i(t) = \frac{\sum_{\tau=-w}^{w} \prod_{m=0}^{M} S_{i-m}\left(t-\tau-m\Delta x k_{i,t}\right)}{\sqrt{\prod_{m=0}^{M} \sum_{\tau=-w}^{w} S_{i-m}^2\left(t-\tau-m\Delta x k_{i,t}\right)}},$$
$$\left(t-\tau-m\Delta x k_{i,t} \in (0,n)\right), \tag{6}$$

where Δx is the interval of geophones, and n is sample number. The maximum correlation of trace i is determined through

$$C_i(t_{i\,max}) = max\{C_i(t)\}. \tag{7}$$

Setting the orientation of the horizontal geophone as α_d, the signals of R- and T-components can be rotated as follows:

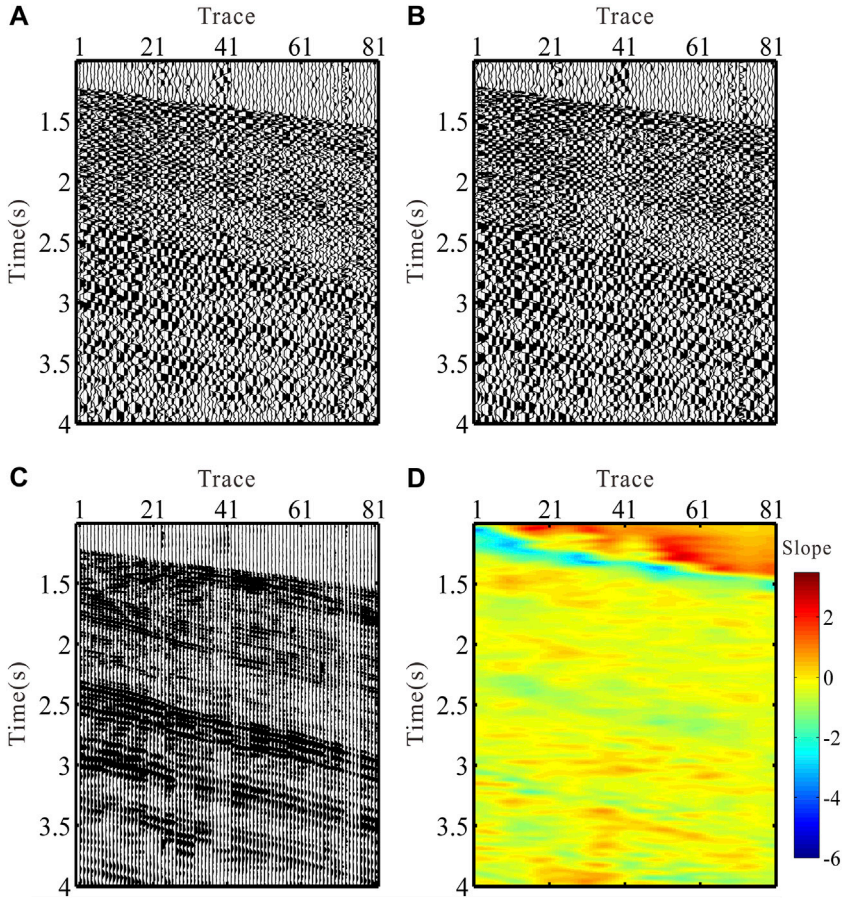

FIGURE 7 | Field zero-offset VSP data before rotation. **(A)** X-component. **(B)** Y-component. **(C)** Scalar field of the horizontal components data. **(D)** Corresponding slope of the scalar field.

$$\begin{bmatrix} R_i(t) \\ T_i(t) \end{bmatrix} = \begin{bmatrix} sin\,\alpha_d & cos\,\alpha_d \\ -cos\,\alpha_d & sin\,\alpha_d \end{bmatrix} \begin{bmatrix} x_i(t) \\ y_i(t) \end{bmatrix}. \tag{8}$$

The objective function of orientation scanning is the sum of the correlation of R- and T-components constrained by the slope of events in the scalar field:

$$C_{RTi}(\alpha_d) = \frac{\sum_{\tau=-w}^{w}\prod_{m=0}^{M} R_{i-m}\left(t_{imax}-\tau-m\Delta xk_{i,t}\right)}{\sqrt{\prod_{m=0}^{M}\sum_{\tau=-w}^{w} R_{i-m}^2\left(t_{imax}-\tau-m\Delta xk_{i,t}\right)}} + \frac{\sum_{\tau=-w}^{w}\prod_{m=0}^{M} T_{i-m}\left(t_{imax}-\tau-m\Delta xk_{i,t}\right)}{\sqrt{\prod_{m=0}^{M}\sum_{\tau=-w}^{w} T_{i-m}^2\left(t_{imax}-\tau-m\Delta xk_{i,t}\right)}}, i \geq H_0, \tag{9}$$

where H_0 is the number of geophones in the shallow region. Because the orientations of the shallow geophones are obtained by the eigenvalue method, the shallow trace data need to satisfy the following conditions: 1) the polarizability is small enough; 2) the SNR of the first-arrival is high, which is the basis of the eigenvalue method to obtain relatively accurate results. When the objective function attains the maxima, α_{dmax} is the orientation of the ith trace, that is,

$$C_{RTi}(\alpha_{d\,max}) = max\{C_{RTi}(\alpha_d)\}. \tag{10}$$

The workflow is summarized in **Figure 1**. First, we pick the first-arrival based on the Z-component data. This is followed by dividing the VSP shot gather into shallow and deep parts based on the polarizations of the first-arrivals. Then, the orientations of geophones in the shallow and deep parts are obtained by the eigenvalue and scalar field methods, respectively. Finally, the horizontal components are rotated based on the orientation, and accurate R- and T-component data can be obtained.

DATA EXAMPLE

In this section, both synthetic and field data are used to examine the effectiveness of the proposed workflow. To model the VSP data, we establish a horizontal 4-layer model, the parameters of which are given in **Table 1**. The VSP acquisition is as follows: the

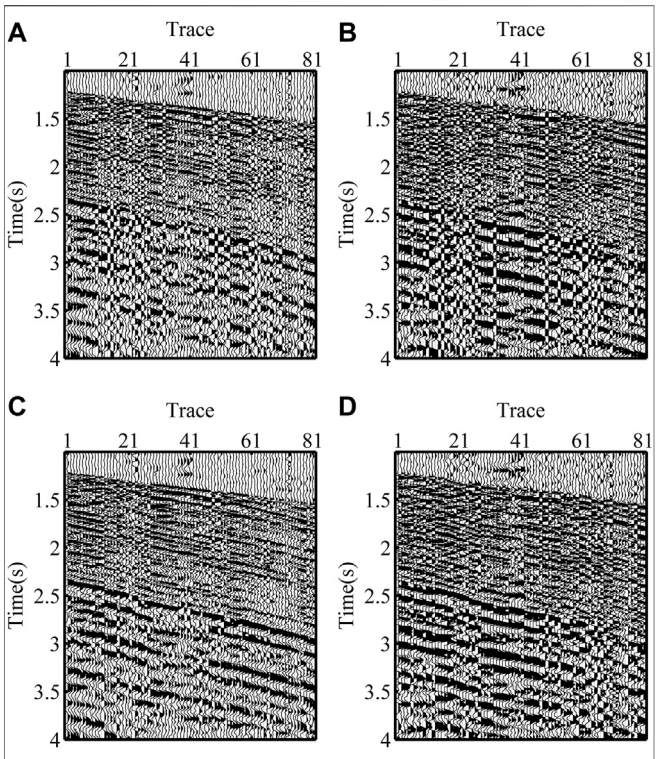

FIGURE 8 | Field seismic data after rotation. **(A)** R- and **(B)** T-component VSP data generated by the eigenvalue method. **(C)** R- and **(D)** T-component generated by the scalar field method.

geophones are located at the depth of 500–1,400 m in a well with an interval of 5 m. The shot point is located at the surface with a zero-offset. **Figure 2** shows the single-shot record simulated using finite difference elastic wave simulation. As indicated by the red arrow, the first-arrivals of the P-wave received by geophones at greater depth show weak amplitude. In the abovementioned example, the geophones are aligned, and the data are noise-free. In the second example, the noises are added with a signal-to-noise ratio of 10dB to the simulated data. In addition, a random rotation is assigned to each geophone to mimic the actual VSP acquisition in a well. The data with noises and random geophone rotation are shown in **Figure 3**. As indicated by the red arrow, we can barely identify the first-arrivals which are masked by noises. Therefore, it is almost impossible to determine the polarization direction of the first-arrival. The continuity of the wavefields also deteriorates.

The scalar field of the horizontal components and the slope of events are calculated based on **Eq. 4** and **Eq. 5**, respectively. The results are shown in **Figure 4**. To fully test the scalar field method based on slope constraint, we set the shallow part as the first five traces and the parameter M in **Eq. 6** and **Eq. 9** as 5. Using **Eq. 8** and **Eq. 9**, the X- and Y-component data are rotated to R- and T-components based on the results of the orientation scanning. The R- and T-components are shown in **Figures 5C,D**. For comparison, we also present the results from the eigenvalue method in **Figures 5A,B**. As shown in **Figures 5C,D**, the orientation scanning is constrained by scalar field results in the R/T components that closely resemble the original data (see **Figure 2**). In **Figures 5A,B**, the noises persist in the data, and the eigenvalue method produces rotated data with poor continuity of the events.

In order to evaluate the accuracy of the two methods, we apply the eigenvalue and the scalar field methods to synthetic data with different noise levels. We take the absolute value of the difference between the predicted and the accurate orientations of the geophones as the error. In **Figure 6**, the blue and red histograms show the error distributions associated with the eigenvalue and the scalar field methods, respectively. The error is expressed in terms of angle degree. The SNR of the data in **Figures 6A,B**, **Figures 6C,D**, and **Figures 6E,F** are 2, 15, and 5dB, respectively. **Figure 6** clearly shows that the scalar field method is superior to the eigenvalue method especially when the data are of poor quality (with a low SNR). The scalar field method is efficient in predicting the geophone orientation angle, regardless of the noise level. In contrast, the eigenvalue method becomes less effective in handling noisy data.

Finally, the proposed scalar field method is applied to a field zero-offset VSP dataset shown in **Figures 7A,B**. The borehole geophones are located between 2,800 and 3,600 m in a well with a spacing of 10 m. **Figures 7C,D** show the scalar field of the horizontal components and the slope of events calculated using **Eq. 4** and **Eq. 5**, respectively. We first show results associated with the eigenvalue method in **Figures 8A,B**. We can see that there are some abrupt amplitude changes and phase reversals in the R/T components. This leads to poor continuity of the reflection events. For the same purpose as the model test, we set the shallow part as first five traces and M as 5. The results from the scalar field method are shown in **Figures 8C,D**. It is evident that the SNR of VSP data becomes much higher, and the continuity of events is significantly improved.

In order to compare the wavefield recovery of the two methods in more detail, we selected different types of wavefields for comparison, as shown in **Figure 9**. The left and right columns are the results of the eigenvalue method and the scalar field method, respectively. **Figures 9A,B** show the first-arrivals. The results shown in the right column have better continuity. **Figures 9C,D** show the upgoing wavefield. The results shown in the right column contain the upgoing wavefield (the slopes of the upgoing and downgoing wavefield events are opposite) as shown by the red quadrilateral in **Figure 9D**. **Figures 9E,F** show the first-arrivals of shear wave, and it is obvious that the continuity of the results on the right is better. The comparison clearly shows that the developed workflow is efficient in determining the geophone orientations. The latter forms the basis for an accurate R/T component wavefield recovery.

DISCUSSION

In the deep layer, the orientations of the geophones are calculated one by one from the first to the last. As the objective function in **Eq. 9**, the orientation of the current geophone is determined by the signals of the previous M traces, and it is necessary to ensure that there are enough traces in the shallow layer when calculating the first trace in the deep layer. Therefore, the number of geophones (H_0) in the shallow part should be greater than M. In addition, the orientation scanning of the current trace is constrained by the previous M trace data. Such a procedure

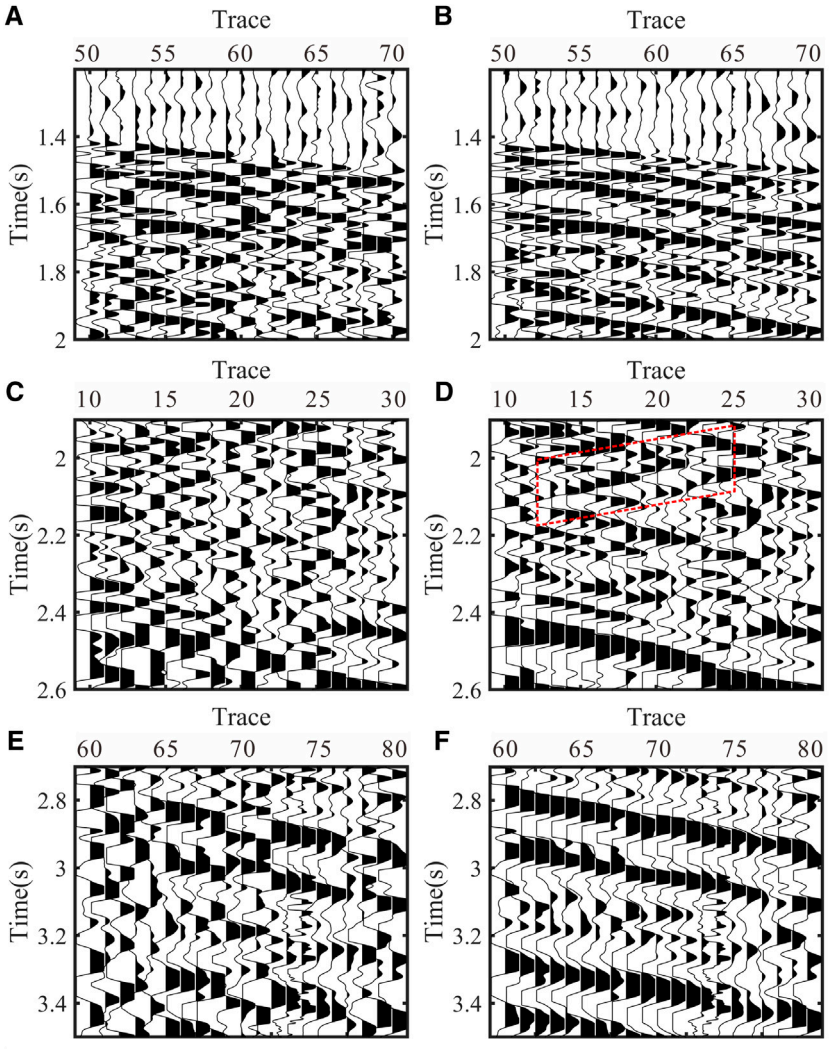

FIGURE 9 | Typical wavefields of field seismic data after rotation. **(A), (C)**, and **(E)**: VSP data generated by the eigenvalue method. **(B), (D)**, and **(F)**: VSP data generated by the scalar field method.

increases the stability of the algorithm compared with the calculation that uses only two adjacent traces. Especially for the VSP acquisition with a long geophone array, the scalar field method produces less cumulative error and is less sensitive to noises. However, the proposed method is based on the accurate results of shallow geophone orientations. If the shallow results are not accurate, it is also difficult to obtain accurate results using the scalar field method. This shows that the implementation of this method is not independent.

We have demonstrated that this method is effective for zero-offset VSP data. Moreover, it is expected that the method can also be applied to non–zero-offset VSP data. This is because the slope of the scalar field in any VSP survey system can be used in constraining the rotation of horizontal components. On the other hand, since seismic waves may not propagate along the Z-component direction of the geophones, the horizontal and vertical components can receive both P- and S-wave signals. After geophone orientation correction, the pure P- and S-waves shall be extracted from horizontal and vertical components for the subsequent PP and PS imaging/inversion. This will be a subject of future research.

CONCLUSION

Aiming at the problem that the first-arrivals of zero-offset VSP data can be weak and contaminated by noises, we propose a scalar field method for accurately determining the geophone orientations. The method uses the scalar field of the horizontal component as a constraint in the orientation scanning process and yields reliable orientation angles of geophones. To achieve this, we need to divide the shot gather data into shallow and deep parts based on the polarization characteristics of the first-arrivals. Shallow data can be processed by the eigenvalue method. For deep data, we calculate the scalar field of the horizontal

component. The slopes of events are obtained by the Hilbert transform of the scalar field data. Making use of these slopes, orientation scanning, which is the sum of the correlation between X- and Y-components, can be carried out in a constrained time window. The synthetic and field data applications show that the scalar field method is efficient in determining geophone orientations from zero-offset VSP data.

DATA AVAILABILITY STATEMENT

The original contributions presented in the study are included in the article/Supplementary Material, further inquiries can be directed to the corresponding author.

AUTHOR CONTRIBUTIONS

YY, QQ, and ZW developed the method and performed the applications. HZ supervised the findings of this study. All authors discussed the results and contributed to the final manuscript.

FUNDING

This study was funded by the National Natural Science Foundation of China (Grant Numbers, 41904113 and 42074160) and the Sichuan International Science and Technology Innovation Cooperation Program (Grant Numbers, 2021YFH0050 and 2021YFG0257).

REFERENCES

Becquey, M., and Dubesset, M. (1990). Three-component Sonde Orientation in a Deviated Well. *Geophysics* 55 (10), 1386–1388. doi:10.1190/1.1442786

DiSiena, J. P., Gaiser, J. E., Corrigan, D., and Toksöz, M. N. (1984). "Horizontal Components and Shear Wave Analysis of Three-Component VSP Data," in *Vertical Seismic Profiling, Part B: Advanced Concepts*. Editors M. N. Toksöz and R. R. Stewart (London: Geophysical Press Ltd.), 177–235.

Greenhalgh, S. A., and Mason, I. M. (1995). Orientation of a Downhole Triaxial Geophone. *Geophysics* 60 (4), 1234–1237. doi:10.1190/1.1443852

Grigoli, F., Cesca, S., Dahm, T., and Krieger, L. (2012). A Complex Linear Least-Squares Method to Derive Relative and Absolute Orientations of Seismic Sensors. *Geophys. J. Int.* 188 (3), 1243–1254. doi:10.1111/j.1365-246X.2011.05316.x

Guevara, S. E., and Stewart, R. R. (2001). "3-C Geophone Orientation and Wave Modes Polarization," in *SEG Technical Program Expanded Abstracts* (Tulsa, Oklahoma, USA: Society of Exploration Geophysicists), 799–801. doi:10.1190/1.1816754

Hendrick, N., and Hearn, S. (1999). Polarisation Analysis: What Is it? Why Do You Need it? How Do You Do it? *Exploration Geophys.* 30 (4), 177–190. doi:10.1071/eg999177

Huo, Y., Zhang, W., Zhang, J., and Yang, H. (2021). Using Microseismic Events to Improve the Accuracy of Sensor Orientation for Downhole Microseismic Monitoring. *Geophys. Prospecting* 69 (6), 1167–1180. doi:10.1111/1365-2478.13099

Jolliffe, I. T. (1986). *Principal Component Analysis*. New York: Springer.

Katou, M., Abe, S., Saito, H., and Sato, H. (2018). Reciprocal Data Acquisition and Subsequent Waveform Matching for Integrated Onshore-Offshore Seismic Profiling. *Geophys. J. Int.* 212 (1), 509–521. doi:10.1093/gji/ggx374

Knowlton, K. B., and Spencer, T. W. (1996). Polarization Measurement Uncertainty on Three-component VSP. *Geophysics* 61 (2), 594–599. doi:10.1190/1.1443985

Krieger, L., and Grigoli, F. (2015). Optimal Reorientation of Geophysical Sensors: A Quaternion-Based Analytical Solution. *Geophysics* 80 (2), F19–F30. doi:10.1190/GEO2014-0095.1

Lagos, S., and Velis, D. (2019). A Simple Energy-Based Strategy for Sensor Orientation in Borehole Microseismic Monitoring. *J. Geophys. Eng.* 16 (1), 85–91. doi:10.1093/jge/gxy007

Li, X.-Y., and Yuan, J. (1999). Geophone Orientation and Coupling in Three-Component Sea-Floor Data: a Case Study. *Geophys. Prospecting* 47 (6), 995–1013. doi:10.1046/j.1365-2478.1999.00160.x

Liu, C., Chen, C.-L., Wang, D., Liu, Y., Wang, S.-Y., and Zhang, L. (2015). Seismic Dip Estimation Based on the Two-Dimensional Hilbert Transform and its Application in Random Noise Attenuation. *Appl. Geophys.* 12 (1), 55–63. doi:10.1007/s11770-014-0474-4

Liu, E., Queen, J. H., Li, X. Y., Chapman, M., Maultzsch, S., Lynn, H. B., et al. (2003). Observation and Analysis of Frequency-dependent Anisotropy from a Multicomponent VSP at Bluebell-Altamont Field, Utah. *J. Appl. Geophys.* 54 (3–4), 319–333. doi:10.1016/j.jappgeo.2003.01.004

Lu, J., Shi, Y., and Yang, C. (2018). Vector Wave Separation in Anisotropic media and its Application. *Chin. J. Geophys.* 61 (8), 3310–3323. doi:10.6038/cjg2018L0387

Lu, J., Wang, Y., Chen, J., and Sun, P. (2019). P- and S-Mode Separation of Three-Component VSP Data. *Exploration Geophys.* 50 (4), 430–448. doi:10.1080/08123985.2019.1606205

Menanno, G., Vesnaver, A., and Jervis, M. (2013). Borehole Receiver Orientation Using a 3D Velocity Model. *Geophys. Prospect.* 61, 215–230. doi:10.1111/j.1365-2478.2012.01106.x

Michaels, P. (2001). Use of Principal Component Analysis to Determine Down-Hole Tool Orientation and Enhance SH-Waves. *Jeeg* 6, 175–183. doi:10.4133/JEEG6.4.175

Oye, V., and Ellsworth, W. L. (2005). Orientation of Three-Component Geophones in the San Andreas Fault Observatory at Depth Pilot Hole, Parkfield, California. *Bull. Seismological Soc. America* 95 (2), 751–758. doi:10.1785/0120040130

Park, J., Kim, W., and Baag, C.-E. (2004). Phase Identification Analysis Using Directionality and Rectilinearity Functions in Three Component Seismograms. *Geosci. J.* 8 (2), 199–209. doi:10.1007/BF02910196

Zaręba, M., and Danek, T. (2019). Correction to: VSP Polarization Angles Determination: Wysin-1 Processing Case Study. *Acta Geophys.* 67 (2), 737. doi:10.1007/s11600-019-00277-3

Zeng, X., and McMechan, G. A. (2006). Two Methods for Determining Geophone Orientations from VSP Data. *Geophysics* 71 (4), V87–V97. doi:10.1190/1.2208935

Zhu, Y., Lin, J., Zhao, F., Chen, Z., Sun, F., and Lv, H. (2018). A Least Squares Method Based on Quaternions to Derive Absolute Orientation of Geophones with AHRS. *J. Geophys. Eng.* 15 (6), 2614–2624. doi:10.1088/1742-2140/aadd2f

Conflict of Interest: The authors declare that the research was conducted in the absence of any commercial or financial relationships that could be construed as a potential conflict of interest.

Publisher's Note: All claims expressed in this article are solely those of the authors and do not necessarily represent those of their affiliated organizations, or those of the publisher, the editors, and the reviewers. Any product that may be evaluated in this article, or claim that may be made by its manufacturer, is not guaranteed or endorsed by the publisher.

frontiers in Earth Science

ORIGINAL RESEARCH
published: 16 February 2022
doi: 10.3389/feart.2022.848763

The Structure and Elasticity of CaO_3 Under High Pressure by First-Principles Simulation

Hanyu Wang[1], *Lei Liu*[1]*, *Longxing Yang*[1,2], *Fengxia Sun*[1,2], *Li Yi*[1] *and Hong Liu*[1]

[1]United Laboratory of High-Pressure Physics and Earthquake Science, Institute of Earthquake Forecasting, CEA, Beijing, China, [2]State Key Laboratory of Geological Processes and Mineral Resources, and School of Earth Sciences and Resources, China University of Geosciences, Beijing, China

The structure, electrical properties, elasticity, and anisotropy of the newly discovered mantle mineral, CaO_3, are obtained under 10–50 GPa by first-principles simulation to understand their relations with the composition and structure of the mantle transition zone. Crystal structure and phonon frequencies under 0–50 GPa indicate that CaO_3 can exist stably under 10–50 GPa. Here, the band gap of CaO_3 is 2.32–2.77 under the explored pressure and indicates its semiconductor property. The Mulliken population analysis shows that the Ca–O bond is an ionic bond, and O–O bond is a covalent bond, and the strength of the O–O bond is higher than that of the Ca–O bond. The density, bulk modulus, and shear modulus of CaO_3 increase with increasing pressure. The compressional wave velocity (*Vp*) and shear wave velocity (*Vs*) of CaO_3 increase with increasing pressure. The seismic wave velocity of CaO_3 is smaller than that of the Preliminary Reference Earth Model (PREM) and common mantle transition zone minerals, and it is a very exceptional low seismic wave velocity phase. The anisotropies of *Vs* are 36.47, 26.41, 23.79, and 18.96%, and the anisotropies of *Vp* are 18.37, 13.91, 12.75, and 10.64% under 15, 25, 35, and 50 GPa, respectively. Those seismic velocity anisotropies are larger than those of the mantle transition zone's main component, so CaO_3 may be an important source of seismic wave velocity anisotropy in the mantle transition zone. Our results provide new evidence for understanding the material composition and the source of anisotropy in the mantle transition zone.

Keywords: structure, electrical properties, elastic and anisotropic properties, CaO_3, mantle transition zone, high pressure, first-principles simulation

OPEN ACCESS

Edited by:
Lidong Dai,
Institute of Geochemistry (CAS), China

Reviewed by:
Jin Liu,
Center for High Pressure Science and Technology Advanced Research, China
Qiaomu Qi,
Chengdu University of Technology, China

***Correspondence:**
Lei Liu
liulei@ief.ac.cn

Specialty section:
This article was submitted to Solid Earth Geophysics, a section of the journal Frontiers in Earth Science

Received: *05 January 2022*
Accepted: *17 January 2022*
Published: *16 February 2022*

Citation:
Wang H, Liu L, Yang L, Sun F, Yi L and Liu H (2022) The Structure and Elasticity of CaO_3 Under High Pressure by First-Principles Simulation. Front. Earth Sci. 10:848763. doi: 10.3389/feart.2022.848763

1 INTRODUCTION

The research studies on the physical and chemical behavior of rocks and minerals under deep Earth conditions through high-temperature and high-pressure experiments and simulation are two of the important ways to understand the composition, structure, and dynamic processes of the Earth. Due to the difficulty in entering the Earth's interior, most of our understanding of the Earth's interior derives from seismic and geophysical observation. By comparing observed seismic properties of the Earth with properties of particular minerals under deep Earth conditions, the physical and chemical properties of the Earth can be constrained (Sun, 2019).

The Earth's mantle plays a vital role in the evolution of the crust and provides the thermal and mechanical driving forces for plate tectonics. The mantle transition zone is a particular area in the

mantle with a particular structure and composition (Birch, 1952; Frost, 2008). The mantle transition zone refers to the part of the Earth between the 410 and 660 km that is of great significance in the study of structure and dynamics in the Earth's interior (Zhou et al., 2010). The seismic discontinuities at 410 and 660 km depths that distinguish the transition zone from the upper and lower mantle are globally observed (Dziewonski and Anderson, 1981; Flanagan and Shearer, 1998). The seismic discontinuities provide important clues that clarify the physical and chemical nature of the transition zone (Anderson, 1989; Lay, 1989). The pressure in the mantle transition zone begins at ~ 14 GPa (410 km depth) (Wei and Shearer, 2017; Zhang et al., 2018), where $(Mg,Fe)_2SiO_4$ olivine transforms into wadsleyite with a denser structure (Ringwood and Major, 1970; Ringwood, 1979; Katsura and Ito, 1989), sometimes referred to as β-phase or modified spinel. At ~ 17.5 GPa (520 km), wadsleyite transforms into ringwoodite (Gossler and King, 1996; Shearer, 1996; Gu et al., 1998; Deuss and Woodhouse, 2001), sometimes termed γ-phase or silicate spinel (Ringwood, 1975; Shearer, 1990). At approximately 23–24 GPa (660 km), ringwoodite breaks down into an assemblage of perovskite-structured $(Mg,Fe)SiO_3$ and (Mg,Fe) O magnesiowüstite (Ito and Takahashi, 1989), which marks the beginning of the lower mantle. Except for the olivine and its high pressure polymorphic phases, garnet is also an important component of the mantle transition zone (Palke et al., 2015; Fan et al., 2018). The clinopyroxene and orthopyroxene components would be incorporated into garnet with increasing pressure (Akaogi and Akimoto, 1977; Ringwood, 1991). Garnet accepts Mg and Fe into the octahedral site but not Ca, and all pyroxene components are hosted by garnet under the mid-transition zone conditions. At pressures higher than 18 GPa, $CaSiO_3$ perovskite starts to exsolve from garnet (Canil, 1994). At depths greater than 660 km, garnet also transforms into $(Mg,Fe)(Al,Si)O_3$ perovskite (Kubo and Akaogi, 2000; Akaogi et al., 2002) over a wider pressure interval than the ringwoodite transformation (Chantel et al., 2016). If the Al content is low, the $(Mg,Fe)SiO_3$ pyroxene component will not be entirely incorporated into garnet under transition zone conditions. However, an additional phase, akimotoite, will form at approximately 600 km (Ishii et al., 2011).

The most apparent seismic wave discontinuity in the mantle is at 660 km, which was confirmed worldwide (Dziewonski and Anderson, 1981; Flanagan and Shearer, 1998). At 660 km, the seismic wave velocity increases rapidly, the shear wave velocity changes from 5.61 to 5.96 km/s, and the compression wave velocity changes from 10.2 to 10.79 km/s, but there are different opinions on the exact causes of the mutation. It is generally believed that olivine's post-spinel transformation causes such changes (Ito and Takahashi, 1989). However, with further research, garnet–ilmenite transformation and ilmenite–perovskite transformation (Kubo and Akaogi, 2000; Akaogi et al., 2002) have been proved, which can also explain the seismic wave discontinuity at 660 km. The pressure relationship between them is still controversial and needs further study. At the same time, some scholars believe that phase transition is not the only solution to explain the discontinuous splitting of seismic waves. The change of the mantle material composition can also explain this phenomenon, such as the discontinuity of seismic waves caused by the stagnant slab material (Fukao et al., 2009).

Recently, Wang et al. (2020) proposed an alternative mechanism, that is, CaO_3 may decompose into CaO and O_2 at 20 GPa, resulting in the change of the material composition at this depth to explain seismic wave velocity anomalies near 660 km depth in the Earth's mantle. CaO_3 is a newly discovered material that may exist in the mantle transition zone, and CaO_3 may form at 35 GPa and existence under reduced pressure to 20 GPa. Once reaching the transition zone at depths of less than 500 km, CaO_3 would decompose to provide a sporadic source of extra O_2 that would work its way up toward the surface of the Earth to complete the oxygen cycle (Wang et al., 2020). Therefore, this new mineral and reaction phenomenon may affect the composition and structure of the mantle transition zone and the lower mantle. However, the crystal structure and elastic properties of the CaO_3 under high pressure are still not well constrained. The first-principles calculation is an algorithm to directly solve the Schrodinger equation according to the principle of interaction between the nucleus and electron and its fundamental motion law, starting from specific requirements and after some approximate processing (Kohn and Sham, 1965). Based on the principle of quantum mechanics and density functional theory, it uses the Hohenberg–Kohn theorem (Hohenberg and Kohn, 1964) to determine the system's energy and calculate the properties of molecules and condensed matter. First-principles calculations have been successfully applied to geosciences for understanding mineral properties such as structural, elastic, and electrical properties under high pressure and temperature (Gillan et al., 2006; Jahn and Kowalski, 2014; Karki, 2014; Liu et al., 2015; Zhang et al., 2015a; Zhang et al., 2015b; Zhao et al., 2015; Wu and Wentzcovitch, 2016; Lv et al., 2017; Umemoto et al., 2017). Therefore, we investigate the crystal structural and elastic properties of CaO_3 under high pressure using first-principles calculations to discover the far-reaching significance and influence of CaO_3 in the mantle transition zone and lower mantle.

2 SIMULATION METHODS

CaO_3 belongs to the tetragonal system, and the space group is p-421 m (Wang et al., 2020). In this study, first-principles calculations are performed using the density functional theory (Hohenberg and Kohn, 1964; Kohn and Sham, 1965) with the plane wave pseudopotential. The calculations are implemented in the CASTEP code (Clark et al., 2005), and the generalized gradient approximation (GGA) with PBE parameterization (Perdew et al., 1996) is used to describe exchange–correlation interactions. OTFG norm-conserving pseudopotential (Bachelet and Schlüter, 1982) is used to model electron–ion interactions with a plane-wave energy cutoff of 700 eV. A 3 × 3 × 5 Monkhorst–Pack grid of k-points is adopted for sampling the Brillouin zone. The self-consistent-field calculations use a convergence criterion of 5×10^{-7} a.u. for total energy.

TABLE 1 | Structural and volume of CaO_3 at 20, 25, 30, and 35 GPa.

Phase	Pressure	Lattice parameter				Volume		Reference
		a/Å	b/Å	c/Å	Δ	Å3/f.u.	Δ	
CaO_3	35 GPa	4.87	4.87	2.98		31.75	0.72%	Wang et al. (2020)
		4.88	4.88	2.98	0.30%	31.98		This study
	30 GPa					32.69	0.09%	Wang et al. (2020)
		4.92	4.92	3.00		32.72		This study
	25 GPa					33.68	0.32%	Wang et al. (2020)
		4.96	4.96	3.03		33.57		This study
	20 GPa					34.85	0.86%	Wang et al. (2020)
		5.00	5.00	3.07		34.55		This study

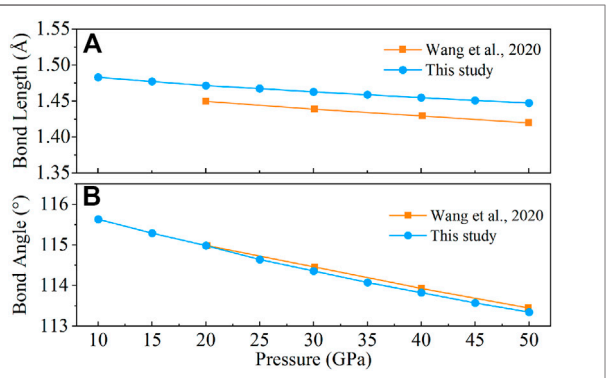

FIGURE 1 | Bond length **(A)** and bond angle **(B)** of the O–O–O bond under 0–50 GPa.

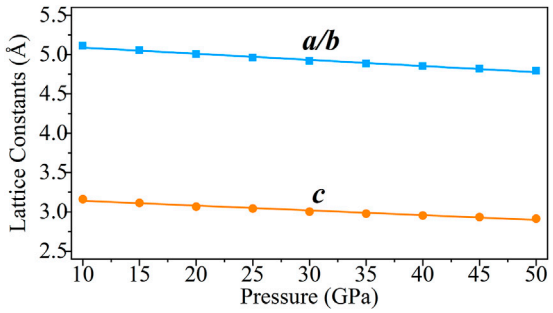

FIGURE 2 | Lattice constants of CaO_3 under 10–50 GPa. The blue squares represent the lattice constant of *a* and *b*, and the orange circles represent the lattice constant of *c*.

The structures of the CaO_3 at given pressures are calculated by simultaneously optimizing both atomic positions and lattice constants under Hellmann–Feynman forces and stresses acting on nuclei and lattice parameters, respectively (Nielsen and Martin, 1983). The phonon is calculated by finite displacement (Baroni et al., 2001) to determine the molecular stability. The Mulliken population analysis (Mayer, 1995; Segall et al., 1996a) is used to determine the bonding characters. The elastic constants are determined by stress–strain relations (Karki et al., 2001). The magnitudes of all applied strains are 0.003, and the linear relation was ensured for this strain range.

3 RESULTS AND DISCUSSION

3.1 Benchmark Calculation

To assess the performance of the total-energy density functional theory approach used in our calculations, we calculated the bond angle, density, and volume of CaO_3 and compared them with the reported values.

As shown in **Table 1**, the differences between the calculated lattice parameters and the reported values are less than 0.3%, and the differences in volume are between 0.09 and 0.86%.

To further verify the validity of our calculation approach, the O–O bond length and bond angle of the O–O–O bond were calculated under 0–50 GPa (**Figure 1**) and compared with the previous experimental results. With the increase of pressure, the O–O bond length and O–O–O bond angle decrease linearly. The calculated O–O bond lengths (**Figure 1A**) are 1.45–1.87% larger than the previous values (Wang et al., 2020); however, the calculated O–O–O bond angles (**Figure 1B**) are 0.08–0.11% smaller.

Those slight differences between our calculated values with previous results are mainly due to the calculated temperature difference and the insufficient binding energy of GGA (Liu et al., 2018). Therefore, the general agreement of our calculations with previous results demonstrates the validity of our computational method and its ability to reproduce the properties of CaO_3.

3.2 Crystal Structure Under High Pressure

3.2.1 Lattice Constants

The lattice constants (***a***, ***b***, and ***c***) of the CaO_3 are calculated from 10 to 50 GPa (**Figure 2**) by the CASTEP code. The lattice constants of the CaO_3 decrease linearly with increasing pressure, and the fitted result is also listed in **Figure 2**. The results indicate that the influence of pressure on the lattice constants of CaO_3 is uniform.

3.2.2 The Phonon Dispersion

The thermodynamic properties of crystals can be evaluated by the phonon frequencies across the Brillouin zone (Sham, 1965; Ashcroft and Mermin, 1976; Kern et al., 1999). For understanding the structural stability of CaO_3, the phonon

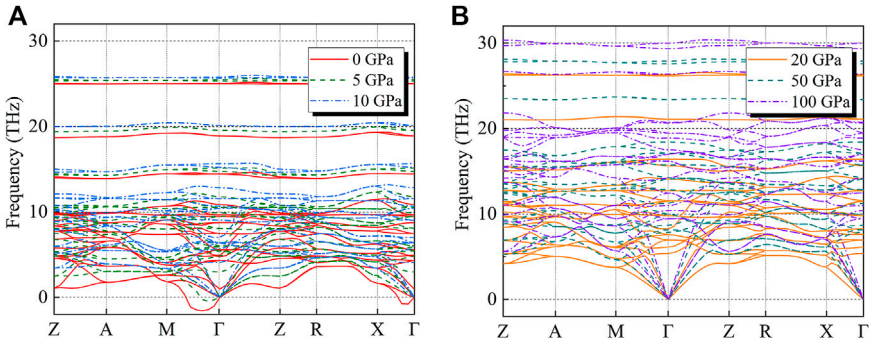

FIGURE 3 | (A,B) show the phonon dispersion relations along with select high-symmetry points in the Brillouin zone for CaO_3 at **(A)** 0 (solid red lines), 5 (dashed olive green lines), 10 (dot-dash blue lines), **(B)** 20 (solid orange lines), 50 (dashed dark green lines), and 100 GPa (dot-dash purple lines).

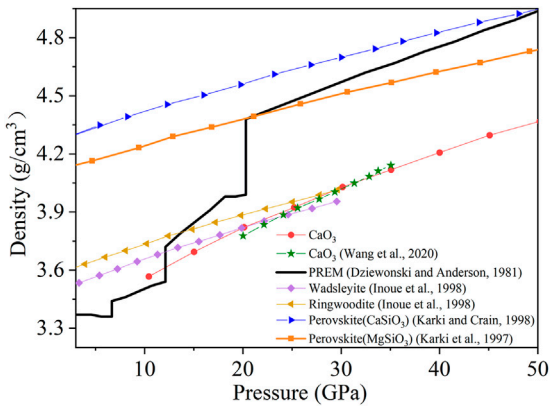

FIGURE 4 | Density of CaO_3 and some selected phases for comparison under 3–50 GPa. The red circles represent CaO_3, the green stars represent the previous data of CaO_3, the black thick solid line represents the PREM model, the purple diamonds represent wadsleyite, the yellow left triangles represent ringwoodite, the blue right triangles represent perovskite ($CaSiO_3$), and the orange squares represent perovskite ($MgSiO_3$).

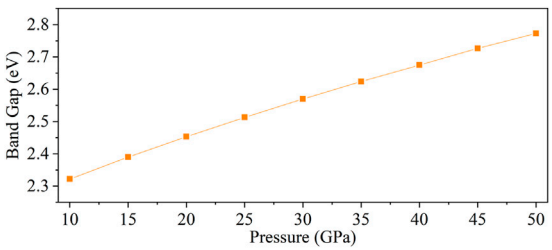

FIGURE 5 | Band gap of CaO_3 under 10–50 GPa.

dispersion along select high-symmetry points in the Brillouin zone is calculated at 0–100 GPa (**Figure 3**).

Under 0–10 GPa, the lattice vibration produces a negative value (frequency less than 0) in the Brillouin region (**Figure 3A**) which means the CaO_3 structure is not stable (Gonze, 1997), but it is stable in the range of 10–100 GPa (**Figure 3B**). These results are consistent with the previous result (Wang et al., 2020) that the CaO_3 may exist stably in the mantle transition zone.

3.2.3 Density

The CaO_3 density increases linearly with the increased pressure (Earth's depth) (**Figure 4**). The CaO_3 is dynamically stable at 20–50 GPa and may exist in the mantle transition zone and the lower mantle (Wang et al., 2020). Therefore, the densities of several main mineral phases in this area are also listed in **Figure 4**, including wadsleyite (Inoue et al., 1998), ringwoodite (Inoue et al., 1998), $CaSiO_3$ perovskite (Karki and Crain, 1998), and $MgSiO_3$ perovskite (Karki et al., 1997) under high pressure and density of the Preliminary Reference Earth Model (PREM) (Dziewonski and Anderson, 1981).

The density of CaO_3 increases with pressure, but the density is lower than the typical density structure profile of the Earth. During 10–20 GPa, the density of CaO_3 is lower than that of wadsleyite and ringwoodite. During 20–30 GPa, the density of CaO_3 is higher than that of wadsleyite but still lower than that of ringwoodite. When the pressure increases to 30 GPa, the density of CaO_3 becomes higher than that of wadsleyite and ringwoodite. At all pressure, the density of CaO_3 is less than that of two kinds of perovskite ($CaSiO_3$ and $MgSiO_3$). At the same time, the density of $CaSiO_3$ perovskite is higher than that of the $MgSiO_3$ perovskite. So, the content of Ca and the Ca-bearing mineral such as CaO_3 maybe have an important effect on the composition of the mantle.

3.3 Electrical Property

To explore the electrical property of CaO_3, its energy band structure, density of states, and Mulliken population were calculated under 10–50 GPa. Here, the band gap of CaO_3 is 2.32–2.77 under the explored pressure and indicates its semiconductor property (Guo et al., 2009) (**Figure 5**). With the increase of pressure, the band gap increases and conductivity decreases.

The characteristics of the electronic density of states (DOS) are mainly contributed by p-orbits (**Figure 6**). The contribution of the p-orbitals for the total DOS is about 54.8 and 55.0%, and the rest is contributed by the **s**-orbitals (22.4 and 22.2%) and the

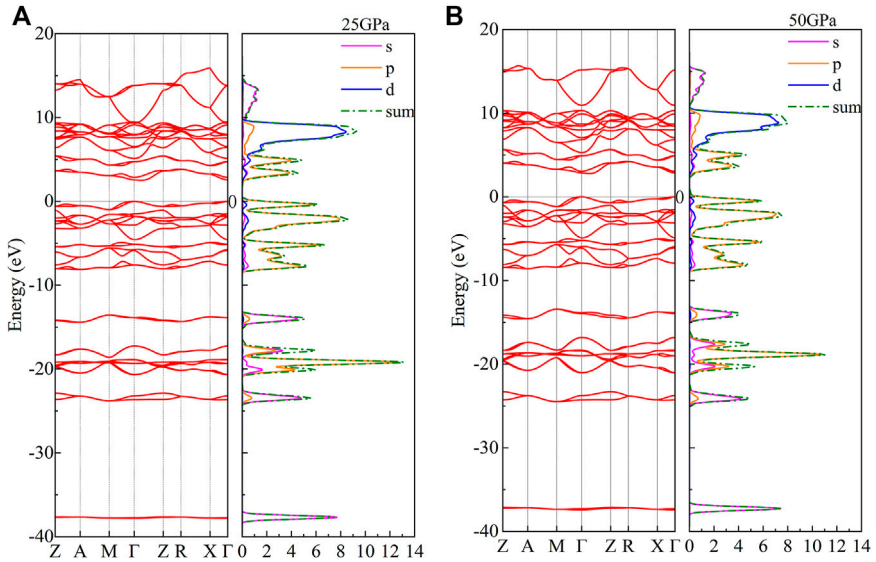

FIGURE 6 | Density of states and band structure of CaO_3 at **(A)** 25 GPa and **(B)** 50 GPa. The red curve represents the band structure; the magenta curve, orange curve, and blue curve represent the DOS of s-orbitals, p-orbitals, and d-orbitals, respectively; and the green dot-dash line represents the total value of the DOS.

TABLE 2 | Mulliken population analysis of CaO_3 at 10, 35, and 50 GPa.

Pressure	Species	s	p	d	f	Total	Charge (e)	Bond	Population	Length (Å)
10 GPa	O_1	1.88	4.30	0.00	0.00	6.18	−0.18	O–O	0.16	1.48285
	O_2	1.90	4.65	0.00	0.00	6.55	−0.55	O–Ca	0.14	2.38125
	Ca	2.12	6.00	0.61	0.00	8.73	1.27			
35 GPa	O_1	1.87	4.30	0.00	0.00	6.16	−0.16	O–O	0.15	1.45887
	O_2	1.88	4.64	0.00	0.00	6.52	−0.52	O–Ca	0.12	2.29074
	Ca	2.10	6.00	0.70	0.00	8.79	1.21			
50 GPa	O_1	1.86	4.30	0.00	0.00	6.16	−0.16	O–O	0.15	1.44764
	O_2	1.88	4.64	0.00	0.00	6.51	−0.51	O–Ca	0.11	2.24958
	Ca	2.08	5.99	0.74	0.00	8.82	1.18			

d-orbitals (22.8 and 22.8%) at 25 and 50 GPa, respectively. With the increase of pressure, the distance between the conduction band and valence band increases; however, the morphological characteristics of the electronic density of states do not change.

The d-orbits of the DOS have relatively large peaks (**Figure 6**). The electrons are relatively local, and the corresponding energy band is observed to be narrow, showing transition metal-like properties (Imai et al., 2000). The bottom of the valence band is mainly contributed by s-orbitals. The upper part of the valence band is mainly contributed by s-orbitals and p-orbitals. Most of the conduction band is contributed by p-orbitals and d-orbitals. The lowest point of the conduction band and the highest point of the valence band are located at the different K points, and the band gap is an indirect gap.

In order to further verify the electrical relationship among atoms, we calculate the Mulliken population of CaO_3 (**Table 2**). The spilling parameter of the spin component in the system is less than 1%, ranging from 0.26 to 0.28%, which means that our calculation results are reasonable and reliable (Segall et al., 1996b).

Through the Mulliken population analysis, the overlap population may be used to assess the covalent or ionic nature of the atomic bond. The Mulliken population analysis shows that the Ca–O bond is an ionic bond, and the O–O bond is a covalent bond (**Table 2**), and the strength of the O–O bond is higher than that of the Ca–O bond. When the pressure increases from 10 to 50 GPa, the population value of the Ca–O bond decreases from 0.14 to 0.11 (21.43%), but the population value of the O–O bond decreases from 0.16 to 0.15 (6.25%). The electron localization function in CaO_3 shows the strong charge localization between the nearest-neighbor O atoms in the O_3 units that indicates the clear covalent O–O bond, and less localized charge distribution on the asymmetric Ca–O bonds indicates its ionicity (Wang et al., 2020). Our calculations are consistent with those previous results and deepen the understanding of the electrical characteristics of CaO_3.

3.4 Elasticity and Seismic Wave Velocity

The elastic parameters of minerals and their dependence on pressure are essential in earth science to understand processes

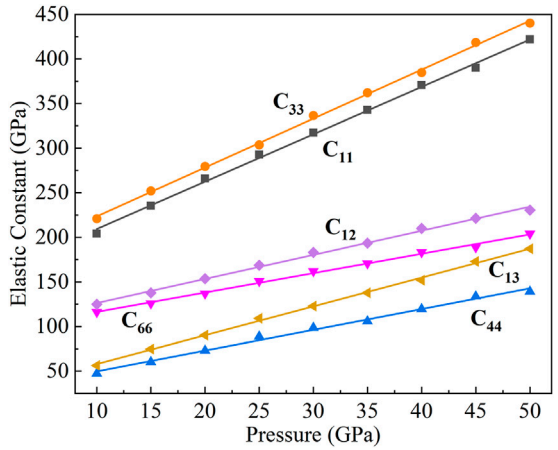

FIGURE 7 | Elastic constants of CaO_3 under 10–50 GPa. The black squares represent C_{11}, the purple diamonds represent C_{12}, the oblique yellow triangles represent C_{13}, the orange circles represent C_{33}, the regular blue triangles represent C_{44}, and the inverted magenta triangles represent C_{66}.

ranging from brittle failure to flexure to the propagation of elastic waves. Seismology revealed the structure of the Earth, including the radial (one-dimensional) profile, lateral heterogeneity, and anisotropy. These results are mainly determined by the elastic parameters of minerals and their dependence on pressure (Karki et al., 2001).

CaO_3 belongs to the tetragonal system and has six independent elastic constants (C_{11}, C_{12}, C_{13}, C_{33}, C_{44}, and C_{66}). In **Figure 7**, we calculated the elastic constants under 10–50 GPa according to the relationship between stress and strain: $\sigma_i = C_{ij}\varepsilon_j$ (Ashcroft and Mermin, 1976). Studying the elastic constants of Earth materials at high pressure provides a solid foundation for exploring the material properties in the relationship between structure and bonding. The elastic constants of CaO_3 increase linearly with the increase of pressure. According to the Born elastic stability criteria (Mouhat and Coudert, 2014), the elastic constants of CaO_3 at 10–50 GPa always conform to the following formula ($C_{11} > |C_{12}|$, $C_{44} > 0$, $C_{66} > 0$, $2C_{13}^2 < C_{33}(C_{11} + C_{12})$), which means that the elasticity of our calculation is stable.

Among the six elastic constants, C_{33} and C_{11} are the largest, which means that C_{33} and C_{11} have the highest elastic strength. When the pressure increases, the elastic constants of C_{33} and C_{11} increase faster. The slopes are 5.48 and 5.31, respectively, which is determined by the nonbonding atomic force between Ca atoms in the c-axis direction (C_{33}) and a-axis direction (C_{11}). The distance between Ca and Ca atoms on the c-axis is less than that on the a-axis, which makes the nonbonding atomic force on the c-axis greater than that on the a-axis, so C_{33} has a larger elastic constant and a higher elastic strength than C_{11}.

The elastic constants of C_{44} and C_{66} linearly increase with pressure and have similar pressure derivatives (2.32 and 2.17). The value of C_{44} is the lowest that caused by the relatively weak bond of Ca–O in the [111] direction. The elastic constants of C_{12} and C_{13} also linearly increase with pressure, and C_{13} tends to approach C_{66} with the increase of pressure.

An elastic modulus is an important parameter to describe minerals' physical and chemical properties. In polycrystalline systems, assuming that the arrangement direction is random, the bulk modulus and shear modulus can be obtained by Voigt, Reuss, and Hill formulas (Finger, 1983). The Hill formula of elasticity is used in this article (Hill, 1952), which is the average of Voigt and Reuss formulas.

The bulk modulus (K) and shear modulus (G) of CaO_3 from 10 to 50 GPa are shown in **Figure 8**. The K and G linearly increase with increasing pressure. The pressure derivatives of the bulk and shear moduli, K' and G', are directly calculated from the pressure dependence of K *and* G and yield 3.82 and 1.81, respectively.

Simulated and laboratory studies of the seismic wave velocities in minerals at high pressure and temperature be conducive to scientists to describe seismic data for the variation of sound velocities and density with depth in the Earth's interior (Li and Liebermann, 2014).

As a potentially important component in the lower mantle and mantle transition zone, the seismic wave velocity of CaO_3 under high pressure is of great significance for understanding the structure and composition of the deep Earth. We calculated the shear wave velocity (Vs) (**Figure 9A**) and compressional wave velocity (Vp) (**Figure 9B**) of CaO_3 under 10–50 GPa with the following formula:

$$V_P = \sqrt{\frac{3K + 4G}{3\rho}}, \quad V_S = \sqrt{\frac{G}{\rho}}.$$

For exploring the effect of CaO_3 on the structure of the mantle, the seismic wave velocity of the wadsleyite (Liu et al., 2009), ringwoodite (Li, 2004), $MgSiO_3$ perovskite (Karki et al., 1997), and $CaSiO_3$ perovskite (Karki and Crain, 1998) under high pressure and the seismic wave velocity of PREM (Dziewonski and Anderson, 1981) are also listed in **Figure 9**. The Vs and Vp values of CaO_3 increase with increasing pressure. Under pressure explored in this work, Vs and Vp of CaO_3 are smaller than mantle

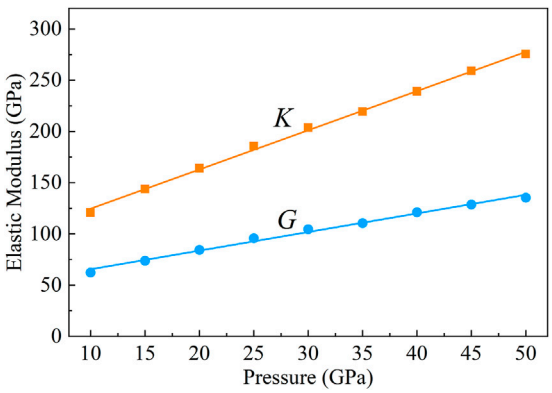

FIGURE 8 | Bulk modulus (K) and shear modulus (G) of CaO_3 under 10–50 GPa. The orange squares represent bulk modulus, and the blue circles represent shear modulus.

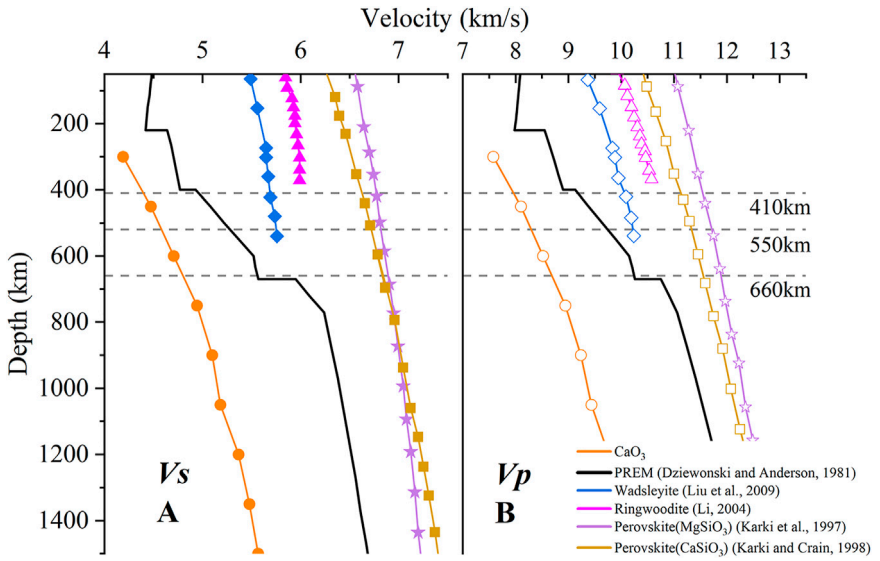

FIGURE 9 | Shear wave velocity **(A)** and compressional wave velocity **(B)** of CaO_3, PREM model, wadsleyite, ringwoodite, perovskite ($MgSiO_3$), and perovskite ($CaSiO_3$) within 50–1500 km. The hollow legend represents *Vs*, the solid legend represents *Vp*, the orange circle represents CaO_3, the solid black line represents the PREM model, the blue diamonds represent wadsleyite, the regular magenta triangles represent ringwoodite, the yellow squares represent perovskite ($MgSiO_3$), and the purple stars represent perovskite ($CaSiO_3$).

seismic wave velocity (PREM). At the same time, the seismic wave velocity of CaO_3 is also lower than the seismic wave velocities of the main mineral phases of the mantle, including wadsleyite, ringwoodite, $MgSiO_3$ perovskite, and $CaSiO_3$ perovskite. So, CaO_3 is an exceptional low seismic wave velocity phase.

The formation of CaO_3 at about 20 GPa was proposed to explain seismic wave velocity anomalies near 660 km depth in the Earth's mantle (Wang et al., 2020). Our calculated results show no evident increase in CaO_3 seismic wave velocity at 660 km. CaO_3 also has very low seismic wave velocity, which means that CaO_3 is unlikely to be the cause of the sharp seismic wave velocity increase of the 660 km depth. However, the existence of the CaO_3 in the mantle may lead to the formation of a low velocity zone because of its low seismic wave velocity.

3.5 Anisotropy

Seismic wave anisotropy of the material reveals the difference in physical and chemical properties of the mineral in various directions. Seismic anisotropy describes the dependence of seismic velocity on the propagation or polarization directions of seismic waves. It is produced by two primary deformation mechanisms within the Earth: the lattice-preferred orientation (LPO) of anisotropic minerals or the shape-preferred orientations (SPOs) of distinct isotropic materials.

When the elastic constants *Cij* and density ρ are known, the Christoffel equation (Musgrave, 1970) can be solved to obtain the compressional wave velocity (*Vp*) and two orthogonally polarized shear wave velocities with different velocities (Vs_1, Vs_2, and defined $Vs_1 > Vs_2$):

$$\Delta \mid c_{ijkl} n_j n_i - \rho V^2 \delta_{ij} \mid = 0,$$

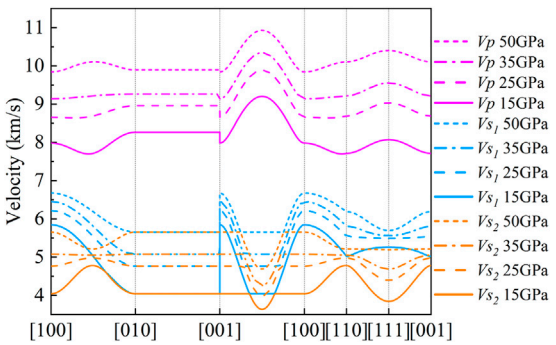

FIGURE 10 | Seismic wave velocity of CaO_3 at different crystal axis directions at 15, 25, 35, and 50 GPa. The solid lines represent 15 GPa, dashed lines represent 25 GPa, dot-dash lines represent 35 GPa, dotted lines represent 50 GPa, blue represents Vs_1, orange represents Vs_2, and magenta represents *Vp*.

where *n*, *ρ*, *V*, and δ_{ij} represent the propagation direction of seismic elastic wave, medium density, seismic elastic wave velocity, and the Kronecker symbol, respectively.

The seismic wave velocities at different crystal axis directions are different. So, the azimuthal anisotropy coefficient (*A*) of compressional wave (P wave) and shear wave (S wave) is defined as:

$$AVp = \frac{Vp_{max} - Vp_{min}}{Vp} \times 100\%;$$

$$AVs = \frac{Vs_1 - Vs_2}{Vs} \times 100\%,$$

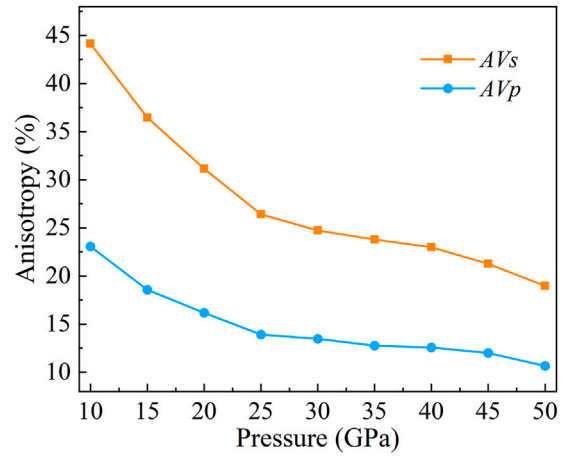

FIGURE 11 | Anisotropy of CaO_3 at 10–50 GPa. The orange squares represent *AVs*, and the blue circles represent *AVp*.

where AVp, Vp_{max}, Vp_{min}, and Vp are the maximum azimuthal anisotropy coefficient of P wave, the maximum velocity of P wave in all directions of the crystal, the minimum velocity of P wave in all directions of the crystal, and the compressional wave velocity at the same pressure, respectively; AVs, Vs_1, Vs_2, and Vs are the maximum azimuthal anisotropy coefficient of S wave, Vs_1 and Vs_2 are the velocities in the same crystal direction, and shear wave velocity at the same pressure, respectively.

In **Figure 10**, we can find that the Vp and Vs have the same wave velocity from the [010] direction to the [001] direction. Vs has the largest wave velocity differences in the [100] and [001] directions, and the anisotropies are 36.47, 26.41, and 23.79% at 15, 25, and 35 GPa, respectively (**Figures 10**, **11**). The largest wave velocity difference of Vs under 50 GPa is between [100] and [110] direction, and the AVs = 18.96%. In general, the anisotropy of Vs decreases with increasing pressure (**Figure 11**).

The maximum value of Vp is always in the [101] direction (**Figure 10**). However, the direction of the minimum value of Vp changes with increasing pressure. At 15 GPa, the minimum value of Vp is close to the [110] direction, and the anisotropy is 18.37%. At 25 GPa, the minimum value of Vp is in the middle of the [100] to [110] direction, and the anisotropy is 13.91%. At 35 GPa and 50 GPa, the minimum value of Vp is in the [100] direction, and the anisotropy is 12.75 and 10.64%, respectively. In general, the anisotropy of Vp decreases with increasing pressure (**Figure 11**).

The observation of shear wave splitting shows seismic anisotropy near the 660 km discontinuity beneath the Tonga-Kermadec subducting slabs (Wookey et al., 2002). Li et al. (2018) used the moment tensor of deep, non-double-couple earthquakes to invert for *in situ* seismic anisotropy assuming the shear-dislocation faulting mechanism and found 25% anisotropy in the mantle transition zone. Under the mantle transition zone conditions, wadsleyite has 14% S-wave anisotropy (Sawamoto et al., 1984; Zha et al., 1997; Sinogeikin et al., 1998); ringwoodite, present in 520–660 km of the mantle transition zone, is nearly isotropic with only ~2% shear wave anisotropy (Weidner et al., 1984; Kiefer et al., 1997; Sinogeikin et al., 2003; Li et al., 2006). At the same time, the same abundant majorite-rich garnet in the mantle transition zone is also close to isotropy (Bass and Kanzaki, 1990; Pamato et al., 2016). Therefore, it is difficult to explain anisotropy in the mantle transition zone with combinations of the known mineral phases in the uppermost mantle and the transition-zone regions.

Here, we calculated the anisotropy of CaO_3 under high pressure. The results show that the anisotropies of Vs are 36.47, 26.41, 23.79, and 18.96%, and the anisotropies of Vp are 18.37, 13.91, 12.75, and 10.64% under 15, 25, 35, and 50 GPa, respectively. The anisotropy of CaO_3 is larger than that of the main components of the mantle transition zone, including the wadsleyite (Sawamoto et al., 1984; Zha et al., 1997; Sinogeikin et al., 1998), ringwoodite (Weidner et al., 1984; Kiefer et al., 1997; Sinogeikin et al., 2003; Li et al., 2006), and majorite (Bass and Kanzaki, 1990; Pamato et al., 2016). The results are very close to the anisotropy of the mantle transition zone (Li et al., 2018). Therefore, CaO_3 may be an important source of seismic wave velocity anisotropy in the mantle transition zone.

4 CONCLUSION

CaO_3 is a newly discovered mineral that may exist in the mantle transition zone. However, its physical properties under high pressure are still not well understood. Here, the structural parameters, stability, and electronic and elastic properties of CaO_3 under 0–50 GPa are calculated by the first-principles method. Crystal structure and phonon frequencies under 0–50 GPa indicate that CaO_3 can exist stably under 10–50 GPa. Here, the band gap of CaO_3 is 2.32–2.77 under the explored pressure, indicating its semiconductor property, and the band gap increases with the increase of pressure. The Mulliken population analysis shows that the Ca–O bond is an ionic bond, and the O–O bond is a covalent bond, and the strength of the O–O bond is higher than that of the Ca–O bond. The bulk modulus and shear modulus of CaO_3 increase linearly with increasing pressure from 10 to 50 GPa, and their pressure derivatives are 3.82 and 1.81, respectively. The seismic wave velocity of CaO_3 is significantly lower than that of the PREM and the major minerals of the mantle transition zone, including wadsleyite, ringwoodite, $MgSiO_3$ perovskite, and $CaSiO_3$ perovskite. There is also no obvious increase in CaO_3 seismic wave velocity at 660 km, which means that CaO_3 is unlikely to be the cause of the sharp wave velocity increase at 660 km depth. However, the existence of the CaO_3 in the mantle may lead to the formation of a low velocity zone because of its very low seismic wave velocity. The anisotropy of CaO_3 is larger than that of the main compositions of the mantle transition zone and very close to the anisotropy of the mantle transition zone, so it may be an important source of seismic wave velocity anisotropy in the mantle transition zone. Our work provides new data for studying the influence of CaO_3 in the mantle transition zone.

DATA AVAILABILITY STATEMENT

The original contributions presented in the study are included in the article/Supplementary Material; further inquiries can be directed to the corresponding author.

AUTHOR CONTRIBUTIONS

HW and LL contributed to the conception and design of this study. HW built the model and calculated the data and plotted them. LoY and FS performed supplementary calculations on the data. LiY and HL checked and modified the data. HW wrote the first draft of the manuscript. All authors reviewed the manuscript and read and approved the submitted version.

FUNDING

This work was supported by the State Key Laboratory of Earthquake Dynamics (Project No. LED2021B02), the Special Fund of the Institute of Earthquake Forecasting, CEA (Grant Nos 2021IEF0101-1, 2019IEF0502, and 2017KLEP03), and the National Natural Science Foundation of China (Grant No. 42174115).

REFERENCES

Akaogi, M., and Akimoto, S. (1977). Pyroxene-Garnet Solid-Solution Equilibria in the Systems $Mg_4Si_4O_{12}$-$Mg_3Al_2Si_3O_{12}$ and $Fe_4Si_4O_{12}$-$Fe_3Al_2Si_3O_{12}$ at High Pressures and Temperatures. *Phys. Earth Planet. Interiors* 15 (1), 90–106. doi:10.1016/0031-9201(77)90013-9

Akaogi, M., Tanaka, A., and Ito, E. (2002). Garnet–Ilmenite–Perovskite Transitions in the System $Mg_4Si_4O_{12}$-$Mg_3Al_2Si_3O_{12}$ at High Pressures and High Temperatures: Phase Equilibria, Calorimetry and Implications for Mantle Structure. *Phys. Earth Planet. Interiors* 132 (4), 303–324. doi:10.1016/S0031-9201(02)00075-4

Anderson, D. L. (1989). *Theory of the Earth*. Boston: Blackwell Scientific, 34–44.

Ashcroft, N., and Mermin, N. (1976). *Solid State Physics*. Philadelphia: Saunders College.

Bachelet, G. B., and Schlüter, M. (1982). Relativistic Norm-Conserving Pseudopotentials. *Phys. Rev. B* 25 (4), 2103–2108. doi:10.1103/PhysRevB.25.2103

Baroni, S., de Gironcoli, S., dal Corso, A., and Giannozzi, P. (2001). Phonons and Related Crystal Properties from Density-Functional Perturbation Theory. *Rev. Mod. Phys.* 73 (2), 515–562. doi:10.1103/RevModPhys.73.515

Bass, J. D., and Kanzaki, M. (1990). Elasticity of a Majorite-Pyrope Solid Solution. *Geophys. Res. Lett.* 17 (11), 1989–1992. doi:10.1029/GL017i011p01989

Birch, F. (1952). Elasticity and Constitution of the Earth's interior. *J. Geophys. Res.* 57 (2), 227–286. doi:10.1029/JZ057i002p00227

Canil, D. (1994). Stability of Clinopyroxene at Pressure-Temperature Conditions of the Transition Region. *Phys. Earth Planet. Inter.* 86 (1-3), 25–34. doi:10.1016/0031-9201(94)05059-7

Chantel, J., Manthilake, G. M., Frost, D. J., Beyer, C., Ballaran, T. B., Jing, Z., et al. (2016). Elastic Wave Velocities in Polycrystalline Mg3Al2Si3O12-Pyrope Garnet to 24 GPa and 1300 K. *Am. Mineral.* 101 (4), 991–997. doi:10.2138/am-2016-5335

Clark, S. J., Segall, M. D., Pickard, C. J., Hasnip, P. J., Probert, M. I. J., Refson, K., et al. (2005). First Principles Methods Using CASTEP. *Z. für Kristallographie.* 220 (5-6), 567–570. doi:10.1524/zkri.220.5.567.65075

Deuss, A., and Woodhouse, J. (2001). Seismic Observations of Splitting of the Mid-Transition Zone Discontinuity in Earth's Mantle. *Science* 294 (5541), 354–357. doi:10.1126/science.1063524

Dziewonski, A. M., and Anderson, D. L. (1981). Preliminary Reference Earth Model. *Phys. Earth Planet. Interiors* 25 (4), 297–356. doi:10.1016/0031-9201(81)90046-7

Fan, D., Li, B., Chen, W., Xu, J., Kuang, Y., Ye, Z., et al. (2018). The Research Progress of the Equation of State for Garnet Minerals. *Chin. J. High Press. Phys.* 32 (1), 597. doi:10.11858/gywlxb.20170597

Finger, L. W. (1983). Physical Properties of Crystals, Their Representation by Tensors and Matrices. *Eos Trans. AGU* 64 (45), 643. doi:10.1029/EO064i045p00643-01

Flanagan, M. P., and Shearer, P. M. (1998). Global Mapping of Topography on Transition Zone Velocity Discontinuities by stackingSSprecursors. *J. Geophys. Res.* 103 (B2), 2673–2692. doi:10.1029/97JB03212

Frost, D. J. (2008). The Upper Mantle and Transition Zone. *Elements* 4 (3), 171–176. doi:10.2113/GSELEMENTS.4.3.171

Fukao, Y., Obayashi, M., and Nakakuki, T. (2009). Stagnant Slab: A Review. *Annu. Rev. Earth Planet. Sci.* 37 (1), 19–46. doi:10.1146/annurev.earth.36.031207.124224

Gillan, M. J., Alfè, D., Brodholt, J., Vočadlo, L., and Price, G. D. (2006). First-Principles Modelling of Earth and Planetary Materials at High Pressures and Temperatures. *Rep. Prog. Phys.* 69 (8), 2365–2441. doi:10.1088/0034-4885/69/8/R03

Gonze, X. (1997). First-Principles Responses of Solids to Atomic Displacements and Homogeneous Electric Fields: Implementation of a Conjugate-Gradient Algorithm. *Phys. Rev. B* 55 (16), 10337–10354. doi:10.1103/PhysRevB.55.10337

Gossler, J., and Kind, R. (1996). Seismic Evidence for Very Deep Roots. *Earth Planet. Sci. Lett.* 138 (1-4), 1–13. doi:10.1016/0012-821X(95)00215-X

Gu, Y., Dziewonski, A. M., and Agee, C. (1998). Global De-Correlation of the Topography of Transition Zone Discontinuities. *Earth Planet. Sci. Lett.* 157 (1-2), 57–67. doi:10.1016/S0012-821X(98)00027-2

Guo, L., Wu, H., Liu, J., Ma, H., Song, K., and Li, D. (2009). Density Functional Theory Study on Energy Band and Density of States of ZnO. *J. Synth. Crystals* 38, 440–444.

Hill, R. (1952). The Elastic Behaviour of a Crystalline Aggregate. *Proc. Phys. Soc. A.* 65 (5), 349–354. doi:10.1088/0370-1298/65/5/307

Hohenberg, P., and Kohn, W. (1964). Inhomogeneous Electron Gas. *Phys. Rev. B* 136 (3), B864. doi:10.1007/s12045-017-0529-3

Imai, Y., Mukaida, M., and Tsunoda, T. (2000). Comparison of Density of States of Transition Metal Disilicides and Their Related Compounds Systematically Calculated by a First-Principle Pseudopotential Method Using Plane-Wave Basis. *Intermetallics* 8 (4), 381–390. doi:10.1016/S0966-9795(99)00125-9

Inoue, T., Weidner, D., Northrup, P., and Parise, J. (1998). Elastic Properties of Hydrous Ringwoodite (γ-phase) in Mg_2SiO_4. *Earth Planet. Sci. Lett.* 160 (1-2), 107–113. doi:10.1016/S0012-821X(98)00077-6

Ishii, T., Kojitani, H., and Akaogi, M. (2011). Post-Spinel Transitions in Pyrolite and Mg2SiO4 and Akimotoite-Perovskite Transition in MgSiO3: Precise Comparison by High-Pressure High-Temperature Experiments with Multi-Sample Cell Technique. *Earth Planet. Sci. LettersSci. Lett.* 309 (3), 185–197. doi:10.1016/j.epsl.2011.06.023

Ito, E., and Takahashi, E. (1989). Postspinel Transformations in the System Mg2SiO4-Fe2SiO4and Some Geophysical Implications. *J. Geophys. Res.* 94, 10637–10646. doi:10.1029/JB094iB08p10637

Jahn, S., and Kowalski, P. M. (2014). Theoretical Approaches to Structure and Spectroscopy of Earth Materials. *Rev. Mineralogy Geochem.* 78 (1), 691–743. doi:10.2138/rmg.2014.78.17

Karki, B. B., and Crain, J. (1998). First-principles Determination of Elastic Properties of CaSiO3perovskite at Lower Mantle Pressures. *Geophys. Res. Lett.* 25 (14), 2741–2744. doi:10.1029/98GL51952

Karki, B. B., Stixrude, L., Clark, S. J., Warren, M. C., Ackland, G. J., and Crain, J. (1997). Elastic Properties of Orthorhombic MgSiO3perovskite at Lower Mantle Pressures. *Am. Mineral.* 82 (5-6), 635–638. doi:10.2138/am-1997-5-623

Karki, B. B., Stixrude, L., and Wentzcovitch, R. M. (2001). High-Pressure Elastic Properties of Major Materials of Earth's Mantle from First Principles. *Rev. Geophys.* 39 (4), 507–534. doi:10.1029/2000RG000088

Karki, B. B. (2014). First-Principles Computation of Mantle Materials in Crystalline and Amorphous Phases. *Phys. Earth Planet. Interiors* 240, 43–69. doi:10.1016/j.pepi.2014.11.004

Katsura, T., and Ito, E. (1989). The System Mg2SiO4-Fe2SiO4at High Pressures and Temperatures: Precise Determination of Stabilities of Olivine, Modified Spinel, and Spinel. *J. Geophys. Res.* 94 (B11), 15663–15670. doi:10.1029/JB094iB11p15663

Kern, G., Kresse, G., and Hafner, J. (1999). Ab Initiocalculation of the Lattice Dynamics and Phase Diagram of boron Nitride. *Phys. Rev. B* 59 (13), 8551–8559. doi:10.1103/PhysRevB.59.8551

Kiefer, B., Stixrude, L., and Wentzcovitch, R. M. (1997). Calculated Elastic Constants and Anisotropy of Mg2SiO4spinel at High Pressure. *Geophys. Res. Lett.* 24 (22), 2841–2844. doi:10.1029/97GL02975

Kohn, W., and Sham, L. J. (1965). Self-Consistent Equations Including Exchange and Correlation Effects. *Phys. Rev.* 140 (4A), A1133–A1138. doi:10.110310.1103/physrev.140.a1133

Kubo, A., and Akaogi, M. (2000). Post-Garnet Transitions in the System $Mg_4Si_4O_{12}$-$Mg_3Al_2Si_3O_{12}$ up to 28 GPa: Phase Relations of Garnet, Ilmenite and Perovskite. *Phys. Earth Planet. Inter.* 121 (1-2), 85–102. doi:10.1016/S0031-9201(00)00162-X

Lay, T. (1989). Structure of the Core-Mantle Transition Zone. *Eos Trans. AGU* 70 (4), 49. doi:10.1029/89EO00024

Li, B., and Liebermann, R. C. (2014). Study of the Earth's Interior Using Measurements of Sound Velocities in Minerals by Ultrasonic Interferometry. *Phys. Earth Planet. Interiors* 233, 135–153. doi:10.1016/j.pepi.2014.05.006

Li, L., Weidner, D. J., Brodholt, J., Alfè, D., and Price, G. D. (2006). Elasticity of Mg2SiO4 Ringwoodite at Mantle Conditions. *Phys. Earth Planet. Interiors* 157 (3-4), 181–187. doi:10.1016/j.pepi.2006.04.002

Li, J., Zheng, Y., Thomsen, L., Lapen, T. J., and Fang, X. (2018). Deep Earthquakes in Subducting Slabs Hosted in Highly Anisotropic Rock Fabric. *Nat. Geosci* 11, 696–700. doi:10.1038/s41561-018-0188-3

Li, B. (2004). Compressional and Shear Wave Velocities of Ringwoodite γ-Mg2SiO4to 12 GPa. *Am. Mineral.* 88 (8-9), 1312–1317. doi:10.2138/am-2003-8-913

Liu, L., Du, J., Zhao, J., Liu, H., Gao, H., and Chen, Y. (2009). Elastic Properties of Hydrous Forsterites under High Pressure: First-Principle Calculations. *Phys. Earth Planet. Interiors* 176 (1), 89–97. doi:10.1016/j.pepi.2009.04.004

Liu, L., Lv, C.-J., Zhuang, C.-Q., Yi, L., Liu, H., and Du, J.-G. (2015). First-Principles Simulation of Raman Spectra and Structural Properties of Quartz up to 5 GPa. *Chin. Phys. B* 24 (12), 127401. doi:10.1088/1674-1056/24/12/127401

Liu, L., Yi, L., Liu, H., Li, Y., Zhuang, C.-Q., Yang, L.-X., et al. (2018). The Structure and Elasticity of Phase B Silicates under High Pressure by First Principles Simulation. *Chin. Phys. B* 27 (4), 047402. doi:10.1088/1674-1056/27/4/047402

Lv, C.-J., Liu, L., Gao, Y., Liu, H., Yi, L., Zhuang, C.-Q., et al. (2017). Structural, Elastic, and Vibrational Properties of Phase H: A First-Principles Simulation. *Chin. Phys. B* 26 (6), 067401. doi:10.1088/1674-1056/26/6/067401

Mayer, I. (1995). Non-Orthogonal Localized Orbitals and Orthogonal Atomic Hybrids Derived from Mulliken's Population Analysis. *Chem. Phys. Lett.* 242 (4-5), 499–506. doi:10.1016/0009-2614(95)00748-S

Mouhat, F., and Coudert, F.-X. (2014). Necessary and Sufficient Elastic Stability Conditions in Various Crystal Systems. *Phys. Rev. B* 90, 22. doi:10.1103/PhysRevB.90.224104

Musgrave, M. J. P. (1970). *Crystal Acoustics: Introduction to the Study of Elastic Waves and Vibrations in Crystals*. San Francisco: Holden Day.

Nielsen, O. H., and Martin, R. M. (1983). First-Principles Calculation of Stress. *Phys. Rev. Lett.* 50 (9), 697–700. doi:10.1103/PhysRevLett.50.697

Palke, A. C., Stebbins, J. F., Geiger, C. A., and Tippelt, G. (2015). Cation Order-Disorder in Fe-Bearing Pyrope and Grossular Garnets: A 27Al and 29Si MAS NMR and 57Fe Mossbauer Spectroscopy Study. *Am. Mineral.* 100 (2-3), 536–547. doi:10.2138/am-2015-5062

Pamato, M. G., Kurnosov, A., Boffa Ballaran, T., Frost, D. J., Ziberna, L., Giannini, M., et al. (2016). Single Crystal Elasticity of Majoritic Garnets: Stagnant Slabs and Thermal Anomalies at the Base of the Transition Zone. *Earth Planet. Sci. Lett.* 451, 114–124. doi:10.1016/j.epsl.2016.07.019

Perdew, J. P., Burke, K., and Ernzerhof, M. (1996). Generalized Gradient Approximation Made Simple. *Phys. Rev. Lett.* 77 (18), 3865–3868. doi:10.1103/PhysRevLett.77.3865

Ringwood, A. E., and Major, A. (1970). The System Mg2SiO4 Fe2SiO4 at High Pressures and Temperatures. *Phys. Earth Planet. Interiors* 3 (2), 89–108. doi:10.1016/0031-9201(70)90046-4

Ringwood, A. E. (1975). *Composition and Petrology of the Earth's Mantle*. New York: McGraw-Hill.

Ringwood, A. E. (1979). *Origin of Earth and Moon*. New York: Springer-Verlag.

Ringwood, A. E. (1991). Phase Transformations and Their Bearing on the Constitution and Dynamics of the Mantle: Geochim. *Geochim. Cosmochim. Ac.* 55 (8), 2083–2110. doi:10.1016/0016-7037(91)90090-R

Sawamoto, H., Weidner, D. J., Sasaki, S., and Kumazawa, M. (1984). Single-Crystal Elastic Properties of the Modified Spinel (Beta) Phase of Magnesium Orthosilicate. *Science* 224 (4650), 749–751. doi:10.1126/science.224.4650.749

Segall, M. D., Pickard, C. J., Shah, R., and Payne, M. C. (1996a). Population Analysis in Plane Wave Electronic Structure Calculations. *Mol. Phys.* 89 (2), 571–577. doi:10.1080/002689796173912

Segall, M. D., Shah, R., Pickard, C. J., and Payne, M. C. (1996b). Population Analysis of Plane-Wave Electronic Structure Calculations of Bulk Materials. *Phys. Rev. B* 54 (23), 16317–16320. doi:10.1103/PhysRevB.54.16317

Sham, L. (1965). A Calculation of the Phonon Frequencies in Sodium. *Proc. R. Soc. Lond. A.* 283 (1392), 33–49. doi:10.1098/rspa.1965.0005

Shearer, P. M. (1990). Seismic Imaging of Upper-Mantle Structure with New Evidence for a 520-km Discontinuity. *Nature* 344 (6262), 121–126. doi:10.1038/344121a0

Shearer, P. M. (1996). Transition Zone Velocity Gradients and the 520-km Discontinuity. *J. Geophys. Res.* 101 (B2), 3053–3066. doi:10.1029/95JB02812

Sinogeikin, S. V., Katsura, T., and Bass, J. D. (1998). Sound Velocities and Elastic Properties of Fe-Bearing Wadsleyite and Ringwoodite. *J. Geophys. Res.* 103 (B9), 20819–20825. doi:10.1029/98JB01819

Sinogeikin, S. V., Bass, J. D., and Katsura, T. (2003). Single-Crystal Elasticity of Ringwoodite to High Pressures and High Temperatures: Implications for 520 Km Seismic Discontinuity. *Phys. Earth Planet. Inter.* 136 (1-2), 41–66. doi:10.1016/S0031-9201(03)00022-0

Sun, N. (2019). High Pressire-Temperature Experimental Studies on the Physical Properties of Lower-Mantle Minerals. [dissertation]. Hefei(Anhui): University of Science and Technology of China.

Umemoto, K., Wentzcovitch, R. M., Wu, S., Ji, M., Wang, C.-Z., and Ho, K.-M. (2017). Phase Transitions in MgSiO3 post-perovskite in Super-Earth Mantles. *Earth Planet. Sci. Lett.* 478, 40–45. doi:10.1016/j.epsl.2017.08.032

Wang, Y., Xu, M., Yang, L., Yan, B., Qin, Q., Shao, X., et al. (2020). Pressure-Stabilized Divalent Ozonide CaO3 and its Impact on Earth's Oxygen Cycles. *Nat. Commun.* 11 (1), 4702. doi:10.1038/s41467-020-18541-2

Wei, S. S., and Shearer, P. M. (2017). A Sporadic Low-Velocity Layer Atop the 410 Km Discontinuity beneath the Pacific Ocean. *J. Geophys. Res. Solid Earth* 122 (7), 5144–5159. doi:10.1002/2017JB014100

Weidner, D. J., Sawamoto, H., Sasaki, S., and Kumazawa, M. (1984). Single-Crystal Elastic Properties of the Spinel Phase of Mg2SiO4. *J. Geophys. Res.* 89 (B9), 7852–7860. doi:10.1029/JB089iB09p07852

Wookey, J., Kendall, J.-M., and Barruol, G. (2002). Mid-Mantle Deformation Inferred from Seismic Anisotropy. *Nature* 415, 777–780. doi:10.1038/415777a

Wu, Z., and Wentzcovitch, R. M. (2016). Composition Versus Temperature Induced Velocity Heterogeneities in a Pyrolitic Lower Mantle. *Earth Planet. Sci. Lett.* 457, 359–365. doi:10.1016/j.epsl.2016.10.009

Zha, C. S., Duffy, T. S., Mao, H. K., Downs, R. T., Hemley, R. J., and Weidner, D. J. (1997). Single-Crystal Elasticity of β-Mg_2SiO_4 to the Pressure of the 410 Km Seismic Discontinuity in the Earth's Mantle. *Earth Planet. Sci. Lett.* 147 (1-4), E9–E15. doi:10.1016/S0012-821X(97)00010-1

Zhang, P., Kong, C.-G., Zheng, C., Wang, X.-Q., Ma, Y., Feng, J.-B., et al. (2015a). First-Principles Study of Structure and Nonlinear Optical Properties of CdHg(SCN) 4 crystal. *Chin. Phys. B* 24 (2), 024221. doi:10.1088/1674-1056/24/2/024221

Zhang, S., Cottaar, S., Liu, T., Stackhouse, S., and Militzer, B. (2015b). High-pressure, Temperature Elasticity of Fe- and Al-Bearing $MgSiO_3$: Implications for the Earth's Lower Mantle. *Earth Planet. Sci. Lett.* 434, 264–273. doi:10.1016/j.epsl.2015.11.030

Zhang, J. S., Bass, J. D., and Schmandt, B. (2018). The Elastic Anisotropy Change Near the 410-km Discontinuity: Predictions from Single-Crystal Elasticity

Measurements of Olivine and Wadsleyite. *J. Geophys. Res. Solid Earth* 123 (4), 2674–2684. doi:10.1002/2017JB015339

Zhao, W., Dong, Z., Shao, X.-H., Lu, Y., and Zhang, P. (2015). First-Principles Study of Structural, Elastic, and Thermodynamic Properties of ZrHf alloy. *Chin. Phys. B* 24 (4), 043102. doi:10.1088/1674-1056/24/4/043102

Zhou, C., Jin, Z., and Zhang, J. (2010). Mantle Transitionzone: An Important Field in the Studies of Earth's Deep Interior. *Earth Sci. Front.* 17 (3), 090–113.

Conflict of Interest: The authors declare that the research was conducted in the absence of any commercial or financial relationships that could be construed as a potential conflict of interest.

Publisher's Note: All claims expressed in this article are solely those of the authors and do not necessarily represent those of their affiliated organizations, or those of the publisher, the editors, and the reviewers. Any product that may be evaluated in this article, or claim that may be made by its manufacturer, is not guaranteed or endorsed by the publisher.

frontiers in Earth Science

ORIGINAL RESEARCH
published: 17 February 2022
doi: 10.3389/feart.2022.854816

Anisotropic Elastic Properties of Montmorillonite With Different Layer Charge Densities and Layer Charge Distributions Through Molecular Dynamic Simulation

Xueying Wang[1], *Tongcheng Han*[1,2]* *and Li-Yun Fu*[1,2]

[1]Shandong Provincial Key Laboratory of Deep Oil and Gas, China University of Petroleum (East China), Qingdao, China, [2]Laboratory for Marine Mineral Resources, Pilot National Laboratory for Marine Science and Technology, Qingdao, China

OPEN ACCESS

Edited by:
Lidong Dai,
Institute of geochemistry (CAS), China

Reviewed by:
Guohui Chen,
China University of Geosciences Wuhan, China
Junfang Zhang,
Commonwealth Scientific and Industrial Research Organisation (CSIRO), Australia

***Correspondence:**
Tongcheng Han
hantc@upc.edu.cn

Specialty section:
This article was submitted to Solid Earth Geophysics, a section of the journal Frontiers in Earth Science

Received: *14 January 2022*
Accepted: *28 January 2022*
Published: *17 February 2022*

Citation:
Wang X, Han T and Fu L-Y (2022) Anisotropic Elastic Properties of Montmorillonite With Different Layer Charge Densities and Layer Charge Distributions Through Molecular Dynamic Simulation. Front. Earth Sci. 10:854816. doi: 10.3389/feart.2022.854816

The knowledge of the anisotropic elastic properties of clay minerals is of crucial importance for the exploration and development of shale oil and gas. Montmorillonite (MMT) is a common natural clay mineral with different layer charge densities and layer charge distributions due to different geological conditions. Therefore, it is important to understand the currently poorly known effect of layer charge density and layer charge distribution on the anisotropic elastic properties of MMTs. This work aims to obtain such knowledge by studying the anisotropic elastic properties of different MMTs under stratigraphic conditions through molecular dynamic simulations. We showed that the in-plane compressional coefficients C_{11}, C_{22} and C_{12} decrease with the increasing layer charge density for MMTs with different layer charge distributions, and the MMTs with the layer charges distributed on the two tetrahedral (T) sheets were found to have the smallest C_{11}, C_{22} and C_{12}. We also showed that the out-of-plane compressional coefficients C_{33}, C_{13} and C_{23} of the MMTs with the layer charges distributed in the two T sheets decrease, while those with the layer charges in the octahedral (O) sheet increase and those with layer charges distributed in both the O sheet and the T sheets do not vary much with the increasing layer charge density. The variations of the anisotropic compressional elastic coefficients with different layer charge densities and layer charge distributions were found to be a result of the impact of the density and distribution of layer charges on the molecular interactions within the MMT layer. We further demonstrated that the layer charge density and layer charge distribution do not influence significantly the shear coefficients C_{44}, C_{55}, and C_{66}. The results revealed the mechanisms of how the density and distribution of layer charges affect the anisotropic elastic properties of MMTs and will contribute to the more successful exploration and development of unconventional resources in MMT bearing shale reservoirs.

Keywords: montmorillonite, molecular dynamic simulation, elastic property, layer charge density, layer charge distribution

INTRODUCTION

In recent years, shale oil and gas have a contribution to a country's energy security by lowering the dependence on imported energy (Kobek et al., 2015; Raszewski, 2016), and specifically the shale gas is considered to play a role as a bridging fuel to a low-carbon future (Kirkland, 2010; Few et al., 2017). Exploration and development of shale oil and gas are drawing a lot of attentions (Chen et al., 2021; Pu et al., 2021), in which the knowledge about the elastic properties of shale is of vital importance because the elastic properties provide crucial geomechanical information required by seismic inversion to predict "sweet spot" (Han et al., 2021) and by hydraulic fracturing projects to increase permeability for the flow of the hydrocarbon (Rahm, 2011; Bian et al., 2019). Clay minerals, as the main mineral type and the matrix of shale, cause shale to be elastically anisotropic because of their layered structure (Bailey, 1966; Weaver and Pollard, 2011). In the process of shale oil and gas exploration and development, problems such as poor fracturing effect, high development cost, and great difficulty in finding sweet spot and stabilizing the borehole wall would arise if the influence of anisotropy is ignored (Gao et al., 2021). Therefore, it is of great significance to study the anisotropic elastic properties of clay minerals for the exploration and development of shale oil and gas.

Clay minerals, any of a group of important hydrous aluminum silicates with a layer (sheet-like) structure (Grim and Kodama, 2014), consist of some combinations of silicon tetrahedra (T) and aluminum octahedra (O) (Ebrahimi et al., 2012). This work considers montmorillonite (MMT), a kind of clay mineral that has more significant swelling properties and expands more considerably than the other clay minerals, and therefore can more seriously affect the anisotropic elastic properties of shale (Dewhurst and Siggins, 2006; Sridharan, 2014; Sayers and den Boer, 2016). The experimental measurement of the anisotropic elastic properties of MMTs can be challenging because of their small grain particle size (Vanorio et al., 2003; Zartman et al., 2010). Alternatively, all-atom molecular simulation makes it possible to study the anisotropic elastic parameters of MMTs by simulating the motion of the MMT molecular system based on Newtonian mechanics. Many successful results, to date, have been obtained reporting the anisotropic elastic properties of MMTs under the effect of pressure, temperature, water content and interlayer cation types (Ebrahimi et al., 2012; Carrier et al., 2014; Zhao et al., 2021), which are of significance to understand the elastic anisotropy of clay minerals.

However, isomorphous substitution is always associated with MMTs, making them contain different layer charge densities and different layer charge distributions because of the number and locations of the isomorphous substitution (Zartman et al., 2010; Herling et al., 2012). Previous researches show that the different layer charge densities and layer charge distributions can significantly affect the physicochemical properties of MMTs such as the exfoliation performance (Zhong et al., 2021), the adsorption capacity (Lee et al., 2005; Barrientos-Velázquez et al., 2016; Koutsopoulou et al., 2020), the hydration performance (Qiu et al., 2019), the swelling properties (Teich-McGoldrick et al., 2015; Daab et al., 2018; Ghasemi and Sharifi, 2021), and the thermal stability (Qin et al., 2021) among others. Moreover, the structures of MMTs are also influenced by different layer charge densities and layer charge distributions. For instance, the basal layer spacing and interlayer spacing can be affected by different layer charge densities and distributions (Peng et al., 2021) and the introduction of the substitutions generates structural tension to the layer structure leading to the structure expansion (Lavikainen et al., 2016). Since the anisotropic elastic properties of MMTs are strongly correlated with their structure (Zhong et al., 2021), the variation of structure may potentially cause a change in the anisotropic elastic properties of MMTs. However, there are very few studies reporting the anisotropic elastic properties of MMTs with different layer charge densities and layer charge distributions. Therefore, it is necessary to study the influences of different layer charge densities and layer charge distributions on the anisotropic elastic properties of MMTs to strengthen our understanding of the elastic properties of clay minerals.

This work aims to investigate the influence of different layer charge densities and layer charge distributions on the anisotropic elastic properties of MMTs through dedicated molecular dynamic simulation. To achieve this goal, we first build a series of MMT models with different layer charge densities and layer charge distributions by molecular mechanics. The anisotropic elastic parameters of the different MMT models are subsequently calculated under stratigraphic conditions using molecular dynamic simulation. The relationships between the anisotropic elastic parameters and the different charge densities and layer charge distributions are finally analyzed and interpreted.

METHODS

Model Establishment

In this study, we construct the MMT model from the structure of pyrophyllite unit cell with the crystal constant a = 0.5160 nm, b = 0.8966 nm, c = 0.9347 nm, and α = 91.18°, β = 100.46°, and γ = 89.64° (Lee and Guggenheim, 1981; Skipper et al., 1995). The pyrophyllite unit cell $(Al_4O_4(OH)_4)(Si_8O_{12})$ is then replicated (8 × 6 × 2) along the a, b, and c crystallographic directions, respectively to form a supercell of two TOT clay layers. The sizes of the replicated cell are Lx = 4.1280 nm, Ly = 5.3796 nm and Lz = 1.8694 nm. The constructed supercell not only decreases the subsequent excessive ordering of isomorphous substitution but also ensures that the atom in MMTs does not interact with its image in the next cell, when three-dimensional periodic boundary conditions are applied.

Based on the formed supercell, the isomorphous substitutions of octahedral Mg atom for Al atom and tetrahedral Al atom for Si atom with various compositions are introduced to establish different MMT models needed in this paper. Since one isomorphous substitution produces one negative charge (referring to the Supporting Information for details), which is referred to as the layer charge (Karnland, 2010), we introduce 48, 60, 72, 96, and 108 isomorphous substitutions to obtain the MMT models with the layer charge density (defined as the ratio between the number of layer charge to the number of unit cell, which is 96)

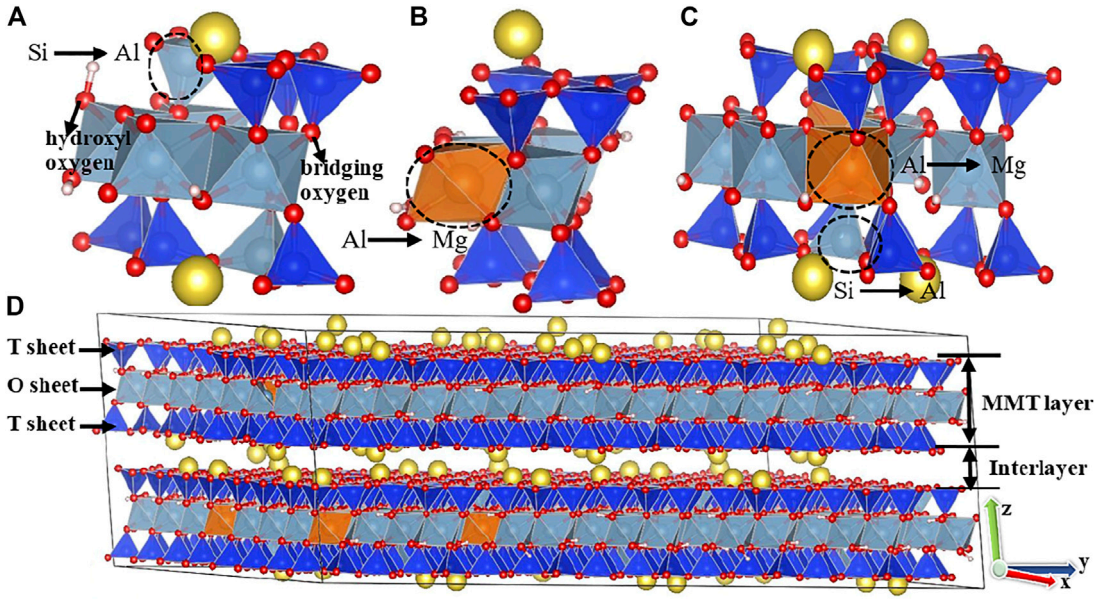

FIGURE 1 | Schematic views of **(A)** the two unit cells for the M1 Model, **(B)** the unit cell for the M2 Model, and **(C)** the four unit cells for the M3 Model and snapshot of **(D)** the molecular dynamic simulation supercell for the M3 Model with the layer charge of 0.75 e/uc. The color code is Si (blue), Al (blue-grey), Mg (orange), O (red), H (pink), and Na (yellow). The atoms in the black circle are the representative atoms of replacement.

of −0.5, −0.625, −0.75, −1.0, and −1.125 e/uc, respectively. For the MMT models with each layer charge density, three different isomorphous substitution positions, i.e., complete tetrahedral substitutions in the T sheet, entire octahedral substitutions in the O sheet and the ratio of the tetrahedral to octahedral substitutions is 1:1, are designed and the corresponding MMT models are denoted as M1, M2, and M3, respectively. All isomorphous substitutions obey Lowenstein's substitution rule (i.e., the substitution sites cannot be adjacent to each other). We finally add the same number of Na cations as the layer charge between the layers of the MMT models to make sure that each MMT system is electrically neutral. Eventually, fifteen MMT models are established. **Figure 1** shows the schematic view of the three MMT models and the snapshot of the molecular dynamic simulation supercell for the M3 Model with the layer charge of 0.75 e/uc.

Elastic Tensor Computation

In our molecular dynamic simulation, the Parinello−Rahman (PR) strain fluctuation formula (Ray and Rahman, 1985; Cui et al., 2007; Carrier et al., 2014) is used to calculate the anisotropic elastic parameters in the constant-pressure and constant-temperature (NPT) ensemble. The PR strain fluctuation formula is given as

$$C_{ijkl} = \frac{K_B T}{\langle V \rangle}\left[\langle \varepsilon_{ij}\varepsilon_{kl}\rangle - \langle \varepsilon_{ij}\rangle\langle \varepsilon_{kl}\rangle\right]^{-1} \quad (1)$$

where K_B is the Boltzmann constant, equal to 1.38065×10^{-23} J/K, T is the temperature in Kelvin, V is the volume in cubic meters, ε_{ij} is the strain tensor, and $\langle \blacksquare \rangle$ denotes the ensemble average. The subscripts i, j, k and l run from one to three and represent the three dimensions in the Cartesian coordinates. The indexes one and two correspond to the x- and y-axes, respectively, which are parallel to the MMT layer, and the index three corresponds to the z-axis, which is perpendicular to the MMT layer. The strain tensor ε_{ij} can be determined by

$$\varepsilon_{ij} = \frac{1}{2}\left[\langle h\rangle_{ik}^{-T} h_{kl}^{T} h_{lm} h_{mj}^{-1} - \delta_{ij}\right] \quad (2)$$

where δ_{ij} is the Kronecker tensor, and h is the scaling matrix, which can be obtained through molecular dynamic simulation.

In this work, the LAMMPS code (Plimpton, 1995) is employed to perform the molecular dynamic simulation to obtain the scaling matrix h. In the simulation, a force field is required to describe the interactions of the atoms in the MMT, and we use the CLAYFF force field (Cygan et al., 2004) for this purpose (the interaction parameters and charge of the relevant atoms are shown in the Supporting Information). The CLAYFF force field consists solely of the electrostatic terms, the Lennard-Jones terms and the O-H bond constrained by a harmonic bond stretch potential and is widely used in the simulations of clay minerals (Ebrahimi et al., 2012; Carrier et al., 2014). In our molecular dynamic simulations, we set the time step to be 1 fs in the NPT ensemble under stratigraphic conditions (i.e., p = 10 MPa, and T = 323 K). The Langevin dynamics and Nosé−Hoover barostat are used to control the pressure and temperature, respectively. The cutoff distance of the nonbonded interaction is set to be 10.0 Å, and the long-range electrostatic interactions are calculated employing the particle-particle particle mesh (PPPM) method with an accuracy of 10^{-4}. The system is equilibrated for 2 ns. The box size (lx, ly, lz), tilt

TABLE 1 | Comparison of calculated the elastic coefficients of the MMT at 1 Bar and 300 K by Carrier et al. (2014) and by the method provided in this work.

C_{ij} (GPa)	C_{11}	C_{22}	C_{12}	C_{13}	C_{23}	C_{33}	C_{44}	C_{55}	C_{66}
Carrier et al. (2014)	292.3	274.2	132.4	17.0	17.3	35.2	10.6	18.5	82.3
This study	292.0	276.1	136.3	16.3	15.6	37.4	10.2	17.5	81.8

factors (*xy*, *xz*, *yz*) and volume of box (*V*) are then sampled every ten steps for 8 ns. After that, the sample data (*lx*, *ly*, *lz*, *xy*, *xz*, *yz*) are sorted to form the scaling matrix *h* in the form of

$$h = \begin{bmatrix} lx & xy & xz \\ 0 & ly & yz \\ 0 & 0 & lz \end{bmatrix} \tag{3}$$

Then the resulting scaling matrix *h* is substituted into **Eq. 2** to obtain the strain tensor ε_{ij}, which are further integrated into **Eq. 1** with *V* and *T* to determine the elastic tensors C_{ijkl} of the MMTs.

When we show the elastic tensors, the Voigt notation is used to represent the calculated fourth-order stiffness tensor C_{ijkl} by the second-order tensors C_{ij} . The indexes change as follows: 11 → 1, 22 → 2, 33 → 3, 23 → 4, 13 → 5, and 12 → 6. The indexes 1, 2, and three correspond to the compressions in the *x*, *y*, and *z* directions, respectively, and the indexes 4, 5, and six correspond to the shears in the *yz*-, *xz*-, and *xy*-planes, respectively. Although 36 coefficients of the stiffness tensor are computed, we only report the nine coefficients C_{11}, C_{22}, C_{12}, C_{33}, C_{13}, C_{23}, C_{44}, C_{55}, and C_{66} because of the transverse isotropic characteristics of MMT (Ebrahimi et al., 2012; Carrier et al., 2014). According to the deformation modes involving the crystalline structure of the clay layer and interlayer space, the nine data are divided into three groups: the in-plane compressional coefficients C_{11}, C_{22}, and C_{12}, the out-of-plane compressional coefficients C_{33}, C_{13}, C_{23}, and the shear coefficients C_{44}, C_{55}, and C_{66}.

RESULTS AND DISCUSSION

Before presenting the simulation results of the anisotropic elastic coefficient with varying layer charge density and layer charge distribution, we need to test the validity of the employed method for the computation of the anisotropic elastic tensors. This is achieved by performing the calculation on the elastic coefficients of the MMT model $[(Na_6[Si_{62}Al_2][Al_{28}Mg_4]O_{160}(OH)_{32})]$ at the pressure and temperature of 1 Bar and 300 K, respectively, and comparing the results with those published by Carrier et al. (2014) using the same model at the same pressure and temperature. The comparison of the calculated elastic coefficients is given in **Table 1**, from which we can see that our calculated elastic coefficients are in good agreement with those of Carrier et al. (2014). The excellent agreement validates the computation method for the elastic tensors, and lays the foundation for the study of the anisotropic elastic properties of MMTs with different layer charge densities and layer charge distributions.

In-Plane Compressional Coefficients

The variations of the in-plane compressional coefficients C_{11}, C_{22}, and C_{12} with different layer charge densities for the three models with different layer charge distributions are shown in **Figure 2**. It is interesting that all the three in-plane compressional coefficients decrease approximately linearly with the increasing layer charge density in the three models. The reduction in the three coefficients indicates that the compressional resistance of the three models decreases with the increasing layer charge density. Specifically, the decreasing C_{11} and C_{22} represents the reduction in the compressional resistance in the *x*-axis and *y*-axis, respectively, and the declining C_{12} stands for the decrease of the compressional resistance in the *y*-direction when a given positive pressure is applied to the *x*-axis.

Since C_{11} and C_{22} reflect the strength of the intermolecular interactions of the MMT molecules in the *x*-axis and *y*-axis, respectively, and C_{12} reflects the strength of the intermolecular interactions in the *xy*-plane, the decrease of C_{11}, $C_{22,}$ and C_{12} can be explained by the weakening of the intermolecular interactions of the MMT in these directions. The intermolecular interaction is inversely proportional to the atomic distance (Cygan et al., 2004; Davarcioglu, 2011), and thus the decrease of the three coefficients with the increasing layer charge density may be related to the increase in the atomic distance of the MMT. **Figure 3** shows the atomic distances (distance between the replaced atom or replacement atom and the adjacent oxygen atom) before and after the substitutions, and the results clearly demonstrate that the atomic distances in the MMT layer (composed of three sheets) after the substitutions are increasing, no matter whether the tetrahedral substitutions or the octahedral substitutions are introduced into the MMT. The increase in the atomic distance in the MMT layer may lead to the weakening of the intermolecular interactions within the MMT layer in all directions.

To further support the explained variation of the interaction strength, we also calculate the interaction energy (the difference between the molecules' combined energy and all of their isolated energies) between the replaced atom or replacement atom and the adjacent oxygen atom (i.e., the forming atom pair) as shown in **Figure 4**. It can be seen that the interaction energy between the atom pair increases after the tetrahedral substitutions or the octahedral substitutions, directly indicating that the interaction within the MMT layer is weakened (Šponer et al., 1999; Lovelock, 2017). Considering the in-plane compressional coefficients are related to the intermolecular interactions in the *x*- and *y*-axes of the MMT layer (Carrier et al., 2014), the increase in the atomic distances will reduce these intermolecular interactions in these directions and hence the in-line compressional elastic coefficient C_{11}, C_{22}, and C_{12}.

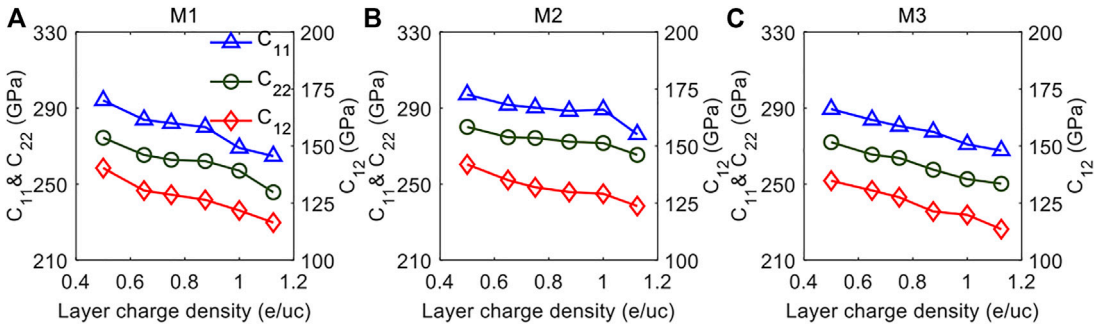

FIGURE 2 | The in-line compressional elastic constants C_{11}, C_{22}, and C_{12} as a function of layer charge density for the **(A)** M1 Model, **(B)** M2 Model and **(C)** M3 Model.

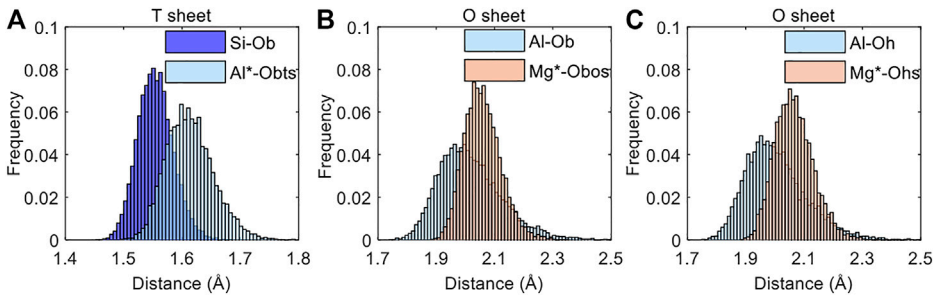

FIGURE 3 | The frequency of the distance between the substituted atom or replacement atom and the adjacent oxygen atom in the **(A)** T sheet and **(B, C)** O sheet of the MMT layer before and after the isomorphous substitution. The symbol * represents the atoms after substitution. In the O sheet, the Al/Mg-O distances are classified into the Al/Mg-Ob(os) and Al/Mg-Oh(s) distances according to the type of the connected oxygen atoms (i.e., bridging oxygen or hydroxyl oxygen) as shown in **Figure 1**.

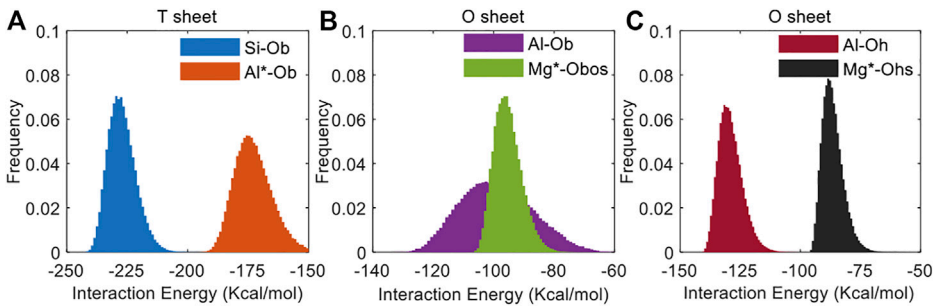

FIGURE 4 | The frequency of the interaction energy between the replaced atom or replacement atom and the adjacent oxygen atom in the **(A)** T sheet and **(B,C)** O sheet of the MMT layer before and after the isomorphous substitution.

It is worth noting that although C_{11}, C_{22}, and C_{12} of all the models are decreasing, we find the values and the variations of C_{11}, C_{22}, and C_{12} in the three models are different. First, it is evident that C_{11}, C_{22}, and C_{12} in the M2 Model are larger than those in the other two models when the layer charge densities are the same. This means that C_{11}, C_{22}, and C_{12} of the MMT with the layer charges distributed in the O sheet are greater than those of the MMT with the layer charges distributed in the two T sheets and in both the O sheet and the T sheets. This result can be closely related to the structure of the MMT. As shown in **Figure 1D**, the MMT consists of a sandwich of one O sheet between two T sheets, called a TOT structure. Since the O sheet is constrained by the two T sheets and there are interactions among the sheets, the increase in the atomic distance and in the interaction energy between the atomic pairs in the O sheet after the octahedral substitution is weakened. As a result, the intermolecular interactions in the *xy*-plane are less reduced, leading to a greater C_{11}, C_{22}, and C_{12} in the M2 model.

In addition to the difference in the values of the three in-plane compressional coefficients, it is also interesting to note that the

TABLE 2 | The linear-fit slopes of the compressional elastic constants C_{11}, C_{22}, and C_{12} with the varying layer charge density for the three models.

Model	M1	M2	M3
Slope of C_{11}	−45.08	−26.59	−35.10
Slope of C_{22}	−39.45	−19.82	−35.81
Slope of C_{12}	−34.61	−25.94	−33.58

changing rates of the compressional coefficient with layer charge densities in the three models are different. **Table 2** tabulates the slopes of C_{11}, C_{22}, and C_{12} after linear fitting for the three models. By comparing the slopes of the same parameter in the three models, we find that the M1 model has the largest slopes of C_{11}, C_{22}, and C_{12}, followed by the M3 model and the M2 model. This result implies that the layer charge density has a greater effect on C_{11}, C_{22}, and C_{12} of MMT with the layer charges distributed in the T sheet. The difference in the slopes of the in-plane compressional coefficients in the three models can again be explained through the structure of the MMT, where the TOT architecture will confine the expansion of the O sheet, and hence the octahedral substitution has less impaction on the elastic properties, resulting in a gentler slope of the in-plane compressional coefficients with varying layer charge density.

Out-of-Plane Compressional Coefficients

Figure 5 shows the variations of the out-of-plane compressional coefficients C_{33}, C_{13}, and C_{23} with the increase of layer charge density for the three models with different layer charge distributions. Unlike the in-plane compressional coefficients that show consistent downward trends in the three models, the out-of-plane compressional coefficients show very different variations with layer charge density in the three models. Therefore, to more conveniently understand the influences of the layer charge distribution on the out-of-plane compressional coefficients, we choose to analyze the same elastic coefficient in the different models.

We first compare the variations of C_{33} with layer charge density in the three models that represents the compressional resistance of the MMT in the z-axis. As shown in **Figure 5A**, C_{33} of the M1 Model increases slightly and then decreases linearly with the increase of layer charge density. The initial increasing and then decreasing C_{33} indicates that the increasing layer charge density first increases and then reduces the compressional resistance of the M1 Model in the z-axis. In a different manner, C_{33} of the M2 Model consistently increases with increasing layer charge density, suggesting that the compressional resistance of the M2 Model in the z-axis is increasing with the increasing layer charge density. For the M3 Model, C_{33} doesn't vary much as the layer charge density increases, implying that the layer charge density is not affecting significantly the compressional resistance of the M3 Model in the z-axis.

Because C_{33} reflects the strength of the intermolecular interactions of the MMT in the z-axis, the different trends of C_{33} with the increase of layer charge density in the different models can be explained by the difference in the z-axis intermolecular interaction strength of the MMT caused by the layer charge distributions. The intermolecular interactions of the MMT in the z-axis involve the intermolecular interactions in the z-axis both within the MMT layer (each layer is composed of three sheets) and between the neighboring MMT layers because the MMT contains the MMT layers and the interlayers in the z-axis as shown in **Figure 1D**. We have employed atomic distance inversely to represent the strength of the intermolecular interactions in the previous section, however, the atomic distance can only reflect the intermolecular strength of the MMT layer in the x- and y-axes, but will not fully represent the intermolecular strength in the z-axis. This is because the z-axis intermolecular interaction includes not only the z-axis intermolecular interaction within each MMT layer but also that between the MMT layers (i.e., the interlayers). To characterize the strength of the intermolecular interactions of the MMT in the z-axis, we will use the interaction energy of the MMT layer and the interlayer. However, the interaction energy will not directly quantify the interaction strength in a particular direction because it contains the information of the intermolecular interactions in all directions. Therefore, we combine the interaction energy with the calculated atomic distance (as shown in **Figure 3**) that reflects the intermolecular interactions in the x- and y-axes for the better characterization of the intermolecular strength in the z-axis.

Figure 6 shows the simulated interaction energy in the MMT layer and the interlayer as a function of layer charge density for the three models. In the three models, the interaction energy in

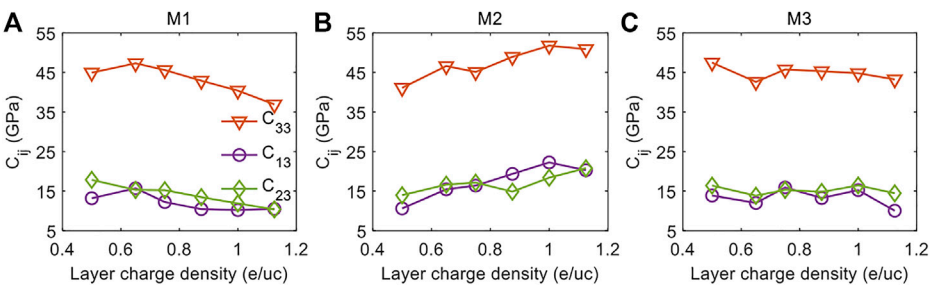

FIGURE 5 | The out-of-plane compressional elastic constants C_{33}, C_{13}, and C_{23} as a function of layer charge density for the **(A)** M1 Model, **(B)** M2 Model and **(C)** M3 Model.

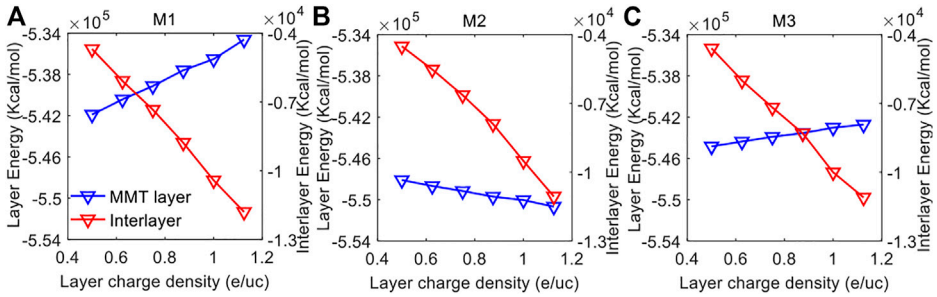

FIGURE 6 | The interaction energy of each MMT layer and interlayer as a function of layer charge density for the **(A)** M1 Model, **(B)** M2 Model and **(C)** M3 Model.

the interlayer all decreases with the increasing layer charge density, indicating enhanced interlayer interactions (Shiu and Tsai, 2014; Wang et al., 2018). The decreasing interlayer interaction energy with increasing layer charge density can be explained by the fact that with increasing layer charge density there are more compensating Na cations in the interlayer that bind stronger the MMT layers (Zhong et al., 2021), resulting in lower interlayer interaction energy. On the contrary, the interaction energy in the MMT layer varies differently with the increase of layer charge density in the three models. The layer interaction energy of the MMT increases remarkably with the increasing layer charge density in the M1 model, and the increase becomes less significant in the M3 model, indicating the strength of the intermolecular interactions within the MMT layer are reducing significantly and gently in the M1 Model and M3 Model, respectively. In a different way, the interaction energy of the MMT layer reduces with the increasing layer charge density in the M2 Model, suggesting an increasing interaction strength of the intermolecular within the MMT layer with the increasing layer charge density.

The decreasing interaction strength of the MMT layer (the increasing layer interaction energy) in the M1 Model can be understandable, because the isomorphous substitutions in the T sheet will increase the atomic distance (as shown in **Figure 3A**) and hence reduce the interaction strength, and therefore more isomorphous substitutions with greater layer charge density will result in the more significant reduction in the interaction strength. However, the increasing atomic distance due to the isomorphous substitutions cannot explain the obtained increasing interaction strength (decreasing layer interaction energy) in the M2 Model. Although the isomorphous substitutions in the O sheet (M2 Model) will increase the atomic distance, the increase occurs only in the O sheet, and with the increasing atomic distance in the O sheet, the distance of the atoms between the O and T sheets is reduced. As a result, the interaction strength between the O sheet and the T sheets gets enhanced, leading to an increasing layer interaction strength. Accordingly, the obtained increasing layer interaction strength with layer charge density in the M2 Model implies that the increasing interaction strength between the O sheet and the T sheets overwhelms the decreasing interaction strength in the O sheet. Similarly, the gently decreasing interaction strength of the MMT layer with layer charge density in the M3 Model indicates that the effects of the increasing interaction strength between the O sheet and the T sheets are less significant than the decreasing interaction strength in the O and T sheets.

After analyzing the impact of the layer charge density on the two interactions and on the interactions in the *x*- and *y*-axes (which can be represented by the in-plane compressional coefficients presented above) in the three models, the variations of the calculated C_{33} in the three models that reflect the interaction strength in the *z*-axis can be more understandable. For the M2 Model, the interaction strength in the *x*- and *y*-axes decreases with increasing layer charge density, however, the total interaction strength (i.e., the interaction strength in both the MMT layer and the interlayer) increases with layer charge density, and accordingly the *z*-axis interaction strength (i.e., C_{33}) must increase with the increasing layer charge density. Unlike C_{33} in the M2 Models, C_{33} in the M1 Model and M3 Model can not be directly explained by the total interaction strength and the interaction strength in the *x*- and *y*-axes, but can reflect the competition between the interaction strength of the layer and interlayer in the *z*-axis (i.e., the difference between the layer and interlayer interaction strength and their contribution from the *x*- and *y*-axes, respectively).

For the M1 Model, because the total interlayer interaction strength increases while the interaction strength in the *x*- and *y*-axes decreases with increasing layer charge density, the *z*-axis interlayer interaction strength must increase with the increasing layer charge density. On the other hand, the variation of the layer interaction strength in the *z*-axis with the increasing layer charge density cannot be determined because both the layer interaction strength and the interaction strength in the *x*- and *y*-axes decrease with layer charge density. When the layer charge density is low, it can be difficult to deduce the variation of the layer interaction strength in the *z*-axis from the increasing C_{33}, because the interlayer interaction strength in the *z*-axis also increases with increasing layer charge density. However, when the layer charge density increases from 0.625 e/uc, the decreasing C_{33} indicates the layer interaction strength in the *z*-axis also decreases and the decreasing of the layer interaction strength in the *z*-axis is playing a more significant role than the increasing interlayer interaction strength in the *z*-axis.

Since the trends of the interlayer interaction strength and the layer interaction strength in the M3 Model are similar to those in the M1 Model, it is reasonable that the *z*-axis interlayer interaction

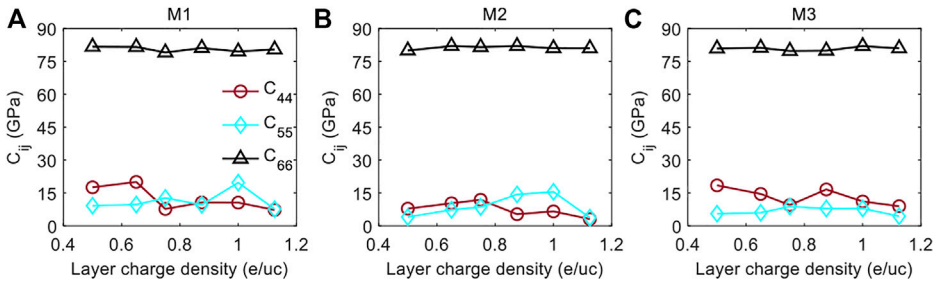

FIGURE 7 | The shear elastic constants C_{44}, C_{55}, and C_{66} as a function of layer charge density for the **(A)** M1 Model, **(B)** M2 Model, and **(C)** M3 Model.

strength increases (because the interaction strength in the *x*- and *y*-axes decreases) and the layer interaction strength in the *z*-axis can not be determined (because both the layer interaction strength and the interaction strength in the *x*- and *y*-axes decrease) in the M3 Model. However, according to the fact that the C_{33} of the M3 Model doesn't vary much with the increase of the layer charge density and the *z*-axis interlayer interaction strength increases, we can infer that the layer interaction strength in the *z*-axis decreases and the decreasing interlayer interaction in the *z*-axis balances with the increasing layer interaction in the *z*-axis.

Having analyzed the variations of C_{33} with layer charge density and provided a plausible explanation through the interaction energy, we proceed to present and interpret the variations of C_{13} and C_{23} with layer charge density in the three models with different layer charge distributions. Interestingly, although the values are much smaller, C_{13} and C_{23} show very similar trends with C_{33} in each model, and this indicates that the interaction strength in the *z*-axis that determines C_{33}, may also be the main factor influencing C_{13} and C_{23}. Therefore, it can be reasonable that the difference in variations of the out-of-plane compressional coefficients with layer charge density in the three models with different layer charge distributions is controlled mainly by the layer interaction strength in the *z*-axis.

Shear Coefficients

Figure 7 shows the variations of the in-plane shear coefficient C_{66} and the out-of-plane shear coefficients C_{44} and C_{55} with the increasing layer charge density. We can see that C_{66} of the three models keeps almost constant at around 80 GPa as the layer charge density increases, indicating the shear deformation resistance in the *xy*-plane is independent of the density and distribution of the layer charges. Unlike the flat in-plane shear coefficient C_{66}, the out-of-plane shear parameters C_{44} and C_{55} are fluctuant with the increasing layer charge density in all the three models, and their values in each model are approximately the same. This suggests the shear deformation resistance in the *yz*-plane and *xz*-plane is not significantly affected by the layer charge density and the layer charge distribution. Since the shear coefficients are mainly reflecting the torsion interaction of the bonding atoms at the molecular level (Sridharan, 2014; Yang and Xu, 2021), the unchanging shear coefficients indicate that the torsion interaction of the bonding atoms is independent of the varying layer charge density and layer charge distribution.

Although the layer charge density and layer charge distribution are not impacting greatly the shear coefficients, it is found that the out-of-plane shear elastic coefficients C_{44} and C_{55} are considerably smaller than the in-plane shear elastic constant C_{66}. This result indicates that the shear deformation is more likely to occur in the *yz*-plane and *xz*-plane than in the *xy*-plane of the MMTs. This may be related to the interlayer structure of the MMTs as shown in **Figure 1D**. Because the interlayer structure is perpendicular to the *z*-axis and the interlayer interactions are much weaker than the intermolecular interactions within the MMT layer (Zhang et al., 2018; Zhao et al., 2021), the *yz*- and *xz*-planes are easier to form slip deformation than the *xy*-plane when a shear force is applied, resulting in the smaller shear coefficients C_{44} and C_{55} than C_{66}.

CONCLUSION

We have studied the elastic coefficients of MMTs with different charge densities and different charge distributions under stratigraphic conditions using molecular dynamic simulations. The following conclusions can be drawn from the results and analyses presented in the context.

1) The in-plane compressional coefficients C_{11}, C_{22} and C_{12} decrease with increasing layer charge density in the MMTs with different layer charge distributions. The C_{11}, C_{22} and C_{12} of the MMTs with the layer charges distributed in the octahedral (O) sheet are respectively greater than those distributed in both the octahedral (O) sheet and the tetrahedral (T) sheets, which in turn are greater than those distributed in the tetrahedral (T) sheets.
2) The out-of-plane compressional coefficient C_{33} shows different trends with increasing layer charge density in the MMTs with different layer charge distributions. C_{33} decreases overall with the increasing layer charge density when the layer charges are on the two tetrahedral (T) sheets, whereas it shows an increasing trend with layer charge density when the layer charges are distributed on the octahedral (O) sheet. For the MMTs with the layer charges distributed on both the octahedral (O) sheet and the tetrahedral (T) sheets, the increasing layer charge density shows a weak impact on C_{33}. The variations of C_{13} and C_{23} with the layer charge

density in the MMTs with different layer charge distributions are similar to that of C_{33}.

3) All the shear coefficients C_{44}, C_{55}, and C_{66} of MMT show no strong correlation with the layer charge density and layer charge distribution, and C_{66} is considerably greater than C_{44} and C_{55}.
4) The variations of the anisotropic compressional elastic coefficients with different layer charge densities and layer charge distributions are found to be a result of the impact of the density and distribution of layer charges on the molecular interactions within the MMT layer.

DATA AVAILABILITY STATEMENT

The raw data supporting the conclusion of this article will be made available by the authors, without undue reservation.

AUTHOR CONTRIBUTIONS

XW and TH conceive this research. XW writes the manuscript and prepares the figures. TH reviews and supervises the manuscript. The co-author L-YF is involved in the discussion of the manuscript. All authors finally approve the manuscript and thus agree to be accountable for this work.

FUNDING

The research is supported by the National Natural Science Foundation of China (41821002, 42174136, and 41874151), the Shandong Provincial Natural Science Foundation, China (ZR2021JQ14), and the Postgraduate Innovation Project of China University of Petroleum (East China) (YCX2021009).

REFERENCES

Bailey, S. W. (1966). The Status of clay mineral Structures. *Clay. Clay Miner.* 14, 1–23. doi:10.1016/B978-0-08-011908-3.50003-7

Barrientos-Velázquez, A. L., MarroquinCardona, A., Liu, L., Phillips, T., and Deng, Y. (2016). Influence of Layer Charge Origin and Layer Charge Density of Smectites on Their Aflatoxin Adsorption. *Appl. Clay Sci.* 132-133, 281–289. doi:10.1016/j.clay.2016.06.014

Carrier, B., Vandamme, M., Pellenq, R. J.-M., and Van Damme, H. (2014). Elastic Properties of Swelling clay Particles at Finite Temperature upon Hydration. *J. Phys. Chem. C* 118, 8933–8943. doi:10.1021/jp412160e

Chen, G., Li, C., Lu, S., Guo, T., Wang, M., Xue, Q., et al. (2021). Critical Factors Controlling Adsorption Capacity of Shale Gas in Wufeng-Longmaxi Formation, Sichuan Basin: Evidences from Both Experiments and Molecular Simulations. *J. Nat. Gas Sci. Eng.* 88, 103774. doi:10.1016/j.jngse.2020.103774

Cui, Z., Sun, Y., Li, J., and Qu, J. (2007). Combination Method for the Calculation of Elastic Constants. *Phys. Rev. B* 75, 214101. doi:10.1103/PhysRevB.75.214101

Cygan, R. T., Liang, J.-J., and Kalinichev, A. G. (2004). Molecular Models of Hydroxide, Oxyhydroxide, and clay Phases and the Development of a General Force Field. *J. Phys. Chem. B* 108, 1255–1266. doi:10.1021/jp0363287

Daab, M., Eichstaedt, N. J., Habel, C., Rosenfeldt, S., Kalo, H., Schießling, H., et al. (2018). Onset of Osmotic Swelling in Highly Charged clay Minerals. *Langmuir* 34, 8215–8222. doi:10.1021/acs.langmuir.8b00492

Davarcioglu, B. (2011). The General Characteristic of Weak Intermolecular Interactions in Liquids and Crystals [Online]. *Int. J. Eng. Sci.* 1, 443–454. Available at: https://citeseerx.ist.psu.edu/viewdoc/download?doi=10.1.1.416.5044&rep=rep1&type=pdf

Dewhurst, D. N., and Siggins, A. F. (2006). Impact of Fabric, Microcracks and Stress Field on Shale Anisotropy. *Geophys. J. Int.* 165, 135–148. doi:10.1111/j.1365-246X.2006.02834.x

Ebrahimi, D., Pellenq, R. J.-M., and Whittle, A. J. (2012). Nanoscale Elastic Properties of Montmorillonite upon Water Adsorption. *Langmuir* 28, 16855–16863. doi:10.1021/la302997g

Few, S., Gambhir, A., Napp, T., Hawkes, A., Mangeon, S., Bernie, D., et al. (2017). The Impact of Shale Gas on the Cost and Feasibility of Meeting Climate Targets-A Global Energy System Model Analysis and an Exploration of Uncertainties. *Energies* 10, 158. doi:10.3390/en10020158

Gao, K., Liu, X., Xiong, J., and Liang, L. (2021). Elastic Parameter Inversion of Longmaxi Formation Shale Based on the Least Squares Method. *Arab. J. Geosci.* 14, 1–10. doi:10.1007/s12517-021-06657-8

Ghasemi, M., and Sharifi, M. (2021). Effects of Layer-Charge Distribution on Swelling Behavior of Mixed-Layer Illite-Montmorillonite Clays: A Molecular Dynamics Simulation Study. *J. Mol. Liquids* 335, 116188. doi:10.1016/j.molliq.2021.116188

Grim, R. E., and Kodama, H. (2014). Clay Mineral [Online]. Available at: https://www.britannica.com/science/clay-mineral.

Han, T., Yu, H., and Fu, L.-Y. (2021). Correlations between the Static and Anisotropic Dynamic Elastic Properties of Lacustrine Shales under Triaxial Stress: Examples from the Ordos Basin, China. *Geophysics* 86, MR191–MR202. doi:10.1190/geo2020-0761.1

Hantal, G., Brochard, L., Laubie, H., Ebrahimi, D., Pellenq, R. J.-M., Ulm, F.-J., et al. (2014). Atomic-scale Modelling of Elastic and Failure Properties of Clays. *Mol. Phys.* 112, 1294–1305. doi:10.1080/00268976.2014.897393

Herling, M. M., Kalo, H., Seibt, S., Schobert, R., and Breu, J. (2012). Tailoring the Pore Sizes of Microporous Pillared Interlayered Clays through Layer Charge Reduction. *Langmuir* 28, 14713–14719. doi:10.1021/la303573e

Huiyuan, B., Wang, F., Chengen, Z., Gao, X., Zhang, Y., Duan, C., et al. (2019). A New Model between Dynamic and Static Elastic Parameters of Shale Based on Experimental Studies. *Arab. J. Geosci.* 12, 1–10. doi:10.1007/s12517-019-4777-2

Karnland, O. (2010). Chemical and Mineralogical Characterization of the Bentonite Buffer for the Acceptance Control Procedure in a KBS-3 Repository [Online]. Available at: https://www.skb.com/publication/2137257/TR-10-60.pdf.

Kirkland, J. (2010). Natural Gas Could Serve as a 'bridge' Fuel to Low-Carbon Future [Online]. Available at: https://www.scientificamerican.com/article/natural-gas-could-serve-as-bridge-fuel-to-low-carbon-future/.

Knowles, K. M., and Howie, P. R. (2014). The Directional Dependence of Elastic Stiffness and Compliance Shear Coefficients and Shear Moduli in Cubic Materials. *J. Elasticity* 120, 87–108. doi:10.1007/s10659-014-9506-1

Koutsopoulou, E., Koutselas, I., Christidis, G. E., Papagiannopoulos, A., and Marantos, I. (2020). Effect of Layer Charge and Charge Distribution on the Formation of Chitosan - Smectite Bionanocomposites. *Appl. Clay Sci.* 190, 105583. doi:10.1016/j.clay.2020.105583

Lavikainen, L. P., Hirvi, J. T., Kasa, S., and Pakkanen, T. A. (2016). Interaction of Octahedral Mg(II) and Tetrahedral Al(III) Substitutions in Aluminium-Rich Dioctahedral Smectites. *Theor. Chem. Acc.* 135, 85. doi:10.1007/s00214-016-1846-4

Lee, J. H., and Guggenheim, S. (1981). Single Crystal X-ray Refinement of Pyrophyllite-1T. *Am. Mineral.* 66, 350–357.

Lee, S. Y., Cho, W. J., Hahn, P. S., Lee, M., Lee, Y. B., and Kim, K. J. (2005). Microstructural Changes of Reference Montmorillonites by Cationic Surfactants. *Appl. Clay Sci.* 30, 174–180. doi:10.1016/j.clay.2005.03.009

Lovelock, K. R. J. (2017). Quantifying Intermolecular Interactions of Ionic Liquids Using Cohesive Energy Densities. *R. Soc. Open Sci.* 4, 171223. doi:10.1098/rsos.171223

Parraguez Kobek, M. L., Ugarte, A., Ugarte, A., and Campero Aguilar, G. (2015). Shale Gas in the united states: Transforming Energy Security in the Twenty-First century. *Norteamérica* 10, 7–38. doi:10.20999/nam.2015.a001

Peng, C., Wang, G., Zhang, C., Qin, L., Zhu, X., and Luo, S. (2021). Molecular Dynamics Simulation of NH4+-smectite Interlayer Hydration: Influence of Layer Charge Density and Location. *J. Mol. Liquids* 336, 116232. doi:10.1016/j.molliq.2021.116232

Plimpton, S. (1995). Fast Parallel Algorithms for Short-Range Molecular Dynamics. *J. Comput. Phys.* 117, 1–19. doi:10.1006/jcph.1995.1039

Pu, B., Wang, F.-q., Dong, D.-z., and Sun, J.-b. (2021). Challenges of Terrestrial Shale Gas Exploration and Development from Chang 7 Shale in the Ordos Basin. *Arab. J. Geosci.* 14, 1–14. doi:10.1007/s12517-021-06914-w

Qin, Y., Peng, T., Sun, H., Zeng, L., Li, Y., and Zhou, C. (2021). Effect of Montmorillonite Layer Charge on the thermal Stability of Bentonite. *Clay. Clay Miner.* 69, 328–338. doi:10.1007/s42860-021-00117-w

Qiu, J., Li, G., Liu, D., Jiang, S., Wang, G., Chen, P., et al. (2019). Effect of Layer Charge Density on Hydration Properties of Montmorillonite: Molecular Dynamics Simulation and Experimental Study. *Ijms* 20, 3997. doi:10.3390/ijms20163997

Rahm, D. (2011). Regulating Hydraulic Fracturing in Shale Gas Plays: The Case of Texas. *Energy Policy* 39, 2974–2981. doi:10.1016/j.enpol.2011.03.009

Raszewski, S. (2016). Shale Gas and Energy Security [Online]. Available at: https://www.academia.edu/34900304/Shale_Gas_and_Energy_Security.

Ray, J. R., and Rahman, A. (1985). Statistical Ensembles and Molecular Dynamics Studies of Anisotropic Solids. II. *J. Chem. Phys.* 82, 4243–4247. doi:10.1063/1.448813

Sayers, C. M., and den Boer, L. D. (2016). The Elastic Anisotropy of clay Minerals. *Geophysics* 81, C193–C203. doi:10.1190/geo2016-0005.1

Shiu, S.-C., and Tsai, J.-L. (2014). Characterizing thermal and Mechanical Properties of Graphene/epoxy Nanocomposites. *Composites B: Eng.* 56, 691–697. doi:10.1016/j.compositesb.2013.09.007

Skipper, N. T., Sposito, G., and Chang, F. R. C. (1995). Monte Carlo Simulation of Interlayer Molecular Structure in Swelling clay Minerals. 2. Monolayer Hydrates. *Clay. Clay Miner.* 43, 294–303. doi:10.1346/CCMN.1995.043030310.1346/ccmn.1995.0430304

Šponer, J., Hobza, P., and Leszczynski, J. (1999). "Computational Approaches to the Studies of the Interactions of Nucleic Acid Bases," in *Computational Molecular Biology*. Editor J. Leszczynski (Amsterdam: Elsevier), 8, 85–117.

Sridharan, A. (2014). Fourth IGS-Ferroco Terzaghi Oration: 2014. *Indian Geotech. J.* 44, 371–399. doi:10.1007/s40098-014-0136-0

Teich-McGoldrick, S. L., Greathouse, J. A., Jové-Colón, C. F., and Cygan, R. T. (2015). Swelling Properties of Montmorillonite and Beidellite clay Minerals from Molecular Simulation: Comparison of Temperature, Interlayer Cation, and Charge Location Effects. *J. Phys. Chem. C* 119, 20880–20891. doi:10.1021/acs.jpcc.5b03253

Vanorio, T., Prasad, M., and Nur, A. (2003). Elastic Properties of Dry clay mineral Aggregates, Suspensions and Sandstones. *Geophys. J. Int.* 155, 319–326. doi:10.1046/j.1365-246X.2003.02046.x

Wang, Y., Liao, B., Kong, Z., Sun, Z., Qiu, L., and Wang, D. (2018). Oscillating Electric Field Effects on Adsorption of the Methane-Water System on Kaolinite Surface. *Energy Fuels* 32, 11440–11451. doi:10.1021/acs.energyfuels.8b02961

Weaver, C. E., and Pollard, L. D. (2011). *The Chemistry of clay Minerals*. Amsterdam: Elsevier.

Yang, Y., and Xu, G. (20212011). Molecular Dynamics Simulation of the Mechanical Behavior of Mixed-Layer clay upon Hydration. *J. Phys. Conf. Ser.* 2011, 012053. doi:10.1088/1742-6596/2011/1/012053

Zartman, G. D., Liu, H., Akdim, B., Pachter, R., and Heinz, H. (2010). Nanoscale Tensile, Shear, and Failure Properties of Layered Silicates as a Function of Cation Density and Stress. *J. Phys. Chem. C* 114, 1763–1772. doi:10.1021/jp907012w

Zhang, J., Pervukhina, M., and Clennell, M. B. (2018). Nanoscale Elastic Properties of Dry and Wet Smectite. *Clay. Clay Miner.* 66, 209–219. doi:10.1346/CCMN.2018.064094

Zhao, J., Cao, Y., Wang, L., Zhang, H.-J., and He, M.-C. (2021). Investigation on Atomic Structure and Mechanical Property of Na- and Mg-Montmorillonite under High Pressure by First-Principles Calculations. *Minerals* 11, 613. doi:10.3390/min11060613

Zhong, L., Hu, S., Yang, X., Yang, M., Zhang, T., Chen, L., et al. (2021). Difference in the Preparation of Two-Dimensional Nanosheets of Montmorillonite from Different Regions: Role of the Layer Charge Density. *Colloids Surf. A: Physicochemical Eng. Aspects* 617, 126364. doi:10.1016/j.colsurfa.2021.126364

Conflict of Interest: The authors declare that the research was conducted in the absence of any commercial or financial relationships that could be construed as a potential conflict of interest.

Publisher's Note: All claims expressed in this article are solely those of the authors and do not necessarily represent those of their affiliated organizations, or those of the publisher, the editors and the reviewers. Any product that may be evaluated in this article, or claim that may be made by its manufacturer, is not guaranteed or endorsed by the publisher.

frontiers in Earth Science

BRIEF RESEARCH REPORT
published: 18 February 2022
doi: 10.3389/feart.2022.851813

Pressure Calibration of Large-Volume Press: A Case Study of Hinged 6-8 Type Large-Volume High-Pressure Apparatus

Dongsheng Ren[1] *and Heping Li*[2]*

[1]Institute of Geology, China Earthquake Administration, Beijing, China, [2]Institute of Geochemistry, Chinese Academy of Sciences, Guiyang, China

In this study, methods for the pressure calibration of 6–8 static high-pressure apparatus were investigated. The relationship between the pressure of DS 6 × 1,400 t pressing oil and the chamber pressure was calibrated using water, ZnTe, ZnS, and GaAs at room temperature. Also, the relationship between the pressure of the DS 6 × 1,400 t pressing oil and the chamber pressure was calibrated by the phase transition experiments using KCl, LiCl, KCl + LiCl, and quartz-coesite at high temperatures. We found a linear relationship between the chamber pressure and the oil pressure at room temperature. However, when the temperature and pressure increased to certain values, the chamber pressure and the oil pressure deviated from the linear relationship.

Keywords: pressure calibration, 6–8 large-volume high-pressure apparatus, high temperature and high pressure, phase transition, fusion

OPEN ACCESS

Edited by:
Lidong Dai,
Institute of Geochemistry (CAS), China

Reviewed by:
Shuo Xue,
Guangzhou Institute of Geochemistry (CAS), China
Zhankun Liu,
Central South University, China

***Correspondence:**
Heping Li
liheping@vip.gyig.ac.cn

Specialty section:
This article was submitted to Solid Earth Geophysics, a section of the journal Frontiers in Earth Science

Received: *10 January 2022*
Accepted: *17 January 2022*
Published: *18 February 2022*

Citation:
Ren D and Li H (2022) Pressure Calibration of Large-Volume Press: A Case Study of Hinged 6-8 Type Large-Volume High-Pressure Apparatus. Front. Earth Sci. 10:851813. doi: 10.3389/feart.2022.851813

INTRODUCTION

High-pressure geoscience is the study area on the physicochemical properties of matters at high pressure including the mechanical, thermal, optical, electrical, and magnetic properties of matters as well as the microstructure, equation of state, and phase transition of matters. It also provides theoretical and experimental bases for the discovery of new phenomena, new laws, and the synthesis of new materials at high pressure. The production of static high temperature and high pressure depends on various high-pressure apparatus such as anvil devices including the piston cylinder and diamond anvil cell. Multi-anvil instruments are comprised of the quaternary-plane anvil and senary-plane anvil assemblies. Nevertheless, among various large-volume, multi-anvil static high-pressure assemblies, due to the wide range of temperatures and pressures that can be obtained and the ease of the combination with various *in-situ* measurement techniques, 6–8 high-pressure assemblies are becoming increasingly important in the fields of Earth and planetary physics, mineralogy, and petrology. The pressure and temperature of 6–8 large-volume high-pressure assemblies can reach up to several tens GPa and 2,500°C, respectively. However, they use solid as a pressure-transfer medium whose internal friction is large. As a result, the pressure calibration of their chamber is required (Baumann, et al., 2015; Klier, et al., 2015; Richter, et al., 2016).

Currently, methods for large-volume pressure calibration can be divided into pressure calibrations at room temperature and high temperatures. The main methods of the pressure calibration at room temperature are the phase transition, the X-ray cell parameter measurement, and the fluorescence manometry. The principle of the phase transition method is to establish the relationship between the chamber pressure and the load by determining the resistance mutation or

the metallization pressure transition point of known metals or semiconductors such as Bi, Tl, Cs, Ba, Sn, ZnSe, ZnS, and GaAs. The X-ray cell parameter measurements are used to determine the variation of cell parameters of matters with a known equation of state at high pressure to calibrate the cavity pressure. The fluorescence manometry uses the fluorescence spectral lines of R_1 = 694.2 nm and R_2 = 692.9 nm of ruby at room temperature and ambient pressure. As the pressure increases, the spectral lines move in the direction of longer wavelengths. The linear relationship between the R1 spectral wavelength and the pressure is $dp/d\lambda = 2.740 \pm 0.016$ GPa/nm for the chamber pressure calibration (Hülsmans, et al., 2015; Morales, et al., 2015; Wang, et al., 2015; Klemm, et al., 2020; Kosari, et al., 2020).

Pressure measurement at high temperatures is more complex than that at room temperature. The physical properties and the state changes of matters are not only controlled by the pressure but also affected by the temperature. So it is necessary to obtain the relationship between the temperature and the pressure when the phase transition, fusion, or decomposition reaction of the calibrated matter occurs. This relationship can be used as the basis for the pressure calibration. In the measurement process, the temperature at which the material or physical state of the calibrated matter changes is measured at several pressures of the force load. The corresponding chamber pressure is calculated by the relational equation to obtain the relationship between the force load pressure and the chamber pressure. Thermocouples are generally used for temperature measurement in large-volume press. In the case of happening of phase transition, fusion, or other reactions in the matter, the thermoelectric potential changes abruptly. So thermocouples can be used to determine the temperature at which the phase transition, fusion, or decomposition occurs, and the products can be analyzed to verify that this reaction has occurred. Commonly used pressure calibration methods at high temperatures include the phase transition method and the high-pressure fusion curve method (Kawazoe, et al., 2008; Farla, et al., 2015; Farla, et al., 2017). When the phase transition of the matter occurs, the relationship between the temperature and the pressure is called the phase transition equation. The phase transition reactions used for the pressure calibration at high temperatures include quartz-coesite, coesite-stishovite, α fayalite -γ fayalite, α forsterite-β forsterite, β forsterite-γ forsterite, and zinc pyroxene-zinc pyroxene in the Perovskite structure (Lebron, et al., 2009; Wang et al., 2010; Chen, et al., 2016; Wang, et al., 2019). The relationship between the temperature and the pressure when a metal, alloy, or chlorinated salt is fused at high pressure is called the fusion equation. The fused materials used for the pressure calibration at high temperatures include Au, Ag, Cu, KCl, and NaCl (Wong and Xiong, 2018).

In this study, the pressure calibration methods commonly used in existing large-volume multi-anvil static high-pressure assemblies were employed to conduct systematic pressure calibration experiments for the hinged 6 × 1,400 t 6-8 high-pressure assembly using various methods. The relationship between the chamber pressure and the oil pressure of this large-volume assembly was established for a specific sample size at different temperatures (Room-T~1,500°C).

EXPERIMENTAL

Instrument

The DS 6 × 1,400 t large-volume assembly was comprised of the pressing body, the oil tank system, and the control system. The pressing body extruded the sample assembly through the pressing anvil. The oil tank system provided the force source to push the pressing anvil. The control system set the temperature and pressure program for the experiment. The six hydraulic cylinders were interconnected by a hinge and all pistons were controlled by the same oil pump. The first-stage anvil was made of tungsten carbide with a Co content of 8 wt% and the edge length was 43.5 mm. The multimeter model used to measure the variation of the resistance of the sample was Agilen-34401A.

Method

The pressure calibration of the first-stage anvil at room temperature was conducted based on the water-ice phase transition where water was sealed in a copper tube as the starting material. The pressure calibration of the first-stage anvil at high temperatures was conducted using KCl, LiCl, and KCl + LiCl (molar mass ratio = 1: 1). The high-purity starting material was purchased from Aladdin, and the starting material with a particle size of 200 μm was pressed into a cylinder with a diameter of 4 mm and a height of 8 mm by a powder press. The second-stage anvil was made of the WC alloy with a single cubic side length of 25.4 mm and a truncated triangular side length of 5 mm. The octahedral pressure transfer medium was made of MgO +5% Cr_2O_3 with a side length of 10 mm. The pressure calibration of the second-stage anvil at room temperature was performed by using ZnTe with the I-II conversion pressure of 5 GPa, the II-III conversion pressure of 8.9–9.5 GPa, the ZnTe semiconductor/metal conversion pressure of 11.5–13 GPa, the ZnS semiconductor/metal conversion pressure of 15.6 GPa, and the GaAs semiconductor/metal conversion pressure of 18.8 GPa for the chamber pressure.

The phase transition material used for the pressure calibration at high temperatures was a quartz-coesite with a quartz particle size of 150 um. This was pressed into a sample with a diameter of 2 mm and a height of 2 mm by a press. The samples were assembled as shown in **Figure 1**.

The pressure calibration method for the first-stage and second-stage anvils at room temperature was to increase the oil pressure of the large-volume assembly at a rate of 10 *MPa/h* while observing the resistance change of the sample *in-situ* to find the sudden change point in the resistance as the phase transition point. Then the relationship between the oil pressure and the cavity pressure at the phase transition point was established. **Figures 2A,B** show the resistance change of water in the first-stage anvil and the resistance change of ZnS in the second-stage anvil. The calibration method for the pressure in the first-stage anvil was as follows. Firstly, the oil pressure of the large-volume assembly was raised to a designated pressure at a rate of 10 MPa/h. Then the resistance change of the sample was observed *in situ* when the cavity

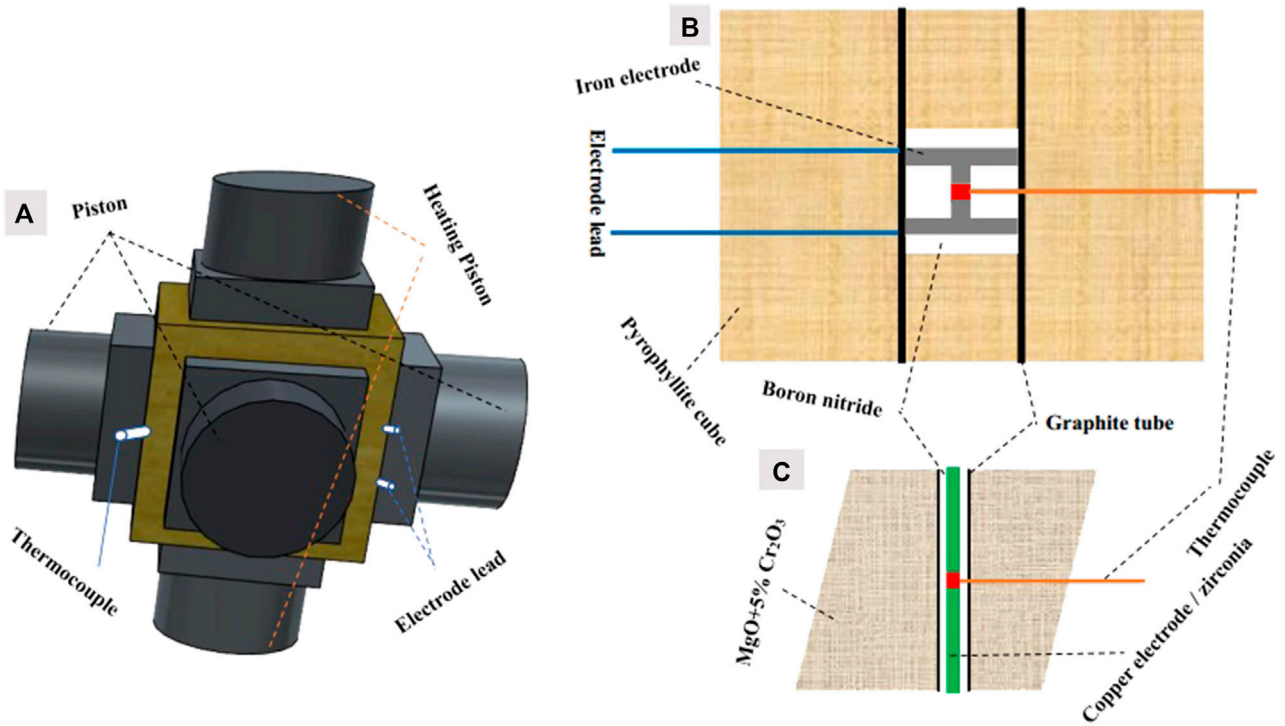

FIGURE 1 | Sample assembly drawing; **(A)** drawing of the large-volume pressing assembly, **(B)** drawing of the first-stage anvil pressure calibration assembly, and **(C)** drawing of the second-stage anvil pressure calibration assembly.

temperature was raised at a rate of 10 °*C*/*min* at the designated pressure. The sudden change point in the resistance of the sample was considered as its melting point at this pressure, and the corresponding pressure at this melting point can be found according to the phase diagram. Finally, the relationship between the assembly pressure and the oil pressure in the first-stage anvil at a high temperature was established.

For instance, the KCl fusion at an oil pressure of 10 MPa in the first-stage anvil is shown in **Figure 2C**. The pressure calibration for the second-stage anvil at high temperatures was achieved using the phase transition of the quartz-coesite. At 1,000°C, the coesite was found in the product when the oil pressure reached 3 MPa. At 1,500°C, the coesite was found in the product when the oil pressure reached 5 MPa. The Raman spectra of the product after the quartz phase transition are shown in **Figures 2D,E**, and that of the starting material is shown in **Figure 2F**.

RESULTS AND DISCUSSION

Figures 3, **4** illustrate the experimental results of the pressure calibration for the first-stage and second-stage anvils at different temperatures. The experimental error was small and the goodness of fit of the fitted curves was larger than 0.95. As shown in these figures, the chamber pressure and the oil pressure showed an ideal linear relationship at room temperature for both first-stage and second-stage anvils. In the pressure calibration at high temperatures, when the oil pressure and temperature were higher than certain values, the chamber pressure deviated from the linear relationship with the oil pressure. The higher the temperature was, the greater the deviation from the linear relationship was. The main reasons were as follows. Firstly, with an increase in the temperature, the inner pressure transfer medium was sintered and hardened so that its pressure transfer performance decreased. Secondly, with an increase in the oil pressure and temperature, the mobility of the outer pressure transfer medium was enhanced. This resulted in a large amount of extrusion of the outer pressure transfer medium which lost the anvil surface pressure in the process of transferring to the sample chamber. In addition, the temperature and pressure were too high and the WC anvil approached the yield strength.

CONCLUSIONS AND LIMITATIONS

In this study, the pressure calibration methods for a 6–8 type large-volume pressing assembly at room temperature and high temperatures were investigated. The relationship between the pressure of the pressing oil and the chamber pressure of the DS 6 × 1,400 t assembly was calibrated by conducting the phase transition experiments using water, ZnTe, ZnS, and GaAs at room temperature and using KCl, LiCl, KCl + LiCl, and quartz-coesite at high temperatures. These pressure calibration results provided the basis for future experiments and the feasibility of these calibration methods has been verified through these

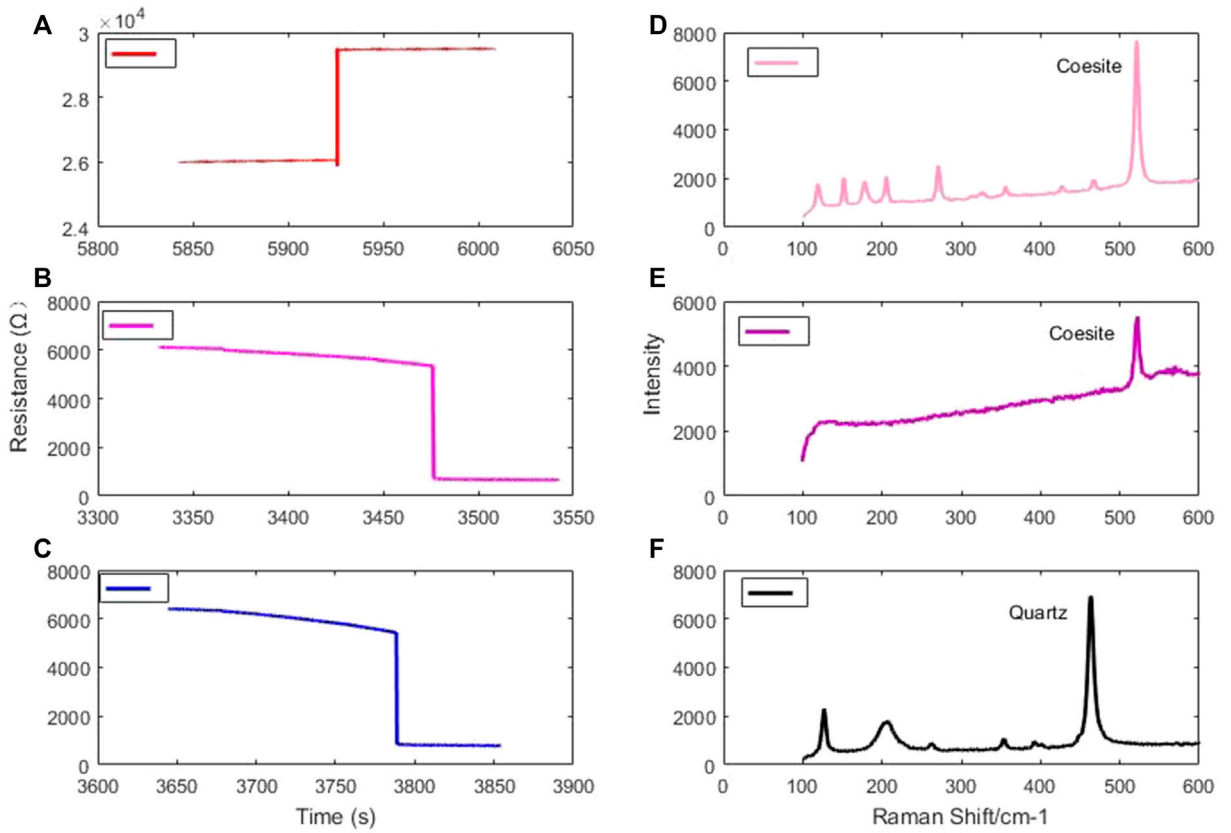

FIGURE 2 | (A) Time trend of water resistance, **(B)** Time trend of ZnS resistance, **(C)** Time trend of KCl resistance at an oil pressure of 10 MPa, **(D)** Raman spectrum of the experimental product of the phase transition of quartz at 1,000°C, **(E)** Raman spectrum of the experimental product of the phase transition of quartz at 1,500°C, and **(F)** Raman spectrum of quartz before the phase transition.

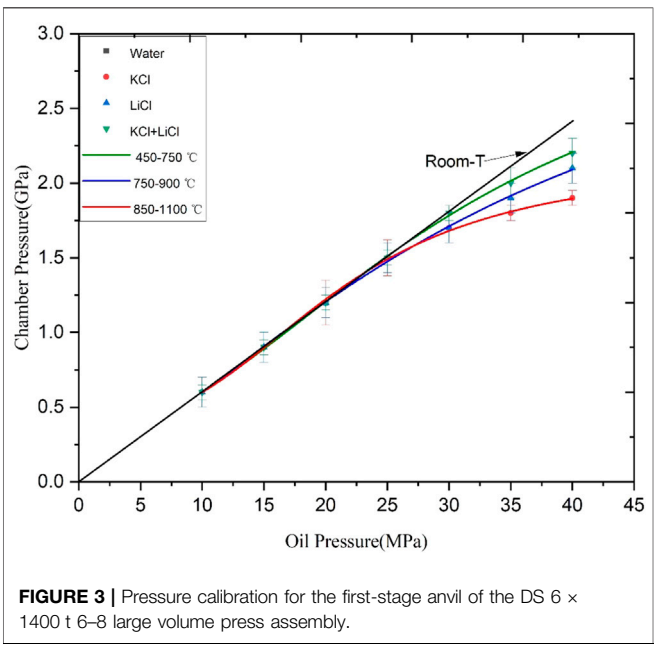

FIGURE 3 | Pressure calibration for the first-stage anvil of the DS 6 × 1400 t 6–8 large volume press assembly.

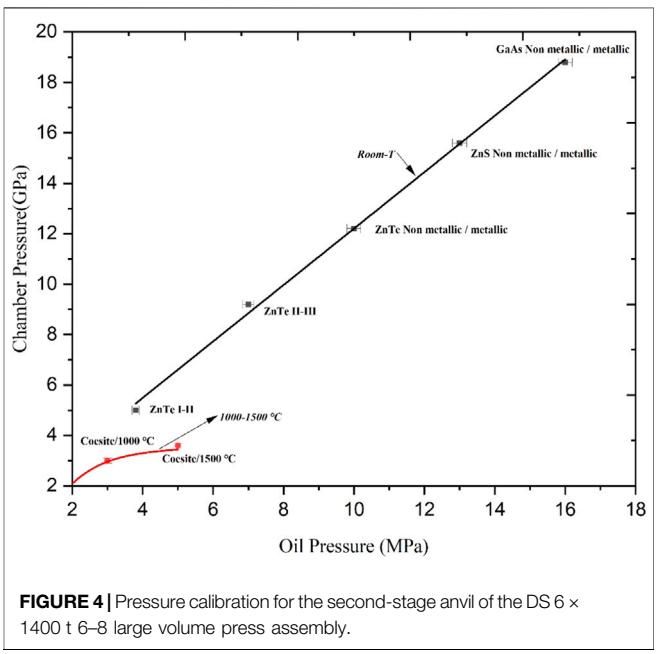

FIGURE 4 | Pressure calibration for the second-stage anvil of the DS 6 × 1400 t 6–8 large volume press assembly.

experiments. However, no other methods such as the coesite-stishovite phase transition method have been applied to obtain more extensive and reliable pressure calibration results for the second-stage anvil at high temperatures (Wang et al., 2015).

DATA AVAILABILITY STATEMENT

The original contributions presented in the study are included in the article/Supplementary Material, further inquiries can be directed to the corresponding author.

AUTHOR CONTRIBUTIONS

All authors listed have made a substantial, direct, and intellectual contribution to the work and approved it for publication.

FUNDING

This project is supported by the National Natural Science Foundation of China with Grant No. 42104176.

REFERENCES

Baumann, D., Niklaus, R., and Schnick, W. (2015). Cheminform Abstract: A High-pressure Polymorph of Phosphorus Oxonitride with the Coesite Structure. *Cheminform* 46 (24), 369–382. doi:10.1002/chin.201524002

Chen, S., Guo, X., Zhou, C., and Jin, Z. (2016). Negative Pressure Effect on the Electrical Conductivity of San Carlos Olivine and its Implication to the Electrical Structure in the Upper Mantle. *Sci. China Earth Sci.* 59 (10), 2078–2088. doi:10.1007/s11430-015-0216-y

Farla, R., Amulele, G., Girard, J., Miyajima, N., and Karato, S.-i. (2017). Erratum to: High-Pressure and High-Temperature Deformation Experiments on Polycrystalline Wadsleyite Using the Rotational Drickamer Apparatus. *Phys. Chem. Minerals* 44, 541–558. doi:10.1007/s00269-017-0872-7

Farla, R., Amulele, G., Girard, J., Miyajima, N., and Karato, S.-i. (2015). High-pressure and High-Temperature Deformation Experiments on Polycrystalline Wadsleyite Using the Rotational Drickamer Apparatus. *Phys. Chem. Minerals* 42, 576–581. doi:10.1007/s00269-015-0742-0

Hülsmans, A., Schmücker, M., Mader, W., and Schneider, H. (2015). The Transformation of Andalusite to Mullite and Silica: Part I. Transformation Mechanism in [001] Direction. *Am. Mineral.* 85 (7), 980–986. doi:10.2138/am-2000-0712

Kawazoe, T., Karato, S., Otsuka, K., Jing, Z., and Mookherjee, M. (2008). Shear Deformation of Dry Polycrystalline Olivine under Deep Upper Mantle Conditions Using a Rotational Drickamer Apparatus (RDA). *Phys. Earth Planet. Interiors* 174 (1-4), 128–137. doi:10.1016/j.pepi.2008.06.027

Klemm, D. H. W., Prieto, D. M. J., Xiong, F., Hassine, G. B., Heyde, M., Menzel, D., et al. (2020). A Silica Bilayer Supported on Ru(0001): Following the Crystalline-to Vitreous Transformation in Real Time with Spectro-microscopy. *Angew. Chem.* 132, 10674–10680. doi:10.1002/ange.202002514

Klier, K., Spirko, J. A., and Landskron, K. M. (2015). Optical Absorption Anisotropy of High-Density, wide-gap, High-Hardness SiO2 Polymorphs Seifertite, Stishovite, and Coesite. *Am. Mineral.* 100 (1), 120–129. doi:10.2138/am-2015-4890

Kosari, M., Borgna, A., and Zeng, H. C. (2020). Transformation of Stöber Silica Spheres to Hollow Nanocatalysts. *Chemnanomat* 6 (6), 889–906. doi:10.1002/cnma.202000147

Lebron, I., Herrero, J., and Robinson, D. (2009). Determination of Gypsum Content in Dryland Soils Exploiting the Gypsum–bassanite Phase Change. *Soil Sci. Soc. America J.* 73 (2), 136–139. doi:10.2136/sssaj2008.0001

Morales, J. M., Moragues, A., El Haskouri, J., Guillem, C., Latorre, J., Murcia-Mascarós, S., et al. (2015). Low-Cost Synthesis of Bimodal Mesoporous Silica-Based Materials by Pseudomorphic Transformation. *Chempluschem* 80 (6), 1014–1028. doi:10.1002/cplu.201402383

Richter, B., Stünitz, H., and Heilbronner, R. (2016). Stresses and Pressures at the Quartz-to-coesite Phase Transformation in Shear Deformation Experiments. *J. Geophys. Res. Solid Earth* 121 (11), 8015–8033. doi:10.1002/2016jb013084

Wang, Z, Zhao, Y., and Kohlstedt, D. L. (2010). Dislocation Creep Accommodated by Grain Boundary Sliding in Dunite. *J. Earth Sci.* 21 (5), 541–554. doi:10.1007/s12583-010-0113-1

Wang, J., Rajendran, A. M., and Dongare, A. M. (2015). Atomic Scale Modeling of Shock Response of Fused Silica and α-quartz. *Mineralogical Soc. America* 50 (24), 212–227. doi:10.1007/s10853-015-9386-1

Wang, Z., Jin, Z., Mungall, J. E., and Xiao, X. (2019). Transport of Coexisting Ni-Cu Sulfide Liquid and Silicate Melt in Partially Molten Peridotite. *Earth Planet. Sci. Lett.* 536, 112–118. doi:10.1016/j.epsl.2020.116162

Wong, L. N. Y., and Xiong, Q. (2018). A Method for Multiscale Interpretation of Fracture Processes in Carrara Marble Specimen Containing a Single Flaw under Uniaxial Compression. *J. Geophys. Res. Solid Earth* 123 (8), 58–62. doi:10.1029/2018jb015447

Conflict of Interest: The authors declare that the research was conducted in the absence of any commercial or financial relationships that could be construed as a potential conflict of interest.

Publisher's Note: All claims expressed in this article are solely those of the authors and do not necessarily represent those of their affiliated organizations, or those of the publisher, the editors and the reviewers. Any product that may be evaluated in this article, or claim that may be made by its manufacturer, is not guaranteed or endorsed by the publisher.

frontiers in Earth Science

ORIGINAL RESEARCH
published: 07 March 2022
doi: 10.3389/feart.2022.851236

Effect of Terrigenous Sediment Addition on the Generation of Arc Silicic Magma: Constraints From the Comparative Partial Melting Experiment at 1.5 GPa

Chunjuan Zang[1,2,3] *and Mingliang Wang*[1,2,3]*

[1]School of Resource and Civil Engineering, Suzhou University, Suzhou, China, [2]National Engineering Research Centre of Coal Mine Water Hazard Controlling, Suzhou, China, [3]Key Laboratory of Mine Water Resource Utilization of Anhui Higher Education Institutes, Suzhou University, Suzhou, China

To assess the effects of sediment addition on the partial melting of subducted oceanic crust and generation of arc silicic magma, a series of comparative partial melting experiments on a garnet plagioamphibolite and a 90 wt% garnet plagioamphibolite + 10 wt% plagioclase slate mixture at 850–1,000°C/1.5 GPa were conducted on a Piston-cylinder apparatus. In the experimental products, partial melt coexists with amphibole + plagioclase + garnet + clinopyroxene at 850–950°C and plagioclase + garnet + clinopyroxene at 1000°C. Compared with pure garnet plagioamphibolite, partial melting of mixture get a higher melting percentage and generates the silicic melt with geochemical characteristics of higher Na_2O/K_2O and lower Al_2O_3 in major element and high Rb content in trace element at over 950°C. This result indicates that silicic arc magma may generate from partial melting of metamorphic subducted oceanic crust with sediments thereon, sediment addition contributes to their chemical component and generation dynamic process.

Keywords: arc silicic magma, partial melting, subducted oceanic crust, sediment, experimental petrology

OPEN ACCESS

Edited by:
Lidong Dai,
Institute of geochemistry (CAS), China

Reviewed by:
Sheqiang Miao,
China Earthquake Administration, China
Dawei Fan,
Institute of Geochemistry (CAS), China

***Correspondence:**
Mingliang Wang
wangapple1999@126.com

Specialty section:
This article was submitted to Petrology, a section of the journal Frontiers in Earth Science

Received: *09 January 2022*
Accepted: *26 January 2022*
Published: *07 March 2022*

Citation:
Zang C and Wang M (2022) Effect of Terrigenous Sediment Addition on the Generation of Arc Silicic Magma: Constraints From the Comparative Partial Melting Experiment at 1.5 GPa. Front. Earth Sci. 10:851236. doi: 10.3389/feart.2022.851236

INTRODUCTION

According to plate tectonics, convergent plate margins are the most active areas on earth. The oceanic plate is dehydrated during subduction at these margins. During this subduction, the oceanic plate releases fluids, and these fluids join the overlying mantle wedge, causing partial melting of the mantle wedge and generating island arc basaltic magma (Sun et al., 2014; Zheng et al., 2015; Li and Ni, 2020; Liu et al., 2019; Zheng et al., 2019; Wei and Zheng, 2020; Xiong et al., 2020). Besides the basalt, there are a number of silicic magmas located on convergent plate margins (even typical oceanic island arcs, such as Tonga and the Kuril Islands), as shown in **Figure 1**. These magmas cannot be formed by partial melting of the peridotite mantle wedge, even ~52 wt% SiO_2 melt could be generated by a very low degree (~2 wt%) partial melt of peridotite in the upper mantle wedge (Baker et al., 1995), but such a low percentage partial melting cannot generate real magma due to magmatic dynamic characteristics. While the melting percentage increases, the SiO_2 content of melts from partial melting of peridotite will decrease rapidly, so partial melting of the mantle cannot generate silicic magma generally.

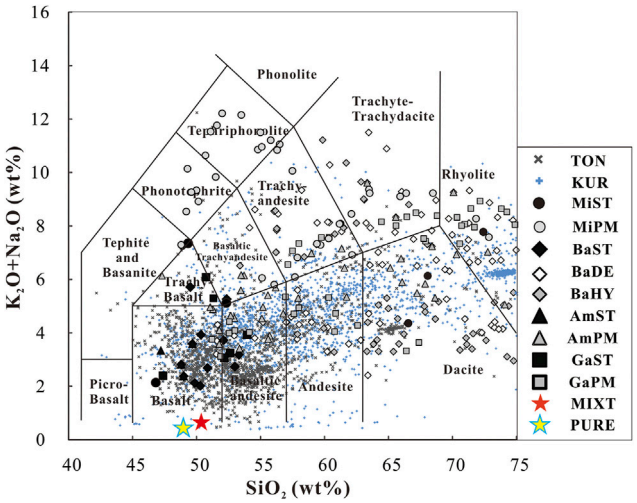

FIGURE 1 | Total alkali versus silica (TAS) variation diagram of basic rocks and their product-melts in partial melting experiments. This figure is modified from **Figure 2** in Zang et al. (2020), Classification and nomenclature of TAS diagram follow Maitre (1989). BaST, starting material of basalts; BaDE, melts generate in basalts' partial melting experiments; BaHY, melts generate in partial melting of hydrous basalt (Beard and Lofgren 1991; Qian and Hermann 2013; Rapp and Watson 1995; Rapp, et al., 1991; Rushmer 1991; Sisson, et al., 2005; Takahahshi, et al., 1998; Xiong, et al., 2005, 2006; Yaxley and Green 1998). AmST, starting material of amphibolites; AmPM, melts generated in partial melting experiments on amphibolites (Sen and Dunn 1994; Rapp and Watson 1995). GaST, starting material of gabbros; GaPM, melts generate in partial melting experiments on gabbros (Koepke, et al., 2004; Sisson,et al., 2005). MiST, starting material of mixtures (basalt + sediment or mélange); MiPM, melts from partial melting experiments on these mixtures (Cruz-Uribe et al., 2018; Zang et al., 2020). PURE, pure starting material used in this paper, 18TH-02 (garnet plagioamphibolite, as a representative of metamorphic oceanic crust), MIXT, mixture starting material used in this paper, 90wt% 18TH-02 + 10wt% 18 TH-07 (plagioclase slate, as a representative of metamorphic terrigenous sediment), TON, magmatic rocks located at Tonga island arc; KUR, magmatic rocks located at the Kuril Islands, data on TON and KUR are from the GEOROC web site (http://georoc.mpch-mainz.gwdg.de/georoc/).

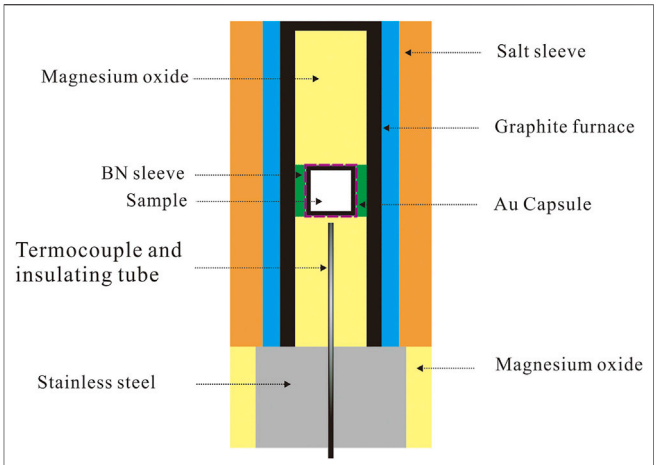

FIGURE 2 | Sketch map of sample assemblage.

The magmas on oceanic islands that arc without a continental crust (such as Tonga) are not generated by hybridized basaltic magma by crust or the partial melting of continental lower crust *via* the heating process. These silicic magmas could then generate from: 1) fractionation of basaltic or andesitic parents magma (Nandedkar et al., 2014; Peter et al., 2018); 2) partial melting of subducted sediments (Tatsumi, 2001); 3) partial melting of subducted basaltic oceanic crust with or without sediments. For the 1) fractionation model, the sticky silicic magmas need to separate from amphibole (Amp) ± clinopyroxene (Cpx) ± orthopyroxene (Opx) utterly, avoiding the reduction of their whole rock SiO_2 content. This dynamic process makes the fractionation model unacceptable. For the 2) partial melting of sediments individually, there are also some insoluble problems. These oceanic sediments could partially melt individually (Tatsumi, 2001; Hermann and Spandler, 2008; Hu et al., 2017; Frster and Selway, 2021), but the characteristic of major-trace element and isotope for the overwhelming majority of arc magma needs oceanic crust in their magmatic source (Hildreth and Moorbath, 1988; Elliott, 2003; Cruz-Uribe et al., 2018; Wang et al., 2021). This indicates that the silicic magmas could only generate *via* partial melting of subducted basaltic oceanic crust with or without sediments. For the same reasons as those oputlined in hypothesis 2), these silicic magmas need sediments in their magmatic source, and the sediments in arc could detect the magmatic source *via* characteristics of trace elements and isotopes (Tera et al., 1986; Hildreth and Moorbath, 1988; Morris et al., 1990; Plank, 2005; Hu et al., 2017; Nielsen and Marschall, 2017; Shu et al., 2017; Cruz-Uribe et al., 2018; Zang et al., 2020). How these sediments effect magma generation during mixture cases is a key question that it is difficult to answer *via* field observation. The studies mentioned above (Tera et al., 1986; Morris et al., 1990; Hu et al., 2017; Nielsen and Marschall, 2017; Shu et al., 2017) could not only reveal the existence of sediments at magmatic source, but not their affect. The only way to solve this problem is by conducting high temperature and high pressure partial melting experiments, comparing the difference in partial melting behavior between pure basic rocks and basalt-sediments mixture.

A number of previous studies have focussed on the partial melting of basic rocks (Beard and Lofgren, 1991; Rapp et al., 1991; Rushmer, 1991; Sen and Dunn, 1994; Rapp and Watson, 1995; Takahahshi et al., 1998; Yaxley and Green, 1998; Koepke et al., 2004; Sisson et al., 2005; Xiong et al., 2005; Xiong et al., 2006; Qian and Hermann, 2013). These findings have revealed the partial melting behavior of pure basaltic oceanic crust during the subduction process; however, studies focussing on the partial melting of basic rock and sediment are very limited (Mccarthy and Patiño Douce, 1997; Zang et al., 2020). The studies that have been conducted show that even a small amount of sediment addition in basalt could effect the partial melting behavior, which is noteworthy. The effects include: 1) that sediment addition enhanced the partial melting ratio of basalt, as confirmed by similar studies (Zhang et al., 2019; Zhang Y. et al., 2020; Pelleter et al., 2021); 2) sediment addition changed the chemical component of the partial melts generated in these experiments, compared with the one from pure basalt.

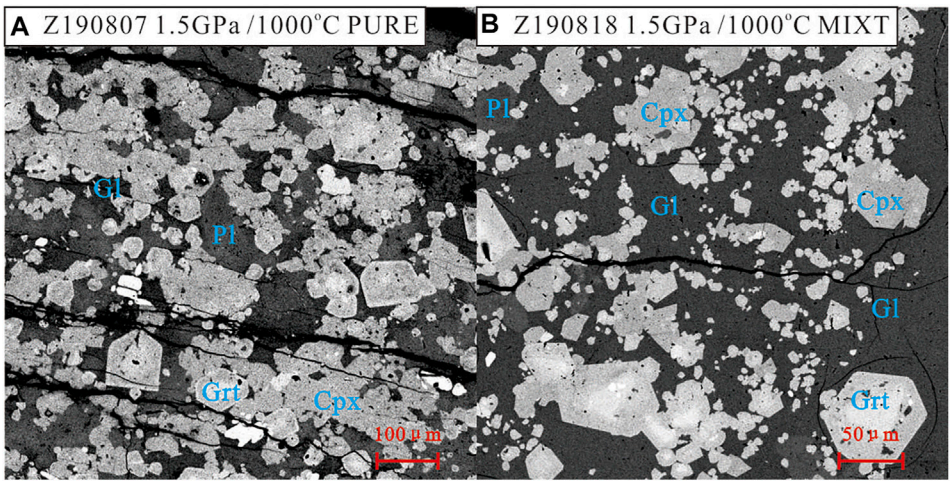

FIGURE 3 | Representative BSE photos of experiment products. Phase abbreviation: Gl = glass (melt), Cpx = clinopyxene, Grt = garnet, Pl = plagioclase.

According to existing research, we could get an outline of the effect caused by the addition of sediments during the partial melting of subducted basaltic oceanic crust; however, there are some important questions remaining, including: 1) that sediment addition could enhance the partial melting ratio, but in what conditions? How much is the increase of ratio; 2) what is the composition difference between melts from pure basalt and mixture of basalt-sediment? These two questions are very important for understanding the effect of sediment addition in basalt and the generation of silicic magmas located on convergent plate margins. In order to understand the effect of the partial melting of the subducted basaltic oceanic crust, caused by the addition of a small amount terrigenous sediment, a series of comparative partial melting experiments were conducted on a garnet plagioamphibolite and a 90 wt% garnet plagioamphibolite + 10 wt% plagioclase slate at 850–1,000°C/1.5 GPa in this study. In the following sections, we will describe the starting materials and analytical methods, firstly, and then comparing partial melts from pure and mixture. At last, we will highlight a natural example of rocks from Tonga and Kuril, which verifies the strong effects of the addition of a small amount of sediment during the partial melting of subducted oceanic basalt at convergent plate margins.

EXPERIMENTAL AND ANALYTICAL METHODS

Starting Materials

During the subduction process, the basaltic oceanic crust may become garnet plagioamphibolite while the terrigenous sediments (mud) may transform into slate at 1.5–2.0 GPa. As the oceanic crust could then partially melt at high geothermal gradient (at approximately 1.5–2.0 GPa and ~900°C), we chose 1.5 GPa and 850–1,000°C as run conditions in this study (Zheng et al., 2015; Wei and Zheng, 2020; Zhang Z. et al., 2020).

Two metamorphic rocks were chosen to prepare the starting materials. The 18TH-02 is a garnet plagioamphibolite and contains 50 vol% Amp, 35 vol% plagioclase (Pl), 12 vol% garnet (Grt), and trace amounts of V-Ti magnetite. Its major element composition is very similar to the average composition of oceanic crust, and several important trace elements (such as V, Cr, Rb, and Sr) of 18TH-02 are also close to the average composition of oceanic crust. The terrigenous sediment is represented by a plagioclase slate (18TH-07), this sample contains 85 vol% feldspar (orthoclase + albite + plagioclase), 10 vol% mica, and trace amounts of quartz. Their major element composition and selected trace elements are very close to the Upper Continental Crust (UCC) (the data of these two metamorphic rocks is listed in **Supplementary Table S1**).

Both of these rocks were collected from Susong, Anhui Province, China. The two rocks (18TH-02 and 18TH-07) were ultrasonically cleaned in distilled water and alcohol successively, and then crushed to powder to ~120 meshes separately. In order to simulate the partial melting process of the oceanic crust with or without terrigenous sediments thereon during subduction process, two starting materials were used: PURE and MIXT. The PURE is representative of pure basaltic oceanic crust, which was made by 18TH-02 power only. The MIXT is representative of basaltic oceanic crust with terrigenous sediment, which was made by mixture 90 wt% 18TH-02 power and 10 wt% 18TH-07 power. The proportion was determine by typical geochemical studies (Gan et al., 2010; Niu, 2013), for more detail refer to Zang et al. (2020). Then these two materials were placed in an agate mortar and ground for >3 h separately, ensuring the particle size of their power was inner 10 μm. Before being used, these prepared powers were stored in a 110°C drying oven for more than 48 h to remove adsorbed water.

Experimental Procedure

The sample assemblage consisted of NaCl sleeve, Pyrex Glass, graphite furnace (with a cap), magnesium oxide (after 1,000°C heating), and the sample capsules. The power of the starting

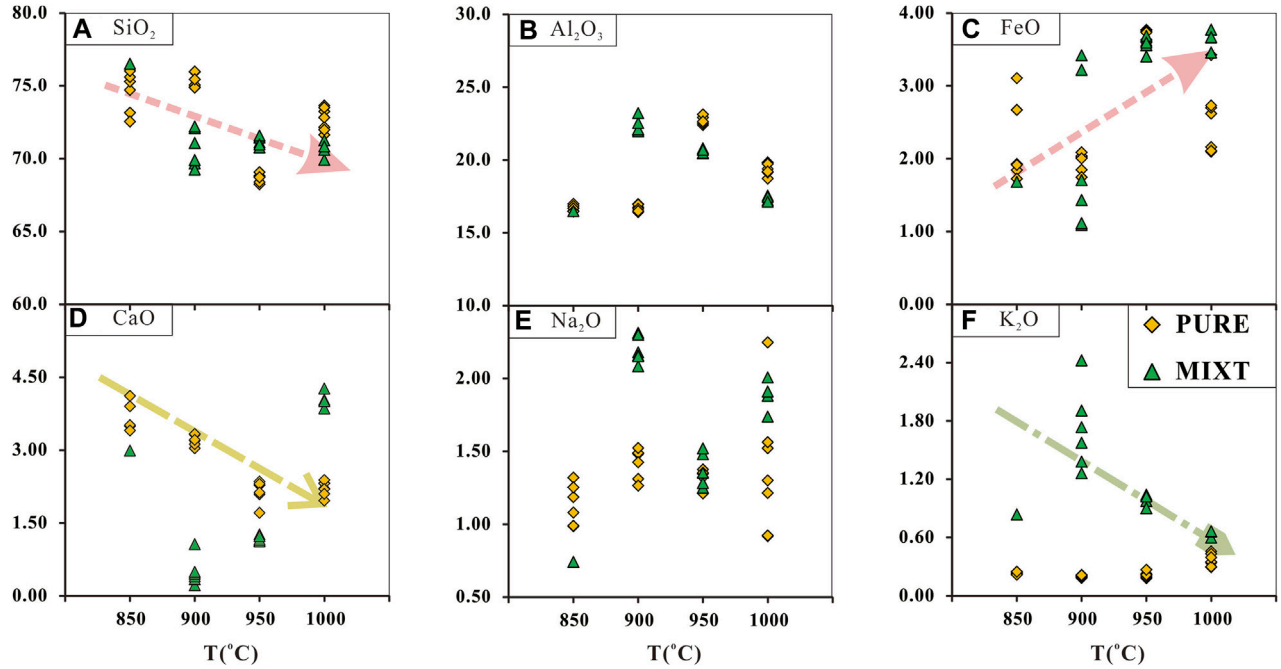

FIGURE 4 | Plots of major elements abundance of partial melts. PURE, melts generated from pure 18TH-02 (garnet plagioamphibolite, as the representative of metamorphic subducted oceanic crust); MIXT, melts generated from a mixture of 90 wt% 18TH-02 power and 10 wt% 18TH-07 (plagioclase slate, as the representative of metamorphic subducted terrigenous sediments). All the qualified original data of partial melts are shown in this figure; these data are listed in **Supplementary Table S4** original major data. The pink arrows mark the variation trend of oxide abundance in partial melts from both these two starting materials as the temperature rose. The golden yellow arrow marks the variation trend of CaO in partial melts from PURE as the temperature rose. The grass green arrow marks the variation trend of K_2O in partial melts from MITX as the temperature rose.

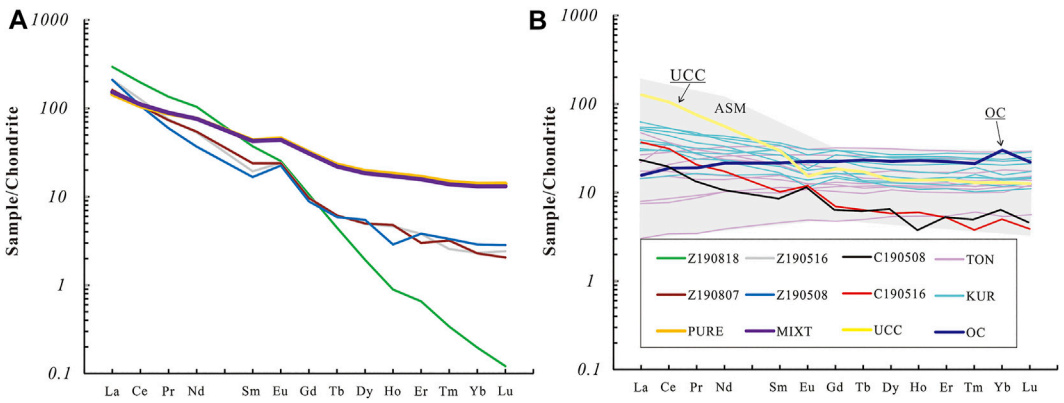

FIGURE 5 | Chondrite-normalized rare earth element (REE) abundance patterns of the partial melts **(A)** and calculated results compared with field observations **(B)**. C1-Chondrite data are from Sun and Mcdonough (1989). Z190818, Z190516, Z190708, and Z190508, partial melts from our experiment; PURE and MIXT, our starting materials. C190508 and C190516, calculated results based on our experiment data, the partition coefficient (D_i) between melts and starting material from our experiment in runs at 950°C could be got [D_i = (i in Melt)/(i in Starting material)], then we used this partition coefficient to calculate the i content in melts from pure OC (OC = oceanic crust) (C190508) and 10%UCC (UCC = Upper Continental Crust) + 90%OC (C190516), we use this method comparing the REE abundance from partial melting experiment and silicic arc magma located at Tonga Island and Kuril Island.; TON = typical REE abundance patterns from silicic magma located at Tonga Island, KUR = typical REE abundance patterns from silicic magma located at Kuril Island. ASM = arc silicic magma, REE abundance patterns from TON and KUR. Data of TON and KUR are also from the GEOROC website (http://georoc.mpch-mainz.gwdg.de/georoc/).

material was filled in gold sample capsules (with 3 mm outer diameter, 2.6 mm inner diameter, and 2.5 ± 0.2 mm height) and sealed, and then the capsule was covered by a thin hexagonal boron nitride sleeve and placed into the graphite heater. The centre of the capsule is 1 mm below the geometric centre of the graphite heater (close to the stainless steel) to get a stable thermal

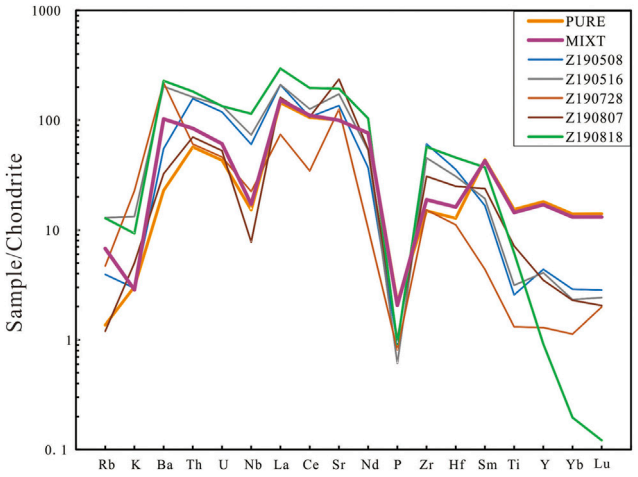

FIGURE 6 | Chondrite-normalized spidergram for the partial melts. C1-Chondrite data are from Sun and Mcdonough (1989), Z190728, Z190818, Z190516, Z190708, and Z190508, partial melts in runs from our experiment; PURE and MIXT, our starting materials.

field (Xia et al., 2014). In order to minimize adsorbed water, all the assemblies used in our experiment were heated at 110°C for 48 h before being used. Then the sample was fitted into a 10 mm diameter pressure plate one by one as shown in **Figure 2**.

All experiments were performed on a Rocktek-PC-1 type Piston-cylinder apparatus located in National Engineering Research Centre of Coal Mine Water Hazard Controlling, Suzhou University. The temperature was measured and controlled *via* NiCr-NiAl thermocouples with an accuracy of ±3°C. The temperature gradient of our sample was about 5°C, based on similar study results (Xia et al., 2014). The pressure was checked by NaCl melting (falling ball method), following the melting curve offered by Tingle et al. (1993). The error was within 0.1 GPa. According to our assessment of similar experiments, the oxygen fugacity within the experiment was close to FMQ (Tao et al., 2015), which is similar to the basaltic oceanic crust in the subducted margins.

In one run, the pressure rose to about 800 PSI by hand first. We then started heating with a 10°C/min increasing speed. When the temperature was up to 400°C, the pressure would continue to rise with a 10 PSI/min to the aim value. After the pressure rising to aim value, the temperature rose to the aim value with 10°C/min increasing speed. The pressure and temperature were maintained for 168 h, then quenched by turning the power off. The temperature fell to room temperature in 1 min. We then depressurized and removed the run product carefully from the capsule and mounted it in epoxy, which was polished for observation and analysis.

Analytical Method

The whole rock compositions (major and trace element) analyses of the two metamorphic rocks (18TH-02 and 18TH-07) were carried out in the State Key Laboratory of Ore Deposit Geochemistry, Institute of Geochemistry, Chinese Academy of Sciences, Guiyang, China. Their major elements were measured by an X-ray fluorescence spectrophotometer (XRF, PW4400, Axios), and the trace elements were measured by an inductively coupled plasma mass spectrometer (ICP-MS), in accordance with the analytical procedures given by Qi et al. (2000). Back-scattered electron (BSE) images and the major element content of minerals in these two metamorphic rocks and in the experimental products were obtained using a JOEL JXA-8100 electron microprobe at the Key Laboratory of Mineralization and Dynamics, Chang'an University, Xi'an, China. The beam used for the analyses of the melt was 5–10 μm, with an accelerating voltage of 15 kV and beam current of 2 nA. The possible losses of Na and K in the melt were addressed using the same method in Zang et al. (2020) Trace-element concentrations within the melts (glass) of run products were measured by laser ablation ICP–MS using a GeoLasPro laser ablation system and an Agilent 7700x ICP–MS instrument at the Sample Solution Analytical Technology Company, Wuhan, China. The analytical procedures used are outlined in detail by Liu et al. (2008).

EXPERIMENTAL RESULTS

Phase Assemblages

The run conditions and mineral assemblages in their products are listed in **Supplementary Table S2**. Representative BSE photographs of the experimental products are shown in **Figure 3**. There is no difference between the mineral assemblages of these two starting materials at all run conditions. In runs at 850–950°C, there are Amp + Cpx + Pl + Grt + Melt in all run products. While in runs at 1,000°C, the Amp disappeared and the mineral assemblage is Cpx + Pl + Grt + Melt. However, melts (quenched to glass) in run products of PURE are very rare. The contents of them are about 2–3 vol% in runs at 850 and 900°C. This content increases to about 5 vol% in run product at 950°C and about 10 vol% in run product at 1,000°C (**Figure 3A**). The content of melts in run products of MIXT is different from those of PURE at over 900°C. In the run at 850°C, the melt in run products of MIXT is also very rare, which is consistent with the run from PURE at 850°C. In runs at 900°C, the content of melt in MIXT's run products increases to about 10 vol%. This content increases to 20 vol % at 950°C and 35 vol% at 1,000°C (**Figure 3B**). The melting trend of MITX is consistent with the result reported by Zang et al. (2020). The mixture starting materials will increase in melting percentage at over ~925°C.

The minerals in run products of PURE at 850°C are all very small; the size of all minerals (Amp, Cpx, Grt and Pl) is all about 15 μm. In run products at over 900°C, the size of mineral crystals increases with run temperature. The size of Amp increases most obviously with the run temperature increasing, it is about 40 μm in run product at 900°C and about 100 μm in run product at 950°C. The size of the other three minerals is also increased with run temperature. The size of Cpx is 20, 30, and 50 μm respectively in runs at 900°C, 950°C, and 1,000°C. The size of Pl is 20, 40, 50 μm respectively in runs at 900°C, 950°C, and 1,000°C. The size of Grt is 20, 25, and 50 μm respectively in runs at 900°C, 950°C, and 1,000°C. The minerals in run products of MIXT at 850°C is also very small. The size of all minerals is the same as those of

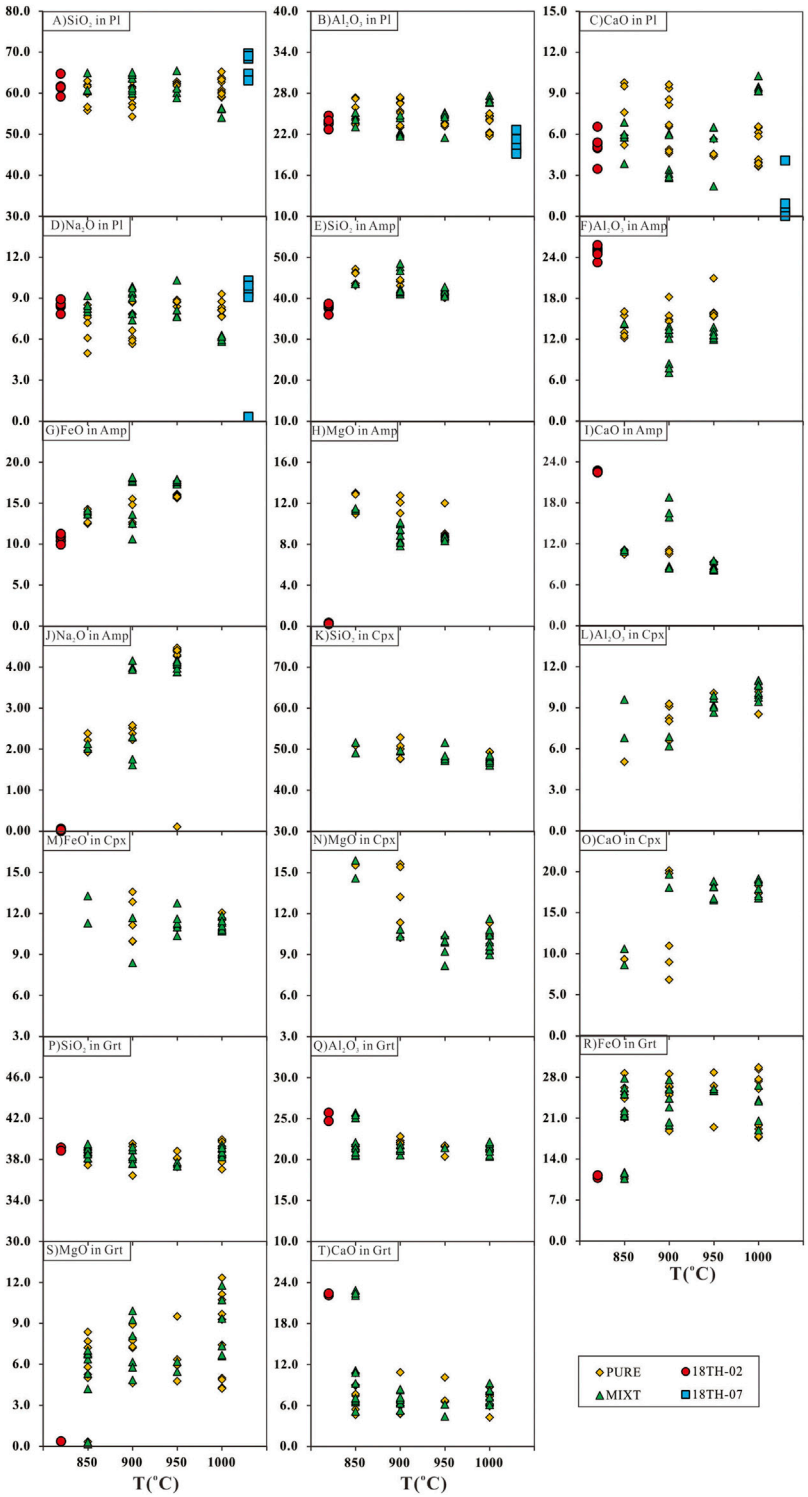

FIGURE 7 | Plots of major-element oxide concentrations in plagioclase **(A-D)**, amphibole **(E-J)**, clinopyroxene **(K-O)**, and garnet **(P-T)**. These minerals are from starting materials (18TH-02 and 18TH-07) run products from PURE and MITX.

PURE, at about 15 μm. The size of minerals in MIXT's run products is also increased with run temperature. The size of Amp is 25 and 50 μm respectively in runs at 900 and 950°C. The size of Cpx is 20, 30, and 50 μm respectively in runs of 900°C, 950°C, and 1,000°C. The size of Pl is 20, 20, and 30 μm respectively in runs at 900°C, 950°C, and 1,000°C. The size of Grt is 20, 30, and 60 μm

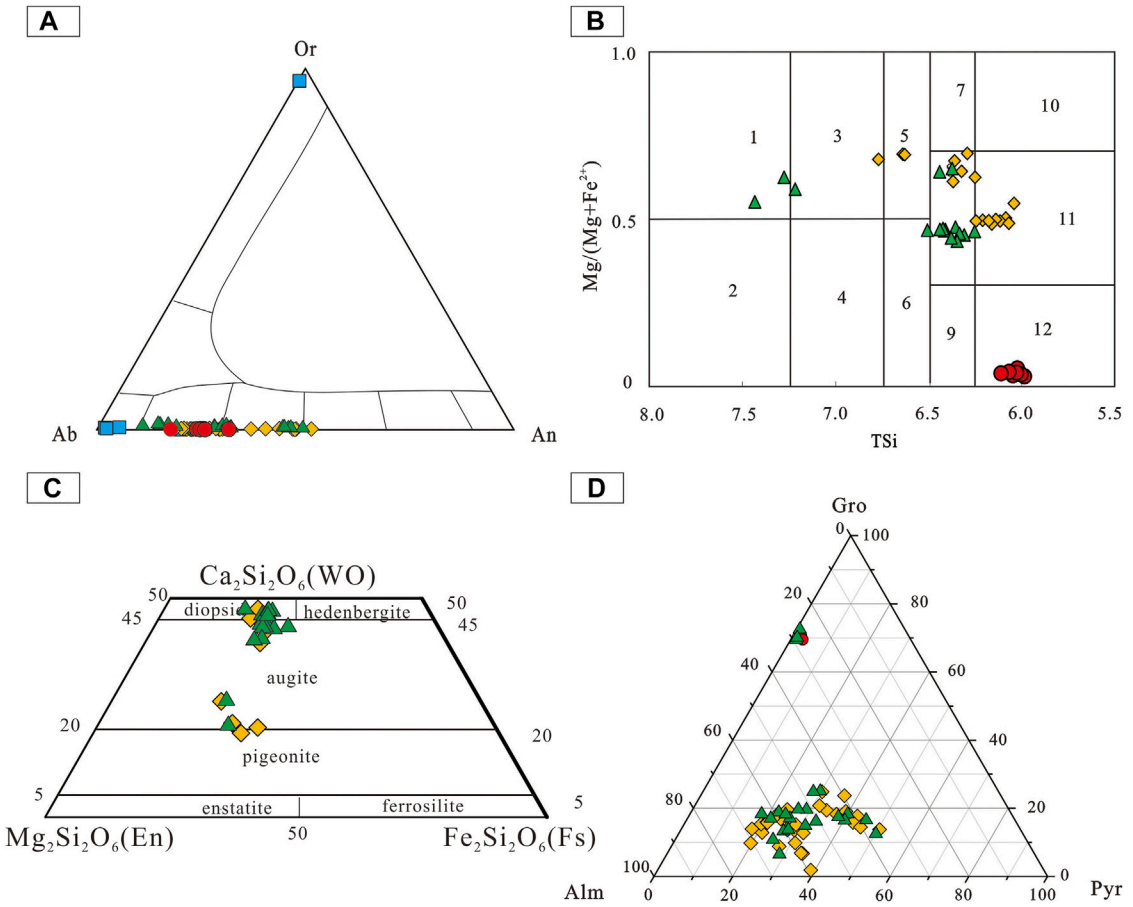

FIGURE 8 | Or-Ab-An classification map of plagioclase **(A)**, classification map of amphibole after Leake et al. (1997) **(B)**, classification map of clinopyroxene after Morimoto (1988) **(C)**, and Alm-Pyr-Gro classification map of garnet **(D)**. These minerals are mentioned in **Figure 7**.

respectively in runs at 900°C, 950°C, and 1,000°C. In all run products, Grt is euhedral crystal and other kinds of minerals are subhedral crystals.

Major Elements and Trace Element Composition of Partial Melts and Residual Minerals

The major and trace element composition of partial melts from run products reported in this paper is listed in **Supplementary Table S3**. The variation trend with run temperature rising is shown in **Figure 4**. As the run temperature rose, the SiO_2 contents of melts in all run products decreased, whereas the FeO contents of these melts show a reverse trend. The CaO content of melts from PURE showed a similar variation trend as SiO_2 contents, while the CaO content of melts from MITX at over 900°C showed a reverse trend. The K_2O content of partial melts from MIXT shows a decreasing trend as run temperature ring, while the K_2O content of partial melts from PURE is almost unchanged due to their starting materials having so little K_2O. The Al_2O_3 content of melts in all runs is between 15 and 25wt% is affected by the amount of feldspar. The Na_2O content of partial melts is about 0.5–2.5wt%. Chondrite-normalized REE patterns for the partial melts are shown in **Figure 5**. The REE patterns of the partial melts are enriched in light REE, compared with their parents, the HREE of partial melts is more depleted (**Figure 5A**). In chondrite-normalized spidergram, the partial melt depleted in Ti, Y, Yb, and Lu compared with starting material, as shown in **Figure 6**.

The SiO_2, Al_2O_3, CaO, and Na_2O content of Pl in the starting material and run products are shown in **Figure 7A–D**. Compared with the Pl in the starting material, the Pl in run products from PURE enriched in CaO and depleted in Na_2O, which was the same as the Pl in the run product at 1,000°C from MIXT. The other Pl in run products from MIXT have the same variation range with their starting material. On the Or-Ab-An classification map, all Pl in run products are plagioclase series (**Figure 8A**). The SiO_2, Al_2O_3, FeO, MgO, CaO, and Na_2O content of Amp in starting material and run products are shown in **Figure 7E–J**. Compared with starting Amp in 18TH-02, Amp in all run products is enriched in SiO_2, FeO, MgO, and Na_2O, and depleted in Al_2O_3 and CaO. This difference is also very obvious in the classification map of amphibole (Leake et al., 1997) as shown in **Figure 8B**. The SiO_2, Al_2O_3, FeO, MgO, and

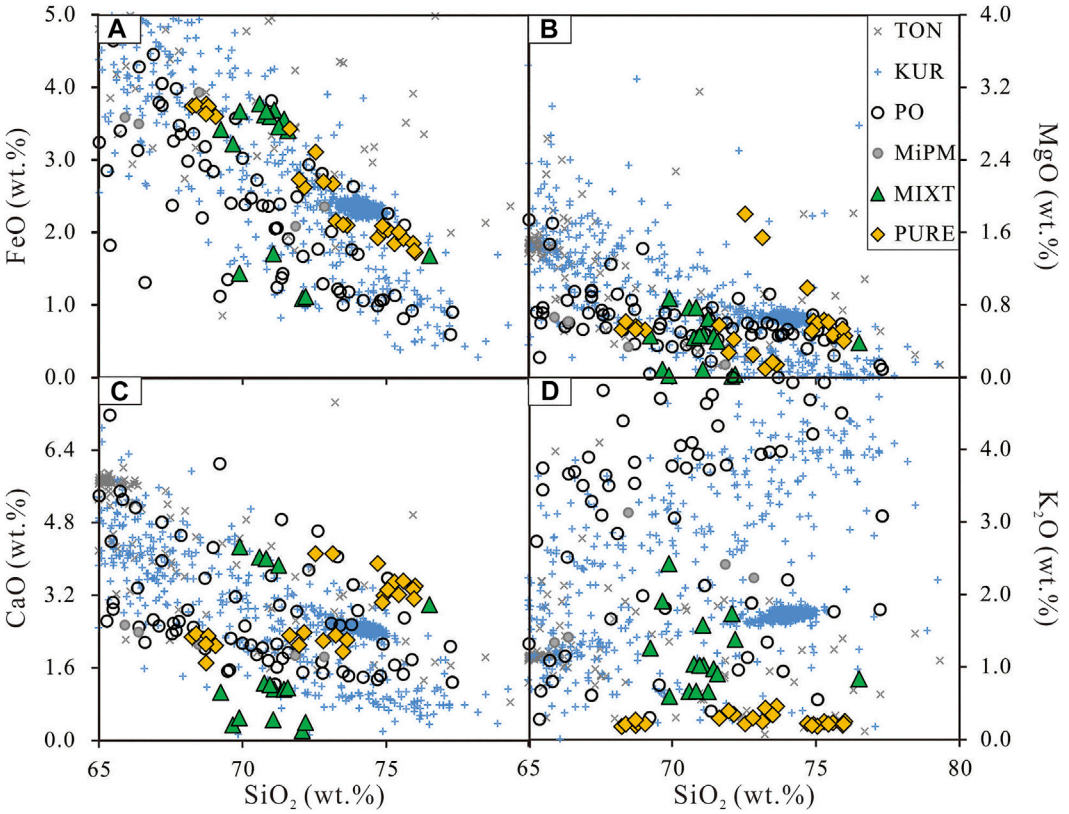

FIGURE 9 | Harker diagrams of melts from partial melting experiment and filed observation. TON, KUR, and MiPM are the same with **Figure 1** on their meaning and data; PO, melts from partial melting experiments of pure basic rocks, the data including BaDE, AmPM, and GaPM in **Figure 1**; PURE and MITX are same to **Figure 4**.

CaO content of Cpx in run products are shown in **Figure 7K–O**. As the run temperature rises, the Al_2O_3 content of Cpx in all run products increases, while the MgO content shows a reverse trend. In the classification map of clinopyroxene (Morimoto, 1988), the Cpx from runs at 850 and 900°C are enriched in En and others enriched in Wo (**Figure 8C**). The SiO_2, Al_2O_3, FeO, MgO, and CaO content of Grt in starting material and run products are shown in **Figure 7P–T**. Compared with the starting Grt in 18TH-02, the Grt in all run products was enriched in FeO and MgO, and depleted in CaO, which is consistent with the Alm-Pyr-Gro classification map, as shown in **Figure 8D**.

DISCUSSION

Firstly, we need to consider whether the equilibrium was approached in our run products. According to similar experimental studies (Beard and Lofgren, 1991; Sen and Dunn, 1994; Xiong et al., 2005; Qian and Hermann, 2013; Zang et al., 2020) that undertook partial experiments at ≥900°C, a run time of ≥96 h could be regarded as approaching equilibrium. Our run time was 168 h, nearly twice as long as the run time used in previous studies to approach equilibrium, meaning the melts (glass) in our run products show component differences (**Figure 4**). The component difference of melt may be caused by poor liquidity due to low degree partial melting. The equilibrium in our run products should be a local one. Furthermore, the Fe–Mg exchange distribution coefficients ($K_{d,\ Fe-Mg}$) of mineral–melt were also calculated. The $K_{d,\ Fe-Mg}$ value of Cpx was 0.06–0.53, the $K_{d,\ Fe-Mg}$ value of Grt was 0.32–1.71, compared with the value of similar studies (Xiong et al., 2005; Qian and Hermann, 2013; Zang et al., 2020). These $K_{d,\ Fe-Mg}$ values of minerals are acceptable, indicating the equilibrium is approached. The major and trace element compositions at different sites are homogeneous (within analytical error), indicating that equilibrium was attained.

Comparison Between Melts From PURE and MITX

We then compared melts from PURE and MITX. With the sediment addition, the MITX increased its melting percentage at over 900°C, which is the same as previous studies (Mccarthy and Patiño Douce, 1997; Zang et al., 2020), but the melting percentage in this study is very small compared with others. The reasons for this may be the following: 1) there is no free water added in our experiment: the water in our run products is from dehydration of Amp in staring materials (18 TH-02). The water content of our experiment is lower than similar experiments with water added before the Amp is destroyed. 2) These two staring

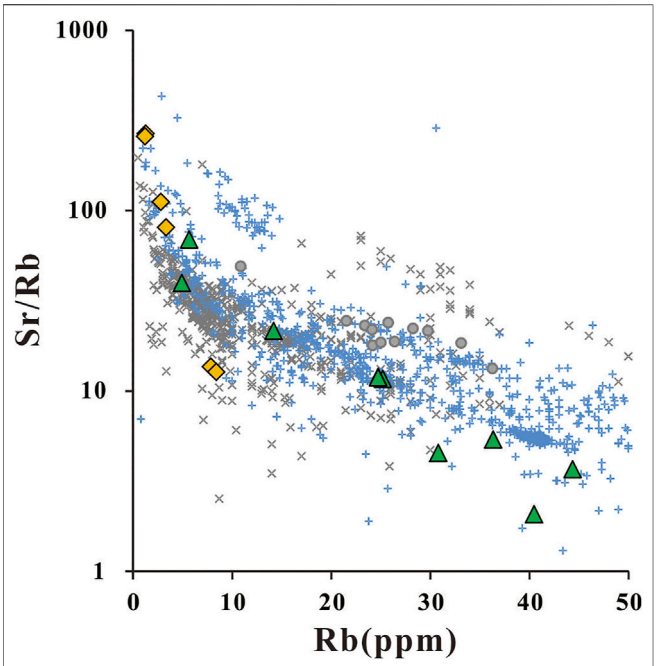

FIGURE 10 | Plots of Sr/Rb VS Rb. Symbols are the same as **Figure 9**, the original data of PURE and MITX are listed in **Supplementary Table S5** original trace data. Then we used the same computing method mentioned in **Figure 5** to revise our data. The trace element data of melts from pure basic rocks (Xiong et al., 2006; Qian and Hermann, 2013) are out of the variation range, so there are no OP data shown in this figure.

materials are metamorphic rocks, unlike basalt, there is no glass in them. By comparing the melting percentage of PURE and MITX, the melt percentage of MIXT is much higher than the one of PURE in runs at 950and 1,000°C, and the increasing value of MITX is more than the total content of addition metamorphic subducted terrigenous sediment. This result indicates the effect of sediment addition on increasing melting percentage needs a "staring temperature" (950°C in this paper). The addition sediments significantly help the partial melting of subducted oceanic crust over this staring temperature.

We then compared the chemical composition of melt from PURE and MIXT over the staring temperature, to consider which one could be the real magma. As shown in **Figure 4** the melt from MIXT are enriched in Na_2O and K_2O and depleted in Al_2O_3 in major elements than the melt from PURE in runs at 950and 1,000°C. For trace elements, the melts from the mixture enrich more in Rb than the PURE because the MIXT has a very high content of Rb compared to PURE.

Affect of Sediment Addition on Silicic Arc Magma Generation

Possible ways in which the silicic arc magma is generated include: 1) that it is generated by partial melting of the subducted altered oceanic crust; or 2) that it could have evolved from mantle-derived mafic magmas (see Clemens et al. (2021) and references therein). It seems unlikely that the majority of silicic melt could be evolved from basalt for the following reasons: 1) silicic melt has a high viscosity and crystallization differentiation is difficult (even this process could be achieved with a large number of chadacrysts that are not completely separated from silicic magma, but the chadacrysts are not so widely distributed); 2) the crystallization differentiation of magma could be detected *via* geochemical data, such as separation of feldspar can lead to Eu anomalies, however, there are no obvious Eu anomalies in current data relating to rocks (SiO2 ≥ 52wt%) from Tonga and Kuril (**Figure 5B**). The partial of subducted altered oceanic crust with or without sediments could be an important way of generating silicic magma at convergent plate margins.

In terms of the effect of sediment addition on silicic arc magma generation, we compared the major element content of rocks from field observation and melt from partial experiments on basic rocks and basalt-sediment mixtures *via* Harker diagrams (**Figure 9**). For major elements, melts from the experiment seem to all cover the variation range of arc silicic magma located on Tonga and the Kuril Islands. The melts from MIXT also match the field observation better on the SiO_2-K_2O diagram because the PURE (and the oceanic crust) is depleted on K_2O. The high K_2O silicic magmas may thus generate from the mixture of magmatic sources. Besides the major elements, the trace element of rocks from field observation and melt from partial experiments are also compared *via* plots of Sr/Rb—Rb (**Figure 10**). Unlike the major elements, the melts from the mixture match the field observation better. Note that the trace element data on melts from pure basic rocks (Xiong et al., 2006; Qian and Hermann, 2013) are out of the variation range shown in **Figure 10**. Furthermore, the REE abundance patterns of partial melts from magmatic sources with sediment addition have an obvious right-leaning than the one from the pure magmatic source. The partial melts from the mixture magmatic sources match the silicic magma from Kuril Island better than the melts from pure magmatic sources. This result indicates that the arc silicic magma is mainly generated from the partial melting of a mixture of basic oceanic crust and sediments. The sediments also offer great help in establishing the partial melting percentage. This may also contribute to the formation of silicic arc magma.

CONCLUSION

Our experiments reveal that the addition of 10 wt% sediment has an obvious effect on the partial melting of basic rocks. These results are based on examination of the chemical composition of experimental partial melts produced from a series of comparative partial melting experiments on a garnet plagioamphibolite and a 90 wt% garnet plagioamphibolite +10 wt% plagioclase slate mixture at 850–1,000°C/1.5 GPa. The importance of sediment addition was also verified and identified in the generation of arc silicic magma. The main conclusions of this study are as follows:

1) A small additional amount of (10 wt%) altered sediment makes the metamorphic subducted oceanic crust generate

more silicic melt with geochemical characteristics of higher Na_2O and K_2O and lower Al_2O_3 in major element and high Rb content in trace element at over 950°C.

2) Silicic arc magma may generate from partial melting of metamorphic subducted oceanic crust with sediments thereon. The addition of sediment contributes to their high Rb content and the partial melting percentage of their parent rock.

DATA AVAILABILITY STATEMENT

The original contributions presented in the study are included in the article/**Supplementary Material**, further inquiries can be directed to the corresponding author.

AUTHOR CONTRIBUTIONS

All authors listed have made a substantial, direct, and intellectual contribution to the work and approved it for publication.

FUNDING

This work was financially supported by the Natural Science Foundation of China (No. 42073059 and No. 41502057), the Youth Project of the Provincial Natural Science Foundation of Anhui (2108085QD162), and the Foundation of Suzhou University (No. gxyq2020060, No. 2019XJZY53).

ACKNOWLEDGMENTS

We are grateful to the two reviewers for their helpful comments and suggestions on the manuscript. We thank Lidong Dai for his invitation, Minwu Liu for support and help in electron microprobe analysis.

SUPPLEMENTARY MATERIAL

The Supplementary Material for this article can be found online at: https://www.frontiersin.org/articles/10.3389/feart.2022.851236/full#supplementary-material

REFERENCES

Baker, M. B., Hischmann, M. M., Ghiorso, M. S., and Stolper, E. M. (1995). Compositions of Near-Solidus Peridotite Melts from Experiments and Thermodynamic Calculations. *Nature* 375, 308–311. doi:10.1038/375308a0

Beard, J. S., and Lofgren, G. E. (1991). Dehydration Melting and Water-Saturated Melting of Basaltic and Andesitic Greenstones and Amphibolites at 1, 3, and 6. 9 Kb. *J. Petrol.* 32, 465–501. doi:10.1093/petrology/32.2.365

Clemens, J. D., Stevens, G., and Mayne, M. J. (2021). Do arc Silicic Magmas Form by Fluid-Fluxed Melting of Older Arc Crust or Fractionation of Basaltic Magmas? *Contrib. Mineral. Petrol.* 176, 44. doi:10.1007/s00410-021-01800-w

Cruz-Uribe, A. M., Marschall, H. R., Gaetani, G. A., and Le Roux, V. (2018). Generation of Alkaline Magmas in Subduction Zones by Partial Melting of Mélange Diapirs-An Experimental Study. *Geology* 46, 343–346. doi:10.1130/g39956.1

Elliott, T. (2003). Tracers of the Slab. *Geophys. Monogr. Ser.* 238, 23–45. doi:10.1029/138gm03

Frster, M. W., and Selway, K. (2021). Melting of Subducted Sediments Reconciles Geophysical Images of Subduction Zones. *Nat. Commun.* 12, 1320. doi:10.1038/s41467-021-21657-8

Gan, L., Tang, H., and Han, Y. (2010). Geochronology and Geochemical Characteristics of Yemaquan Granitic Pluton in East Junggar, Xinjiang. *Act a petrologica sinica* 26, 2374–2388. (in Chinese with English abstract).

Hermann, J., and Spandler, C. J. (2008). Sediment Melts at Sub-arc Depths: an Experimental Study. *J. Petrol.* 49, 717–740. doi:10.1093/petrology/egm073

Hildreth, W., and Moorbath, S. (1988). Crustal Contributions to Arc Magmatism in the Andes of Central Chile. *Contr. Mineral. Petrol.* 98, 455–489. doi:10.1007/bf00372365

Hu, Y., Teng, F. Z., Plank, T. A., and Huang, K. J. (2017). Magnesium Isotopic Composition of Subducting Marine Sediments. *Chem. Geology.* 46, 15–31. doi:10.1016/j.chemgeo.2017.06.010

Koepke, J. r., Feig, S. T., Snow, J., and Freise, M. (2004). Petrogenesis of Oceanic Plagiogranites by Partial Melting of Gabbros: an Experimental Study. *Contrib. Mineralogy Petrol.* 146, 414–432. doi:10.1007/s00410-003-0511-9

Leake, B. E., Woolley, A. R., Arps, C. E. S., Birch, W. D., Gilbert, M. C., Grice, J. D., et al. (1997). Nomenclature of Amphiboles; Report of the Subcommittee on Amphiboles of the International Mineralogical Association Commission on New Minerals and Mineral Names. *Mineral. Mag.* 61, 295–310. doi:10.1180/minmag.1997.061.405.13

Li, W., and Ni, H. (2020). Dehydration at Subduction Zones and the Geochemistry of Slab Fluids. *Sci. China Earth Sci.* 63, 1925–1937. doi:10.1007/s11430-019-9655-1

Liu, Y., Chen, C., He, D., and Chen, W. (2019). Deep Carbon Cycle in Subduction Zones. *Sci. China Earth Sci.* 62, 1764–1782. doi:10.1007/s11430-018-9426-1

Liu, Y., Hu, Z., Gao, S., Günther, D., Xu, J., Gao, C., et al. (2008). In Situ Analysis of Major and Trace Elements of Anhydrous Minerals by LA-ICP-MS Without Applying an Internal Standard. *Chem. Geol.* 257, 34–43.

Maitre, R. W. L. (1989). *A Classification of Igneous Rocks and Glossary of Terms : Recommendations of the International Union of Geological Sciences Subcommission on the Systematics of Igneous Rocks* Blackwell.

Mccarthy, T. C., and Patiño Douce, A. E. (1997). Experimental Evidence for High-Temperature Felsic Melts Formed during Basaltic Intrusion of the Deep Crust. *Geol* 25, 463–466. doi:10.1130/0091-7613(1997)025<0463:eefhtf>2.3.co;2

Morimoto, N. (1988). Nomenclature of Pyroxenes. *Mineralogy Petrol.* 39, 55–76. doi:10.1007/bf01226262

Morris, J. D., Leeman, W. P., and Tera, F. (1990). The Subducted Component in Island Arc Lavas: Constraints from Be Isotopes and B-Be Systematics. *Nature* 344, 31–36. doi:10.1038/344031a0

Nandedkar, R. H., Ulmer, P., and Müntener, O. (2014). Fractional Crystallization of Primitive, Hydrous Arc Magmas: an Experimental Study at 0.7 GPa. *Contrib. Mineral. Petrol.* 167, 1015. doi:10.1007/s00410-014-1015-5

Nielsen, S. G., and Marschall, H. R. (2017). Geochemical Evidence for Mélange Melting in Global Arcs. *Sci. Adv.* 3, e1602402. doi:10.1126/sciadv.1602402

Niu, Y. (2013). *Global Tectonics and Geodynamics : A Petrological and Geochemical Approach*. Beijing: science press.

Pelleter, A. A., Prouteau, G., and Scaillet, B. (2021). The Role of sulphur on the Melting of Ca-Poor Sediment and on Trace Element Transfer in Subduction Zones: an Experimental Investigation. *J. Petrol.* 62, egab005. doi:10.1093/petrology/egab005

Peter, U., Ralf, K., and Othmar, M. (2018). Experimentally Derived Intermediate to Silica-Rich Arc Magmas by Fractional and Equilibrium Crystallization at 1·0 GPa: an Evaluation of Phase Relationships, Compositions, Liquid Lines of Descent and Oxygen Fugacity. *J. Petrol.* 59, 11–58. doi:10.1093/petrology/egy017

Plank, T. (2005). Constraints from Thorium/Lanthanum on Sediment Recycling at Subduction Zones and the Evolution of the Continents. *J. Petrol.* 46, 921–944. doi:10.1093/petrology/egi005

Qi, L., Jing, H., and Gregoire, D. C. (2000). Determination of Trace Elements in Granites by Inductively Coupled Plasma Mass Spectrometry. *Talanta* 51, 507–513. doi:10.1016/s0039-9140(99)00318-5

Qian, Q., and Hermann, J. (2013). Partial Melting of Lower Crust at 10-15 Kbar: Constraints on Adakite and TTG Formation. *Contrib. Mineral. Petrol.* 165, 1195–1224. doi:10.1007/s00410-013-0854-9

Rapp, R. P., and Watson, E. B. (1995). Dehydration Melting of Metabasalt at 8-32 Kbar: Implications for Continental Growth and Crust-Mantle Recycling. *J. Petrol.* 36, 891–931. doi:10.1093/petrology/36.4.891

Rapp, R. P., Watson, E. B., and Miller, C. F. (1991). Partial Melting of Amphibolite/eclogite and the Origin of Archean Trondhjemites and Tonalites. *Precambrian Res.* 51, 1–25. doi:10.1016/0301-9268(91)90092-o

Rushmer, T. (1991). Partial Melting of Two Amphibolites: Contrasting Experimental Results under Fluid-Absent Conditions. *Contr. Mineral. Petrol.* 107, 41–59. doi:10.1007/bf00311184

Sen, C., and Dunn, T. (1994). Dehydration Melting of a Basaltic Composition Amphibolite at 1.5 and 2.0 GPa: Implications for the Origin of Adakites. *Contr. Mineral. Petrol.* 117, 394–409. doi:10.1007/bf00307273

Shu, Y., Nielsen, S. G., Zeng, Z., Shinjo, R., and Shuai, C. (2017). Tracing Subducted Sediment Inputs to the Ryukyu Arc-Okinawa Trough System: Evidence from Thallium Isotopes. *Geochimica Et Cosmochimica Acta* 217, 462–491. doi:10.1016/j.gca.2017.08.035

Sisson, T. W., Ratajeski, K., Hankins, W. B., and Glazner, A. F. (2005). Voluminous Granitic Magmas from Common Basaltic Sources. *Contrib. Mineral. Petrol.* 148, 635–661. doi:10.1007/s00410-004-0632-9

Sun, S. S., and Mcdonough, W. F. (1989). Chemical and Isotopic Systematics of Oceanic Basalts: Implications for Mantle Composition and Processes. *Geol. Soc. Spec. Publ.* 42, 313–345.

Sun, W., Teng, F.-Z., Niu, Y.-L., Tatsumi, Y., Yang, X.-Y., and Ling, M.-X. (2014). The Subduction Factory: Geochemical Perspectives. *Geochimica Et Cosmochimica Acta* 143, 1–7. doi:10.1016/j.gca.2014.06.029

Takahahshi, E., Nakajima, K., and Wright, T. L. (1998). Origin of the Columbia River Basalts: Melting Model of a Heterogeneous Plume Head. *Earth Planet. Sci. Lett.* 162, 63–80. doi:10.1016/s0012-821x(98)00157-5

Tao, R., Zhang, L., and Liu, X. (2015). Oxygen Fugacity of Earth's Mantle and Deep Carbon Cycle in the Subduction Zone. *Acta Petrologica Sinica* 31, 1879–1890.

Tatsumi, Y. (2001). Geochemical Modeling of Partial Melting of Subducting Sediments and Subsequent Melt-Mantle Interaction: Generation of High-Mg Andesites in the Setouchi Volcanic belt, Southwest Japan. *Geol* 29, 323–326. doi:10.1130/0091-7613(2001)029<0323:gmopmo>2.0.co;2

Tera, F., Brown, L., Morris, J., Sacks, I. S., Klein, J., and Middleton, R. (1986). Sediment Incorporation in Island-Arc Magmas: Inferences from 10Be. *Geochimica Et Cosmochimica Acta* 50, 535–550. doi:10.1016/0016-7037(86)90103-1

Tingle, T. N., Green, H. W., Young, T. E., and Koczynski, T. A. (1993). Improvements to Griggs-type Apparatus for Mechanical Testing at High Pressures and Temperatures. *Pageoph* 141, 523–543. doi:10.1007/bf00998344

Wang, X. C., Wilde, Z. A., Li, C., Lei, S. K., and Pandit, K. (2021). Decoupling between Oxygen and Radiogenic Isotopes – Evidence for Generation of Juvenile continental Crust by Partial Melting of Subducted Oceanic Crust. *J. Earth Sci.* 32, 14. doi:10.1007/s12583-020-1095-2

Wei, C., and Zheng, Y. (2020). Metamorphism, Fluid Behavior and Magmatism in Oceanic Subduction Zones. *Sci. China Earth Sci.* 63, 52–77. doi:10.1007/s11430-019-9482-y

Xia, Y., Xing, D., Song, M., Xiong, X., and Hao, X. (2014). Temperature Determination and Thermal Structure Analysis on the Pressure Assembly of a Piston-Cylinder Apparatus. *Chin. J. High Press. Phys.* 28, 262–272. doi:10.11858/gywlxb.2014.03.002

Xiong, X., Adam, J., Green, T. H., Niu, H., Wu, J., and Cai, Z. (2006). Trace Element Characteristics of Partial Melts Produced by Melting of Metabasalts at High Pressures: Constraints on the Formation Condition of Adakitic Melts. *Sci. China Ser. D* 49, 915–925. doi:10.1007/s11430-006-0915-2

Xiong, X. L., Adam, J., and Green, T. H. (2005). Rutile Stability and Rutile/melt HFSE Partitioning during Partial Melting of Hydrous basalt: Implications for TTG Genesis. *Chem. Geology.* 218, 339–359. doi:10.1016/j.chemgeo.2005.01.014

Xiong, X., Xingcheng, L., Li, L., Jintuan, W., Wei, C., Mengfei, R., et al. (2020). The Partitioning Behavior of Trace Elements in Subduction Zones: Advances and Prospects. *Sci. China Earth Sci.* 63, 1938–1951. doi:10.1007/s11430-019-9631-6

Yaxley, G. M., and Green, D. H. (1998). Reactions between Eclogite and Peridotite: Mantle Refertilisation by Subduction of Oceanic Crust. *Schweizerische Mineralogische Und Petrographische Mitteilungen* 78, 243–255.

Zang, C., Tang, H., and Wang, M. (2020). Effects of Sediment Addition on Magma Generation from Oceanic Crust in a post-collisional Extensional Setting: Constraints from Partial Melting Experiments on Mudstone-Amphibolite/basalt at 1.0 and 1.5 GPa. *J. Asian Earth Sci.* 188, 104111. doi:10.1016/j.jseaes.2019.104111

Zhang, Y., Liang, X., Wang, C., Jin, Z., Zhu, L., and Gan, W. (2020). Experimental Constraints on the Partial Melting of Sediment-Metasomatized Lithospheric Mantle in Subduction Zones. *Am. Mineral.* 105, 1191–1203. doi:10.2138/am-2020-7403

Zhang, Y., Wang, C., Zhu, L., Jin, Z., and Li, W. (2019). Partial Melting of Mixed Sediment-Peridotite Mantle Source and its Implications. *J. Geophys. Res. Solid Earth* 124, 6490–6503. doi:10.1029/2019jb017470

Zhang, Z., Ding, H., Dong, X., and Tian, Z. (2020). Partial Melting of Subduction Zone. *Act a petrologica sinica* 36, 27. doi:10.18654/1000-0569/2020.09.01

Zheng, J., Xiong, Q., Zhao, Y., and Li, W. (2019). Subduction-zone Peridotites and Their Records of Crust-Mantle Interaction. *Sci. China Earth Sci.* 62, 1033–1052. doi:10.1007/s11430-018-9346-6

Zheng, Y., Chen, Y., Dai, L., and Zhao, Z. (2015). Developing Plate Tectonics Theory from Oceanic Subduction Zones to Collisional Orogens. *Sci. China Earth Sci.* 58, 1045–1069. doi:10.1007/s11430-015-5097-3

Conflict of Interest: The authors declare that the research was conducted in the absence of any commercial or financial relationships that could be construed as a potential conflict of interest.

Advantages of publishing in Frontiers

OPEN ACCESS
Articles are free to read for greatest visibility and readership

FAST PUBLICATION
Around 90 days from submission to decision

HIGH QUALITY PEER-REVIEW
Rigorous, collaborative, and constructive peer-review

TRANSPARENT PEER-REVIEW
Editors and reviewers acknowledged by name on published articles

Frontiers
Avenue du Tribunal-Fédéral 34
1005 Lausanne | Switzerland

Visit us: www.frontiersin.org
Contact us: frontiersin.org/about/contact

REPRODUCIBILITY OF RESEARCH
Support open data and methods to enhance research reproducibility

DIGITAL PUBLISHING
Articles designed for optimal readership across devices

FOLLOW US
@frontiersin

IMPACT METRICS
Advanced article metrics track visibility across digital media

EXTENSIVE PROMOTION
Marketing and promotion of impactful research

LOOP RESEARCH NETWORK
Our network increases your article's readership